Deformation and damage mechanisms of ODS steels under high-temperature cyclic loading

Zur Erlangung des akademischen Grades
Doktor der Ingenieurwissenschaften
der Fakultät für Maschinenbau
Karlsruher Institut für Technologie (KIT)

genehmigte
Dissertation
von

M.Tech. Ankur Chauhan

Aus

Haridwar, Indien

Abstract

The aggressive operating conditions of future nuclear power plants including generation IV fission and fusion reactors will be beyond those experienced in current nuclear power plants. Hence, the high irradiation resistance, the high creep resistance as well as the high fatigue strength are the main material properties that will be required to build future reactors with enhanced efficiency and safety. Due to their good resistance to swelling under irradiation and their improved mechanical properties, oxide dispersion strengthened (ODS) steels are promising structural material candidates. Nevertheless, a clear understanding of their deformation and damage mechanisms under various loading conditions (especially cyclic loading) are still lacking. In this scope, this work has been performed to obtain a better description of the deformation and damage mechanisms of a tempered martensitic Fe-9%Cr based ODS steel. This includes understanding of its monotonic behavior by testing under tensile loading, pure-fatigue/continuous cycling (PF/CC) response by examining within low-cycle fatigue (LCF) regime and creep-fatigue (CF) behavior by introducing tensile hold-time in PF/CC waveform.

Prior to testing, comprehensive description of the microstructure in undeformed state is necessary, which was uncovered by means of electron backscatter diffraction (EBSD) and transmission electron microscopy (TEM). Thereafter, tensile tests were performed within the temperature range varying from room temperature (RT) to 800 °C at the nominal strain rates of 10^{-3} s^{-1} and 10^{-4} s^{-1}. The obtained results were analyzed to visualize the

influence of temperature, strain rate and applied heat treatment. While the resulting microstructural evolution was characterized via TEM, the fracture surface investigations were carried by using scanning electron microscope (SEM). In addition, various active strengthening mechanism's contributions to measured RT yield stress were estimated and compared. Comparisons were also made with respect to the strength and ductility of the similar non-ODS as well as other ODS steels reported in literature.

High-temperature PF/CC behavior was delineated by performing fully reversed strain-controlled LCF tests (using nominal strain rate of 10^{-3} s^{-1} and triangular waveform with R = -1) in air at 550 °C and 650 °C for different strain amplitude values ranging from $\pm$ 0.4% to $\pm$ 0.9%. The cyclic stress-strain and strain-life relationships were obtained through the test results, and related LCF parameters were calculated. Postmortem microstructural investigations were carried out using both EBSD and TEM to shed light on the active deformation mechanisms. To explore damage mechanisms, fatigue crack initiation/propagation as well as fracture characteristics were examined via SEM. Lastly, thorough comparison of the measured cyclic stress response and lifetime were made with that of the similar non-ODS as well as other ODS steels tested or taken from literature.

Finally, CF interaction was studied at 650 °C by introducing hold-time of up to 30 min at peak tensile strain of 0.7%. The observed cyclic stress response and lifetime were then compared with that obtained under PF/CC waveform. The additional deformation and damage modifications brought by introducing creep into the PF/CC waveform were scrutinized. Here, EBSD and TEM were used to compare microstructural evolution. Whereas, damage modifications in terms of important observations from the fatigue-cracked specimen surfaces, cross-sections and fracture surfaces were examined via SEM.

Kurzfassung

In zukünftigen Fusionsreaktoren und Kernkraftwerken 4. Generation werden im Betrieb deutlich höhere Belastungen erwartet, als dies für heutige Anlagen der Fall ist. Für den sicheren und effizienten Betrieb werden deshalb Materialien mit hoher Bestrahlungstoleranz, Kriechfestigkeit und Ermüdungswiderstandsfähigkeit benötigt. Aufgrund ihrer mechanischen Eigenschaften und insbesondere des geringen Schwellens unter Bestrahlungseinfluss sind oxidpartikelverstärkte (ODS) Stähle potenziell vielversprechende Strukturmaterialien für diese Anwendung. Hierfür ist jedoch ein tiefgreifendes Verständnis der Verformungs- und Schädigungsmechanismen unter den auftretenden Belastungen notwendig. Aus diesem Grund wurde im Rahmen dieser Arbeit das Verformungs- und Schädigungsverhalten von getempert martensitischem Fe-9%Cr ODS Stahl untersucht. Dies umfasst das monotone Verhalten im Zugversuch, das zyklische Verhalten im Kurzzeitermüdungsversuch und die Widerstandsfähigkeit gegen kombinierte Kriechermüdungsbelastungen, die in zyklischen Versuchen mit Zughaltezeit untersucht wurde.

Zum Verständnis des Belastungseinflusses wurde die Mikrostruktur im Ausgangszustand mittels Elektronenrückstreubeugung (EBSD) und Transmissionselektronenmikroskopie (TEM) umfangreich charakterisiert. Im Anschluss wurden Zugversuche im Temperaturbereich zwischen Raumtemperatur und 800 °C bei nominellen Dehnraten von 10^{-3} s^{-1} und 10^{-4} s^{-1} durchgeführt. Anhand der Ergebnisse wird der Einfluss der Temperatur, der Dehnrate und der durchgeführten Wärmebehandlung dargestellt. Die Mikrostruktur im

belasteten Zustand wurde mittels TEM charakterisiert, die Untersuchung der Bruchflächen erfolgte mittels Rasterelektronenmikroskopie (SEM). Basierend auf der mikrostrukturellen Charakterisierung wurden zusätzlich die Beiträge verschiedener Verfestigungsmechanismen zur Fließgrenze bei Raumtemperatur abgeschätzt und verglichen. Des Weiteren wurden die Festigkeit und Duktilität des untersuchten Materials mit ähnlichen, nicht oxidpartikelverstärkten Stählen sowie mit Literaturergebnissen anderer ODS-Stähle verglichen.

Das Kurzzeitermüdungsverhalten wurde mittels dehnungskontrollierten Wechsellastversuchen mit dreieckigem Belastungspfad bei einer nominellen Dehnrate von 10^{-3} s^{-1} untersucht. Versuche wurden an Luft bei 550 °C und 650 °C für Gesamtdehnungsamplituden zwischen $\pm$ 0.4% und $\pm$ 0.9% durchgeführt. Zyklische Spannungs-Dehnungs-Kurven und der Zusammenhang zwischen Dehnung und Lebensdauer konnten anhand dieser Versuche ermittelt werden. Die unter zyklischer Belastung relevanten Verformungsmechanismen wurden durch TEM- und EBSD-Untersuchung der belasteten Proben identifiziert. Um die relevanten Schädigungsmechanismen zu erkennen wurden die Bildung und das Wachstum der Ermüdungsrisse sowie die Bruchflächen mittels SEM untersucht. Im Anschluss wurde das Kurzzeitermüdungsverhalten mit Literaturdaten vergleichbarer ODS- und nicht-ODS-Materialien verglichen.

Abschließend wurde die Wechselwirkung zwischen Kriech- und Ermüdungsbelastung bei 650 °C mittels Wechsellastversuchen mit Haltezeit bei maximaler Dehnung von 0.7% untersucht, dabei wurden Haltezeiten mit einer Dauer von bis zu 30 min betrachtet. Die gemessenen Spannungen und Lebensdauern wurden mit den Kurzzeitermüdungsversuchen ohne Haltezeit bei gleicher Gesamtdehnungsamplitude verglichen. Die durch die Kriechbelastung hervorgerufene zusätzliche Verformung und die Veränderungen des Schädigungsverhaltens wurden eingehend betrachtet. Die resultierende

Veränderung der Mikrostruktur wurde mittels TEM und EBSD analysiert. Mittels SEM wurden Änderungen des Schädigungsverhaltens anhand von Schliffbildern des Probenquerschnitts und der Bruchoberflächen betrachtet.

Contents

1 Introduction

Energy is one of the most fundamental part of our world which drives our day-to-day life. Its continuously rising demand and associated environmental impact lay down a real challenge in front of the mankind. Keeping this in perspective, from centuries lot of emphasis has been put on developing technologies to obtain clean, continuous, safe and efficient energy.

Till now the major part of our energy demands are harnessed from fossil fuels like coal, natural gas and crude oil. But their limited amount and associated curse of greenhouse gases emissions lead us to renewable sources like wind, sunlight, oceanic tides and geothermal heat. However, since these sources are not steady and are availability dependent, an alternate source is required to fulfill our constant energy demand. In this quest nuclear energy surfaced as a perfect source that was clean and can meet our demand for the generations to come.

Obtained by manipulating the internal structure of atoms, the role of nuclear energy to overcome the problems accompanying massive use of fossil resources is ever increasing. Nuclear energy can be obtained by dividing the nucleus (nuclear fission) or by joining of two atoms (nuclear fusion). Like conventional thermal power plants, nuclear reactors work by generating heat (through nuclear reaction), which boils water to produce steam to drive turbo generators and thereby generating electricity.

Nuclear reactors working on these principles represent a harsh environment for components, combining the effects of high operational temperature, an intense neutron irradiation (quantified in terms of displacement per atom (dpa)), thermo-mechanical stresses, vibration and corrosive aqueous environment. Degradation of materials in this environment can lead to reduced performance or in severe cases, sudden failure. Further in order to increase efficiency, the power plant should operate at high pressure, temperature and irradiation doses. Fig. 1.1 compares the proposed operating temperatures and lifetime displacement damage levels for structural materials in the six Generation IV (Gen IV) concepts and three fusion energy systems with the existing knowledge base [1]. As evident, these additional demands impose a complex challenge for material scientists. It is, therefore, very urgent to develop high-performance structural materials which can adapt to the new conditions of advanced power plant concepts including Gen IV fission and fusion reactors.

1.1 Motivation & objective

A diverse range of structural materials have been used for a wide variety of important roles in nuclear reactors. For example, at first, based on their attractive properties like high creep strength, corrosion and oxidation resistance, austenitic stainless steels (ASS) and Ni-base alloys (such as X-750) were considered as structural materials for both fast reactor (including fuel assemblies and core internals) and fusion reactor. However, due to their face centered cubic (FCC) crystal structure, both alloys show radiation-induced void swelling, which limits their application in nuclear reactors [3, 4]. Binary Fe-Cr ferritic/martensitic (F/M) steels with body centered cubic (BCC) crystal structure exhibit higher irradiation resistance in comparison to metals with FCC crystal structure [5, 6]. Hence, since the late 1970s F/M steels (like modified 9Cr-1Mo, P91 and Sandvik HT9), with the additio-
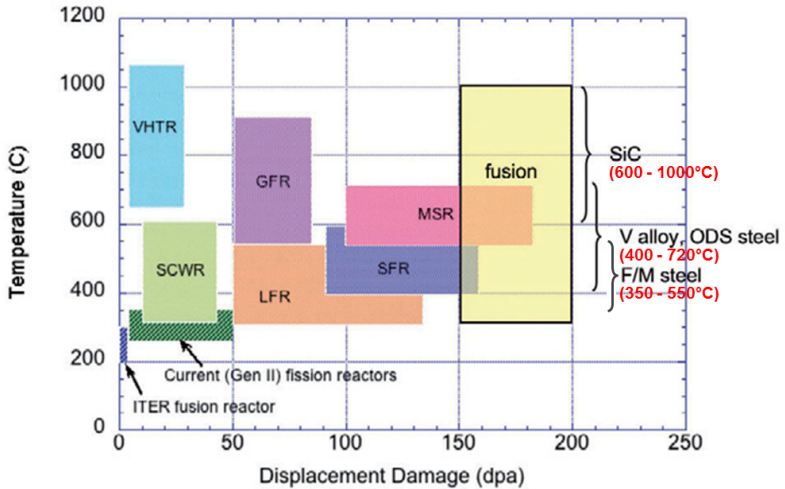
Figure 1.1: Overview of operating temperatures and displacement damage dose regimes for structural materials in current (Generation II) and proposed future (Generation IV) fission and fusion energy systems. The six Gen IV fission systems are Very High Temperature Reactor (VHTR), Super Critical Water Reactor (SCWR), Lead Fast Reactor (LFR), Gas Fast Reactor (GFR), Sodium Fast Reactor (SFR), and Molten Salt Reactor (MSR) [1]. In this plot, the application temperature range of F/M steel is altered according to [2].

nal advantage of higher thermal conductivity and lower thermal expansion, have been considered as an alternative material to ASS for advanced fast rector cladding/duct material as well as fusion DEMO plant first wall and blanket structural materials [6–9]. However, the long-lived radioactive by-products and short-lived radioactive products that cause unacceptable safety consequences (due to high decay heat and/or volatile species that could be released in the event of loss of coolant to the blanket region) put severe limitations on the alloying elements in the structural materials. Therefore, in the mid-1980s, the need for rapid radioactive decay propelled development of reduced activation F/M steels (RAFMS), like F82H and JLF-1 in Japan, ORNL 9Cr-2WVTa in United states, and EUROFER in Europe, by avoiding certain alloying elements such as Nb, N, Ni, Cu, Co, Mo and replacing them

3

by elements like W, V, Ta, Ti, Mn [8, 10–14]. Nevertheless, since 1983 the improved precipitation hardened RAFMS were also developed [15], where stabilized carbides improved creep properties.

Owning to their composition and heat treatment, RAFMS are typically developed to have a tempered martensitic hierarchical structure. The self explanatory schematic illustration of their tempered martensitic is shown in Fig. 1.2. It is apparent that the prior-austenitic grain is subdivided into packets of blocks of laths and sub-grains having high dislocation density (not shown here). In addition, the intergranular regions are decorated with a relatively coarse $M_{23}C_6$ carbides (M = Cr-rich), while fine MX-type carbonitrides (M = Ta/V, X = C/N) are distributed in both trans- as well as inter-granular regions. The as-fabricated RAFM EUROFER97's complex microstructure is shown in Fig. 1.3.

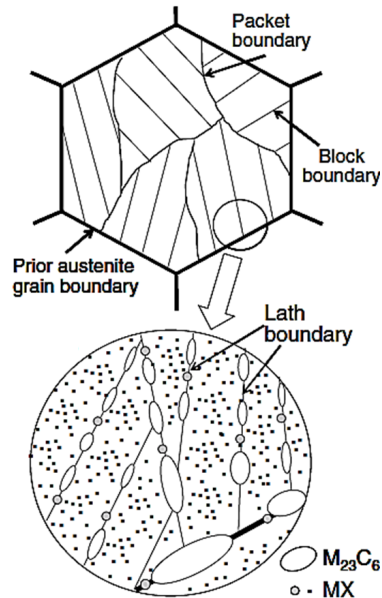Figure 1.2: Schematic illustration of the tempered martensitic microstructure of the F/M steels [16].

Nevertheless, apart from their various advantages, several mechanical investigations [9, 17–27] on RAFMS have led to two important drawbacks which are as follows:

1. Due to recrystallization, particle coarsening and dissolution, these steels rapidly lose their strength above 550 °C [20, 21]. Hence, incom-
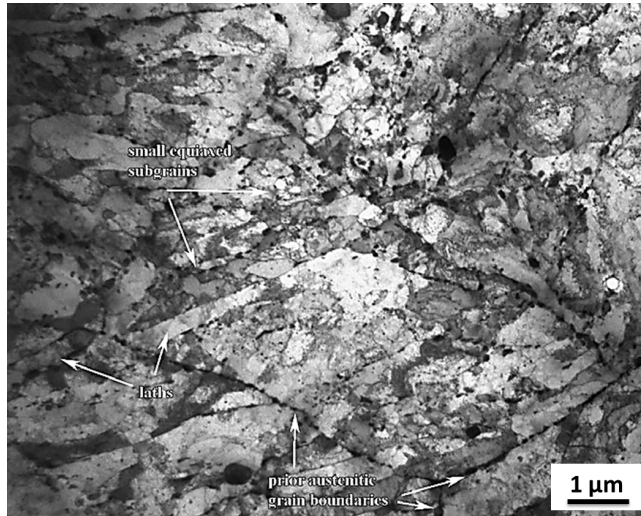
Figure 1.3: Bright-field (BF) TEM micrograph revealing as-fabricated RAFM EUROFER97 microstructure [17]. Complex tempered martensitic hierarchical structure with high dislocation density is evident.

patible for advanced future reactors which are proposed to be operated at even higher temperatures.

2. Under displacement-controlled cyclic loading, they lose strength continuously with number of cycles, i.e. they undergo continuous cyclic softening [17, 22–28], as shown for F/M P91 and RAFM EUROFER97 in Fig. 1.4. This is particularly an issue as the components of power plants are often subjected to repeated thermally induced stresses as a result of thermal gradients, which occur on heating and cooling during start-ups and shut-downs or during temperature transients. The cyclic softening in F/M steels is mostly attributed to the instability of their tempered martensitic structure. As under the influence of both temperature and cyclic straining, mobile dislocations facilitate annihilation processes which leads to almost complete loss of their

original hierarchical sub-grain structure and reduction in dislocation density (see Fig. 1.5). Besides, due to the activation of diffusion processes at high temperature carbides coarsen; and hence, they loose their ability of pinning boundaries [28] which results in grain boundaries migration.
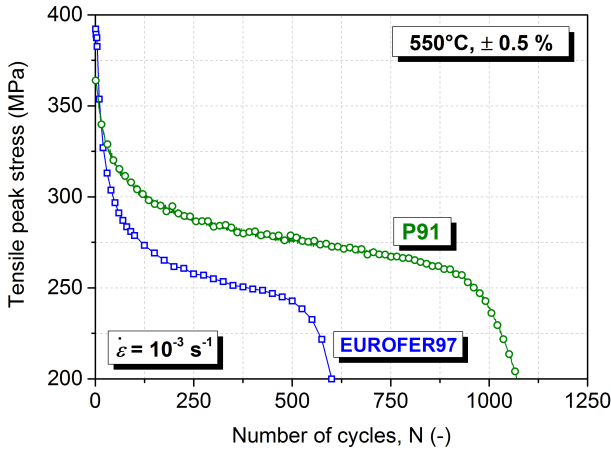
Figure 1.4: Cyclic stress response curves of F/M P91 and RAFM EUROFER97 [29] obtained after testing under ± 0.5% strain amplitude at 550 °C. The reduction of tensile peak stresses with number of cycles is called cyclic softening.

One attractive way to improve thermal creep resistance, which also maintains the inherent advantage of RAFMS at high temperature, is through the addition of highly-stable nano-oxide particles in RAFMS to form so called "Oxide Dispersion Strengthened (ODS) steels". The basic idea behind dispersing impenetrable nanoparticles is to obstruct dislocations from gliding (Fig. 1.6a) which will suppress annihilation processes; and eventually stabilize microstructure against degradation. Keeping this in perspective, numerous variants of ODS steels have been produced for investigations under comprehensive research programs worldwide. Their basic mechanical
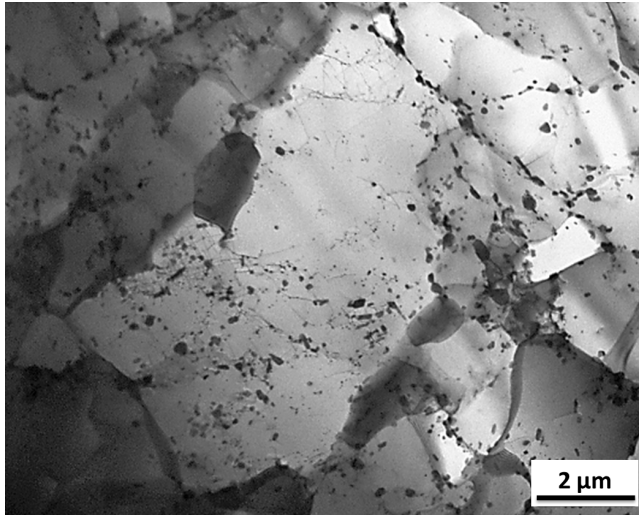
Figure 1.5: Bright-field (BF) TEM micrograph revealing RAFM EUROFER97 microstructure after cyclic testing under ± 0.4% strain amplitude at 550 °C [30]. Upon comparing with Fig. 1.3, the clean microstructure articulates the complete loss of the original hierarchical sub-grain structure, reduction in dislocation density and carbides coarsening.

properties including tensile strength, creep resistance and fracture toughness were studied by several authors, for e.g. see Refs [31–37]. In general, it was reported that the nano-oxide particles not only act as a barrier for dislocation motion and grain boundary migration, which controls the high-temperature tensile properties and creep resistance, but also act as an effective sink for irradiation-induced defects, such as vacancies and interstitials, and helium (Fig. 1.6b) to suppress bubble formation in the matrix, which ultimately offers higher irradiation resistance (Fig. 1.7) [5, 38]. From these preliminary investigations, it was concluded that oxide dispersion strengthening has the capability to improve high-temperature strength of the high-chromium steels. And thus would allow in principle for a higher operating temperature which improves rector's thermal efficiency with a direct positive influence

on economical profit and environmental damage.

Figure 1.6: Schematic illustration showing uniformly dispersed nanoparticles acting as (a) the obstacles for dislocations glide and (b) the effective sink for irradiation-induced defects (vacancies) and He-bubbles.

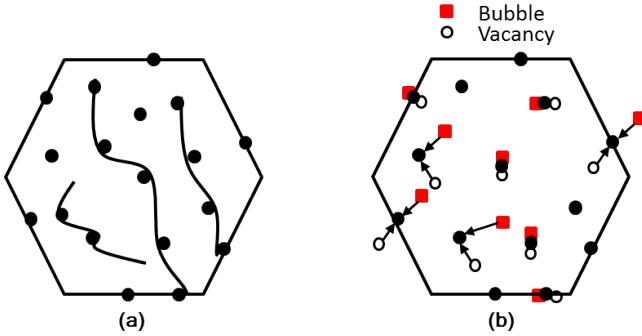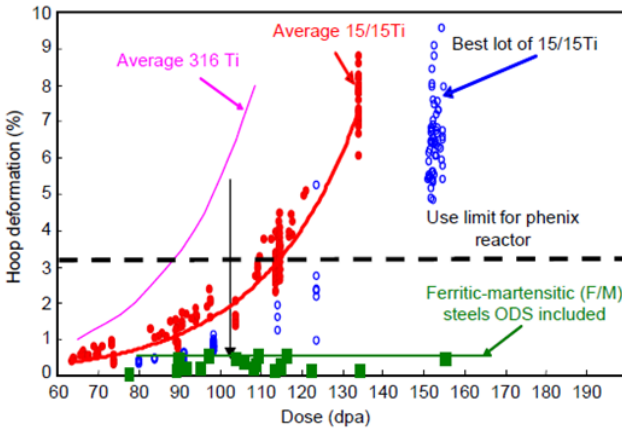Figure 1.7: Maximum hoop deformation of different grades of austenitic Phénix claddings and F/M materials versus dose at temperatures between 400 °C and 550 °C [39].

Nevertheless, even though nanoparticles significantly improve high-temperature strength, it is reckoned to be achieved at an expense of ductility and toughness. Indeed, investigations have shown that ODS steels, in comparison to their non-ODS counterparts, suffer in terms of both lower ductility as well as lower elevated-temperature fracture toughness [34, 40]. For structural applications, such properties are of pivotal importance. Hence, it becomes critically vital to understand their deformation and damage mechanisms and to subsequently manipulate their fabrication routes/parameters to optimize the combination of strength, ductility and toughness. Moreover, due to their complex manufacturing routes, some classes of ODS steels exhibit anisotropic microstructures; and hence, properties [40]. Therefore, these steels are still in there development stage for their further improvement. Furthermore, as already mentioned, the structural stability of materials under cyclic loading is of considerable importance. This stability can be judged by straining material cyclically in the regime of elastic-plastic loading, which yields low-cycle fatigue (LCF). However, at present, the knowledge of LCF behavior of ODS steels is limited since only few studies were dedicated to this issue [30, 41–51]. And even though, these few studies successfully demonstrate the importance of dispersing nano-oxide particles (higher cyclic strength and lower induced inelastic strain), their significance particularly in terms of fully stabilizing cyclic stress response remains questionable (for more, see section 2.4.3). Moreover, the chemical composition as well as processing routes/parameters appear to define their overall LCF behavior. Besides, their deformation and damage mechanisms under cyclic loading were also rarely discussed, especially when considering the influence of temperature and applied strain amplitudes. Furthermore, as the typical in-service conditions require operating temperatures between 500-700 °C, these steels will experience simultaneous creep leading to a loading of creep-fatigue type. Nonetheless, though ODS steels generally outperform their non-ODS counterparts in respect to creep (see section 2.4.2), its inte-

raction with fatigue has not been yet addressed/understood.

Therefore, the present work is undertaken to fill those above-mentioned gaps. For this, an isotropic tempered martensitic Fe-9%Cr based ODS steel was investigated. The objectives of the present work involving this newly developed ODS steel are:

1. To critically characterize its micro- and nano-structural features.

2. To understand its deformation and damage mechanisms under monotonic loading conditions.

3. To estimate the contributions from different strengthening mechanisms and to identify the dominant ones.

4. To recognize its deformation and damage mechanisms under pure-fatigue loading conditions and compare them with that of the non-ODS as well as other ODS steels tested or reported in literature.

5. To apprehend the role of matrix in defining the overall LCF behavior of ODS steels.

6. To visualize possible creep-fatigue interaction and its influence on the cyclic stress response and lifetime.

7. To perceive its deformation and damage mechanisms under creep-fatigue loading conditions and compare them with those of the non-ODS as well as other ODS steels tested or described in literature.

1.2 Structure of thesis

The work in this thesis has been divided into six chapters. The first chapter provides a general introduction to the topic. The following section specifies the importance of carrying out such work in the form motivation. The

objectives of the work are presented in the same section. The subsequent section provides a very brief insight into structure of the thesis.

The second chapter outlines the state of research from literature. This chapter has been further subdivided into smaller sections which provide detailed literature review in context of the theme of this work. These sections concentrate primarily on the development of ODS steels, their conventional fabrication route, possible strengthening mechanisms, various dislocation-particle interactions and mechanical response.

The third chapter, namely material and methods, documents various details regarding investigated Fe-9%Cr based ODS steel, including its chemical composition and production route. Moreover, vital technicalities concerning experimental procedures, that involve both mechanical as well as microstructural characterization, are presented in detail. A special attention in this section has been given to document various used microstructure characterization techniques working principles.

The fourth chapter brings to the reader all experimental results and discussions based on them. This chapter is further subdivided into four main sections. The first section presents results from the microstructural investigations performed on an undeformed state. Discussions are made in comparison to the similar steels described in literature. The second section is dedicated to the understanding of the deformation and damage mechanisms of the studied ODS steel under monotonic loading conditions. Here, results from the tensile tests performed at various temperatures, resulting microstructural evolution and fracture characteristics are presented and discussed. In addition, various active strengthening mechanisms and their contribution to measured room temperature yield stress are estimated and compared. Comparisons are also made in respect to the strength and ductility of the similar non-ODS as well as other ODS steels taken from literature. High-

temperature pure-fatigue behavior of the studied ODS steel is delineated in the third section. In here, mechanical response is linked to both microstructural evolution as well as damage progression. Moreover, thorough comparison of the measured cyclic stress response and lifetime are made with that of the similar non-ODS as well as other ODS steels tested or taken from the literature. Finally, creep-fatigue interaction studies results are documented in the fourth and final section. The additional modifications brought by introducing creep into the pure-fatigue waveform are presented in terms of both microstructural as well as damage characteristics.

The fifth chapter summarizes important results and conclusions from the whole work. Finally, outlook chapter puts forward proposals for the future investigations.

2 State of research

2.1 Oxide dispersion strengthened (ODS) steels

2.1.1 A brief history of ODS steels

Metallic oxides are fundamentally different than their metals. In general, oxides differ in terms of their much higher melting point, lower density and significantly different electronic and crystal structure. These differences mostly can be traced back to the difference in their inter-atomic bonding. Most oxides are covalently or ionically bonded indicating the electron are localized while in metals electrons are delocalized and can float through the atomic lattice. These all-important differences interested researchers in creating a composite with a dispersion of fine oxides in a metallic material matrix that have better physical properties than the original alloy. In past, several ODS alloys with different metallic base have been produced and investigated. For example, in 1916, the W filament dispersed with thorium oxide (ThO_2) was produced in Germany. In 1946, sintered Al powders were developed to increase heat resistance of Al alloy. And, in 1962, ODS-Ni alloy with ThO_2 (TD-Ni) was developed for application in turbine.

The development of Fe based ODS alloys (with thermally stable Al-, Ti-, Mg- and Zr-oxides) dates back to 1960s in the frame of sodium-cooled fast breeders [52, 53]. However, Fisher was the fist to patent a high chromium (14%) ferritic alloy with 0.2-0.25 wt.% Y_2O_3 for the use in fast reactors [54]. These alloys were then later marketed in the 1980s as International Nickel company (INCO) MA956 and MA957. Similar ODS steels

were also produced by Dour metals (Belgium), Special Metals (United states) and Plansee (Austria) [31]. However, due to several barriers to their practical use, these entire suppliers discontinued their fabrication. Till very recently, a small quantities of ODS steels were only supplied by Dour Metal Sro. (Slovack republic) and Kobe Steels (Japan) [55]. However, after a dormant period of few years, there has been a resurgence in the fabrication and study of ODS steels under various national and international projects for their further improvement. Nowadays, these steels are only produced in limited amount in laboratories around the world.

Among various oxides, Y_2O_3 is the mostly widely used oxide particles in the ODS steels. This is due to the fact that Y_2O_3 is one of the most thermodynamically stable compounds (negative large formation energy), and Y and O atoms are insoluble in the ferrite matrix. The nanoparticles developed for these particles during fabrication are relatively chemically inert and therefore are resistant to coarsening up to temperatures in excess of 900 °C for annealing times up to 32000 h and up to 1300 °C for 24 h thermal exposures [56, 57].

Different ODS steels based on their application were developed, which can be sub-divided into three categories: transformable F/M ODS steels containing less than 12 mass% Cr, ferritic ODS steels containing $\sim$ 12 mass% Cr or more and very recently austenitic ODS steels containing higher % of austenite stabilizing elements such as Ni. To maintain the tempered martensitic structure, the F/M ODS steels are generally for application temperatures below $\sim$ 700 °C. Whereas, due to their higher Cr content, ferritic ODS steels are developed to be potentially used under corrosive environment and at temperatures up to 800 °C or more [57]. Although ferritic ODS steels offer higher potential application temperatures and superior high-temperature creep strength, the F/M ODS steels provide several offsetting advantages. Due to the possibility of phase transformation treatment

(martensitic transformation), the F/M ODS steels exhibit more isotropic mechanical properties compared to high-Cr ferritic ODS steels who tends to have anisotropic properties. In addition, F/M ODS steels generally exhibit more favorable fracture toughness properties such as lower DBTT and higher upper shelf energy [19, 58]. Furthermore, upon comparing in terms of irradiation resistance, F/M ODS steels offers superior resistance than the ferritic counterparts due to very high point defect sink strength associated with their fine-scale hierarchical features [5, 38].

As in comparison to ferrite, austenite is a phase with superior strength, creep, corrosion and oxidation resistance [59], in recent years, further improvements are also shown by introducing oxide particles in austenitic steels [59–61].

2.1.2 Fabrication

Due to extremely poor solubility and wettability of main strengthening elements (Y & O) in liquid steel, ODS steels till now are mainly produced via mechanical alloying (MA), followed by powder metallurgy processes. MA enables homogeneous distribution of oxide particles throughout the matrix [62]. In general, the typical fabrication route (see Fig. 2.1) involves MA of a desired gas-atomized pre-alloyed matrix powder with ultra-fine oxide powder. For this purpose, at laboratory scale an attrition ball mill is used, whereas for large-scale planetary ball mills are preferred. For protection against oxidation in the subsequent process steps, the milled powder is then sealed in a soft steel cans and degassed at elevated temperatures. Thereafter, to produce bulk material, consolidation process on vacuum sealed cans is carried out by either hot extrusion or hot isostatic pressing (HIPping) [54,63] and, more recently, pulsed-current-assisted sintering also known as spark plasma sintering (SPS) [64]. It has been shown that hot extruded ferritic ODS steels exhibit a morphological and crystallographic texture [65, 66]

whereas those consolidated with other methods display much more random initial texture and equiaxed morphology [67]. However, subsequently different thermo-mechanical treatments (TMTs) such as annealing, hot and/or cold rolling and various other heat treatment processes, are also applied to optimize microstructure and mechanical properties.
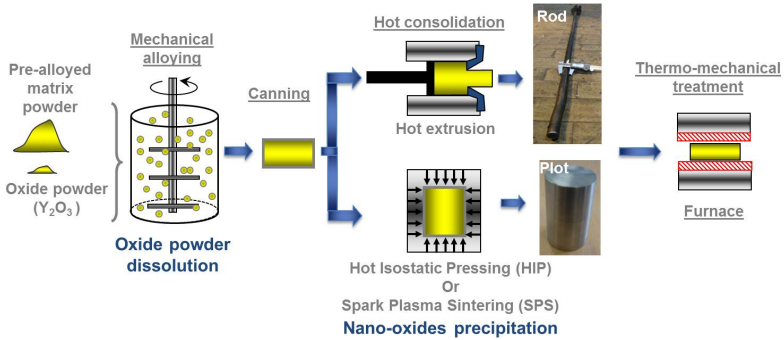

Figure 2.1: A schematic illustration showing commonly used fabrication route for preparing ODS steels. Adapted form [68].

Ordinarily, during ball milling, the mixtures of elemental or master-alloy powders are subjected to high-energy milling. This causes the repeated flattening, welding, fracturing and re-welding of the powders until they mix intimately to form true solid solution. In case of ODS alloys, the milling of the ductile matrix powder with the hard dispersoid (Y_2O_3 powder) leads to the formation of enormous supersaturation of dissolved Y and O [69], the submicron-grain structure and high dislocation densities in the as-milled powders [5]. It is noteworthy that the formation of sub-micron grain size and high dislocation density during milling causes energy storage on the free surface of the particle and substantial enthalpy gain, respectively [62]. This energy gets released during sintering step to reduce total energy of the system allowing grains to remain smaller and enhance solid solubility [62]. The processing temperature of consolidation step is also critical to retain submicron-grain structure generated during previous step and to

impede particle coarsening and grain growth [70–72]. During consolidation at elevated temperatures the oxide particles precipitate in the ODS steels [5, 63, 69, 70, 73]. Analytical TEM studies accomplished on the ODS alloys revealed differences in the characteristics of the particles dispersions developed on the basis of alloy composition [74].

Hot extrusion and/or hot rolling during/after consolidation step leads to a finely elongated and textured grain structure parallel to the rolling or extrusion direction [5, 75] whereas relatively higher number of equiaxed grains perpendicular to the rolling direction. The anisotropic grain morphology and textured grain structure following typical extrusion processing step are generally viewed as undesirable. A strong preferential crystallographic orientation of the grains along <110> in the extrusion direction is shown for ferritic ODS steels [66, 76–78]. This microstructural anisotropy is shown to have a direct effect on the mechanical properties of ODS steels. For example, it is now well-known that in the textured ferritic ODS steels the transverse direction is less ductile than the extruded one [76, 79–81]. In addition, it has been shown that the grain morphology appears to affect the fracture mode [76]. Therefore, to avoid this anisotropy and texture, post-consolidation TMTs are applied in order to obtain isotropic microstructure with homogeneously spread equiaxed grains. In this respect two types of approach has been experimentally explored: First, the reversible α to γ phase transformation for 9%Cr based ODS steels especially aiming at producing radiation resistant alloys with tempered martensite structure [21, 82] and second, the adequate annealing heat treatments following cold rolling for 12%Cr (or more) based ODS steels aiming at producing corrosion resistant alloys with a fully recrystallized ferritic microstructure [21, 83]. In addition to this, ultrafine grain size (of the order of 100 nm) is also obtained by optimizing milling time and decreasing extrusion temperature to 850 °C for ferritic ODS steels [84].

17

However, though powder metallurgy route offers many advantages, it is complex, time consuming and expensive, and the fitness for scaling up to the industrial scale is limited. Therefore, many other possibilities were explored recently which are reviewed by Bergner et al. [64].

2.1.3 Alloying elements and their effects

Chemical compositions of ODS steels are mainly designed to maximize high temperature strength by dispersion and solution hardening mechanism. The number of alloying elements in ODS steels are much less than the conventional precipitation hardened RAFMS. In practice, C, Cr, W, Ti, Y and O are defined to be alloying elements. Whereas, Si, P, S, and Ar are defined as impurity elements [21]. C, Cr, Mn and Ni are usually added to provide phase control [21]. C, a strong austenite stabilizing element and having a very small solubility in ferrite, results in the formation of carbides for precipitation hardening [85]. Cr is not only a ferrite stabilizing element but also offers a superior corrosion resistance [86]. Moreover, increasing Cr content can increase the resistance to irradiation-induced swelling and improve the corrosion-oxidation resistance even further [5]. However, Cr can lower the fracture toughness due to the formation of δ-ferrite phase in 12%Cr-ODS steel. If C or Mn are added in order to suppress δ-ferrite, either extensive $M_{23}C_6$ precipitates are formed (which tend to reduce fracture toughness) or the chi (χ) phase is formed during irradiation which cause embrittlement [87]. Al is also added sometimes to improve corrosion resistance [88] but it converts nano-size oxide particles to the chemical form $2Y_2O_3$-Al_2O_3 while retaining their original size [89]. These particles however are expected to coarsen upon heating, therefore less effective in retarding or preventing recrystallization [63]. Moreover, Al addition also leads to an inhomogeneous dispersion of oxide particles [88]. Ta is sometimes added as a replacement for Nb for forming stable carbonitrides [85,90].

W is added for solid solution strengthening [21].

Yttria is added to introduce the oxide particles for dispersion strengthening. Typically Yttria ODS steels are superior to TiO_2 ODS steels. The addition of TiO_2 during MA process is not as effective in distributing the fine oxide particles in the ferritic matrix as Ti [32]. The co-addition of Ti during MA promotes the decomposition of thermally stable Y_2O_3 into Y and O atoms and dissolving them into matrix by forming amorphous O-enriched regions. In bcc ferrite, these amorphous regions may simply be a disordered structure formed due to the energy preference of O_i-vacancy pairs in the presence of Ti [91]. Followed annealing above 1000 °C leads to bonding of dissolved elements with Ti and extremely fine stable Y-Ti-O oxides (most commonly $Y_2Ti_2O_7$ structure) precipitates [58]. It should be noted that the Fe-Cr binary system has little solubility of Ti and Y; and hence, added in small amount. As mentioned above, Ti reduces the oxide particles size; and hence, significantly improving the creep strength [32, 34, 54, 58, 83]. It is shown that Ti can decrease oxide particle size from more than 10 to 3 nm in 12%Cr-ODS steel [58] and from 4 to 2 nm in 14%Cr-ODS steel [92], with further increased thermal stability and number density of oxide particles by approximately a factor of 10. Nonetheless, if Ti added in excess, it tends to negatively impact the cold rolling and cold workability. Also, it segregate at grain boundaries [93], to form coarse TiO_2 particles [94] and promotes χ phase transformation at temperatures above 800 °C [95], all of which are detrimental to the strength and ductility of the ODS steels [96].

Although both Y_2O_3 and $Y_2Ti_2O_7$ have a cubic structure, the lattice parameter of $Y_2Ti_2O_7$ (1.009 nm) is slightly smaller than that of the Y_2O_3 (1.06 nm) [97]. In addition from the viewpoint of surface energy the formation of $Y_2Ti_2O_7$ is more beneficial than Y_2O_3 [97]. It is observed that the size and distribution of the oxide particles in the ODS steels depends on certain amount of excess oxygen concentration (the value obtained by

subtracting the oxygen concentration coupled with yttrium (in the form of Y_2O_3) from the total oxygen concentration) while the final morphology of the oxide particles depends on the process parameters such as milling time and heat treatment temperature [98]. The narrow particle size distribution which is critical for improving the strength was achieved by controlling the atomic ratio between excess oxygen and Ti (X in TiO_X), at around 1 [99].

2.2 Strengthening mechanisms

Strengthening materials traditionally involves the controlled creation of internal defects and boundaries so as to obstruct dislocation motion. The complex microstructure of ODS steels offers excellent high temperature creep resistance due to favorable superposition of several important strengthening mechanisms. These all mechanisms, apart from lattice friction strengthening, are listed out by schematic in Fig. 2.2. Here, Fig. 2.2A shows strengthening via solid solution, whereby solute atoms strain the matrix to impede the motion of a dislocation (red line) through the lattice; via precipitates or in the preset case dispersed nano-oxide particles that interact with mobile dislocations, leading to overall strengthening of the material; or via elastic interactions between intersecting dislocations (blue and red lines), as well as geometry changes and subsequent obstructions to slip (as, for example, through the formation of sessile dislocation segments) associated with such encounters (dislocation forest strengthening). Grain boundary (GB) strengthening or in other words Hall-Petch/grain size strengthening (Fig. 2.2B) is another commonly used method in which dislocation (red symbol) motion is blocked by GB (whose incoherent structure is schematically shown on the right) so that a dislocation pile-up is formed. The dislocations experience hindrances as they try to move from one grain to other because of abrupt change in orientation of planes. The hindrances experience can be of two types, forcible change of slip direction, and discontinuous slip plane. And

therefore, a higher stress is needed to deform a polycrystalline metal with a smaller grain size (more GBs).
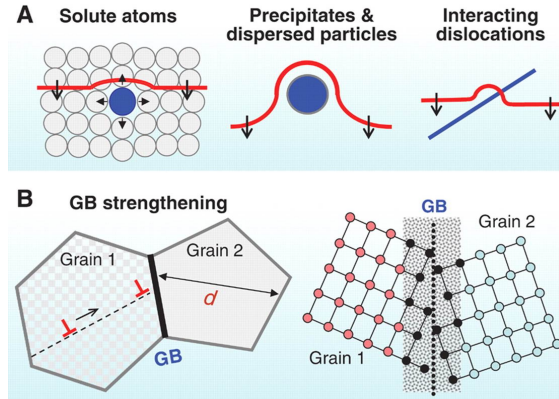

Figure 2.2: A schematic illustration showing commonly used strengthening models [100].

The individual contribution from each mechanisms can be estimated by using reported equations fed with the measured microstructure parameters, for this see section 4.2.4. For ODS steels, the quantitative individual contribution of the mechanisms is still not clear. In literature, different authors reported distinct strengthening mechanisms as the most significant based on the alloy's specific microstructural features. For instance, Schneibel et al. [101], for PM2000 (ODS Fe-20%Cr steel) and 14YWT (ODS Fe-14%Cr steel), reported that Hall-Petch/grain size strengthening is comparable or even greater than the nanoparticles strengthening. Kim et al. [102], for 14YWT, also came to similar conclusion. On the contrary, others [65, 103], for 14YWT and ODS Fe-12%Cr steel, confirmed dislocation forest strengthening as the main contributor. Whereas, recently Zhou et. al. [104], for ODS Fe-9%Cr steel, based on the heat treatment showed either dislocation forest strengthening or the grain boundary strengthening as the major contributors.

Furthermore, it is important to mention that strengthening contributions also alters significantly with temperature [102]. Alinger [105] observed that the effectiveness of a strengthening mechanism can be related to the absolute melting point, T_m, of the metal or alloy. It was reported that, at temperatures greater than $0.5T_m$ (reactor temperatures at $0.5\text{-}0.7T_m$), dispersion strengthening and precipitation strengthening are the most viable techniques for imparting high temperature strength to a material as other strengthening effects will be annealed out at relatively low working temperatures.

2.3 Particle-dislocation interactions

Depending upon their size, oxide-particles in ODS steels can be divided into two categories. The first category is of those particles that are relatively coarse (> 50 nm), have low number density and substantially different in their chemical composition from nanoscale dispersoids. These large particles/precipitates have a minor influence on strength and ductility. In contrast, the second category is of the nanoscale particles which have a much higher number density and volume fraction. They are considered as the most important contributor to improved high-temperature strength, creep resistance and irradiation resistance [106]. Consequently, only the strengthening from nanoscale oxide particles is considered important. Furthermore, as they act as the thermodynamically stable obstacles to dislocation glide, knowledge of the fundamental mechanisms of the dislocation-particle interaction is crucial for understanding the outstanding mechanical strength and creep performance of ODS steels. Apart from the particle and dislocation characteristics (including dislocation type, particle-matrix interface, particles size, its composition and structure), still not very clear this interaction is also a function of temperature. The change in mechanism with temperature is observed by many researchers which will be discussed in detail below.

As shown in Fig. 2.3, under the influence of critical resolved shear stress (CRSS)[1], the dislocation line is in tension and is on the move. As the dislocation meet the second phase particle, the particle can act in two distinct ways to retard the motion of dislocations. Dislocations can either cut through the particles (Fig. 2.3a) or bend around and bypass them (Fig. 2.3b). It is more likely that in dispersion-strengthened system, both of these mechanisms operate, with one typically dominating over the other. In order to know the dominating mechanism, the CRSS for each process has to be estimated. Nevertheless, in both cases, a higher stress is required to move dislocations through a matrix containing a dispersed particle phase, hence making material stronger.

(a) Particle cutting mechanism

Particle/
Precipitate

Coherent particles in Ni-
6%Si crystal

(b) Orowan mechanism

Particle/
Precipitate

Incoherent particles in Ni-
6%Si crystal
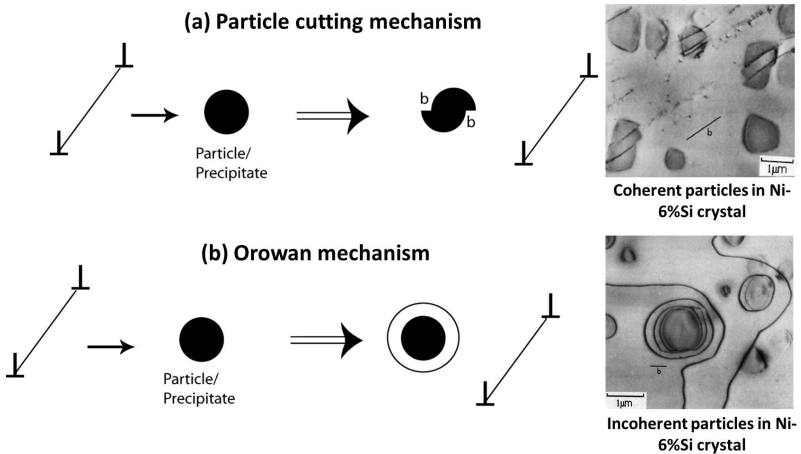
Figure 2.3: A schematic and TEM images illustrating how dislocations can interact with a particle. It can either (a) cut through the particle or (b) bow around the particle and create a dislocation loop as it moves over the particle [107, 108].

The mechanism of particle-dislocation interaction is greatly influenced by the strength of the particle which generally increases with the particle size. Cutting mechanism is possible only when the slip plane is continuous from

---

[1] CRSS is a lowest resolved shear stress necessary to initiate slip in a grain.

the matrix through the precipitate particle (i.e. they posses a coherent inter-ference with matrix) and when the stress to move a dislocation in particle is comparable to that in matrix (Fig. 2.3a). The stress required for a dislocation to cut through an oxide particle is given by Eq. 2.1 [109].

$$\tau_{cutting} = \frac{Gb}{L} \left(\frac{F_m}{2T_d} \right)^{3/2} \tag{2.1}$$

Where, G is the shear modulus, b is Burgers vector, L is the mean parti-cle distance in the glide plane, F_m is the maximum force sustained by the obstacle, $T_d \approx Gb^2/2$ is a simplified expression for the line tension. The factor $(2T_d/F_m)$ describes the obstacle strength. For shearable particle, for which F_m scales with the particle radius R, impart strengthening of the fol-lowing form: $\tau_{cutting} \propto R^{1/2}$. Hence, the smaller particles are relative easier to cut through than the larger particles. Various other particle properties that can dictate the ease of shearing are stacking-fault energy, coherency strains, modulus effect, ordered structure, morphology, lattice friction stress and interfacial energy. In this mechanism the strengthening comes from the increase in the surface area due to particle shearing or the higher stress faced by the part of the dislocation line while moving through the particle.

When there is an interface or an abrupt change in orientation, cutting of par-ticles is not possible. Under this condition, another dislocation-particle interaction often referred to as Orowan strengthening mechanism [110] (Fig. 2.3b) dominates. This strengthening mechanism uses the difference between the modulus of the particle and matrix. This core concept suppo-ses that dislocations are repelled by the hard particles elastically. So as the dislocation approaches the particle, its strain field interacts with the particle, and back stress develops because of that. As a result dislocation line bow around the larger incoherent particles (that are strong, non-deformable and non-shearable) until it reaches a critical curvature. Upon achieving this cri-tical curvature, the dislocation line moves forward without an increase in its

curvature. The segments of dislocation line on either side of particles then join, and as a result of their annihilation a dislocation loop is left around each particle (Fig. 2.3b). The back stress due to trapped closed loops as well as repelling effect of these loops on the next upcoming dislocation causes subsequent increment of stress. As mentioned previously, factor $2T_d/F_m$ describes the obstacle strength and in the case of impenetrable obstacles $F_m = 2T_d$ [109]. Therefore, from Eq. 2.1 the CRSS increase over that for a material without dispersed barriers, τ_{Orowan} is given by Eq. 2.2 [109]:

$$\tau_{Orowan} = \frac{2T_d}{bL} \approx \frac{Gb}{L} \propto \frac{Gb}{R} \tag{2.2}$$

Where, proportionality establishes a connection with R at constant volume fraction of particles. This governing equation shows that for dislocation bowing the strength is inversely proportional to the particle radius. Accordingly, a finner dispersion results in more efficient strengthening.

The τ_{Orowan} is the local stress required for a dislocation to move on its slip plane. In order to relate the resolved shear stress (τ_{Orowan}) to a polycrystalline material yield stress (σ_y) on a macroscopic scale, an average orientation factor M is required:

$$\sigma_y = M\tau_{Orowan} \tag{2.3}$$

Where M is known as the Taylor factor and 3.06 is the most appropriate value for BCC metals and alloys.

As seen above, in both cases (cutting and bowing) stress varies inversely with the spacing between the particles. Now a question arises, if an alloy has a fixed volume fraction of strengthening particles, is it better to have coarser, more widely spaced particles, or fine, closely spaced particles? Considering the equations for cutting and looping mechanism, it is clear that there is a critical radius at which maximum strengthening occurs (see Fig. 2.4). This

critical radius is typically 5-30 nm. However, during long high-temperature service, annealing can lead to the coarsening of the particles. In this case strength may drop over time, and can set a useful working life on e.g. a turbine blade and nuclear reactors. Hence, at higher temperature it becomes important to consider the stability of second phase particles.
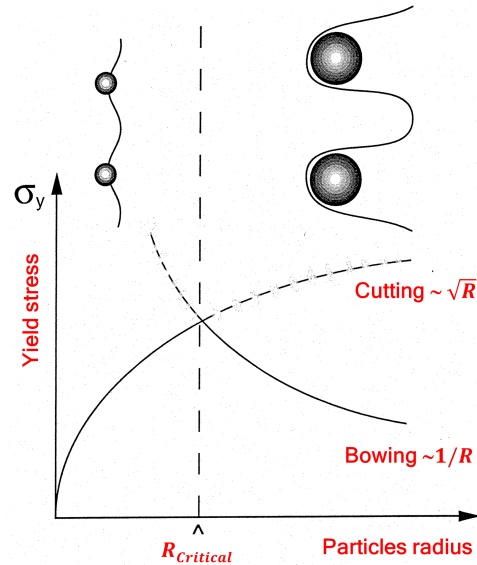

Figure 2.4: A classic size effect resulting from a $\sqrt{R}$-dependence of the cutting stress Eq. 2.1 and a $1/R$-dependence of the bypassing stress Eq. 2.2. This causes a maximum in yield stress σ_y vs particle radius R at a characteristic critical value [109].

In addition to these two fundamental mechanisms, a dislocation can also by-pass particles by cross-slipping into other planes and leaving prismatic dislocation loops. This phenomenon is called the Hirsch mechanism [111]. Due to the nature of cross slip, the Hirsch mechanism is complicated, and may sometimes mix with Orowan looping to form several variants [112, 113]. Typically, the Hirsch mechanism has a CRSS that is only slightly different from that of Orowan looping [114], complicating the competition between

Orowan looping and the Hirsch mechanism.

At low temperatures, complex $Y_2Ti_2O_7$ nanoparticles in F/M 9%Cr-ODS steel are shown to be impenetrable for dislocations whose shear modulus is much higher than that of Fe-Cr matrix [115]. Therefore, cutting process is unexpected and also has not been reported. Moreover, there is a widespread consensus that at low temperatures, ODS alloys high strength is exclusively controlled by Orowan/repulsive mechanism [65, 66, 116] even if the clear evidence of Orowan loop is still missing. Recently, Ijiri et al. [117], for F/M 9%Cr-ODS steel containing Y-Ti-O nanoparticles, confirmed that at room temperature more than 90% of the interactions were repulsive in nature and screw dislocations by-passed oxide particles by cross-slip, which is weaker interaction than the Orowan's one. However, at elevated temperatures, repulsive interaction does not support ODS alloys high strength. Since, at these temperatures, the contribution of diffusion phenomenon increases and climb by-pass of particles becomes possible. Srolovitz et al. [118,119] were the first to explain the change in dislocation-particle interaction from repulsive (Orowan mechanism) to attractive with increase in temperature. They suggested that if the interface between the particle and the matrix do not transfer shear strains (i.e. if it is an incoherent interface) then because of the interfacial diffusion at elevated temperature, the stress field associated the dislocation could be relaxed at the interface leading to reduced dislocation energy. Due to this diffusion relaxation, a dislocation that intersects the particle on any glide plane is always attracted towards the particle. And once dislocation enters matrix-particle interface, the associated core relaxation leads to its pinning. The stress required to unpin the dislocation (σ_{th}) is given by:

$$\frac{\sigma_{th}}{G} = \frac{b}{2\pi(1-\upsilon)L}\left(\frac{\pi^2}{12} + \ln\frac{R}{R_0}\right) \tag{2.4}$$

Where υ is the Poisson's ratio and R_0 is the inner cut-off radius. This magnitude of stress is similar to Orowan stress.

Nardone and Tein [120] suggested this "non-mechanical pinning"as a potential and promising candidate for explaining high temperature strength of Ni-based ODS alloys (Fig. 2.5). They were the first to use the term "departure side pinning", a dislocation's lower energy configuration, in which after overcoming particles by climb they are pinned on the departure side of the oxide particles. Rösler and Arzt [121] later described it as "interfacial pinning". They proposed that upon moving away from the dispersoid dislocation achieves higher energy configuration, and therefore by pinning on the departure side of the oxide particle dislocation stays in a lower energy configuration. This reduction in the system's energy can be because of: i) dislocation in contact with dispersoid may be able to reduce its line energy; ii) particle/dislocation surface energy is lower than the particle/matrix surface energy [120]. Preston et al. [122] firstly observed the same mechanism for the ferritic ODS steel in 1990. Thereafter, this theory has been considered by many authors [36, 66] without solid experimental evidence for explaining high-temperature creep properties of ODS steels.
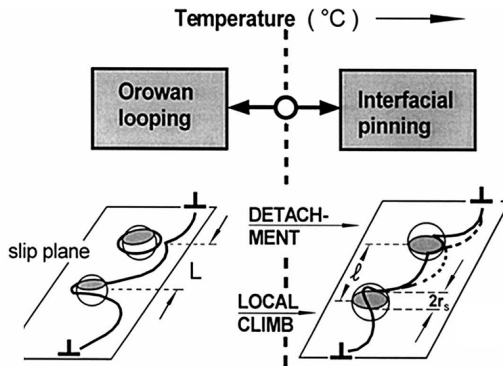
Figure 2.5: Sketch showing the change in dislocation-particle interaction mechanism with temperature [123].

2.4 Mechanical response

A wide range of mechanical tests have been performed on ODS steels at several experimental conditions. However, since these steels are still in their development stage majority of the testing were only dedicated towards understanding their monotonic behavior including tensile, creep and fracture toughness tests etc. Whereas, costly and time consuming cyclic testing on these steels are still very limited. Considering the theme of the present work, important key findings as well as shortcomings from tensile, creep and cyclic testing of these steels are reviewed below.

2.4.1 Tensile testing

The tensile test is the most important and widely used test to characterize the basic mechanical properties of structural materials. Here, the specimen is subject to uniaxial tension until failure.The most important materials parameters, which can be directly measured via a tensile test, are yield strength (0.2% strain offset), ultimate tensile strength, uniform elongation, total elongation and reduction in cross-section area. For ODS steels, a vast data on their tensile testing at several conditions is available, which is very hard to comprehend. Therefore, only main key findings are summarized below.

Due to oxide particles dispersion, ODS steels in general offers superior strength in comparison to their base materials. However, their strength varies with respect to the variation in particles composition, their level of distribution and various other microstructural features. It has been reported that the steel containing uniformly distributed Y-Ti-O nanoparticles shows superior tensile strength than the steel containing less uniformly distributed pure, coarser and crystalline Y_2O_3 particles [35]. The strength is also shown to vary with other matrix features such as composition, grain size and dislocation density. It is now well-know that for the highest strength, the steel should posses a uniformly distributed nano-sized (2-4 nm) incoherent

oxide particles, with nanometer sized grains and high dislocation density. Based on these characteristics, many ferritic ODS steels have been developed [70, 80]. However such improvement in strength is usually achieved at an expense of ductility and fracture toughness [124, 125]. And therefore, as mentioned before ferritic ODS steels not only suffers from lower ductility and fracture toughness but also presents undesirable anisotropic properties (transverse direction offers lower ductility than longitudinal direction [126]). Therefore, different class of ODS steels (i.e. F/M versions, see section 2.1.2) based on phase transformation treatments are developed that offers not only isotropic properties but also adequate ductility and toughness but slightly at an expense of strength [19, 58].

In respect to the influence of temperature, both yield stress and mechanical resistance decreases slowly with temperature up to $\sim 400\,°C$ [66] but at higher temperatures more pronounced collapse of strength is noticed [35, 66]. Generally, this is attributed to the annealing out of the strengthening mechanisms such as solid solution strengthening, dislocation forest strengthening and Hall-Petch strengthening [105]. Moreover, this also includes the change in the dislocation-particle interaction from the repulsive to the attractive one.

In respect to the ductility, it is shown to increase with temperature until a peak is reached [35, 55, 66]. For ferritic ODS steels, this is linked to the change in the deformation mechanisms with temperature. In situ TEM straining tests performed at room temperature on ferritic ODS steels have shown dislocations jerky motion between the two pinning points [36, 65, 127]. Under stress, the pinned dislocation bow out and when the stress is high enough the dislocations move to next pinning point [36]. Up till $\sim 400\,°C$ plasticity is shown to be controlled by intragranular dislocation mechanisms leading to homogeneous deformation [36, 65]. Whereas, at higher temperature, the motion of the dislocation was found to be more viscous and the role of the grain boundaries are reported to be more crucial. Lower intragranular

activity with grain boundary decohesion, cavitation plus porosity aligned along the grain boundaries for the samples at high temperature emphasis the intergranular character of the deformation [65]. However, high dislocation density with individual dislocations pinned at nano-oxide particles were still observed at elevated temperatures [36, 65, 127]. This confirms that nanoparticles still plays a crucial role in strengthening. Similar to the change in deformation mechanism, a modification of the fracture mechanism form intragranular at lower temperature to intergranular fracture at elevated temperature has been observed for ferritic ODS steels [65,66,128]. Furthermore, a drastic effect of strain rate on the damage has also been observed above ~ 400 °C [66]. Here, along with the lower ductility, a more severe intergranular damage is noticed at lower strain rate.

Nonetheless, as far as F/M ODS steels are concerned such studies are very rare; and therefore, through investigations are required in this context. Hence, in the present work, an attempt has been made to explore any change in the deformation and damage mechanisms with temperature.

2.4.2 Creep

Creep is a time-dependent permanent deformation of a solid body when a constant load is applied. For most metals creep becomes important at relatively high temperatures (above $0.4T_m$, where T_m is the melting point in K) [129]. The creep curves are visualized by plotting conventional creep strain (ε), creep strain rate ($\dot{\varepsilon}$) as a function of time (t) and/or by plotting stress versus creep rupture time. Basically in ε vs t plot, a distinction between primary/transient, secondary and tertiary creep is made. In principle, upon the application of load the expected instantaneous elastic-plastic strain (ε_0) is realized. Thereafter permanent deformation develops as a function of time. In primary/transient stage, the strain rate is relatively high, but decreases with increasing time and strain due to a process analogous to work

hardening at lower temperatures. The strain rate diminishes to a minimum and becomes near constant (strain increases linearly with time) as the secondary stage begins. It is therefore also referred to as steady-state creep. This is due to the balance between recovery (thermal softening) and work hardening. In the tertiary stage, the strain rate increases exponentially because of the creep damage (which includes nucleation of pores/voids or internal cracks and necking), until finally the material fails. The typical creep curves of a F/M 9%Cr-based ODS steel (also a used material in this work) is shown in Fig. 2.6. Clearly, ODS steel exhibits a "non-classical"creep behavior, with low creep strain and nearly no tertiary creep regime (the later one being undesirable). The comparison of various investigated ODS steels in literature with the conventional F/M steels is shown in Fig. 2.7. It is apparent that ODS steels offer significantly higher thermal creep strength and rupture time than the conventional F/M steels.
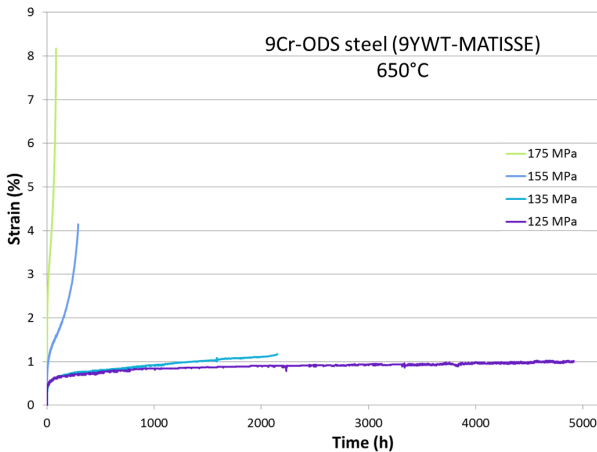
Figure 2.6: Creep strain as a function of time for 9%Cr-ODS steel at 650 °C [68].

The minimum creep rate is of particular importance for the characterization of the underlying deformation mechanism. The steady-state creep rate ($\dot{\epsilon}_s$)
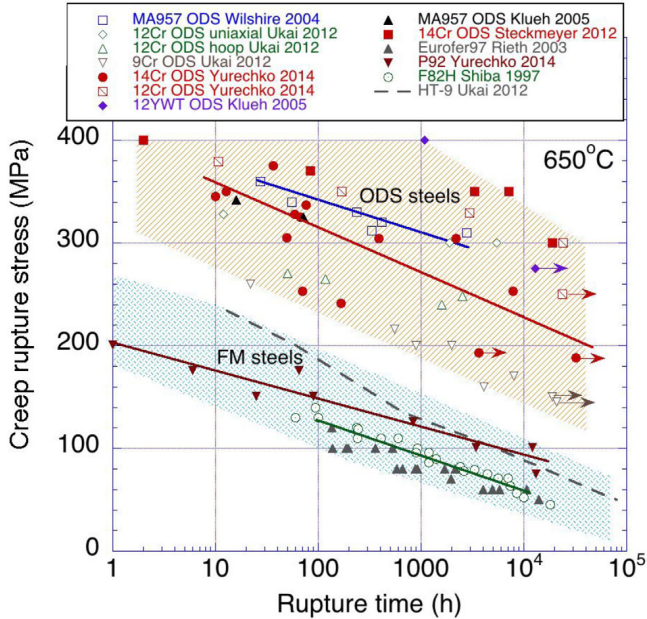
Figure 2.7: Comparison of the thermal creep behavior at 650 °C for ODS versus conventional F/M steels [57].

can be empirically described by a Norton approach which depends on the applied stress (σ) and temperature (T) [129]:

$$\dot{\varepsilon}_s = A\sigma^n exp\left(\frac{-Q}{kT}\right) \quad (2.5)$$

Where A and n are the material constants, Q is the creep activation energy, and k is the Boltzmann constant. Here, n is also referred to as stress or Norton exponent and describes the stress dependence of the minimum creep rate. The n can be obtained from the slope of the double-logarithmic plot of the steady-state strain rate as a function of the applied stress. Depending on the test temperature and applied stress, obtained n can then be used to identify active creep mechanisms such as diffusion creep when $n = 1$ and

dislocation creep if $n > 1$. The former generally occurs at low stress and high temperatures. Here, the transport of the material caused by diffusion is responsible for the creep deformation. Diffusion can occur either through the matrix (Nabarro-Herring creep) or along the grain boundaries (Coble creep). The dominant mechanism can be derived from Frost and Ashby's developed strain maps.

Creep behavior of various ODS alloys have been studied extensively and they are characterized by a high sensitivity of the strain rate to the applied load [130–132]. This is usually indicated by their high stress exponent n compared to other metallic materials. However, the creep mechanism in conventional ODS alloys (with slightly larger particle size) is shown to be affected not only by the applied stress and testing temperature, but also by the microstructural features such as grain size [133]. A double-logarithmic creep strain rate versus applied stress plot for such ODS alloys is shown schematically in Fig. 2.8. Here, the fine-grained ODS alloys (n is around 3-5) at higher strain rate behave like the dispersion-free alloys [121, 133, 134]. In coarse-grained ODS alloys (n can be more than 100), dislocation creep is a dominant mechanism and dislocation detachment from particles controlled creep at higher strain rate [133]. Whereas, at low stress and low strain rate ($n = 1$), diffusional creep is the main creep mechanism [121, 127, 133, 134]. For intermediate grain size alloy ($n = 11$-25), it was assumed that a second creep mechanism such as Coble creep or grain boundary sliding acts in parallel to control the steady-state creep strain rate [133]. In contrast to this, recently developed ODS steels with so called nano-clusters (oxide clusters with size < 5 nm) have shown no dependency on the grain size [135].

The typical high Norton exponent of ODS alloys can also be explained by assuming a threshold stress σ_{th} below which the creep deformation becomes negligibly small (Fig. 2.8). Taking this into account Eq. 2.5 becomes:
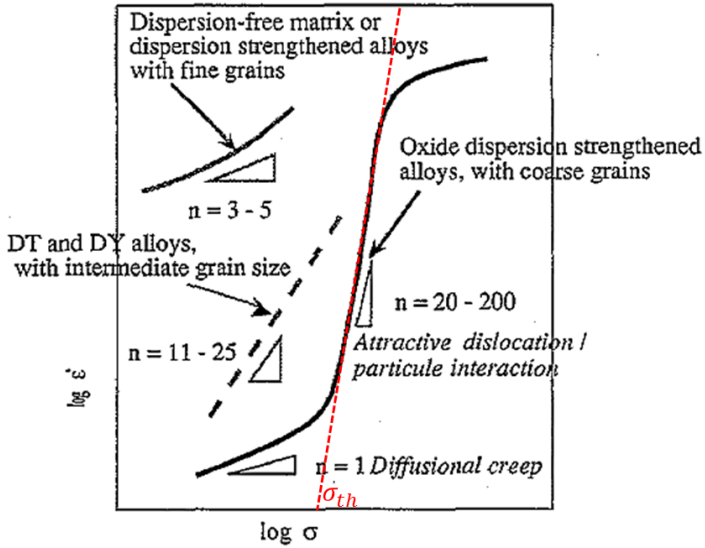
Figure 2.8: Comparison between creep behavior of coarse-grained, intermediate-grained (DT and DY alloys) and fine-grained ODS alloys and dispersoid free matrix [133].

$$\dot{\varepsilon}_s = A'(\sigma - \sigma_{th})^{n'} exp\left(\frac{-Q}{kT}\right) \qquad (2.6)$$

For this purpose, a new stress exponent A' and the constant n' are introduced. However, the threshold stress concept is purely phenomenological and does not reflect physical background of the effect. It nevertheless allows an adequate description of the creep behavior of ODS alloys, without the use of high stress exponents or activation energies. Dislocation climb can not explain this phenomenon alone. TEM investigations on conventional ODS alloys have shown dislocations pinning on the departure side of the oxide particles (backside-pinning) [133]. Therefore, the overcoming of obstacles

is no longer now a dominant effect but the detachment of the dislocation from the back side is.

2.4.3 Fatigue

Fatigue is a process of progressive localized permanent structural changes that ultimately lead to the failure of a material when it is subjected to conditions that produce fluctuating stresses and strains at particular point or points after a sufficient number of fluctuations. In application, fatigue is a detailed analysis, trying to assess what will occur at a particular location of a component or assembly under cyclic loading. For a design engineer, fatigue analysis is mainly dealing with the estimation of probable fatigue life. Depending upon the amplitude of stress or strain acting on to a component, fatigue life varies significantly and accordingly classified. For example, when the stress (or strain) amplitude exceeds yield strength (or 0.2% strain which is plastic deformation regime) of a material then the fatigue crack initiates easily and propagates to final fracture leading to lower number of cycles to failure (N_f). And generally, when the fatigue failure occurs within 10^4 number of cycle (N) then it is called low cycle fatigue (LCF). Unlike LCF, when stress/strain amplitude falls within elastic limit, the failure occurs at comparatively higher number of cycles ($10^7 > N > 10^5$); and therefore, termed as high cycle fatigue (HCF). In this regime, the maximum life is spent on the crack initiation/nucleation and even if crack is initiated, it may not propagate, thus leading to higher N_f. In addition, when N_f exceeds 10^7 cycles this is termed as very high cycle fatigue or in short VHCF.

Fatigue tests are carried out either with stress or strain control. Historically, these tests have been carried out with symmetrical stress in tension and compression. To date, these stress-controlled tests have been used for the design of the components whose loads are predominantly elastic. In HCF and VHCF case, the strength determines the fatigue resistance of the material,

the cracking (crack nucleation) being the life determining event. Strain-controlled fatigue tests are preferred when high stresses, e.g. at notches, and the inelastic deformation is large compared to the elastic deformation portion. Here, the cyclic life depends on the ductility of the material and the crack propagation determines the fatigue resistance.

Materials and components in power plants are often subjected to thermal as well as thermo-mechanical alternating loads as a result of the constraint in their free expansion and contraction due to temperature gradients which occurs during start-up and shut-down operation, respectively or due to power change during operation. Therefore, it critically important to know fatigue lives of material/components beforehand to avoid any severe accidents. One possibility to determine the service life of power plant components experimentally is to conduct thermo-mechanical fatigue tests. However, these tests are very complex because of the simultaneous variation of temperature and mechanical strain. Moreover, these tests require a great deal of time and are accordingly costly. In addition, no standards procedure are still available for these type of tests. The second possibility is to carry out isothermal fatigue tests. They are standardized [136] and their results can be used to predict fatigue life using well-developed empirical laws. Here, to represent the component behavior in a laboratory test, the thermal strains are usually replaced by mechanical strains, introduced and controlled under isothermal conditions [137]. The slow start-up and shut-down cycle of the power plants is replaced by a symmetrical and a continuous fatigue cycle of equal strain rates in tension and compression which yields low-cycle fatigue (LCF) and with a hold period at a constant peak strain to simulate the on-load period i.e. creep-fatigue (CF).

In this work, the strain-controlled fatigue tests have been carried out in the LCF regime. Here, the material is usually subjected to a triangular waveform with constant strain amplitude (see Fig. 2.9). The resulting material

resistance is recorded in the form of a stress response. The stress-strain (σ-ε) hysteresis represents the stress profile as a function of the strain in each cycle. Depending on the material, usually two types of response are observed. If the maximum stress increases with the number of cycles than this is known as cyclic/strain hardening (see Fig. 2.9) whereas if maximum stress decreases with number of cycles than this is termed as cyclic/strain softening (Fig. 2.9). The cyclic hardening and softening behavior is generally illustrated in terms of the peak stress versus number of cycles curves (see Fig. 2.10). As observed often, after an initial decrease or increase in the peak stress, a saturation region (steady state) follows, i.e the shape and size of the hysteresis remains constant, until peak tensile stress decreases as a result of the nucleation/propagation of the fatigue cracks.
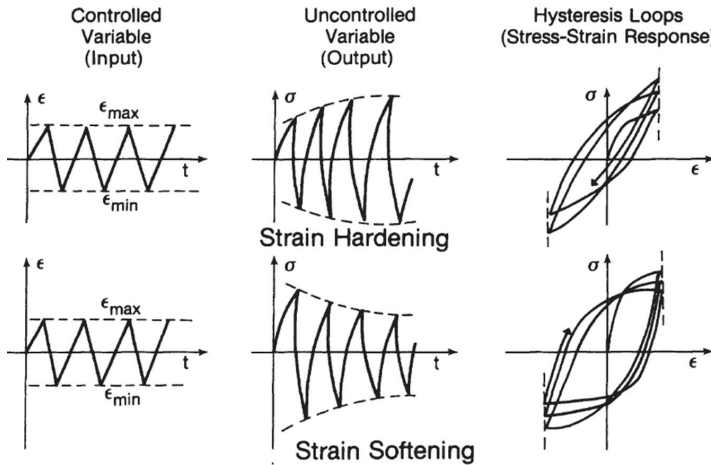
Figure 2.9: Schematic material response to the symmetrical strain-controlled cyclic input [138].

In respect to the material's fatigue life, three aspects play crucial role:

1. Cyclic deformation

2. Nucleation of fatigue damage which later develops into a crack
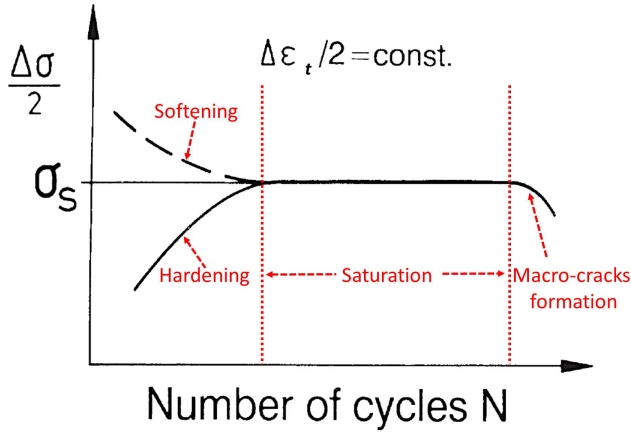
Figure 2.10: Schematic representation of cyclic stress response curves obtained in tests with constant strain amplitude [139].

3. Propagation of a fatigue crack

During cyclic deformation, microstructural modifications transpire in order to achieve stable low-energy configurations. Here, modifications rate and amount precisely depend upon two important factors: (1) testing conditions which include deformation rate (strain rate), its extent (amplitude) and temperature; and (2) microstructural factors such as crystal structure, stacking fault energy, dislocation density and the presence or absence of the coherent or incoherent particles [140]. In materials, where cyclic deformation is a function of dislocation density, the competition between dislocations generation/multiplication and their annihilation/storage (via dislocation-dislocation annihilation and dislocation-grain boundary interaction) occurs initially before achieving steady state. And the dominance of one mechanism over the other defines the evolution of dislocation density; and hence, the overall material behavior. For example, materials with high initial dislocation density (e.g. mentioned F/M steels in section 1.1) undergo cyclic softening mainly due to the overall reduction in disloca-

tion density [17, 22–28]. Here, the rate of dislocations annihilation/storage is significantly large than that of their generation/multiplication. In contrast, materials with low initial dislocation density (or with FCC crystal structure like austenitic steel [61, 141]), exhibit cyclic hardening due to the increment in dislocation density [139, 141, 142]. Here, the rate of dislocations generation/multiplication is obviously far greater than that of their annihilation/storage. Nevertheless, once steady state is reached, the rate of dislocations generation/multiplication as well as their annihilation/storage is balanced. And hence, a stable dislocations density leads to a stable cyclic response with constant peak stress (saturation stage) until failure.

In case of ODS or precipitation-hardened materials, apart from matrix, the fatigue behavior is strongly dependent on the nature of the particle-matrix inference, particles size, their distribution and the nature of their interactions with the dislocations [140]. For example, as the small and coherent particles can be sheared/cut by the dislocations, they do not contribute to the strength and the cyclic behavior is mainly matrix controlled. On the other hand, the larger particles, which are incoherent, act as the barrier for dislocations motion; and hence, provide strengthening as well as influence cyclic response. A literature review concerning the LCF behavior of ODS steels which usually contains incoherent particles is presented separately, see further.

It is now well-known that in crystalline materials, dislocations low-energy configurations (which are generally three-dimensional (3D) dislocation structures e.g. ladder, vein and labyrinth etc.) result in the localization of cyclic slip in surface grains regions in the form of persistent slip bands (PSBs) which intersects free surface to form persistent slip markings (PSMs) including intrusion and extrusions (see Fig. 2.11a). These intrusions act as notches which incorporate local stress concentration sites and favor formation of micro-cracks, as shown in Fig. 2.11b [140, 143–145]. However, in

addition to this various other microstructural features such as grain bounda-
ries (whose orientation coincides roughly with the direction of slip [146]),
secondary phase particles, defects (pores/voids), fabrication induced surface
imperfections can also act as preferred crack initiation sites, see Fig. 2.12
and associated text. Independently, environment and temperature based ef-
fects, e.g. oxidation, can also result or assist in the nucleation the fatigue
crack [138, 147], which will be discussed later in this work.
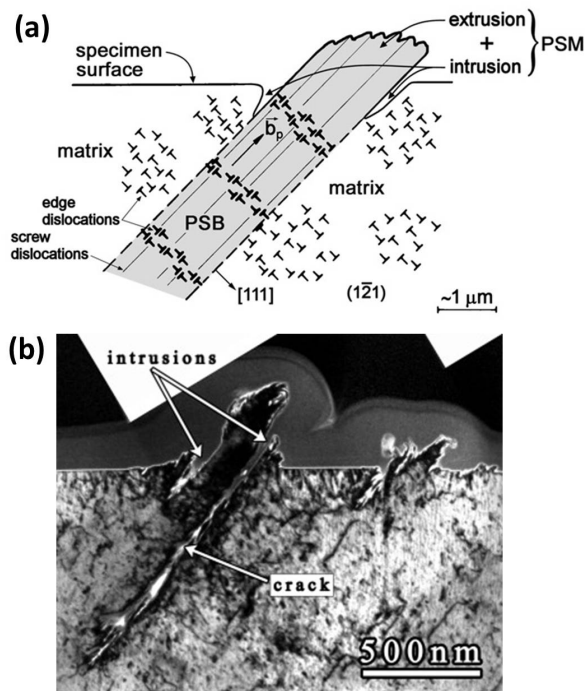
Figure 2.11: (a) Section through the grain showing surface profile of mature PSM formed at the
side where the PSB intersects the free surface. Dislocation distributions in PSB with a so-called
ladder structure embedded in the matrix with a vein structure are indicated schematically [144].
(b) Surface profile of two PSMs as imaged in TEM of a surface foil produced by FIB of fatigued
austenitic 22% Cr steel [145].
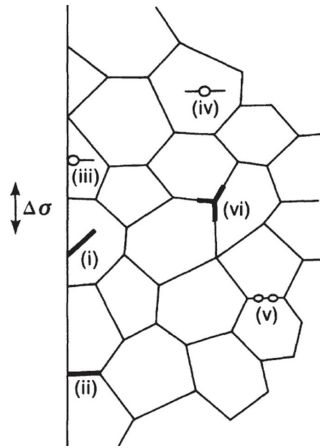
Figure 2.12: Various sites for crack initiation in polycrystalline materials. (i) Transgranular, (ii) intergranular, and (iii) surface inclusion or pore. The first two are PSB induced surface cracks, and the latter type is observed in some commercial alloys. There are also internal defects such as (iv) inclusions, (v) grain boundary voids and (vi) triple point grain boundary intersections which may be sources of crack initiation. The latter two are commonly observed at elevated temperatures [138].

Once a fatigue crack is initiated, it grows as a result of further cyclic deformation. In polycrystalline materials, grain boundaries often act as a barrier for micro-crack growth. On the other hand, in high temperature or corrosive environments grain boundaries can not only act as the sources of crack initiation but the initiated crack may also grow along the grain boundaries (see Fig. 2.13a) [138]. In general, fatigue crack propagates initially along the plane of maximum resolved shear stress up to few grain diameters (Fig. 2.13a). In ductile solids, cyclic crack growth is envisioned as a process of intense localized deformation in slip bands near the crack tip which leads to the creation of new crack surfaces by shear decohesion. When the crack or zone of plastic deformation surrounding the crack tip is confined to within a few grain diameters, crack growth occurs predominantly by single shear in the direction of primary slip system and is termed as stage-I crack growth, as shown in Fig. 2.13a. The crack growth rate of stage-I is

generally very low and the fracture surface is practically featureless [138]. Thereafter, with further cyclic deformation, the crystallographic crack changes direction and propagate in a non-crystallographic plane (forming stable crack growth region), which is perpendicular to the loading direction, and is called stage-II fatigue damage (see Fig. 2.13a). The stage-II crack growth is often called a continuum crack propagation (mode 1), which is due to more constrained interior grains having more than one slip plane activation [138]. With respect to fracture surface, Stage-II is characterized by ductile features called "striations"which are ripples on the fracture surface as shown in Fig. 2.13b. In general, spacing between adjacent striations correlates well with the experimentally measured crack growth rate although each striation may correspond to more than one fatigue cycle in some cases. According to plastic blunting model, originally given by Laird and Smith [138], a crack tip amenable to duplex slip plastically blunts upon the application of tensile stresses and the blunting process also results in crack extension of the order of crack tip opening displacement. During compression, crack tip will re-sharpen. Since crack closure cannot fully negate blunting and due to crack extension during previous tensile load striations will form. This model applies to wide variety of ductile materials including polymers. Fatigue crack propagates in a stable manner until the net section stress attains a critical level thereafter total fracture occurs by ductile rupture (stage-III).

With a rise in temperature, several time dependent phenomena such as dynamic strain aging (DSA), sub-structural recovery, creep and environment (oxidation) interact with the fatigue process. These time dependent effects may act independently or in combination in a synergistic way leading to premature fatigue failure. As a general rule, fatigue enhances the time dependent mechanism and in turn, cyclically induced changes are enhanced at high temperatures. These issues will be discussed in more detail in the results and discussion sections 4.3 and 4.4.
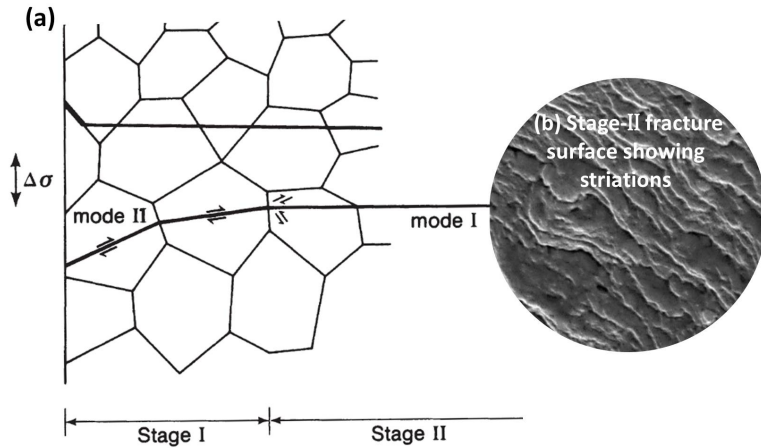
Figure 2.13: (a) Transgranular and intergranular crack initiation and transgranular crack growth, stage I and stage II crack growth [138] along with the stage-II fracture features called striations in (b) [51].

LCF behavior of ODS steels

The fatigue behavior of Fe-based ODS steels has been so far very less investigated. Precisely, till now majority of studies were carried on high-Cr (12%Cr or more) ferritic ODS steels (6 in number, see Ref. [41, 42, 50, 51]). However, only three different F/M 9%Cr ODS steels [42, 50, 148] and two similar austenitic ODS steels [61] were investigated.

In the early development phase of ODS steel, Banhardt et al. in 1995 investigated the influence of grain size and morphology on the fatigue resistance of PM 2000 (20%Cr ferrtic ODS steel) [41]. Although no clear tendency was found, the highest cyclic life was achieved by a relatively fine microstructure. Thereafter, other groups successfully demonstrated the significance of oxide dispersion with respect to the cyclic properties. In comparison to their non-ODS counterparts, ODS steels offered higher cyclic stress levels with significantly lower inelastic strain amplitudes [42, 45, 149]. This

was mainly attributed to the strengthening effect of the nano-oxide particles [45, 148, 149]. In respect to fatigue life, ODS steels were found superior only under lower strain amplitudes ($< \pm 0.5\%$) i.e. towards approaching HCF regime [42, 61, 148, 149]. However, this was not surprising since stronger materials are known to offer better cyclic strain-life under lower strain amplitudes and ductile materials are acclaimed to perform better under higher strain amplitudes [150]. This is due to the fact that strong materials resist imposed strain elastically on the basis of their strength, while ductile materials (for e.g. non-ODS F/M steels) resist strain plastically on the basis of their ductility [150]. In 2014, Hutař et al. investigated the effect of oxide dispersion on small fatigue crack propagation [151]. Their study concluded that the resistance of ODS materials against fatigue crack propagation is lower than that of the original base materials. Therefore, sincere efforts are required to improve ductility of ODS steels which fundamentally depends on the understanding of their deformation and damage mechanisms.

In addition, oxide dispersion is supposed to stabilize the cyclic response of a conventional ferritic and F/M steels. Indeed, Ukai et al. reported stable cyclic response for tempered martensitic 9%Cr, as well as ferritic 12%Cr, ODS steels [42]. On the other hand, Kuběna and others showed that while the ferritic 14%Cr ODS steels undergoes slight initial softening with a subsequent minor hardening or stabilization depending on the testing conditions [45], the tempered martensitic 9%Cr ODS EUROFER and T91 still exhibits cyclic softening but to a lower extent than their non-ODS variants [49, 148]. Therefore, the significance of oxide particles particularly in terms of stabilizing the cyclic stress response remains questionable. Moreover, the processing routes, parameters, and hence developed matrix appears to play a critical role in defining the overall LCF behavior of these steels.

In literature, the promising fatigue properties of ODS steels have been correlated to the ability of oxide particles in stabilizing microstructure

[30, 49, 51, 148]. However, the number of scientific work discussed above shows that the investigations concerning the fatigue behavior of ODS steels are still in their early stage. Especially, when considering the gaps that needs to be filled in respect to (1) the effects of cyclic loading on the interactions between oxide particles and dislocations; (2) the understanding of the microstructural modifications and damage characteristics under varying amplitudes, strain rate and temperature; (3) the clarification on the independent role of the matrix in defining the overall LCF behavior; (4) the examination of the ability of oxide particles in inhibiting the strain localization (as in some ODS steels 3D dislocation structures are reported [46, 51]) which could constraint damage accumulation and (5) the understanding of the modifications brought by introducing creep during fatigue. Therefore, these topics need to be studied extensively in order to optimally adjust their cyclic strength and fatigue resistance.

Therefore, keeping above-mentioned gaps in perspective, this work was conduced on a newly developed tempered martensitic 9%Cr ODS steel. The pure LCF behavior was investigated at elevated temperatures under varying strain amplitudes, see section 4.3. In addition, the associated deformation and damage mechanisms were studied at both micro- as well as nano-scale via electron microscopy. Furthermore, for first time the creep-fatigue investigations of a F/M ODS steel was conducted by introducing a hold-time at the peak tensile strain, see section 4.4. Such a hold period simulates the loading of a component under stationary operation. Here, the tests were also accompanied by thorough microstructural investigations for identifying the modifications in the deformation and damage mechanisms by introducing creep during fatigue.

3   Material and methods

This chapter documents various details regarding investigated material that include its chemical composition and production route. Moreover, vital technicalities concerning experimental procedures, that involve both mechanical as well as microstructural characterization, are presented in detail.

3.1   Material

In present work, a Fe-9%Cr based ODS steel (designated herein as 9YWT-MATISSE) was produced under the supervision of Commissariat à l'Énergie Atomique et aux Énergies Alternatives (CEA), France, and was provided for investigations within the framework of MatISSE (Material's innovations for safe and sustainable nuclear energy in Europe) [152], a project dealing with materials for transmutation technologies and advanced reactors. The production route includes conventional powder metallurgy followed by a distinct heat treatment to develop an optimized tempered martensitic structure (see Fig. 2.1 in section 2.1.2).

The fabrication steps are as follows: Firstly, the gas-atomized pre-alloyed metal powders, obtained from Aubert & Duval, France, were mechanically alloyed (MA) under hydrogen atmosphere with 0.25 wt.% Y_2O_3 in a vertical attrition ball mill at Plansee, Austria. The chemical composition of the steel after MA is presented in Table. 3.1. Subsequently, the MA powder was sealed in soft steel cans, degassed and hot extruded into rods at around 1100 °C. The air cooled rods, in ferritic state, were semi-finished in form

Table 3.1: Chemical composition (all in wt. %) of the investigated 9Cr-ODS steel.

Cr	W	Ti	Si	Mn	Ni	C	Y_2O_3	Fe
9.1	1.1	0.3	0.3	0.3	0.2	0.1	0.25	Bal.

of cylinders (30 mm in length and 4.2 mm in diameter) using wire electrical discharge machining (EDM). Thereafter, a typical phase transformation treatment, including austenitization (at 1050 °C for 10 min) and quenching (using helium gas with a cooling rate of 6-7 °C/s), was applied to develop an isotropic martensitic microstructure. Finally, to obtain a better compromise between strength and ductility, a tempering treatment, involving annealing at 750 °C for 20 min followed by air cooling, was performed to obtain required tempered martensitic structure. The microstructural investigations results are documented separately in section 4.1.

3.2 Mechanical testing

The mechanical characterization includes tensile testing to understand material's response under monotonic loading, pure fatigue testing to comprehend material's behavior under cyclic loading, and creep-fatigue testing to realize possible creep-fatigue interaction. Due to the limited quantity of material (as it was produced in a laboratory scale) and in order to maximize the number of specimens/tests, miniaturized specimen geometries were chosen (see next subsections). As developed material is expected to possess an isotropic microstructure, all characterizations are carried out parallel to the extrusion direction of the fabricated rod.

3.2.1 Tensile testing

For tensile testing, an Instron 4505 universal testing machine equipped with a high-temperature furnace and an extensometer (from Mess & Feinwerk-

tecknick with model MFHT5 having a gauge length of 10 mm) was used (see Fig. 3.1). All tests were performed on a miniaturized specimen geometry (see Fig. A.1 in appendix A.1), with a gauge diameter of 2 mm and a gauge length of 13 mm. The displacement-controlled tests were carried out in air at temperatures ranging from room temperature (RT) up to 800 °C with the nominal strain rates of 10^{-3} s^{-1} and 10^{-4} s^{-1}. At elevated temperatures, the holding time prior to the test start was at least 30 min. The temperature was monitored by a (Ni-Cr)-Ni thermocouple placed in contact with specimen bottom shoulder and was controlled to within $\pm$ 2 °C.
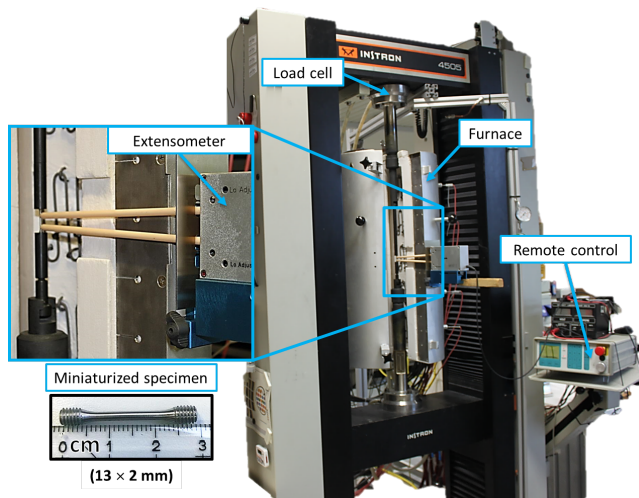
Figure 3.1: Instron testing setup with miniaturized specimen used for monotonic investigations.

The data from each test including time, force and elongation was stored in a text file using Instron software. Thereafter, self-coded MATLAB script was used to calculate engineering stresses on the basis of the initial cross section, engineering strain based on the measured elongation and initial probed gauge length (10 mm), yield stress at 0.2% strain offset, ultimate tensile stress, uniform elongation and total elongation-to-failure. Although

the focus of this research is to investigate the tempered martensitic 9YWT-MATISSE, the tensile tests were also performed on specimens taken from the ferritic state (i.e. after extrusion) in order to compare the influence of heat treatment.

3.2.2 Pure-fatigue/continuous cycling (PF/CC) testing

The PF/CC testing was also carried out on a miniaturized specimen geometry (see Fig. A.2 in appendix A.2). Here, the gauge diameter is 2 mm and the gauge length is 7.6 mm, with an overall length of 27 mm. The specimen design was developed at Karlsruhe Institute of Technology (KIT), Germany within the framework of irradiation programs [153]. These specimens were equipped with threaded ends and specific centering alignment, allowing them to be fixed in a reliable manner. To avoid the influence of surface quality on cyclic life, specimens were axially polished in order to remove the circumferential tool marks developed as a result of a prior turning step. The final average surface roughness (RA) measured using a Sensofar optical profile is $0.26 \pm 0.033 \ \mu$m.

For testing, a computer controlled MTS 810 servo hydraulic testing machine (with MTS flex test TM 40 controller), equipped with a radiative furnace and a high-temperature extensometer (from MAYTEC with model PMA-12/V7/1 having a gauge length of 7 mm), was used (see Fig. 3.2). The axial strain-controlled fatigue tests were conducted with the nominal strain rate of 10^{-3} s^{-1} and with a fully-reversed triangular waveform (R = -1) in air at 550 °C and 650 °C for different strain amplitude values ranging from $\pm$ 0.4% to $\pm$ 0.9%. The chosen testing temperatures lie within the proposed operating temperature range for advanced nuclear reactors. The temperature was controlled to within $\pm$ 2 °C with a type S Pt-Pt10Rh thermocouple attached to the bottom shoulder of the specimens. The dwell time prior to the test start was at least 30 min after achieving the test temperature.

To protect machine as well as extensometer, the test was terminated before the specimen fractured completely, using a simple procedure available in the commercial MTS software. The data from each test including time, cycle number (N), force and strain (ε, based on the measured elongation and initial gauge length) was stored in the text file also using MTS software. Thereafter, self-coded MATLAB script was used to calculate engineering stresses (σ) on the basis of the initial cross section, true stresses based on $\sigma_{true} = \sigma(1 + \varepsilon)$ relation and sort data out for each cycle that includes ε with corresponding σ_{true} for further analysis.
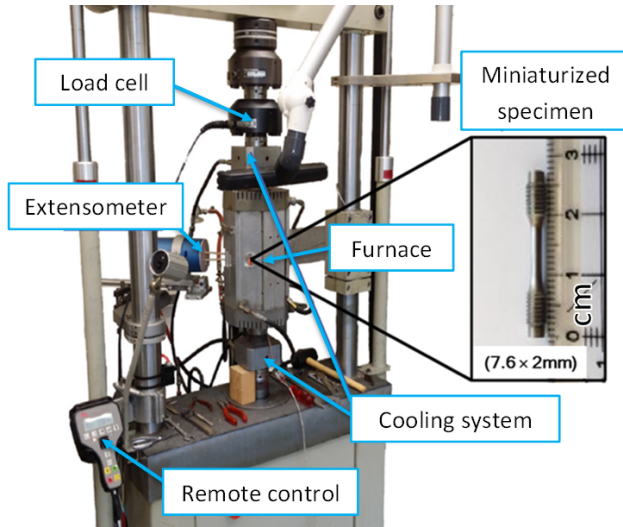
Figure 3.2: MTS testing setup with miniaturized specimen used for cyclic investigations.

Another self-coded MATLAB script was then used to determine various other cyclic parameters like inelastic strain ($\Delta\varepsilon_{in}$), maximum peak stress (σ_{max}), minimum peak stress (σ_{min}) and elastic modulus (E) from the plotted σ_{true} versus ε hysteresis, as shown in Fig. 3.3a, according to the ASTM standard E2714-13 [136]. However, as in the present case $\Delta\varepsilon_{in}$ is almost equivalent to the plastic strain $\Delta\varepsilon_p$, for convenience $\Delta\varepsilon_{in}$ is measured as the

51

width of the hysteresis loop at zero stress and accumulated inelastic strain per cycle is equal to $4 \times \dfrac{\Delta\varepsilon_{in}}{2}$. The number of cycles to failure (N_f) was estimated at each testing condition from the σ_{max} versus N plots, as shown in Fig. 3.3b. Here, N_f is defined at the attainment of a specific percentage (X = 10%) decrease in the σ_{max} in relation to linear stage determined during the test.
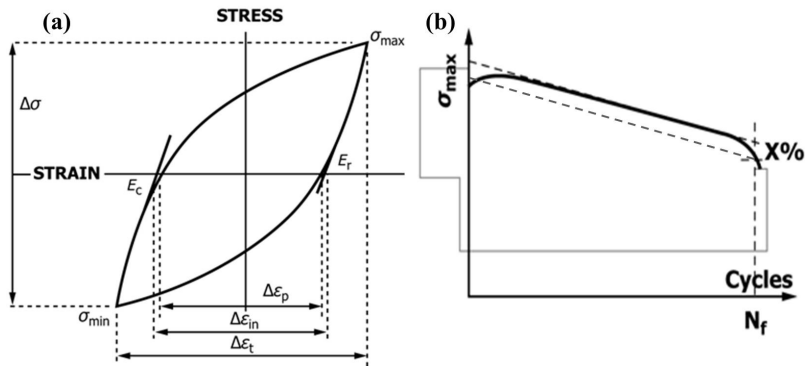
Figure 3.3: (a) Determination and definition of the parameters from the σ_{true} versus ε hysteresis, and (b) schematic representation for the determination of the cyclic life (N_f) according to ASTM standard E2714-13 [136].

3.2.3 Creep-fatigue (CF) testing

CF testing was also carried out on the above-mentioned PF specimens and using same test setup and procedure. However, due to the limited quantity of material, the strain controlled tests (R = -1) were only conducted at 650 °C with a nominal strain rate of 10^{-3} s^{-1}. The creep in PF cycle was introduced by inserting a hold-time segment at peak tensile strain of 0.7% (Fig. 3.4). The influence of hold-time duration was investigated by employing three hold-time durations of 1, 10 and 30 minutes, respectively. Unless otherwise indicated, all stresses here also correspond to the true stresses.
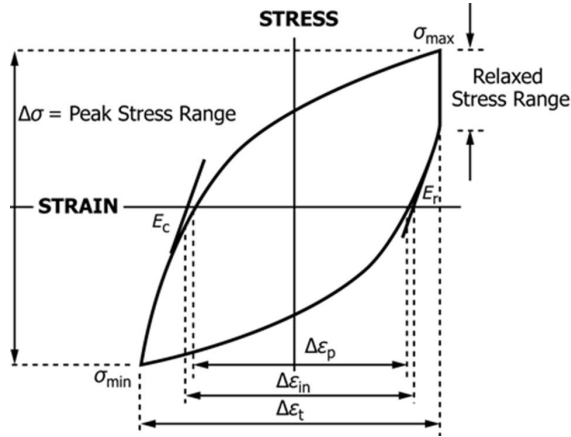
Figure 3.4: Determination and definition of the parameters from the creep-fatigue σ_{true} versus ε hysteresis according to ASTM standard E2714-13 [136].

3.3 Microstructural characterization methods

Microstructural characterization was carried out by using various techniques including transmission electron microscopy (TEM), scanning electron microscopy (SEM) and electron backscatter diffraction (EBSD). The main working principles of these imaging techniques are summarized below.

3.3.1 Transmission electron microscopy (TEM)

The TEM has a similar optical configuration to an light microscope. However, here instead of light, a flood beam of electrons (having shorter wavelength) illuminates an ultra-thin sample (less than 100 nm) in vacuum. A generalized cut-away diagram of the internal structure of a TEM alongside an example of a modern instrument is shown in Fig. 3.5. The first primary image is formed by lower objective lens by focusing transmitted electron beam on its image plane. This image is further magnified using additional intermediate and projector lens to form a highly magnified final image on

the viewing phosphor screen or charge coupled device (CCD) for observation.
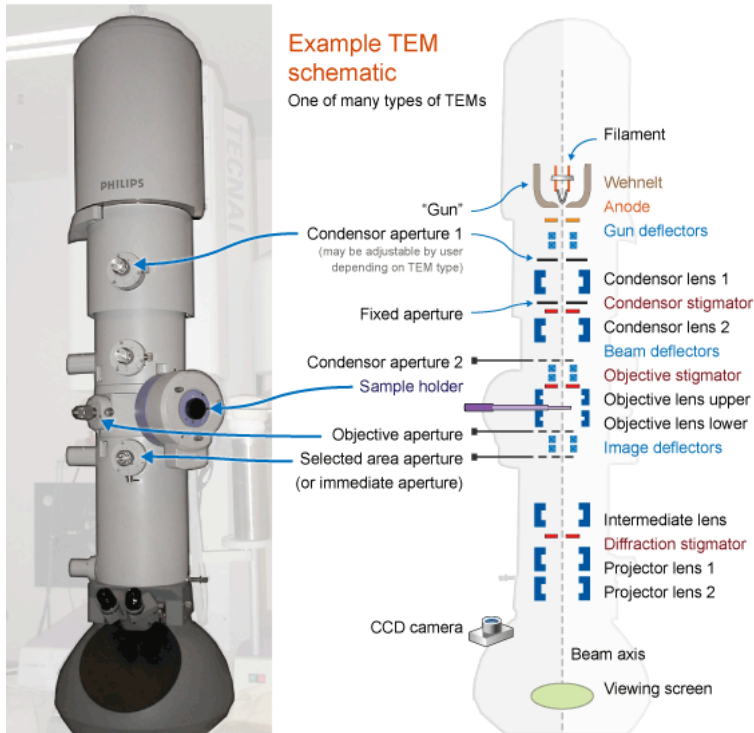
Figure 3.5: A generalized cut-away diagram of the internal structure of a TEM alongside an example of a modern instrument [154].

In the process of making primary image, objective lens forms a reciprocal space of the crystal structure (a regular array of reflections), namely, diffraction pattern on the back focal plane of the lower objective lens. To view this diffraction pattern, image system lens are adjusted such that the back focal plane of the objective lens act as the object plane of the intermediate lens. This causes the diffraction pattern to be projected onto the viewing screen. The appearance of the diffraction pattern can reflect the nature of

phases in the specimen. For example, if the material is micro-crystalline or amorphous the diffraction pattern consists of a series of concentric rings rather than organized spots/discs which signifies distinct crystal structure. In literal sense, diffraction pattern is the Fourier transform of the electron wave, while primary image is the Fourier transform of the diffraction pattern.

Actually, electrons may pass through the sample either without being scattered (called transmitted beam) or scatter/diffract off the axis by interacting with the sample. The scattering occurs from those crystallographic planes (where the lattice act as a diffraction grating) in sample that satisfy Bragg's law, which is given as:

$$2d \sin \theta = n\lambda \tag{3.1}$$

where, d is the atomic spacing of the parallel family of diffracting planes, θ is the diffraction angle, n is a natural number, and λ is the wavelength of the electron. In principle, diffraction according to Bragg's law occurs whenever the Ewald sphere (sphere of radius: $1/\lambda$) touches a point on the reciprocal lattice. In many/multi-beam conditions, diffraction occurs for all the reciprocal lattice points (diffraction directions) according to Weiss zone law and lying close to the Ewald sphere. However, the intensity of those points are not as intense as the central (0) transmitted beam since the former points do not lie exactly on the Ewald sphere. Diffraction contrast images can be formed by either choosing transmitted or diffracted spots using objective aperture. The image formed merely by transmitted beam is called bright field (BF) image, whereas the one formed by selecting scattered/diffracted beam is termed dark field (DF) image. In BF image, areas which scatter or absorb electrons appear darker while those which transmit electrons appear brighter. In DF image, regions where scattering occur appears bright or else emerge black. The analysis of diffraction pattern and its correlation with the

BF and DF images provide vital information about the present phases and their crystal structure in a material.

Often, in diffraction mode, it is necessary to isolate a local region so that only this region produces a diffraction pattern. This is achieved by inserting selected area aperture into the column to obtain so called selected area diffraction pattern (SADP). To obtain diffraction pattern close to zone axis and various other diffraction conditions (e.g. two- or weak-beam condition) sample needs to be tilted carefully with respect to the incident beam (α- or β-tilt). A two-beam condition is a preferred condition for imaging. Here, sample needs to be tilted (reciprocal lattice is rotated by appropriate double tilt (X and Y)) such that a particular G (hkl) satisfying the Weiss zone law is brought exactly on the Ewald sphere (see Fig. 3.6a). This makes that particular diffraction spot as intense as the central transmitted beam (0). It is known as two-beam since only the 0 and G (i.e. only two directions) are on the Ewald sphere. As a result of this tilt, the other directions satisfying the Weiss zone law moves even farther away from the Ewald sphere resulting in significant decrease in their intensities. However, two-beam condition usually yields strong diffraction contrast that might not be appropriate for imaging microstructural defects such as dislocation and stacking faults. For this, weak-beam condition is preferred where the sample firstly is tilted in the opposite direction so that the selected G reflection satisfies the Bragg's condition exactly. Thereafter, incident beam is tilted (done by moving diffraction pattern) such that the G reflection is in the optical axis, whereas the Bragg's condition for the 3G refection is exactly satisfied. Then we get a relatively large excitation error for the G reflection. This condition is shown in Fig. 3.6b.

If the objective aperture is removed or sufficiently large than the scattered electron along with the transmitted ones contribute to form an interference image on the objective lens image plane. This image is a phase contrast
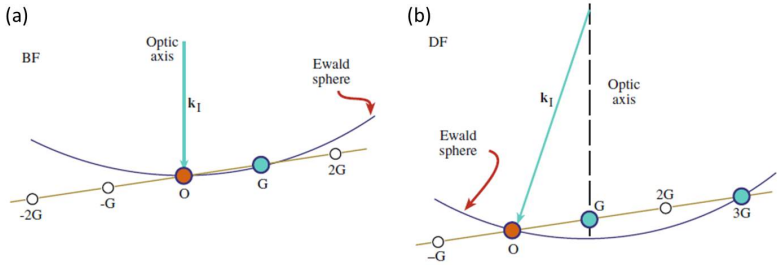
Figure 3.6: (a) Two-beam condition for the BF image and (b) weak-beam condition for the DF image, the G refection is in the optical axis with a large excitation error [155].

image which is capable of providing detailed diffraction information of very localized structures that are way smaller than the lower limit of the selected area aperture. This imaging technique with atomic resolution is generally called high-resolution TEM (HRTEM). HRTEM is ideal to investigate the nanoparticles crystal structure and orientation relationship between them and the matrix in matrix-particles systems. However, the interpretation of these image is complex and requires extra image simulation.

If a convergent beam instead of parallel beam is utilized in TEM, the electron beam can be focused on a narrow spot of the sample. Thus, the transmitted and scattered electrons only contain information of a very localized region of the sample. Therefore, the focused spot, which is called the electron probe, can scan over the sample in a raster, while the transmitted or scattered electrons can be captured by various detectors to form different mappings of the sample. This feature distinguishes the technique, scanning transmission electron microscopy (STEM) from conventional TEM (see Fig. 3.7). The most commonly used detector is the annular dark field (ADF) or high angle annular dark field (HAADF) detectors. Locating at high scattering angle, ADF/HAADF detector can minimize the influence of the Bragg's diffracted electron, and only capture those Rutherford scat-

tered electrons. As the differential cross section of Rutherford scattering is proportional to the square of the atomic number, Z^2, the contrast provided by the HAADF detector is called Z-contrast. Z-contrast image is very sensitive to the element composition of the specimen, making it a strong tool to examine the chemical information. More importantly, STEM can be combine with some powerful spectroscopies, such as the energy dispersive X-ray spectroscopy (EDX) and the electron energy loss spectroscopy (EELS), to provide semi-quantitative chemical information. Hence, STEM-EDX and/or STEM-EELS, also called analytic STEM, are great tools to investigate the chemical composition of the precipitates/particles within the matrix, such as the ODS steel systems studied in this work.

In this work, the TEM studies were performed with a FEI TECNAI-20F (200 kV) TEM equipped with the HAADF detector for STEM. The elemental analysis was performed using EDX spectroscopy.

3.3.2 Scanning electron microscopy (SEM)

Again as the name suggest, SEM uses a beam of electrons which is guided and focused by a series of electromagnetic lens on the sample. A generalized cut-away diagram of the internal structure of a SEM along with the function of each element is shown in Fig. 3.8. As the beam strikes the sample, with the help of the scanning coils it scans from pixel to pixel left to right and top to bottom (like a raster scan). The magnification results from the ratio of the dimensions of the raster on the sample and the raster on the display device. Assuming that the display screen has a fixed size, higher magnification results from reducing the size of the raster on the sample, and vice versa.

Apart from a much higher resolution (better than 10 nm), SEM provides great topological (3D), chemical compositions, crystallographic details etc
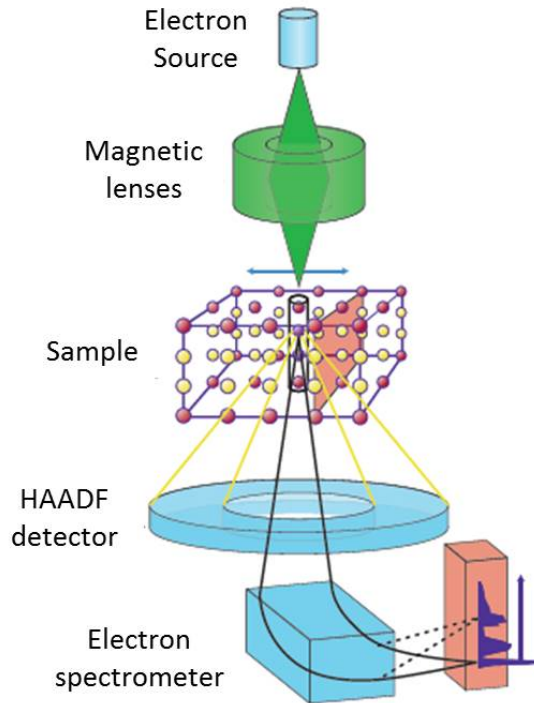
Figure 3.7: Major elements of scanning transmission electron microscopy (STEM) [156].

thanks to different attached detectors which detect various signals emitted from different parts of the interaction volume (see Fig. 3.9). Two of the most important signals which are used in this work for imaging are the secondary electrons (SE) and back scattered electrons (BSE). SE got their name because they are generated from secondary source (sample) other than the primary ones generated from cathode. They are the loosely bound electrons from those atoms which are near to the surface of the sample and are ejected due to inelastic scattering by the incident primary high energy electrons. BSE are the elastically scattered electrons deflected by the nuclei of the atoms. While SE provide more topographical information as they
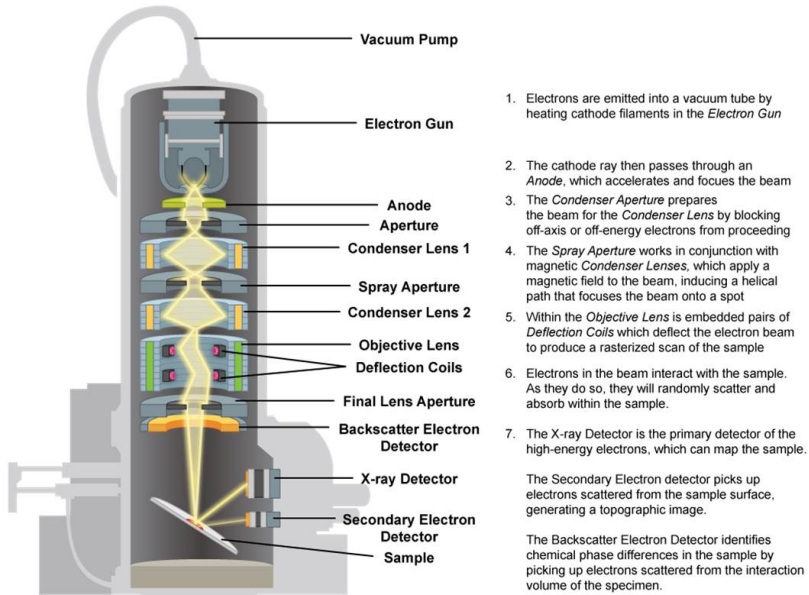
Figure 3.8: A generalized cut-away diagram of the internal structure of a SEM along with the function of each component [157].

come from very shallow region, BSE yield composition and orientation based informations. The X-rays generated as a result of higher energy levels electrons filling the vacancy in lower energy levels can be tapped out using EDX detector to provide elemental information.

In this Work, the fatigue-cracked specimens surfaces, cross-sections and fracture surfaces were investigated with a Zeiss EVO MA 10 SEM equipped with a Bruker EDX detector.

3.3.3 Electron backscattered diffraction (EBSD)

EBSD is a microstructural-crystallographic technique to study any polycrystalline material. It is typically used to characterize materials for present
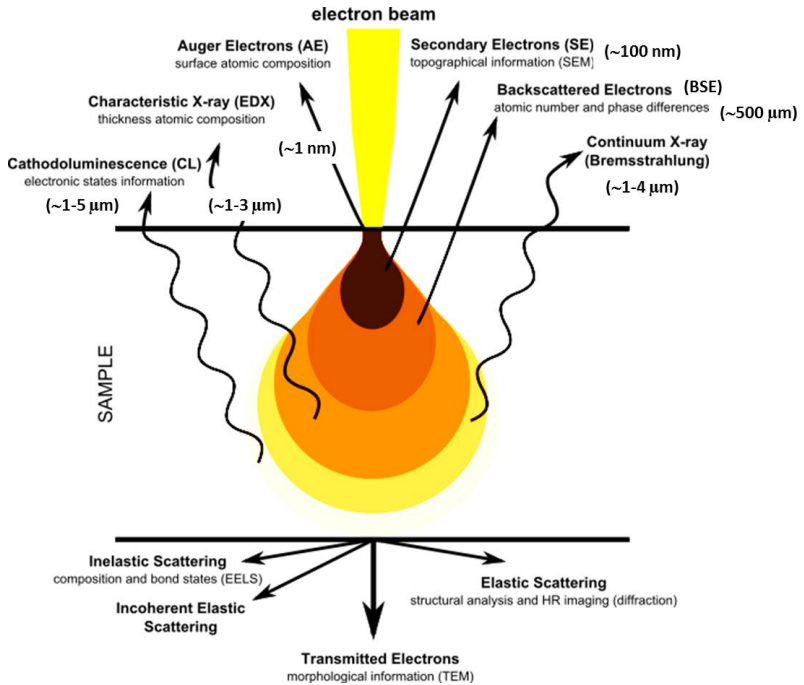
Figure 3.9: Signals emitted from different parts of the interaction volume [158].

phases, texture, grain morphology, defects and deformation. For EBSD, a SEM equipped with a special high-resolution detector is required. This detector contains a phosphor screen at an angle of $\sim 90°$ to the pole piece which is coupled to a compact lens that focuses image from the phosphor screen onto the low light CCD camera. For measurement, a very flat well-polished sample is placed in a SEM chamber at a highly tilted angle ($\sim 70°$ from horizontal) towards phosphorous screen, to increase the contrast in the resultant EBSD pattern (EBSP) (see Fig. 3.10). In this configuration, once a beam of electrons is directed on a point of interest, the atoms in the sample inelastically scatter a fraction of electrons, with a small loss of energy, to form a divergent beam source of electrons close to the surface of the mate-

61

rial. Some of these backscattered electrons, which exit satisfying Bragg's condition, diffract to form a set of large-angle cones that correspond to each of the diffracting planes (Fig. 3.11). The image produced on the phosphor screen contains characteristic Kikuchi bands which are formed where the regions of enhanced electron intensity intersect the screen. Actually, the pattern seen is a gnomonic projection of the diffracted cone, making the band edges appear hyperbolic.
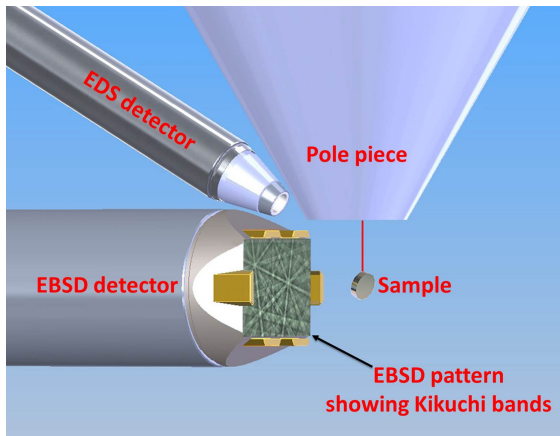
Figure 3.10: An illustration showing the EBSD system integrated with an EDS system [159].

A well described system geometry can be then used to relate Kuckuchi bands in EBSP to underlying crystal phase and its orientation within the electron interaction volume. This done by a means of commercial software where each bands are indexed (position of bands) individually via a mathematical routine using a modified Hough transform (where each pixel in Hough space (with coordinates, ρ and θ) denotes a unique line/band in the EBSP (in the image space, x and y)). This is done by estimating the distance of the lines from the center of the screen (ρ) and the angle that they made with the perpendicular to the center (θ). The Kikuchi bands appear as bright regions or peaks in Hough space, which are easily detected and used
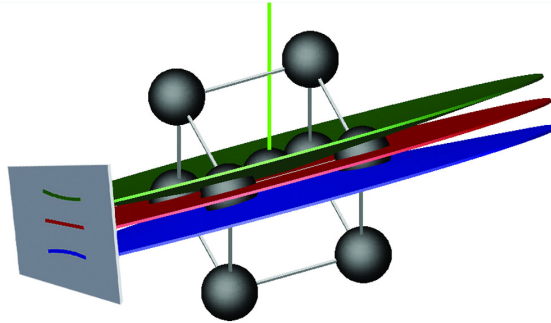
Figure 3.11: The cones (green and blue) generated by electrons from a divergent source which satisfy the Bragg's equation on a single lattice plane. These cones project onto the phosphor screen, and form the Kikuchi bands which are visible in the EBSP [159].

to calculate the original band positions. The angles between bands represent angles between the lattice planes. A computer algorithm is then used to compare these relative position of these points with the expected given type of the crystal structure (see Fig. 3.12). In this way, each point in the selected area on sample can be index with particular orientation and crystal phase.

A grain of any phase can then be defined based on the difference in the crystallographic orientation between two crystallites (misorientation). Actually, the identification of grains requires the definition of a critical misorientation angle, so that all boundary segments with an angle higher than this defined critical angle (usually $15°$) are considered grain boundaries. By measuring the misorientation between all pixel pairs it is possible to identify the boundaries enclosing the individual grains. If this information is used with the phase information then it is possible to determine the grain size distribution for the individual phases within the sample. However, these all quantifications depend on the used pixel or step size. A smaller step size is usually recommended for precision but it can also increase the time required of any fixed scan size. Therefore, compromise has to be made depen-

ding upon the level of information required. Post-processing of the acquired orientation data can be done by using available commercial softwares for getting various informations such grain size, grain boundary characteristics, texture (preferred directional orientation), level of deformation etc.
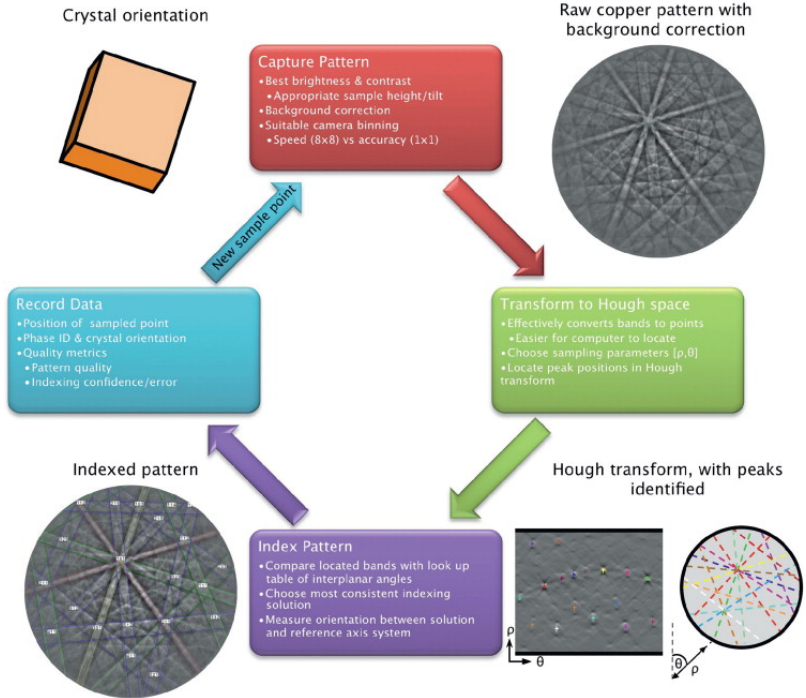
Figure 3.12: Overview of EBSD indexing procedure showing pattern capture through to determination of crystal orientation [160].

The good indicator of strain in crystalline materials are local variations in misorientations. Commercial softwares nowadays provide several tools for characterizing local misorientation. There are essentially two types of local misorientation analyses in the software: 1) Grain based and 2) Kernel based. The Grain based functions are helpful for identifying grains with varying local misorientation or the local orientation variations within a grain.

However, these functions are all quite dependent on the parameters used to define a grain. Kernel based functions are based on a given area - the size of which will be defined by the user.

In this work, EBSD investigations were carried out using a Zeiss Merlin field-emission gun scanning electron microscope (SEM) with GEMINI II electron optics and an acceleration voltage of 20 keV. Kikuchi patterns were recorded with an EDAX Hikari high-speed EBSD camera and evaluated by the OIM Analysis 7.2.1 software. For scans, a step size of 70 nm was used. During post-processing, points with confidence index (CI) lower than 0.1 were discarded. For the maps, a grain was defined as a region surrounded by high-angle boundaries (HABs) with misorientations higher than 15°. All maps are presented in a normal direction with respect to the sample surface.

Kernel average misorientation (KAM) and grain average misorientation (GAM) are used in this work to visualize local misorientation changes. In KAM, the misorientation between the orientation of a certain center point and its neighboring points are calculated and averaged (up to the third nearest neighbors is used), excluding any HABs. Here, the maximum misorientation is restricted to 5°. In GAM, the misorientation between each neighboring pair of points within the grain is calculated. The average misorientation value is then determined and assigned to each point within the grain. While KAM considers only misorientations in a small local neighborhood within a grain which is independent on the grain size and provides a good measure of dislocation density, GAM considers local variations in grain scale deformation and is a typical way of displaying orientation changes inside grains. In both cases, misorientation can be envisaged either in form of a color-coded map or as a graph directly from the commercial software.

3.3.4 Sample preparation

The microstructural characterization were carried out in both undeformed as well as deformed state. In undeformed state, the samples are taken before and after heat treatment parallel to the extrusion direction of the fabricated rod. The samples from the deformed state were prepared by cutting longitudinal platelets using a Well 3242 diamond wire saw from the gauge section of the tested specimens. In all cases, samples for investigations were prepared in a similar manner. For EBSD, the longitudinally sectioned platelets were embedded in conductive Struers Polyfast, grinded (using SiC abrasive papers: P600, P1200, P2500 and P4000), polished (using 9-, 3- and 1-micron water-based diamond suspension) and etched (using a solution consisting of 400 ml Ethanol, 50 ml HCL, 50 ml HNO_3 and 6 g Picric acid).

For TEM samples, one or two discs were punched out from the remaining longitudinal platelets that were grinded to a thickness of $\sim 100~\mu$m. The discs were then thinned to electron transparency electrochemically using a Struers Tenupol-5 twin-jet polisher. As an electrolyte, a mixture of sulfuric acid (20%) and absolute methanol (80%) was used at 23 °C, 14-16 V and a flow rate of 38-40 (full scale 50). Finally, the electro-polished TEM samples were ion-milled at 0.1 KeV (with the gun angle of 8°) for 8-15 min using a Gatan's Argon PIPS II system to obtain clean surface.

4 Results & discussion

4.1 Microstructure in undeformed state

As already stated, the main focus of this work is to investigate the deformation and damage mechanisms of a tempered martensitic ODS steel. Hence, a thorough investigation on its reference/initial/undeformed state is required to comprehend the influence of loading on the microstructure. In addition, to appreciate the influence of heat treatment on mechanical properties, microstructural characterization before heat treatment (i.e. in undeformed ferritic state) is also presented in the following subsections.

4.1.1 EBSD investigations

The typical IPF maps obtained via EBSD for both undeformed states are shown in Fig. 4.1. In both cases, the dissimilar colors of the grains indicate their random orientation, i.e. they possess no preferential crystallographic orientation. Moreover, no texture can be identified in the stereographic projections (not shown here). The average grain sizes (d_g) measured via EBSD for both conditions are listed in Table. 4.1. Clearly, as anticipated, heat treatment (austenitization and quenching) leads to a reduction of grain size. Consequently, according to Hall-Petch relation, improvement in strength is expected. In addition, misorientation analysis reveals that in both states, low- and high-angle boundaries are present, see Table. 4.1. However, it is apparent that before heat treatment the microstructure consists mostly of high-angle boundaries (HABs, >15°). Whereas, after heat treatment, both low- and high-angle boundaries exist almost equally. Therefore, it can be
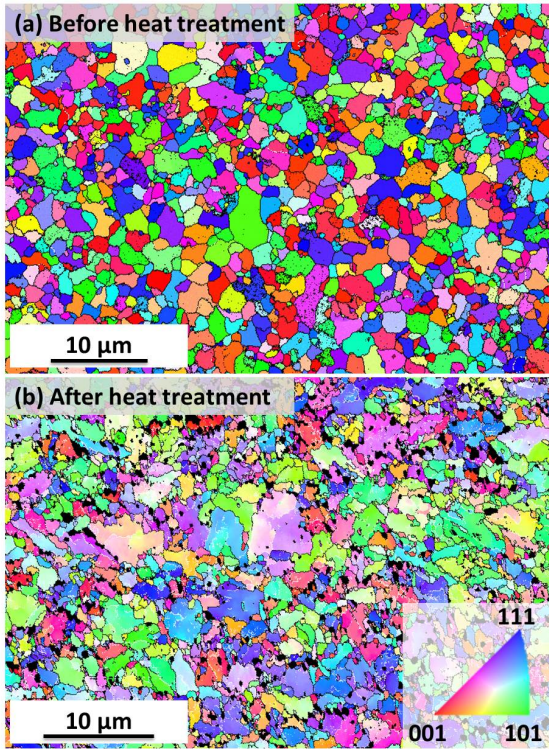
Figure 4.1: IPF maps obtained via EBSD (a) after extrusion (step size: 72 nm) [161] and (b) after heat-treatment (step size: 70 nm). A common color key for the crystallographic orientations is shown in (b); Here, high-angle boundaries (HABs, >15°) are marked with black lines while low-angle boundaries (LABs, 0-15°) are marked by white lines.

concluded that heat treatment also results in an increment of low-angle boundaries (LABs, 0-15°) fraction. Nonetheless, even if misorientation analysis in relative terms indicates a reduction in HABs fraction (see Table. 4.1), in absolute terms HABs fraction increased as there is an obvious reduction in grain size. Hence, from the EBSD studies it can be concluded that heat treatment not only refines the grain size but also leads to a development of

Table 4.1: Average grain size (d_g) as well as LABs and HABs fractions measured before and after heat treatment via EBSD.

Condition	Average grain size d_g (μm)	LABs fraction	HABs fraction
Before	1.28	0.04	0.96
After	0.58	0.46	0.54

sub-grain structures (which have misorientation of $< 15°$, i.e. they manifest LABs, with dominance below $5°$), see Ref. [162] for more.

4.1.2 TEM investigations

To differentiate microstructures at even higher resolution and to obtain details about nano-features, TEM investigations were carried out. Fig. 4.2 presents BF-TEM micrographs obtained from both states. Before heat treatment (Fig. 4.2a), the steel exhibits equiaxed grains with low dislocation density (ρ_d) $(0.46 \pm 0.1) \times 10^{14}$ m^{-2}. The dark contrast Cr-enriched carbides are observed in both trans- as well as inter-granular regions.

(a) Before heat treatment

(b) After heat treatment

1 μm

1 μm
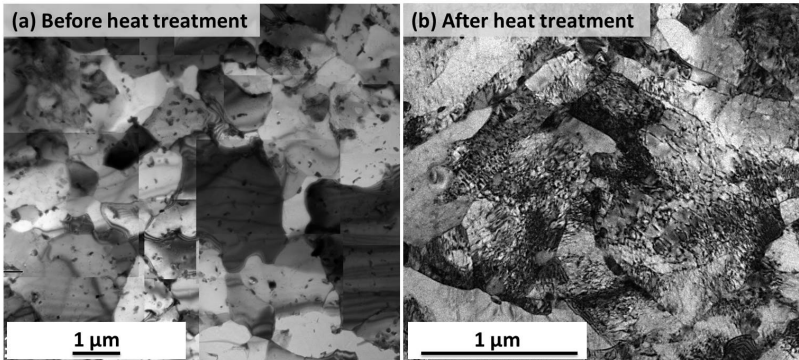
Figure 4.2: BF-TEM micrographs revealing (a) ferritic microstructure after extrusion (the collage was formed using 16 separate micrographs) [161], and (b) tempered martensitic microstructure after heat treatment.

On contrary, after heat treatment (Fig. 4.2b), the steel manifests a tempered martensitic structure with high density $((3.4 \pm 1.0) \times 10^{14}\ \mathrm{m}^{-2})$ of dense and disordered dislocation tangles. As evident from Fig. 4.2b, this high dislocation density makes it hard to appreciate other microstructural features. And therefore, STEM investigations were performed to visualize clear microstructure.
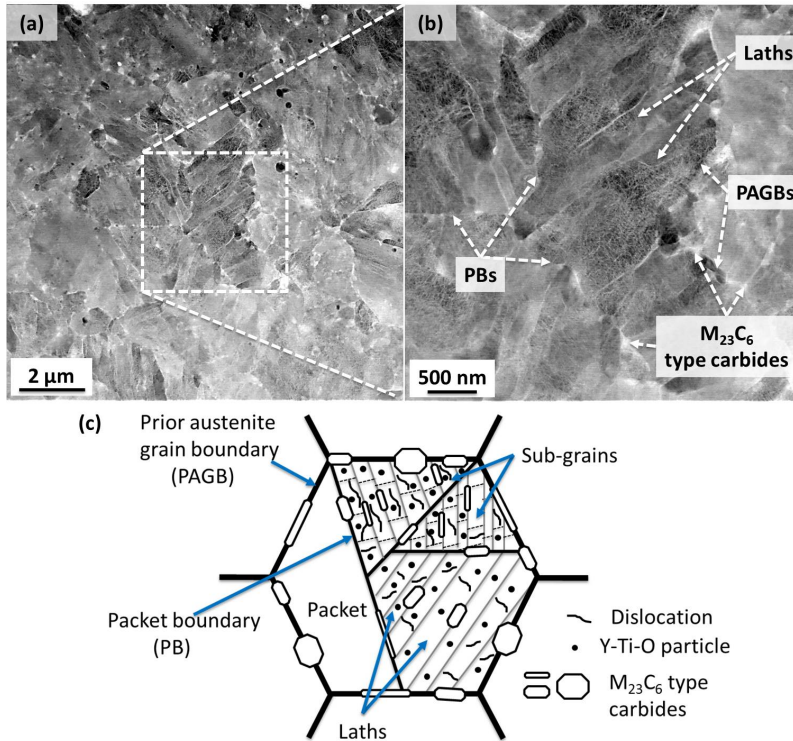
Figure 4.3: HAADF-STEM micrographs (a) and (b) along with its detailed schematic (c) show a typical tempered martensitic microstructure that consists of prior austenitic grains subdivided into packets or blocks of laths and sub-grains having high dislocation density. Bright contrast spots are $M_{23}C_6$ type carbides that decorate different boundaries and Y-Ti-O nanoparticles (not visible here) are also embedded in the matrix (see Fig. 4.5).

Fig. 4.3a and b show HAADF-STEM micrographs for the tempered condition. The additionally shown schematic (Fig. 4.3c) presents a clear picture of the microstructure. It is apparent that the microstructure manifests a high density of hierarchically organized internal interfaces. The prior austenitic grains (PAGs) are subdivided into packets of laths and subgrains having high density of dense and disordered dislocation tangles (Fig. 4.3b). As mentioned earlier in section 4.1.1, these laths and sub-grains manifest LABs (i.e. they have misorientation below 15°). The laths are several μm in length and (0.25 ± 0.01) μm in width.

Additionally, irregular shaped FCC $M_{23}C_6$ carbides precipitate heterogeneously at various interfaces (see bright contrast secondary phase in Fig. 4.4a and Fig. A.3 in appendix A.2). These carbides, 103 ± 53 nm in diameter, are enriched with Fe, Cr and W as shown in the typical

Figure 4.4: HAADF-STEM micrograph (a) shows bright contrast $M_{23}C_6$ carbides and dark contrast Ti-C carbides at various boundaries. (b) and (c) show EDX spectra from marked particles in (a). (Here, Al is an unintended alloying constituent originating from fabrication process).

EDX spectrum in Fig. 4.4b. Occasionally, coarse spherical particles (see

dark contrast secondary phase in Fig. 4.4a), up to 200 nm in diameter, are also observed at different boundaries, and identified to be Ti-enriched carbides (Fig. 4.4c).

However, the majority is of the complex nanoparticles that are inhomogeneously distributed within the matrix of both states. Nevertheless, regions with homogeneous particle distribution were also observed, for example see Fig. 4.5a. EDX analysis (Fig. 4.6) reveals that these particles are the complex Y-Ti-enriched nano-oxidies. The estimated nanoparticles size (d_p) and density (N_p)[1] for both states are listed in Table. 4.2. It is interesting to note that for both states d_p and N_p are almost similar. And therefore, from the TEM investigations, it can be concluded that heat treatment has no influence on the size distribution of nanoparticles. Moreover, complementary observations were also observed through other technique (small-angle neutron scattering), for this see Ref. [161]. HRTEM investigations, performed in order to get an insight into their crystal structure, reveal FCC $Y_2Ti_2O_7$
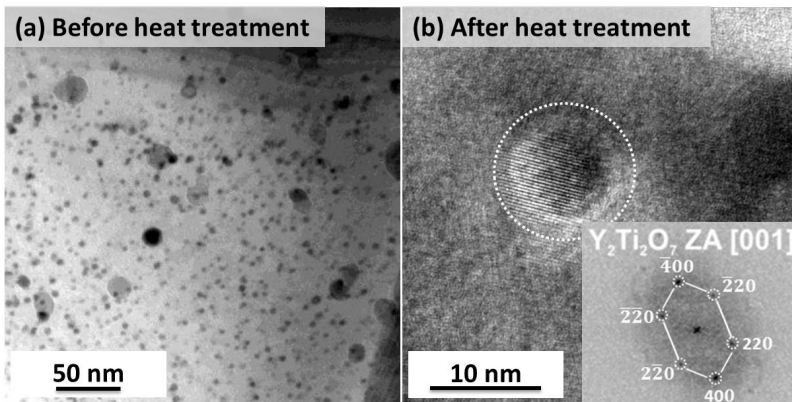
Figure 4.5: (a) BF-TEM micrograph from extruded state reveals region with homogeneous particle distribution. (b) HRTEM micrograph from heat treatment state shows an $Y_2Ti_2O_7$ particle lattice (encircled) with its inverted-contrast FFT diffractogram near to [001] zone axis.

---

[1] Estimated in the regions of their homogeneous distribution

Table 4.2: Dislocation density (ρ_d), average nanoparticle diameter (d_p), and nanoparticles density measured before and after heat treatment via TEM [161].

Condition	Dislocation density ρ_d ($\times 10^{14}$ m^{-2})	Average nanoparticle diameter d_p (nm)	Nanoparticles density N_p ($\times 10^{22}$ m^{-3})
Before	0.46 ± 0.1	4.1 ± 0.9	15 ± 4
After	3.4 ± 1.0	4.7 ± 0.5	10 ± 2

structure for the examined particles. One such particle lattice (encircled) along with its corresponding fast Fourier transformation (FFT) power spectrum diffraction pattern from the heat-treated state is shown in Fig. 4.5b.

4.1.3 Discussion

In general, 9YWT-MATISSE has similar chemical composition as for well known conventional non-ODS 9%Cr steels, such as P91 and EURO-FER97 [9, 19]. However, in respect to P91, the activation elements, Mo and Nb, are replaced by W which is a low-activation solid-solution strengthener. In addition, V and Ta are removed. Whereas, Y_2O_3 and Ni are

Figure 4.6: HAADF-STEM micrograph along with its elemental maps shows complex Y-Ti-enriched nano-oxidies.

added to provide dispersion strengthening and additional phase control, re-

spectively.

Owning to its similar composition and heat treatment, the general microstructure of the tempered 9YWT-MATISSE is also typical for the creep resistant steels like P91 and EUROFER97 [17, 163]. The developed microstructural features can be precisely linked to the applied heat treatments. During quenching, the PAGs are sub-structured by plackets of blocks of martensitic laths. The lath morphology of martensite is due to low carbon content, i.e. 0.1% (as above 0.9% its plate morphology is observed) [129]. This transformation causes a large localized deformation of the matrix, resulting in a high dislocation density. During following tempering process, the high elastic energy stored in the martensite supplies the driving force for the rearrangement of dislocations. This recovery leads to: (1) the overall reduction of free dislocations density due to their annihilation with those of opposite sign, and (2) martensite lath boundaries transform into ferrite sub-grain boundaries (SGBs). However, since the mean width of SGBs after tempering is significantly larger than the mean width of the initial martensite laths, it can be concluded that either not all lath boundaries transform into SGBs or that sub-grains grow during tempering [164]. Finally, carbides precipitate and grow from the supersaturated martensite on or very near to the boundaries.

However, the main difference are in respect to the dispersoids. Conventional non-ODS steels are designed to have MX carbonitrides (M = V, Nb, Cr and X = C, N) which precipitate during annealing/tempering [16, 165]. These carbonitrides are replaced by highly stable and comparatively finer nano-oxides in 9YWT-MATISSE.

The formation of nano-oxides was a long lasting mystery, till very recently number of dedicated studies were conducted to answer this very question. It is now known that oxide forming species are driven into solid solution

during ball milling [69]. The precipitation and coarsening of the nanometre-scale oxides occurs during subsequent consolidation (hot extrusion, hot isostatic pressing, spark plasma sintering) and annealing [69]. Since in the case of 9YWT-MATISSE, heat treatment have no influence on the nanoparticles size distribution, it can be concluded that majority of the particles development already occurred during hot extrusion stage. The structure and composition of the nano-oxide particles have been extensively discussed in literature for various ODS alloys. It has been shown that below certain size nano-oxide particles are usually non-stoichiometric nanoclusters (NC) [166, 167]. Stoichiometry appears with coarsening, as they grow firstly by yttrium diffusion and later also by Ostwald repining mechanism[2] [166–168]. The actual composition/stoichiometry depends upon the yttrium and the added alloying element ratio. The alloying elements, such as Ti, Al, Hf and Zr, are added to refine Y-enriched particles [58, 169–171]. Various complex phases, for example Y-Ti-O [58, 166, 172], Y-Al-O [169], Y-Hf-O [170] and Y-Zr-O [58, 171] are reported in literature. However, out of all above-mentioned elements, Ti is usually preferred due to: (1) it promotes the decomposition of thermally stable Y_2O_3 during milling into Y and O atoms and (2) its strongest refining action [32, 58]. Stoichiometric highly stable $Y_2Ti_2O_7$ (if Y/Ti >1) and $Y_2Ti_2O_5$ usually precipitate with the addition of Ti [58, 166]. The $Y_2Ti_2O_7$ particles in 9Cr-ODS steel are reported to be impenetrable for dislocations, since their modulus of rigidity is much higher than that of the Fe-Cr matrix [115]. And hence, they are expected to act as a barrier for dislocation motion.

4.1.4 Summary

EBSD complemented by TEM investigations reveal:

---

[2] A thermodynamically-driven spontaneous process in which energetic factors will cause large precipitates to grow, drawing material from the smaller precipitates, which shrink.

- Before heat treatment, the 9YWT-MATISSE manifests a ferritic microstructure with equiaxed grains having low dislocation density. HABs are common and are decorated with the Cr-enriched carbides.

- After heat treatment, the 9YWT-MATISSE is characterized by a finer tempered martensitic structure which is typical for the conventional creep resistant steels like P91 and EUROFER97. The main features are the high density of hierarchically organized internal interfaces such as PAGBs, packet or block boundaries, lath boundaries and SGBs with high dislocation density. Here, both LABs and HABs exist almost equally and are decorated by the irregular FCC Fe, Cr and W enriched $M_{23}C_6$ carbides.

- The majority is of the complex Y-Ti-O nanoparticles that are inhomogeneously distributed within the matrix of both states. In tempered state, they are identified to be incoherent $Y_2Ti_2O_7$ FCC phase.

- Heat treatment appears to have no influence on the nanoparticles size distribution which varies in the range of 2 to 25 nm

4.2 Monotonic behavior

In this section, deformation and damage mechanisms of a tempered martensitic (TM) 9YWT-MATISSE under monotonic loading conditions are presented and discussed. For this, the tensile tests were performed in the temperature range of room temperature (RT) to 800 °C at the nominal strain rates of 10^{-3} s^{-1} and 10^{-4} s^{-1}. In order to verify the influence of heat treatment the obtained results are compared with that of the ferritic (F) state (before heat treatment). Thereafter, microstructure evolution and fracture characteristics of the TM state are presented and discussed. Further, discussions are made in respect to the strengthening mechanisms, heat treatments effects and ODS benefits. Finally, comparisons are made with that of the similar non-ODS steels and other experimental ODS steels.

4.2.1 Tensile properties

The engineering stress-strain curves of the F and TM 9YWT-MATISSE at various testing temperatures are shown in Fig. 4.7. The main tensile properties obtained from these curves are summarized in Table. 4.3 and Table. 4.4, respectively. Fig. 4.8 features the comparison of yield strength ($R_{p0.2}$) and ultimate tensile strength (R_m) for both F and TM states at various testing temperatures. In both states, steel displays similar decreasing trends of strength as temperature increases. This trend seems more pronounced above 500 °C. However, the improvement of strength ($\sim$ 26% higher $R_{p0.2}$ for TM state) due to heat treatment is evident at RT. The engineering stress-strain curves at RT (Fig. 4.7) show appreciable strain hardening[3] for both states (F state = 18.0% and TM state = 11.7%). However, strain rate appears to have no influence as similar engineering stress-strain curves are obtained for both 10^{-3} s^{-1} and 10^{-4} s^{-1} strain rate (Fig. 4.9). Interestingly, at RT, the F state

---

[3]

$$\text{Strain hardening (\%)} = \left(\frac{R_m - R_{p0.2}}{R_m} \right) * 100$$

exhibits a yield point phenomenon which indicates the presence of carbon in solid solution at interstitial sites. However, due to carbon's precipitation in form of carbides, this phenomenon is not observed for TM state.
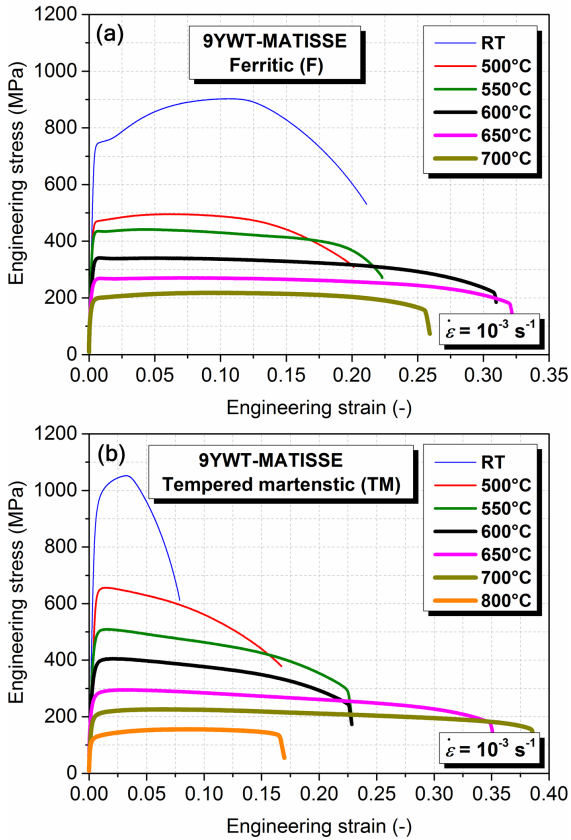
Figure 4.7: Engineering stress-strain curves of the (a) ferritic and (b) tempered martensitic 9YWT-MATISSE at various testing temperatures.

On the contrary, the results obtained at high temperatures are quite different. The prominent improvement in strength for the TM state is gradually lost as both states approach a common low-strength value as temperature increases

Table 4.3: Tensile data for ferritic 9YWT-MATISSE at various temperatures.

$\dot{\varepsilon}$ (s^{-1})	θ (°C)	$\mathbf{R}_{p0.2}$ (MPa)	$\mathbf{R}_m$ (Mpa)	$\mathbf{A}_g$ (%)	$\mathbf{A}$ (%)	$\mathbf{Z}$ (%)
10^{-3}	RT	740	903	10.3	20.9	71.4
	500	468	495	5.3	19.9	66.0
	550	431	442	3.9	22.1	63.4
	600	338	341	5.6	30.6	61.9
	650	261	271	7.5	32	60.5
	700	196	218	8.7	25.6	52.7
10^{-4}	RT	720	885	10.4	24.2	-
	650	184	247	10.8	17.8	-

Table 4.4: Tensile data for tempered martensitic 9YWT-MATISSE at various temperatures.

$\dot{\varepsilon}$ (s^{-1})	θ (°C)	$\mathbf{R}_{p0.2}$ (MPa)	$\mathbf{R}_m$ (Mpa)	$\mathbf{A}_g$ (%)	$\mathbf{A}$ (%)	$\mathbf{Z}$ (%)
10^{-3}	RT	929	1052	2.7	7.6	67.7
	500	633	656	0.9	16.5	60.5
	550	487	509	1.0	22.6	60.3
	600	374	405	1.6	30.7	61.2
	650	264	295	2.6	35.0	58.6
	700	196	226	6.1	38.4	50.0
	800	120	156	8.9	16.7	37.5
10^{-4}	RT	931	1058	3.6	11.5	-
	650	185	256	10.8	19.8	-

(Fig. 4.8). The strain hardening becomes less significant at these temperatures, especially for F state. Nevertheless, the strength and strain hardening is also a function of strain rate. As can be seen in Fig. 4.9, at 650 °C under lower strain rate (10^{-4} s^{-1}), both states exhibit $\sim$ 30% lower yield stress but higher strain hardening (F state = 25.5% and TM state = 27.7%) than that observed under 10^{-3} s^{-1} strain rate (F state = 3.7% and TM state = 10.5%).
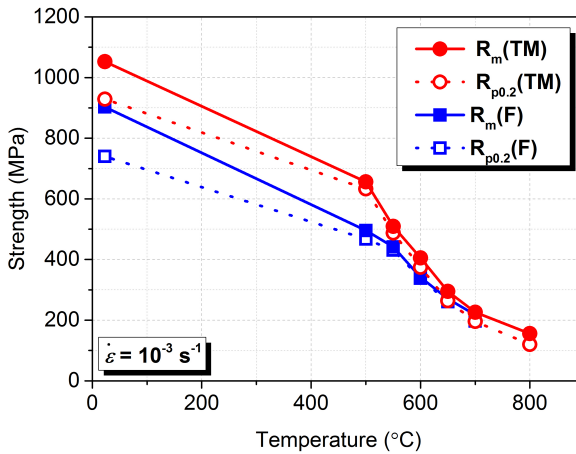
Figure 4.8: Comparison of yield strength ($R_{p0.2}$) and tensile strength (R_m) of 9YWT-MATISSE in ferritic (F) and tempered martensitic (TM) states at various testing temperatures.

The evolution of the uniform elongation (Ag) and total elongation-to-failure (A) for both tested states are shown in Fig. 4.10. Based on the relative strength behavior the elongation results are as expected. Although both states reveal a similar trend, a relatively higher uniform elongation is observed for the F state than for the TM state at all testing temperatures. The total elongation-to-failure for both states increases with increase in testing temperature until a peak is reached. Thereafter, a drop, down to a lower value, is apparent. In comparison to F state, TM state exhibits $\sim$ 63.6% lower total elongation-to-failure at RT. However, with increase in testing tempe-
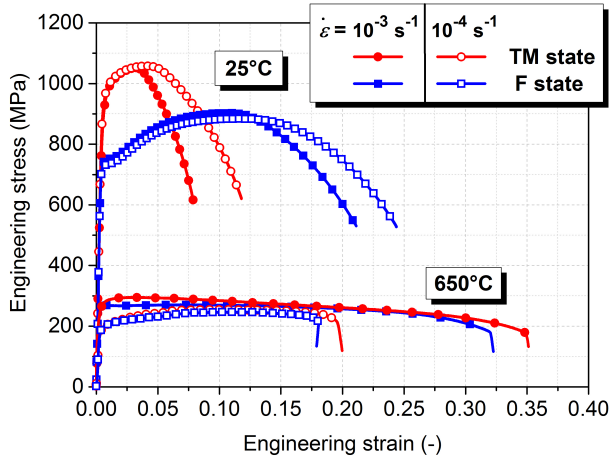
Figure 4.9: Engineering stress-strain curves of 9YWT-MATISSE in both ferritic (F) and tempered martensitic (TM) states.

rature, the total elongation-to-failure becomes comparable and even higher than that of the F state. Hence, at elevated temperatures the two states also present a similar trend of total elongation-to-failure, with the TM state curve coinciding the F state curve. However, the peak ductility for the TM state is shifted towards higher temperature by 50 °C. A difference of the necking appears depending on the testing conditions (as it will be confirmed later in the fracture surface investigations). A strong reduction of cross-section has been noticed, leading to a high necking coefficient (Z^4) for the TM state samples tested up to 600 °C. Thereafter, the gauge section did not vary that much leading to a consistently reduced Z. Furthermore, elongation is also a function of strain rate. As can be seen for Fig. 4.9, under lower strain rate

---

4

$$Z(\%) = \left(\frac{S_{initial} - S_{final}}{S_{initial}} \right) \times 100$$

Where $S_{initial}$ is the initial sample cross-section area and $S_{initial}$ is the fractured cross-section area.

$(10^{-4}\ \mathrm{s}^{-1})$, both states exhibit higher and lower total elongation-to-failure than under $10^{-3}\ \mathrm{s}^{-1}$ strain rate at RT and 650 °C, respectively.
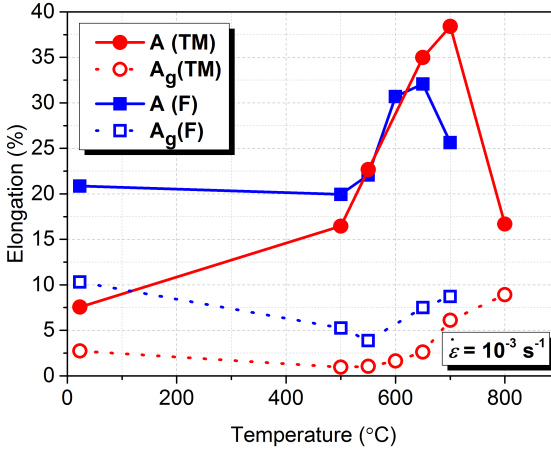
Figure 4.10: Comparison of uniform (A_g) and total elongation (A) of 9YWT-MATISSE in ferritic (F) and tempered martensitic (TM) states at various testing temperatures.

To delineate deformation mechanisms, detailed microstructural investigations were performed only on the TM state tested specimens. The results are presented in the following subsection.

4.2.2 Microstructural evolution

At RT, deformed microstructure shows similar characteristics as those typically observed for an undeformed TM state. In Fig. 4.11a, lath and subgrain structures are clearly visible. However, dislocations are mostly bowed out due to pinning at the Y-Ti-O nanoparticles (Fig. 4.11b). This indicates that oxide particles act as a persistent barrier for dislocations glide which consequently suppresses annihilation processes. Furthermore, as it is evident from Fig. 4.11b, deformation occurs in a homogeneous manner, as disloca-

tions are distributed uniformly across the whole grain.

At elevated temperatures, microstructural evolution becomes prominent. In Fig. 4.11c and d, grains appear equiaxed and are partially clean. This suggests that due to thermal activation, processes such as dislocation density reduction and partial lath/sub-grain structures elimination occurs simultaneously. However, these observations are predominantly observed in the particle deficient regions. Since, in the particles rich regions, individual dislocations, marked in Fig. 4.11c and d, are still pinned to the Y-Ti-O nanoparticles at various locations. In the magnified Fig. 4.11e, pronounced dislocation bowing around Y-Ti-O nanoparticles is apparent. The contrast difference around marked nanoparticles 1 and 2 reveal dislocation pinning at the departure side of the particle 1 and the arrival side of the particle 2. This indicates dislocation pinning at the particle-matrix interface which is an attractive dislocation-particle interaction. Therefore, there still exists a threshold stress to detach dislocation out of this pinning which must be overcome for dislocation to glide; and therefore, plastic deformation to occur. Due to this strong dislocation-particle interaction, annihilation processes at elevated temperatures are also comparatively suppressed, in contrast to if nanoparticles are not there. Moreover, the presence of the sub-grain structures, for e.g. marked low-angle boundary (LAB) in Fig. 4.11d, confirms the significance of nano-oxide particles in stabilizing microstructure at such high temperatures (800 °C). Furthermore, the average grain size, measured via TEM investigations, remains almost unchanged. The temperature dependence of grain size is shown in Fig. 4.12.

Besides, at elevated temperatures, a more intense dislocation activity is realized close to the grain boundaries in the form of a dislocation pile-up (Fig. 4.11d). This is due to fact that at these temperatures dislocation's mobility is relativity easier, in comparison to that at RT, due to activation of the diffusion processes, such as climb, which assists dislocations by-pass
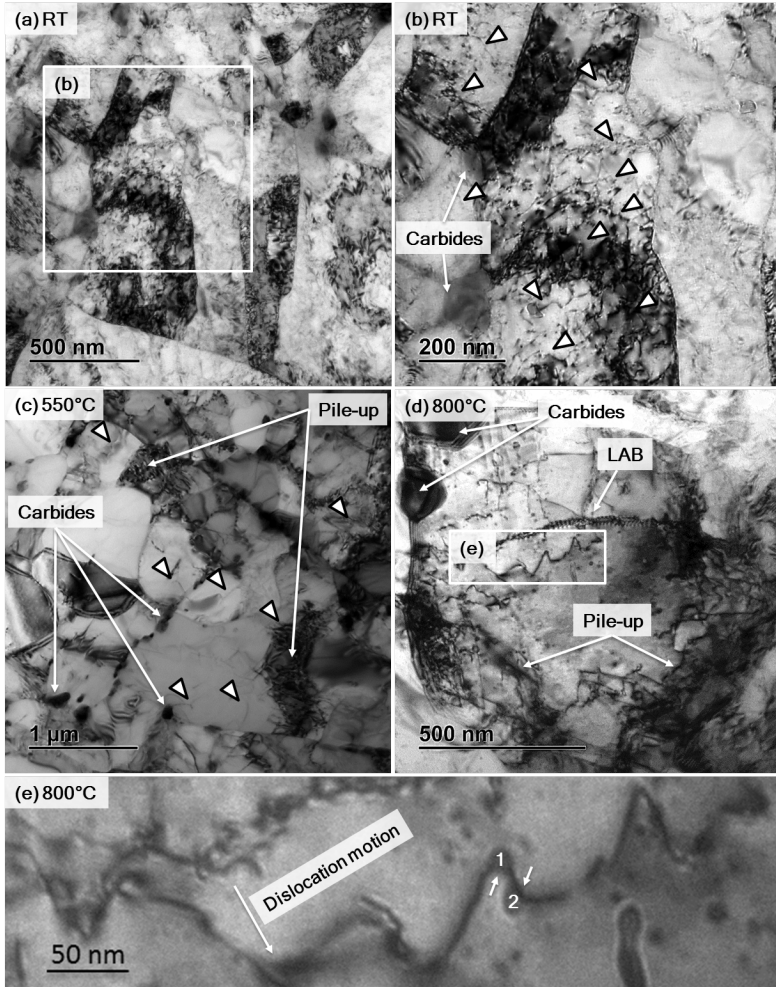
Figure 4.11: BF-TEM micrographs obtained after tensile tests performed on TM state specimens at (a, b) RT, (c) 550 °C and (d, e) 800 °C. Increasing temperature leads to partially clean equiaxed grains, reduced dislocation density, and dislocations pile-up close to grain boundaries. Bowed dislocations around Y-Ti-O nanoparticles are marked in b, c and e. Contrast difference around marked particles in e reveal dislocation pinning at departure side of particle 1 and arrival side of particle 2; hence, attractive particle-dislocation interaction.

over nanoparticles. Therefore, with increase in testing temperature, disloca-
tions stacks and deformation confines close to the grain boundaries which
supposedly strain intergranular regions locally. In addition, $M_{23}C_6$ carbides
appear to have coarsened at elevated temperatures. At 800 °C, the $M_{23}C_6$
precipitates size close to PAGBs is in the range of 100 to 450 nm. However,
Y-Ti-O nanoparticles appeared very stable without any change in shape or
size.
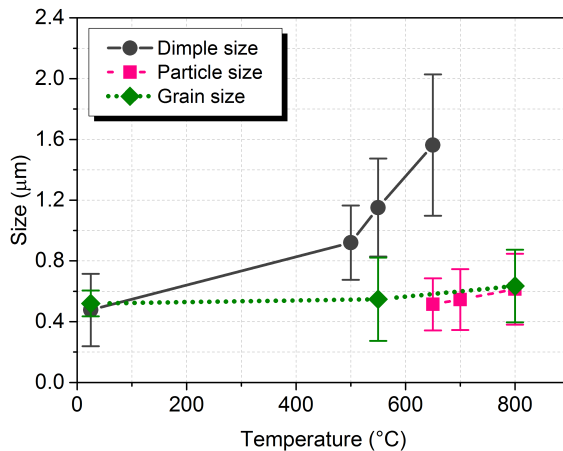
Figure 4.12: Temperature dependence of the TM state grain size estimated after tensile tes-
ting via TEM investigations and dimple and particle size observed on the fracture surface
(section. 4.2.3) via SEM investigations.

4.2.3 Fracture characteristics

The overall view of the fracture surface after RT tensile test is shown in
Fig. 4.13a. This macro view shows presence of distinct radial macrocracks
propagating parallel to the tensile axis (i.e. along the extrusion direction).
These distinct radial macrocracks have also been reported before for diffe-
rent ODS [55, 128, 173], as well as, non-ODS [174, 175] steels (extruded or

laminated in tensile bars taken parallel to the hot-working direction). Based on its morphological features, this typical cracking is commonly referred to as "splitting"or "rosette star-type fracture" [174,175] that generally forms as a result of grain boundary decohesion [55]. Moreover, in Fig. 4.13b, fracture protrusions and steps are evident perpendicular to the final magistral failure. At higher magnification (Fig. 4.14a), the central region mostly exhibits well-defined ductile dimples, having an average size of 0.48 ± 0.24 μm, resulting from the coalescence of microvoids that appear to nucleate from the second phase particles (like oxides and carbides). The dimpled fracture surface suggests intragranular crack growth. Nonetheless, the occurrence of some splitting-related decohesion is also observed (see marked features in Fig. 4.14a).

Similar to RT behavior, the specimens tested at elevated temperatures display significant necking before failure; however, no radial cracks are observed (see Fig. 4.13c). At 500°C, fracture surface forms with a shear-lip zone at outer periphery and unambiguous dimples (0.92 ± 0.24 μm) that are larger and deeper in comparison to those present at RT (c.f. Fig. 4.14a and b). The average dimple size as a function of temperature is shown in Fig. 4.12 which is larger than the corresponding grain size. These observations are associated with the increased ductility witnessed at these temperatures (Fig. 4.10). At 650 °C, the fracture surface reveals two distinct mechanisms of failure. The outer peripheral region (Fig. 4.14c) shows a fracture surface with dimples that are large (1.56 ± 0.47 μm) and prominent (c.f. Fig. 4.14a-c). Conversely, the central region exhibits dimples that are not discernable and have many sub-microcrystalline particles (0.52 ± 0.17 μm) present at their walls (see inset in Fig. 4.14c). At 800 °C, specimen fractured with a minor localized necking (Fig. 4.13d). The entire fracture surface manifests similar small particles (0.62 ± 0.23 μm), as observed in the central region of the 650 °C tested specimen (Fig. 4.14d). The temperature dependence of particle sizes is shown in Fig. 4.12. Interestingly,
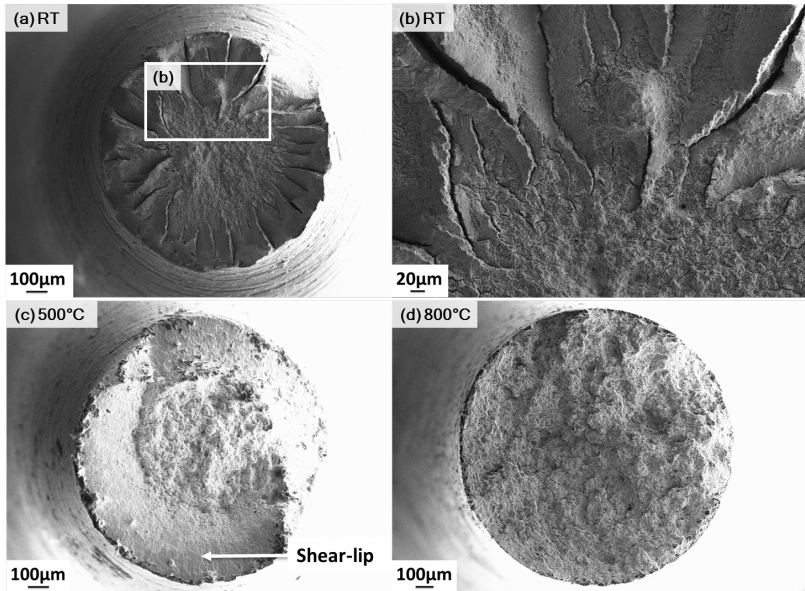
Figure 4.13: SEM micrographs revealing fracture surface of the TM state specimens tested: At RT, macro view (a) shows distinct radial macrocracks propagating parallel to tensile axis, and magnified image (b) shows radial cracks along with fracture protrusion and steps perpendicular to the fracture surface. At 500 °C, macro view (c) shows shear-lip zone at outer periphery with no radial cracks. At 800 °C, macro view (d) shows fracture surface without shear-lip zone and minor localized necking.

the particle size matches the average grain sizes at 800 °C. This suggests that these particles are the sub-microcrystalline grains, which could have separated from each other by boundary decohesion. Therefore, a change in fracture mechanism from an intragranular fracture at the lower temperature to intergranular fracture at higher temperatures. Similar fracture features have also been reported before for ferritic ODS steels [66, 128]; the formation of which was also attributed to "intergranular decohesion". This results in a limited amount of plasticity, which is associated with a reduced ductility and necking at this temperature (Fig. 4.10).
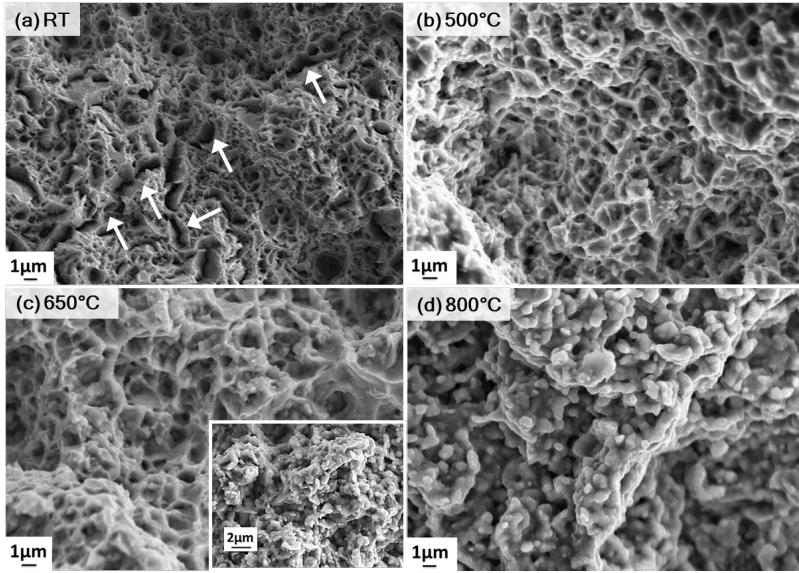
Figure 4.14: High-magnification SEM micrographs revealing fracture surface of the TM state specimens tested at (a) RT, (b) 500 °C, (c) 650 °C, and (d) 800 °C. Increased dimple size with temperature and complete change of fracture mechanism at 800 °C is apparent.

The modification of damage mechanism at elevated temperatures for F/M ODS steel appears to be an outcome of the change in deformation mechanism. As mentioned in previous section 4.2.2, the uniformly distributed dislocations at RT are stacked close to grain boundaries in the form of dislocation pile-up at elevated temperatures. The change in deformation mechanism was also reported before from in situ investigations where activation of dislocation sources close to grain boundaries were observed above 500 °C [65, 176]. This indicates that at higher temperatures deformation localizes close to the grain boundaries, which could lead to cavitation and porosities in these areas, and hence a modification of the damage mechanism too. To confirm, 800 °C tested TM 9YWT-MATISSE specimen was sectioned along the loading/extrusion direction, which indeed reveals development of

microvoids and their coalescence to form cavities (Fig. 4.15). Moreover, it has been reported in literature that the block boundaries in martensite structure sometimes give appropriate sites for fracture, and thus lead to premature rupture [177, 178].
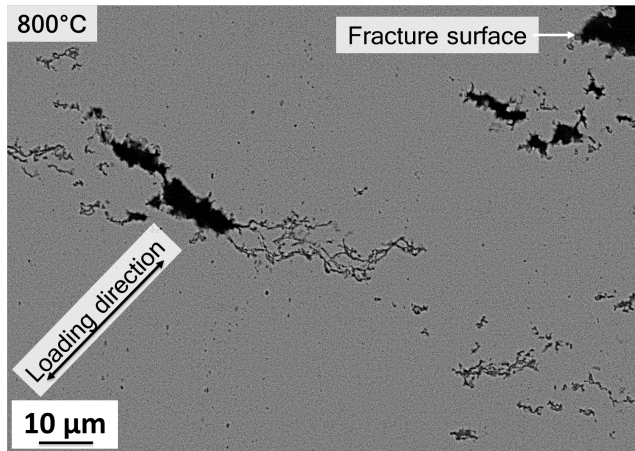
Figure 4.15: Backscattered SEM micrograph of a longitudinal sectioned TM state specimen tested at 800 °C. The microvoids and its coalescence to form cavities are apparent.

4.2.4 Discussion

In the following, firstly an attempt has been made to clarify the strengthening mechanisms in 9YWT-MATISSE by taking all relevant strengthening contributors into consideration. Consequently, a reasonable model is developed to calculate RT yield stress in comparison with the experimental result. Furthermore, a number of suitable Fe-Cr model alloys, for which datasets are reported in the literature [34,49,179–184], are used to additionally underpin the conclusions. Thereafter, the strength of the 9YWT-MATISSE is linked to the deformed microstructures at elevated temperatures. Afterwards, the tensile properties of 9YWT-MATISSE are compared with the

reported data of other commercial non-ODS as well as experimental ODS steels.

Strengthening mechanisms

It is well understood that the resistance of obstacles to dislocation glide determines the flow stress of alloys. The complex microstructure of ODS steels offers excellent strength due to the favorable superposition of several important strengthening mechanisms such as friction stress (σ_0), solid solution strengthening (σ_s), grain size or Hall-Petch strengthening (σ_g), dislocation strengthening (σ_d) and oxide dispersion strengthening (σ_p). It is first assumed here that the yield stress (σ_y) of the materials at RT can be given by a simple sum of strengthening contributions which is as follows:

$$\sigma_y = \sigma_0 + \sigma_s + \sigma_g + \sigma_d + \sigma_p \qquad (4.1)$$

Although pure linear summation according to Eq. 4.1 is an oversimplification, Eq. 4.1 may well serve as a road map to introduce the individual contributions separately. Moreover, it is interesting to see later, to what extent more realistic models modify the prediction. The datasets for Fe-Cr model alloys, EUROFER97 (EU97) and ODS EUROFER (ODS-EU) reported in literature and average material parameters selected for ODS 9Cr (9YWT-MATISSE) steel in both F and TM state is summarized in Table. 4.5.

The lattice friction or Peierls-Nabarro stress (σ_0) is required to move a dislocation through the perfect lattice. As in here, all alloys have an iron lattice, the friction stress of single crystal pure iron is 53.9 MPa [185].

Solid solution strengthening (σ_s) includes both the interstitial strengthening from the carbon in solid solution and the substitution strengthening from all substitutional elements. However, with respect to the present alloys, interstitial strengthening will have a negligible contribution since most of the

Table 4.5: Datasets for Fe-Cr model alloys, EUROFER97 (EU97) and ODS EUROFER (ODS-EU) reported in literature and average material parameters selected for ODS 9Cr (9YWT-MATISSE) steel in both F and TM state [161].

Alloy	Grain size d_g (μm)	Dislocation density ρ_d ($\times 10^{14}$ m^{-2})	Particle mean diameter d_p (nm)	Particles number density N_p ($\times 10^{22}$ m^{-3})	Yield stress† $\sigma_{y,exp}$ (MPa)
Fe2.5Cr [179]	37	0.12	-	-	144
Fe5Cr [179]	10	0.58	-	-	206
Fe9Cr [179]	3	0.63	-	-	289
Fe12Cr [179]	3	0.55	-	-	349
EU97 [180–182]	2	2.2	-	-	550
ODS-EU [34, 49, 183, 184]	0.5	7	3.8	11.5	1050
ODS 9Cr F	1	0.5	4	10	720
ODS 9Cr TM	0.5	3	4	10	931

†All tests carried out with a nominal strain of 10^{-4} s^{-1}

carbon is already precipitated out in form of carbides. The strengthening effects of substitutional alloying elements in BCC iron matrix was experimentally obtained by Lacy and Gensamer [186], who reported a simple expression as:

$$\sigma_s = 0.00689 k X^n \tag{4.2}$$

where X is the equilibrium concentration of substitutional elements in atomic percent, $n = 0.75$ for all elements, and k is the strengthening coefficient measured by Lacy and Gensamer [186]. High values of k imply a large substitutional element effect. The main substitutional strengthening effects

Table 4.6: Strengthening from substitutional alloying elements dissolved in the matrix.

Elements	k	σ_s (MPa)
Cr	1400	53.2
W	11000	33.2
Si	11000	51.7
Mn	7000	19.6
Ni	6100	12.1
Total		169.7

were calculated using Eq. 4.2 for each element and are listed in Table. 4.6. The total substitutional strengthening effects are introduced in Table. 4.7 for each of the considered alloy.

In polycrystalline material, grain size plays an important role on mechanical properties. Grain size or Hall-Petch strengthening (σ_g) expresses the influence of grain boundaries on dislocation behavior. Indeed, dislocations are gradually stacked at grain boundaries and form pile-ups until they reach the threshold to pass to the next grain. As suggested in [65], this strengthening contribution can be estimated as:

$$\sigma_g = \alpha_g G \sqrt{\frac{b}{d_g}} \qquad (4.3)$$

Here $\alpha_g = 0.2$ [65], G is the shear modulus (= 85 GPa at RT [187], measured value for ODS high-Cr steels), b is the Burgers vector (= 0.248 nm, assuming all dislocations have a Burgers vector of the type $1/2 \langle 111 \rangle$) and d_g is the mean grain size. The estimated values of Hall-Petch strengthening for the studied ODS steels and alloys are listed in Table. 4.7.

Dislocation forest strengthening (σ_d) is due to the interaction between dislocations when a mobile dislocation interacts with another one which goes across its gliding plane. The contribution from dislocations strengthening can be estimated by Bailey-Hirsch relationship [188], which is widely accepted as:

$$\sigma_d = \alpha_d M G b \sqrt{\rho_d} \qquad (4.4)$$

where α_d is an obstacle strength for dislocations by dislocations (= 1/3 according to [65]), M is the Taylor factor that was recommended as 3.06 for most polycrystalline BCC metals [189] and ρ_d is the dislocation density. The estimated values of dislocation strengthening for the studied ODS steels and other considered alloys are listed in Table. 4.7.

Particle strengthening (σ_p) is due to the dispersed nano-oxide particles which, as seen in the microstructural investigations, act as impenetrable obstacles for dislocations glide. Several authors suggested detailed equations for calculating this contribution, which were partly based on knowledge or assumptions about the dislocation-particle interaction mechanism [190–192]. For the present purpose, this degree of detailedness seems to be inappropriate, since different interaction mechanisms may be assumed to operate simultaneously depending upon various factors such as particle type, their degree of coherency etc. It is therefore reasonable to use the simplest scaling equation with an empirical constant. One such equation based on the dispersed barrier hardening concept, after the original formulation of Seeger [193], is used often [102] and is as follows [194]:

$$\sigma_p = \alpha_p M G b \sqrt{N_p d_p} \qquad (4.5)$$

where α_p is the obstacle strength for oxide nanoparticles (= 1/3 which may vary between 0.1 and 0.5 depending on particle type and degree of coherency, mean value), N_p is the number density of nano-oxide particles and d_p

is the mean particle diameter. The estimated particle strengthening for the studied ODS steels are briefed in Table. 4.7.

From Table. 4.7, it is evident that the increasing order of strengthening components for ODS 9Cr F is $\sigma_0 <\sigma_d <\sigma_s <\sigma_g <\sigma_p$ and for ODS 9Cr TM is $\sigma_0 <\sigma_s <\sigma_d <\sigma_g <\sigma_p$. Therefore, for the studied ODS steel particle strengthening provides a major contribution to the measured RT yield stress, which is more than 45% in both cases. In addition, dislocation forest and grain size strengthening are also dominant contributors to the yield stress. This dominating share of particle contribution to the yield stress is in contradiction with some previous studies [65, 101–104], where based on distinct microstructural characteristics (fine grained, high dislocation density as well as larger size, lower density and coherency of the particles), dislocation forest and/or grain size strengthening contributions are either comparable or higher than the particle strengthening. Clearly, for ODS 9Cr TM steel, Hall-Petch strengthening is greater than dislocation forest strengthening. On the contrary, dislocation forest strengthening is higher than the Hall-Petch strengthening for similar ODS-EU steel. This is due to the fact that even if both steels manifest similar average grain size; the dislocation density is slightly higher in ODS-EU steel than in heat-treated ODS 9Cr TM steel (Table. 4.6).

The yield stress values of the studied alloys tentatively estimated according to Eq. 4.1 are listed in Table. 4.7 along with corresponding data for the additional alloys reported in literature. Obviously, the linear summation of all contribution leads to a considerable overestimation of the yield stress, which is 32-34% higher than the measured yield stress for the ODS steels of this study. An overestimation of the yield stress is also observed for the binary Fe-Cr alloys, EU97 and ODS-EU, which were additionally introduced into the analysis. In general, the observed overestimation may be due to either the type of superposition or the overestimation of (one or more) individual

Table 4.7: Various strengthening contributions along with the calculated and experimental yield stresses (all in MPa). The materials investigated in this study are placed in the lower part of the table; the results obtained for the additional alloys from the literature are listed in the upper part.

Alloy	σ_s*	σ_g	σ_d	σ_p	$\sigma_{y,th}$ Eq. 4.1	$\sigma_{y,th}$ Eq. 4.6	$\sigma_{y,th}$ Eq. 4.7	$\sigma_{y,exp}$†
Fe2.5Cr	19.6	44.0	73.0	0	191	191	117	144
Fe5Cr	31.9	84.7	160.5	0	331	331	245	206
Fe9Cr	49.8	154.6	167.3	0	426	426	322	289
Fe12Cr	63.5	154.6	156.3	0	428	428	311	349
EU97	126.6	189.3	312.7	0	683	683	502	550
ODS-EU	126.8	378.6	557.7	440.7	1558	1270	1089	1050
ODS 9Cr F	169.7	267.7	149.1	421.6	1064	940	715	720
ODS 9Cr TM	169.7	378.6	365.1	421.6	1391	1162	936	931

*σ_0 = 53.9 MPa for Eq. 4.1 and Eq. 4.6 for all alloys (not included in the table)
†All tests carried out with a nominal strain of 10^{-4} s^{-1}

strengthening contributions. Both options are considered below.

Pythagorean superposition of the contributions from dislocations and particles was suggested by several authors, [192, 195–197] to be more appropriate. Kamikawa et al. [197] also reported an overestimation of the yield stress for low-Cu steels with nano-precipitates in the case of assumed linear superposition and substantiate Pythagorean superposition by the small spacing of dislocations and precipitates, both of which act as short range obstacles. This is because the mean spacings of dislocations and nanoparticles are comparable while grain size is an order of magnitude larger, and the motion of dislocations would be impeded by both dislocations and oxide particles. Therefore, the strengthening contributions from dislocations and particles ought to be mixed together which cannot simply be additive.

Queyreau et al. [192] used dislocation dynamics simulations to show that Pythagorean superposition is appropriate for the combination of both contributions in the underlying model. These arguments led to the replacement of Eq. 4.1 by Eq. 4.6. Furthermore, concerning ODS steels, such superposition has been used several times [103, 198, 199]. The yield stress values calculated according to Eq. 4.6 are included in Table. 4.7.

$$\sigma_y = \sigma_0 + \sigma_s + \sigma_g + \sqrt{\sigma_d^2 + \sigma_p^2} \tag{4.6}$$

It has been foreseeable that Pythagorean instead of linear superposition will reduce (or remove) the overestimation. However, comparison of the calculated and measured yield stress shows that there is still significant though smaller overestimation of the yield stress for all alloys, see Fig. 4.16a. In order to identify the most probable sources of overestimation, it is helpful to analyze the trend of the residuals shown in Fig. 4.16b.

Fig. 4.16b clearly shows that the residuals are composed of an offset, which is independent of the yield stress of the alloys, and a part (trend) that increases with increasing yield stress. The offset led to the removal of the friction stress from Eq. 4.6. Indeed, the friction stress is the only contribution to the total yield stress that is conceptually equal for all alloys. Moreover, the observed offset of 53.8 MPa agrees with the considered friction stress of 53.9 MPa. The following arguments substantiate the elimination of the friction stress:

1. The friction stress depends on the type of dislocation, slip system and temperature. In situations (not too low temperatures, screw dislocations), where the Peierls barrier is overcome by a kink-pair mechanism, the friction stress is close to zero [200, 201].
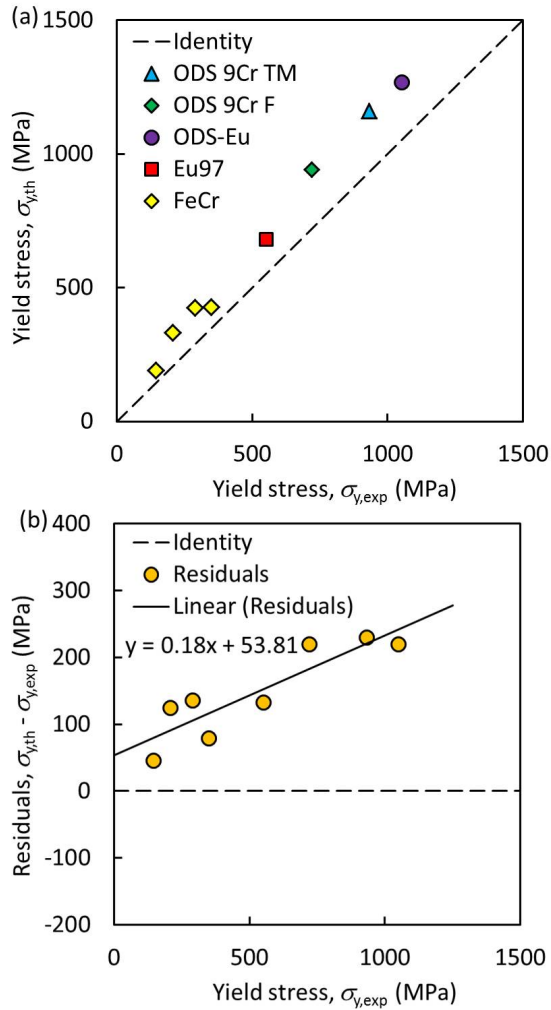
Figure 4.16: (a) Yield stress calculated according to Eq. 4.6 versus experimental yield stress and (b) residuals versus experimental yield stress for the studied alloys.

2. Dislocation unpinning from an obstacle (e.g. oxide nanoparticle) is an instability not reflected well by the balance of forces. The height of the Peierls barrier may be irrelevant for the critical unpinning stress.

3. In literature, smaller values of friction stress, e.g. 30 MPa [202], have also been reported.

In addition to the friction stress, solid solution strengthening can lead to overestimation exhibiting a trend. Lower solid solution strengthening than predicted by Eq. 4.2 (or even its absence) may be justified as follows:

1. Not all Cr and W will contribute to solid solution strengthening, since Cr- and W-containing grain boundary carbides and/or oxide nanoparticles are often observed. These may not alter particle strengthening significantly but reduce Cr and W in solution with respect to the analysis.

2. The contribution of Cr to solid solution strengthening is sometimes reported to be smaller than predicted by the expression used here or even negative [203], the latter corresponding to solid solution softening.

3. Other cases of solid solution softening (e.g. by Si) under certain conditions are reported by Caillard [204].

4. Similar as for the friction stress, solid solution strengthening may also be irrelevant for the critical unpinning stress.

Hence, in order to empirically improve the estimation of the yield stress, only dominant contributors (σ_g, σ_d and σ_p) are considered. The contribution from friction stress and solid solution strengthening are ruled out to reduce both the offset and the trend of the residuals observed in Fig. 4.16b. It is interesting to note that other authors also omitted friction stress and solid solution strengthening contributions for high-strength materials and still found

good agreement with experimental values, for example, see Ref. [65, 66]. This conceptualizes into an equation of the following type:

$$\sigma_y = \sigma_g + \sqrt{\sigma_d^2 + \sigma_p^2} \qquad (4.7)$$

The yield stress values calculated according to Eq. 4.7 are listed in Table. 4.7. The comparison of the calculated and measured yield stress shows that Eq. 4.7 is favorable and describes the whole set of ODS and non-ODS Fe-Cr steels and alloys reasonably well, see Fig. 4.17a. Moreover, an insignificant offset and trend of residuals are apparent in Fig. 4.17b. Furthermore, suitability of the choice of model parameters and determination of microstructure parameters are broadly confirmed.

Finally, the good fit of Eq. 4.7 with the measured yield stress must not be misinterpreted as to represent a strict proof of its absolute validity. For example, a small modification of the model parameters with the value of $\alpha_g = 0.157$ [197] instead of the selected value $\alpha_g = 0.2$ [65] in Eq. 4.3 and 33% of the full calculated solid solution strengthening instead of 0% in Eq. 4.7 will give rise to a similar quality of the fit. Another example is related to the possible inclusion of Hall-Petch strengthening in the Pythagorean-superposition part of Eq. 4.6, which contradicts the reasoning of Kamikawa et al. [197] but complies with Ferguson et al. [205]. This kind of superposition model yields a slightly worse fit and a larger magnitude of the trend (-0.09 versus 0.02) than Eq. 4.7, but again cannot be strictly ruled out.

Influence of temperature and comparison with commercial and experimental non-ODS and ODS steels

As seen above, the RT yield strength of TM 9YWT-MATISSE can be mainly attributed to three dominated contributers i.e. grain size strengthening, dislocation forest strengthening and oxide particle strengthening. However,
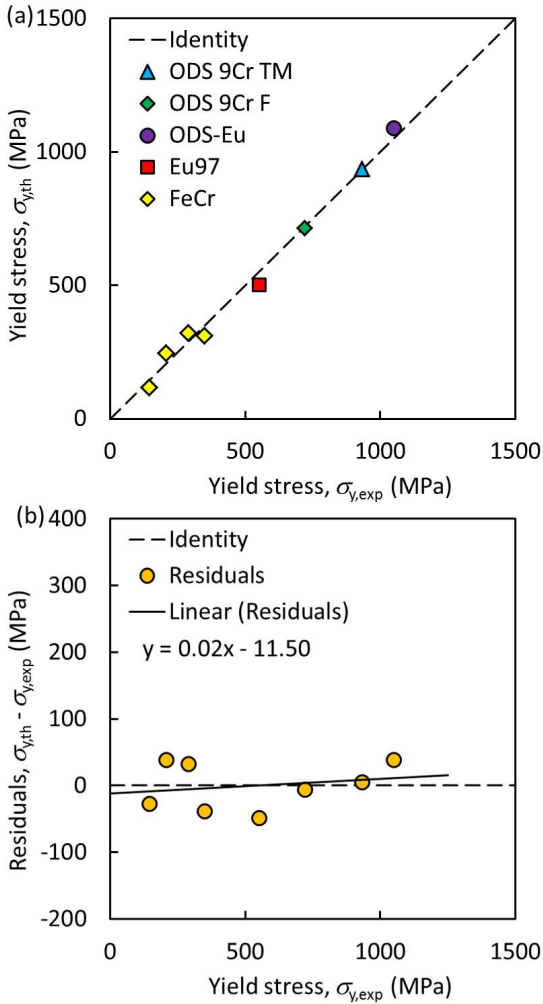
Figure 4.17: (a) Yield stress calculated according to Eq. 4.7 versus experimental yield stress and (b) residuals versus experimental yield stress for the studied alloys.

as investigated by Kim et al. [102] in detail, the roles of individual strengthening contributions alter significantly with temperature. For example,

even though at all temperatures, dislocations appear pinned to the highly stable Y-Ti-O nanoparticles, the associated strengthening contribution will modify due to the temperature dependent nature of the particle-dislocation interactions. In general, it has been shown that at moderate temperatures ODS alloys high strength originates from particle-dislocation interaction that is exclusively controlled by Orowan/repulsive mechanism [110, 117]. Whereas, at elevated temperatures, Orowan/repulsive mechanism does not support such observations, as thermally activated diffusion processes assist dislocations climb leading to the particles by-pass. Nevertheless, this can be explained by an attractive interaction called interfacial pinning [206–208], where a dislocation after overcoming the particle by climb is being pinned on the departure side of the nano-oxide particles (as shown in Fig. 4.11e). Nonetheless, this attractive interaction (interfacial mechanism) at elevated temperatures seems to be less effective in pinning dislocations than the repulsive one at moderate temperatures. This can be concluded from the fact that at elevated temperatures pronounced microstructure evolution befalls, this mainly includes reduced dislocation density and lath/sub-grain structures elimination, which results in a loss of strength. However, it is important to note that there still exists a threshold stress to detach dislocation out of the attractive pinning, which must be overcome for the dislocation to glide and plastic deformation to occur. This ultimately suppresses annihilation processes and hence, reduces microstructural degradation leading to a higher strength in comparison to the conventional non-ODS 9%Cr steels (see Fig. 4.18).

Upon comparing heat-treated TM state with the F state, the nano-phase strengthening is equivalent in both cases (Table. 4.7). Nevertheless, due to its relatively fine grained microstructure and high dislocation density, TM state manifests higher contributions from both dislocation forest as well as the Hall-Petch effect. And therefore, the prominent improvement of strength for TM state at RT becomes obvious. However, at elevated temperatures (>
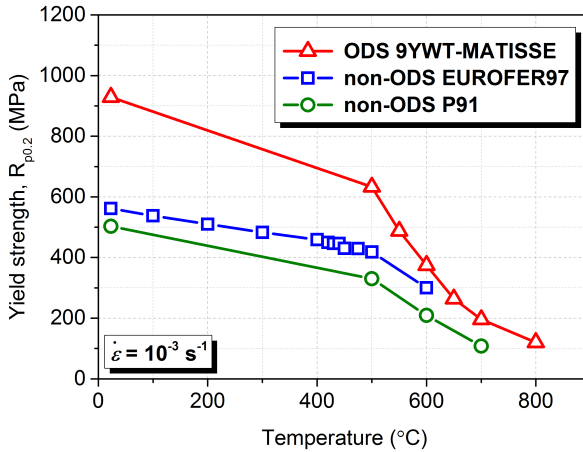
Figure 4.18: Comparison of the TM 9YWT-MATISSE with conventional non-ODS F/M EU-ROFER97 [29] and P91 [209].

600 °C), the two states display similar trends of strength (Fig. 4.8). Similar findings have also been reported before in Refs. [210, 211]. From here, it can be proposed that at elevated temperatures, the specific microstructure of F/M steel induces a low contribution of dislocations and Hall-Petch effect in strengthening mechanisms. Hence, the advantage of TM state over F state is neutralized at elevated temperatures.

The temperature dependence of yield strength of TM 9YWT-MATISSE along with other experimental ODS steels [35,209,212] is shown in Fig. 4.19a. The yield strength progression of 9YWT-MATISSE is in close agreement with the steels like PM2000, 12Y1 and ODS P91. 12YWT type steels have highest yield strength at all temperatures. These steels contains similar Y-, Ti-, and O-rich nanoparticles, having a particle size of about 3-5 nm [35], as in 9YWT-MATISSE (Table. 4.2). And therefore, the strength differences can only be accounted in terms of their different nature and amount of

dislocations and grain boundaries. This suggests that specific characteristics of dislocation structure and boundaries obtained by phase transformation in F/M 9YWT-MATISSE steel is less efficient than those achieved by mechanical deformation (hot rolling or forging) in ferritic 12YWT steels. Furthermore, EUROFER's ODS variant, that was hot rolled prior to the phase transformation and tempering treatment, higher strength further confirms this argument. Recently, Ukai et al. [178] developed F/M 9%Cr ODS steels by hot-rolling in austenitic-phase with subsequent air-cooling. This resulted in a formation of transformed ferrite grains leading to a superior high-temperature tensile and creep strength. However, this is attained at an expense of ductility, which is not the case for 9YWT-MATISSE. The benefit of 9YWT-MATISSE in terms of higher ductility is visible from Fig. 4.19b. And hence, TM 9YWT-MATISSE exhibits an excellent compromise between strength and ductility.

4.2.5 Summary and conclusions

1. The tensile tests on TM 9YWT-MATISSE were performed in the temperature range of room temperature (RT) to 800 °C at two nominal strain rates of 10^{-3} s^{-1} and 10^{-4} s^{-1}. In order to compare the influence of heat treatment the tensile tests were also performed on specimens taken from ferritic (F) as-extruded bar. In both states, steel displays similar decreasing trends of strength as temperature increases. However, the improvement of strength due to heat treatment is evident at RT. Nevertheless, strain rate at RT has no influence on strength and strain hardening. Interestingly, at elevated temperatures both states present similar values of strength and elongation. The total elongation-to-failure for both states increases with increase in testing temperature until a peak is reached. Thereafter, total elongation-to-failure drops down to a lower value. Moreover, elongation is a function of strain rate. Under lower strain rate, both states exhibit
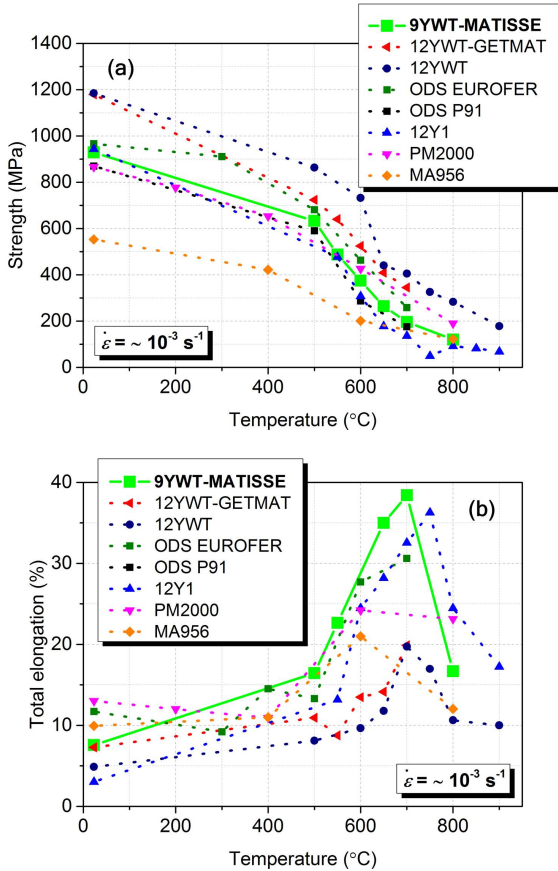
Figure 4.19: Temperature dependence of the yield strength (a) and total elongation (b) of 9YWT-MATISSE and other commercial and experimental ODS steels from literature [35, 209, 212].

higher and lower total elongation-to-failure than under higher strain rate at RT and 650 °C, respectively.

2. Transmission electron microscopy on specimens taken from fractured TM state samples revealed a modification of deformation mechanism

with temperature. The dislocations that were uniformly distributed at RT were localized close to grain boundaries at elevated temperatures. A strong particle-dislocation interaction was observed at all testing temperatures. Orowan/repulsive mechanism is supposed to govern particle-dislocation interaction at moderate temperatures [117]. At elevated temperatures, an attractive particle-dislocation interaction phenomenon called interfacial pinning was identified. This ultimately suppressed annihilation processes and reduced microstructural degradation in comparison to that observed in similar non-ODS steels. Although reduced, the still perceived microstructural evolution that includes reduced dislocation density and partial lath/sub-grain structures elimination, mainly in the particle deficient regions, and $M_{23}C_6$ carbide coarsening, resulted in a loss of strength at elevated temperatures.

3. Fracture surface investigation at RT revealed intragranular fracture with well-defined ductile dimples and distinct radial macrocracks propagating parallel to the tensile axis. As the temperature increased, fracture surface forms with a shear-lip zone at outer periphery and dimples that were larger and deeper in comparison to those formed at lower temperatures. These observations are associated with the increased ductility. A change in fracture mechanism from intragranular to intergranular fracture was observed at 650 °C. This change became fully apparent at 800 °C where it is associated with a reduced ductility. The change in damage mechanism is an outcome of the modification in deformation mechanism.

4. The derived set of microstructure parameters along with reported strengthening equations was used to calculate the RT yield stress. The estimates were critically compared with the measured yield stress for an extended set of alloys including data reported for Fe-Cr model alloys and steels thus covering one order of magnitude or more in

grain size, dislocation density, particle density and yield stress. The comparison shows that among various strengthening sources, particle strengthening provides a major contribution to the measured RT yield stress, which is more than 45% in the studied ODS steel. In addition, dislocation forest and grain size strengthening are also dominant contributors. Furthermore, grain size strengthening along with the Pythagorean summation of dislocation forest strengthening and particle strengthening describes the whole set of ODS and non-ODS Fe-Cr steels and alloys reasonably well. This is particularly remarkable since the whole set of alloys spans an order of magnitude or more in terms of grain size, dislocation density, particle density and yield stress. Furthermore, suitability of the choice of model parameters and determination of microstructure parameters are broadly confirmed.

5. Finally, due to the presence of the highly stable nano-oxide particles, TM 9YWT-MATISSE offers superior strength over similar non-ODS F/M steels e.g. EUROFER97 and P91. Furthermore, in comparison to other commercial, as well as experimental, ODS steels, TM 9YWT-MATISSE offers an excellent compromise between strength and ductility. However, the specific characteristics of dislocation structure and boundaries obtained by phase transformation in F/M 9YWT-MATISSE is less efficient than those achieved by mechanical deformation (hot rolling or forging) in ferritic ODS steels.

4.3 Pure fatigue/continuous cycling (PF/CC) behavior

This section provides an insight into TM 9WT-MATISSE high-temperature PF/CC behavior. Testing basics and details are already described in section 3.2.2. Firstly, the measured mechanical response is outlined at 550 °C and 650 °C under four different strain amplitudes ranging from $\pm\,0.4\%$ to $\pm\,0.9\%$. The cyclic stress-strain and strain-life relationships were obtained through the test results, and related LCF parameters were calculated. Microstructural investigations, using electron microscopy, were carried out to shed light on the deformation mechanisms. In addition, important observations from the fatigue-cracked specimen surfaces, cross-sections and fracture surfaces are presented. Discussions are made (1) to correlate microstructural evolution and damage progression with the cyclic stress response and (2) to compare measured cyclic stress response and lifetime with that of the similar non-ODS as well as other ODS steels tested or taken from the literature. In addition, this section provides a baseline for understanding the influence of hold-time introduction in pure-fatigue waveform; i.e. creep-fatigue interaction, which will be delineated in section. 4.4.

4.3.1 Mechanical response

The stress response curves (tensile peak stress versus number of cycle curves) obtained at both temperatures under various applied strain amplitudes are shown in Fig. 4.20. It is evident from the figure that at both temperatures 9YWT-MATISSE initially manifests transitional stages, i.e. cyclic hardening (increase in peak stresses) and/or steep softening (reduction in peak stresses) corresponding to the small fraction of cyclic life, which is followed by a continuous linear cyclic softening stage that occupies the major fraction of cyclic life until failure. Except two specimens, tested at 550 °C with $\pm\,0.7\%$ and $\pm\,0.9\%$ strain amplitudes which exemplify pure sof-

tening behavior, all specimens initially exhibit hardening. Here, the share of hardening is increasing with decreasing strain amplitude, but decreasing with increase in testing temperature (see fine black lines trend in Fig. 4.20 which mark the transition from hardening stage towards softening stage). In addition, it is seen that the rate and amount of the continuous linear cyclic softening is function of both temperature as well as applied strain amplitude. For instance, as shown in Fig. 4.21, under $\pm$ 0.5% strain amplitude the amount of softening is higher at 550 °C than at 650 °C. Moreover, in respect to accumulated inelastic strain, the rate of cyclic softening increases with the increase in imposed strain amplitude (Fig. 4.22).
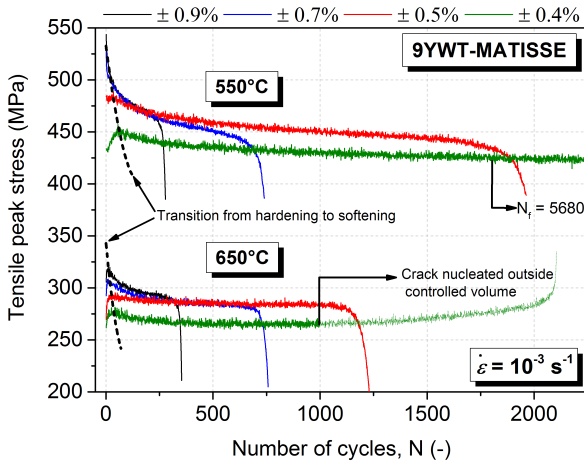
Figure 4.20: Tensile peak stress versus number of cycles curves for 9YWT-MATISSE. The fine black lines mark the transition from hardening stage towards softening stage.

The summary of the LCF tests on 9YWT-MATISSE is provided in Table. 4.8. From the Table, it is apparent that the contribution of elastic and inelastic strain component to the total strain is dependent on the experimental total strain level and temperature. Under lower strain amplitudes, elastic strain is higher than the inelastic strain. On the contrary, under higher strain
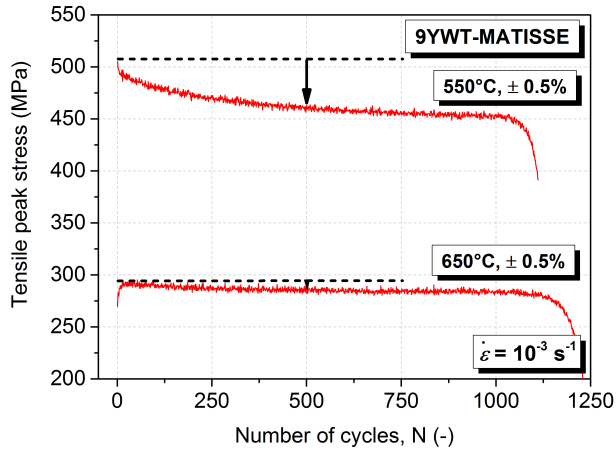
Figure 4.21: Effect of temperature on the amount of softening.
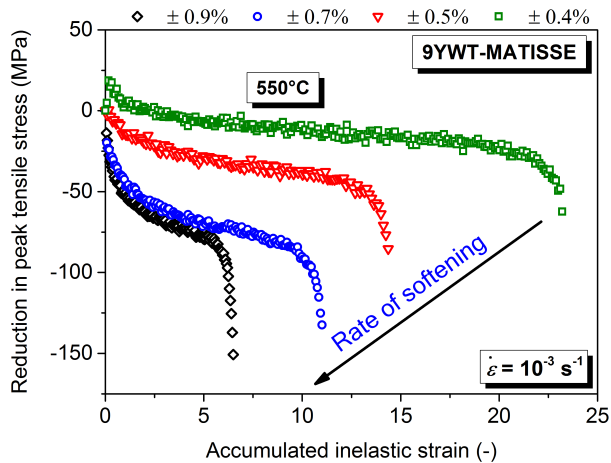
Figure 4.22: Effect of stain amplitude on the rate of softening.

amplitudes, the inelastic strain is the major contributor to the total strain. Furthermore, for a given total strain amplitude, as the temperature increases the inelastic strain amplitude increased and the elastic strain amplitude decreased. Also from Fig. 4.22, the total accumulated inelastic strain at the end of the fatigue life decreased with increase in strain amplitude and testing temperature (not listed here).

The relation between total strain amplitude $\dfrac{\Delta\varepsilon_t}{2}$ and stress amplitude $\dfrac{\Delta\sigma_t}{2}$ can be described by the well-known Ramberg-Osgood type relationship [213], which is given as:

$$\frac{\Delta\varepsilon_t}{2} = \frac{\Delta\varepsilon_e}{2} + \frac{\Delta\varepsilon_{in}}{2} = \frac{\Delta\sigma_t}{2E} + \left(\frac{\Delta\sigma_t}{2K}\right)^{1/n} \tag{4.8}$$

where $\dfrac{\Delta\varepsilon_e}{2}$ is the elastic strain amplitude, $\dfrac{\Delta\varepsilon_{in}}{2}$ is the inelastic strain amplitude, E is the elastic modulus, K is the cyclic strain hardening coefficient and n is the cyclic strain hardening exponent. From Eq. 4.8, the parameters K and n determine the assumed power function relation between stress amplitude and inelastic strain amplitude, hence the inelastic part can be written as:

$$\frac{\Delta\sigma_t}{2} = K\left(\frac{\Delta\varepsilon_{in}}{2}\right)^n \tag{4.9}$$

The bilogarithmic plot of $\dfrac{\Delta\sigma_t}{2}$ versus $\dfrac{\Delta\varepsilon_{in}}{2}$ obtained from the LCF data at both temperatures is shown in Fig. 4.23. These curves are important as designers need them for detailed inelastic analysis of the components. The values of parameters K and n obtained from the linear fit of the data in above plot is shown in Fig. 4.23 and also listed in Table. 4.9. It is evident that with the increase in testing temperature, the cyclic strain hardening coefficient decreased, while the cyclic strain hardening exponent increased. These values are lower than those reported for similar ODS steels, e.g. ODS EU-

Table 4.8: Summary of the PF/CC tests on 9YWT-MATISSE.

Temperature θ (°C)	Total strain amplitude $\frac{\Delta\varepsilon_t}{2}$ (%)	Inelastic strain amplitude* $\frac{\Delta\varepsilon_{in}}{2}$ (%)	Elastic strain amplitude* $\frac{\Delta\varepsilon_e}{2}$ (%)	Stress amplitude* $\frac{\Delta\sigma_t}{2}$ (%)	Lifetime N_f
550	± 0.9	0.55	0.35	481.3	392
		0.63	0.27	474.6	222
		0.59	0.31	474.9	274
	± 0.7	0.38	0.32	458.0	735
		0.39	0.31	466.3	395
		0.40	0.30	462.3	511
	± 0.5	0.19	0.31	456.6	1956
		0.21	0.29	459.2	1107
	± 0.4	0.11	0.29	423.6	5680
650	± 0.9	0.65	0.25	291.4	383
		0.66	0.24	299.8	348
	± 0.7	0.46	0.24	287.5	650
		0.47	0.23	283.1	740
		0.48	0.22	303.7	579
		0.48	0.22	296.3	539
	± 0.5	0.26	0.24	289.0	1448
		0.26	0.24	288.2	1196
	± 0.4	0.17	0.23	272.4	1888†
		0.17	0.23	270.0	2104†
		0.17	0.23	273.4	2034†
		0.17	0.23	270.1	2342†

*Measured at half-life $\left(\frac{N_f}{2}\right)$

†Fatal crack nucleated outside the probed gauge length

ROFER and ODS T91 [45,148]. The lower value of n for 9YWT-MATISSE suggests its lower work hardening ability.
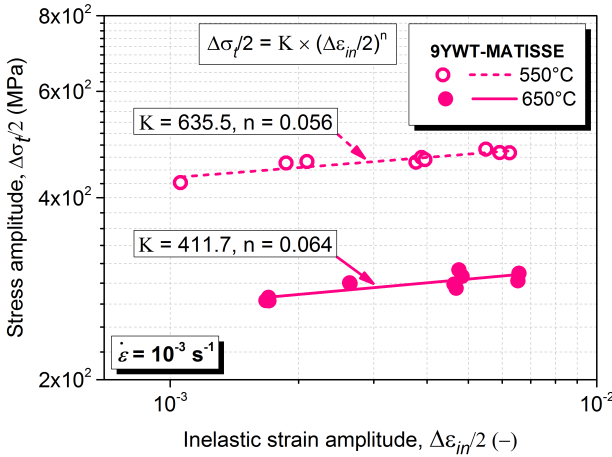
Figure 4.23: Bilogarithmic plot of the stress amplitude $\dfrac{\Delta\sigma_t}{2}$ versus inelastic strain amplitude $\dfrac{\Delta\varepsilon_{in}}{2}$ obtained from the LCF data for different strain amplitudes and fitted linearly with Eq. 4.9

Material's cyclic behavior can also be described by comparing monotonic stress-strain curve (MSSC) with cyclic stress-strain curve (CSSC). It is well known that the material exhibits cyclic hardening if the CSSC lies above MSSC, cyclic softening when CSSC falls below MSSC and cyclic stability if CSSC superimposes MSSC. For comparison, MSSCs at both temperatures were obtained from the first half cycle of the test performed under $\pm$ 0.9% strain amplitude. Whereas, CSSCs were obtained through Ramberg-Osgood relation given in Eq. 4.8 and parameters listed in Table. 4.9. The comparison of the two curves at both temperatures are shown in Fig. 4.24. It can be clearly seen that CSSC lies below MSSC at 550 °C indicating cyclic softening. However, at 650 °C, CSSC almost superimposes MSSC indicating cyclic stability. This however is not the case, since no clear stable

cyclic response could be identified at any stage in Fig. 4.20. Here, the transitional stage representing cyclic hardening followed by subsequent stage illustrating continuous linear cyclic softening creates an illusion of cyclic stability at half-life $\dfrac{N_f}{2}$. Nevertheless, cyclic softening at 650 °C is significantly reduced in comparison to that at 550 °C. Hence, 9YWT-MATISSE degrades under fatigue loads, but the complex course of cyclic softening at 650 °C cannot be visualized through this procedure.
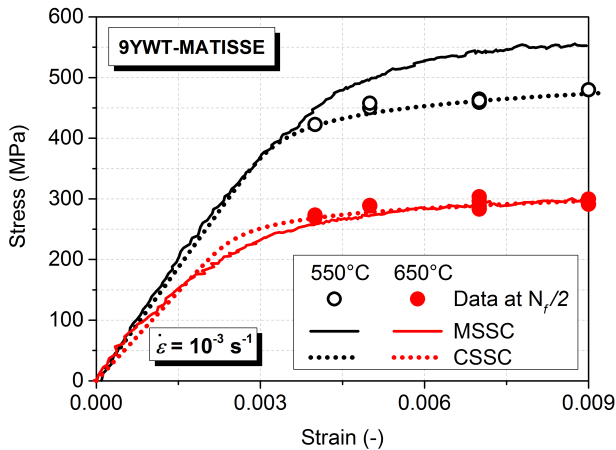
Figure 4.24: Cyclic stress-strain curves (CSSC) obtained with Eq. 4.8 and monotonic stress-strain curves (MSSC) obtained from the first half cycle of the experiment under ± 0.9% strain amplitudes at 550 °C and 650 °C.

Fig. 4.25 shows that the fatigue life of the 9YWT-MATISSE is strongly dependent on the cyclic strain amplitude however weakly on the testing temperature. The scatter in the lifetime for repeated tests lies within the acceptable limits when considering the miniaturized specimen geometry used in work. From Fig. 4.25, it is apparent that the number of cycles to failure decrease rapidly with increase in applied strain amplitude. However, with respect to temperature, 9YWT-MATISSE shows an anomaly. In compari-

son to 550 °C, 9YWT-MATISSE at 650 °C shows slightly higher average lifetime under higher strain amplitudes ($\pm$ 0.9% and $\pm$ 0.7%) and lower average lifetime under lower strain amplitude ($\pm$ 0.4%).
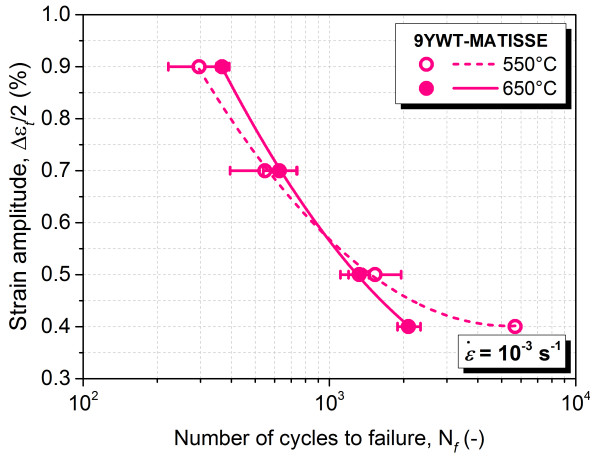
Figure 4.25: Total strain amplitude $\dfrac{\Delta\varepsilon_t}{2}$ versus number of cycles to failure N_f plot showing Wöhler curves.

During LCF, inelastic strain amplitude $\dfrac{\Delta\varepsilon_{in}}{2}$ for various materials have been shown to follow a power type relation with the number of reversals to failure $2N_f$. Coffin and Manson separately found an empirical relationship between $\dfrac{\Delta\varepsilon_{in}}{2}$ and $2N_f$, which can be described by the equation [214, 215]:

$$\frac{\Delta\varepsilon_{in}}{2} = \varepsilon_f'(2N_f)^c \tag{4.10}$$

Where ε_f' is the fatigue ductility coefficient defined by the strain intercept at $2N = 1$ and c is the fatigue ductility exponent. The Coffin-Manson equation particularly describes the cyclic behavior in the LCF regime, $N_f \leq 10^4$, where inelastic strain determines the cyclic life. The bilogarithmic plot of

$\dfrac{\Delta\varepsilon_{in}}{2}$ versus $2N_f$ fitted with Eq. 4.10 is shown in Fig. 4.26. It is evident that in the LCF regime the fatigue lives of the steel can be accurately predicted by using Coffin-Manson model. The values of LCF parameters ε'_f and c determined from the linear fit of the test data is shown in Fig. 4.26 and are also listed in Table. 4.9. The values of fatigue ductility exponent c for 9YWT-MATISSE are within the typical range ($-0.8 \leq c \leq -0.5$) observed for most metals. Furthermore, these values are lower than those obtained for non-ODS 9%Cr steels [216] and in close agreement with those evaluated for other ODS steels [45, 148] at similar temperatures.
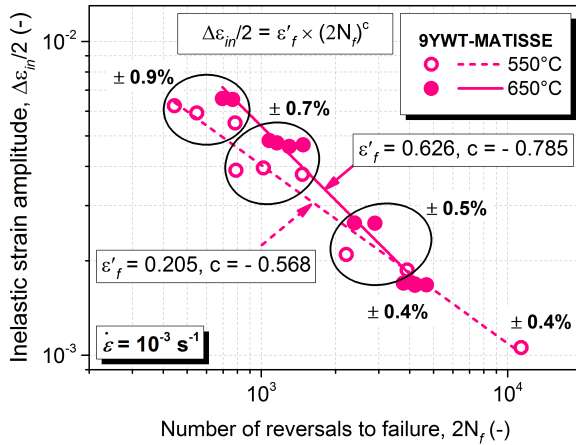
Figure 4.26: Inelastic strain amplitude $\dfrac{\Delta\varepsilon_{in}}{2}$ versus number of reversals to failure $2N_f$ plot showing Coffin-Manson curves.

4.3.2 Microstructural evolution

To understand the deformation mechanisms under cyclic loading, microstructural characterizations, via EBSD and TEM, were carried out, which are

Table 4.9: Values of the parameters obtained from the analysis of LCF data measured at $\frac{N_f}{2}$.

Temperature θ (°C)	Elastic modulus E (GPa)	Cyclic strain hardening coefficient K (MPa)	Cyclic strain hardening exponent n	Fatigue ductility coefficient $\varepsilon_f^{'}$	Fatigue ductility exponent c
550	125	635.5	0.056	0.205	-0.568
650	98	411.7	0.064	0.626	-0.784

presented below.

EBSD investigations

EBSD investigations after cycling straining at both temperatures reveal no obvious overall texture evolution, i.e. grains still manifest random orientations with no preferentiality (compare IPF maps shown in Fig. 4.27). In addition, at 550 °C, the average grain size as well as LABs and HABs fractions are only slightly altered (Fig. 4.28 and Table. 4.10). Nonetheless, with an apparent trend, the evolution becomes conspicuous at 650 °C. In Fig. 4.27c, the grains appear equiaxed with a prominent increment in their average size (Fig. 4.28 and Table. 4.10); i.e. $\sim$ 57% larger than in the undeformed state. This however appears independent of the applied strain amplitude. Furthermore, as shown in Fig. 4.28, the fraction of LABs decrease with a simultaneous increase in relative HABs fraction[5] (Table. 4.10). This suggests partial elimination of the original lath and sub-grain structures, since misorientation between them was measured to be less than 15°. This evolution amplifies with increase in applied strain amplitude. However, it is noteworthy that the remaining sub-grain boundaries (SGBs) or LABs

---

[5] In absolute sense, HABs fraction also decreased due to the coarsening of the grains.

are partly newly-formed due to the rearrangement (to and fro or shuttling motion) of mobile dislocations (see further).

KAM and GAM are used to visualize local misorientation changes. While KAM provides a good measure of dislocation density, GAM is a typical way of displaying orientation changes inside the grains. In both cases, misorientation can be envisaged either in form of a color-coded map or as a graph. For more details about analyzing procedure, see subsection 3.3.3. As shown in Fig. 4.27e and i, both KAM and GAM maps for an undeformed state exhibit a homogeneous spread of relatively high values (Fig. 4.29). Here, prior one (Fig. 4.27e) implies a presence of high dislocation density, while later one (Fig. 4.27i) indicates the existence of sub-grain structures. After cycling, KAM spread reduces with a coexisting peak shift towards lower values (Fig. 4.29a). This can be partly seen with an appearance of blue color (depicting low misorientation values) in KAM map (Fig. 4.27f) indicating a reduction in dislocation density. This exaggerates even further with increase in both temperature and applied strain amplitude (Fig. 4.27g-h and Fig. 4.29a). The dislocation density distribution trends estimated via EBSD are shown separately, see appendix A.3. Moreover, apart from nearly unaltered misorientation spread at 550 °C, GAM shows similar trends at 650 °C as observed for KAM after cyclic straining (Fig. 4.27j-l and Fig. 4.29b). Here, the fraction of grains with low misorientation values increases with increase in both temperature and applied strain amplitude. Hence, it appears that due to the conjoint effect of temperature and cyclic straining, these grains either formed after dynamic recrystallization and/or experienced original sub-grain structures elimination. However, recrystallization is not expected at this temperature. Moreover, sub-grain structures elimination is also in accordance with reduction in LABs fraction (Table. 4.10) which is also confirmed by TEM investigations (see further). EBSD investigations showing microstructural evolution with respect to number of cycles for 9YWT-MATISSE is documented separately, see Appendix A.4.

117
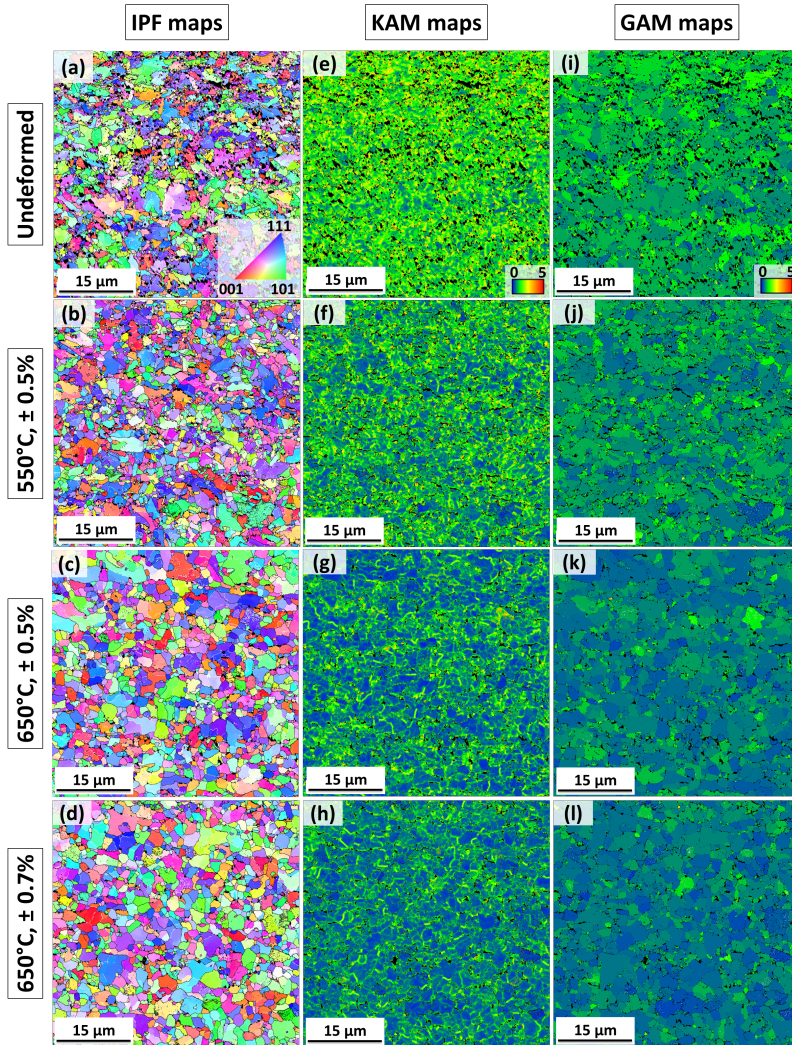
Figure 4.27: IPF (a-d), KAM (e-h) and GAM (i-l) maps obtained by analyzing EBSD scans that were taken before (undeformed) and after cyclic straining (550 °C, ± 0.5%; 650 °C, ± 0.5% and 650 °C, ± 0.7%). Common color keys are provided for each type of maps.
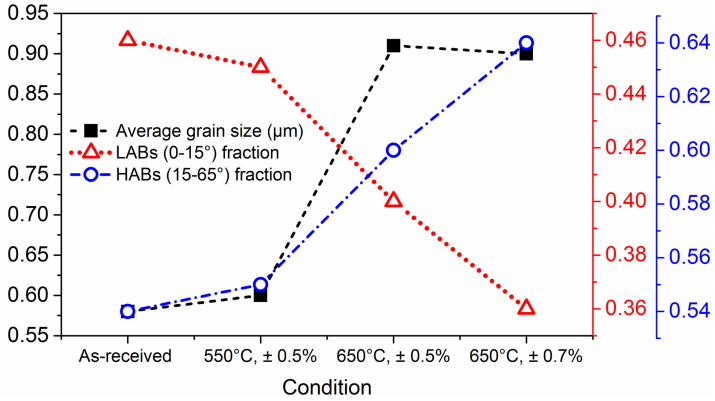
Figure 4.28: Graph showing average grain size as well as LABs and HABs fractions evolution upon cycling at 550 °C and 650 °C for two different strain amplitudes ($\pm$ 0.5% and $\pm$ 0.7%) via EBSD.

Table 4.10: Average grain size (d_g) as well as LABs and HABs fractions measured before (undeformed) and after cyclic straining (550 °C, $\pm$ 0.5%; 650 °C, $\pm$ 0.5% and 650 °C, $\pm$ 0.7%) via EBSD.

Condition	d_g (μm)	LABs fraction	HABs fraction
Undeformed	0.58	0.46	0.54
550 °C, $\pm$ 0.5%	0.60	0.45	0.55
650 °C, $\pm$ 0.5%	0.91	0.40	0.60
650 °C, $\pm$ 0.7%	0.90	0.36	0.64

Therefore, from the local misorientation analysis, it can be concluded that cyclic straining results mainly in a reduction of dislocation density at 550 °C and with additional partial sub-grain structure elimination at 650 °C which intensify even further with increase in applied strain amplitude. Interestingly, the local misorientation analysis also indicates that grain growth appears to have occurred at an expense of smaller grains. For example in Fig. 4.30, grains with lower misorientation values (blue color in GAM map)
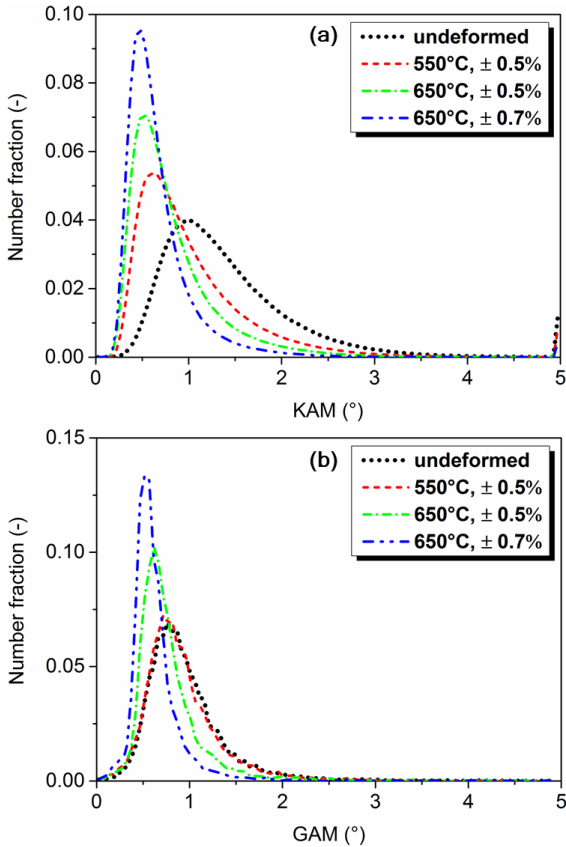
Figure 4.29: KAM (a) and GAM (b) values distributions before (undeformed) and after cyclic straining (550 °C, ± 0.5%; 650 °C, ± 0.5% and 650 °C, ± 0.7%)

appear to have grown by consuming smaller deformed grains with relatively larger misorientation values (green color in GAM map). This growth process seems to have occurred in a continuous manner, where HAB, free of pinning sources (carbides or Y-Ti-O nanoparticles), migrates towards smaller grain (which is thermally assisted) and continuously sweeps over it (see further TEM investigations). Kapp et al. recently reported similar pheno-

menon for an ultra-fined grained copper under in situ cyclic micro-bending investigations at room temperature [217]. The driving force and direction for boundary migration can be dictated by: (1) the curvature of grain boundary, for e.g. smaller grains exhibit a stronger concavity and hence tendency to shrink and disappear [217, 218]; and (2) variance in strain energy density, which is smaller in larger grains due to a lower yield stress, but larger in smaller grains due to an increased yield stress and may act as a driving force [217]. However, to confirm, in situ investigations are required.
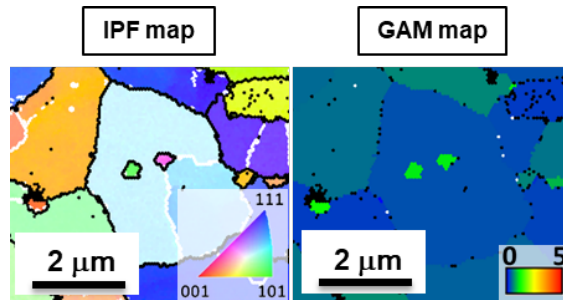
Figure 4.30: IPF map with its corresponding GAM map obtained by analyzing EBSD scan that were taken after cyclic straining (650 °C, ± 0.7%). Larger grains with low GAM values (blue) appear to have grown at the expense of smaller grains with relatively high GAM values (green). Color keys are provided for each type of maps. In IPF map, HABs and LABs are marked by black and white lines, respectively

TEM investigations

In order to delineate microstructural evolution at even higher resolution, TEM investigations were carried out. The overall microstructures after cyclic straining under ± 0.5% strain amplitude at 550 °C and 650 °C are shown in Fig. 4.31. In general, at both temperatures, grains appear equiaxed having sub-grain structures. Even though rarely, well-defined lath structures are still perceived at 550 °C (see marked features in Fig. 4.31a). Nevertheless, at 650 °C, grains appear comparatively coarse and no well-defined lath structures could be distinguished (Fig. 4.31b).

121
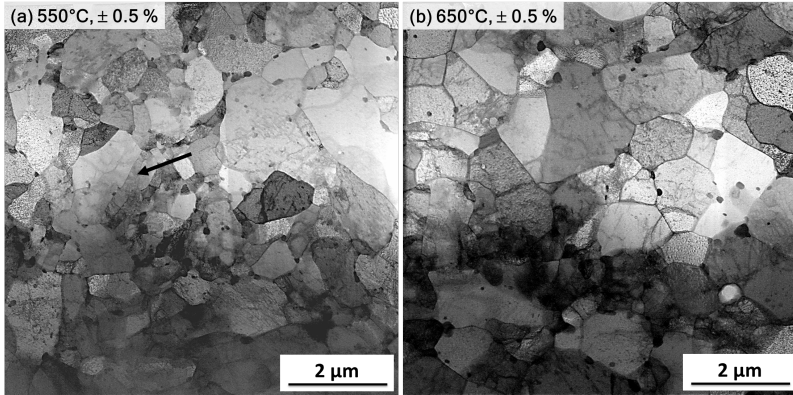
Figure 4.31: Inverted contrast HAADF-STEM micrographs showing microstructures after testing under ± 0.5% strain amplitude at (a) 550 °C and (b) 650 °C.

In addition, at both temperatures, regions of different dislocation densities were observed. Here, areas with lower and higher dislocation densities correspond to those with low and high KAM values, respectively. This is likely to be a question of homogeneity of oxide particles distribution, i.e. their presence or absence in particular grain or even within a single grain (discussed further). Unfortunately, the quantitative dislocation densities could not be estimated due to uncertainty in the determined TEM sample thickness. However, though qualitative, the overall dislocation density is certainly reduced (as microstructure appears relatively clean), in comparison to that of the undeformed state. Yet, high dislocation density within most grains is still apparent (Fig. 4.32a). In these grains, dislocations activity is mainly transgranular which is homogeneously distributed indicating a strong pinning from intragranular obstacles. In most regions, especially at 650 °C, dislocations are aligned in a long thread like arrangements, however few regions adjacent to boundaries exhibit disordered dislocation tangles (Fig. 4.32a). These disordered tangles are those that were frequently observed in undeformed microstructure (see Fig. 4.2b) and vanish upon cycling with increase

in both testing temperature and applied strain amplitude. Nevertheless, no noticeable 3D dislocation arrangements such as the ladder, vein, or labyrinth were identified. Hence, oxide particles are able to inhibit strain localization by not allowing above-mentioned 3D dislocation structures formation.
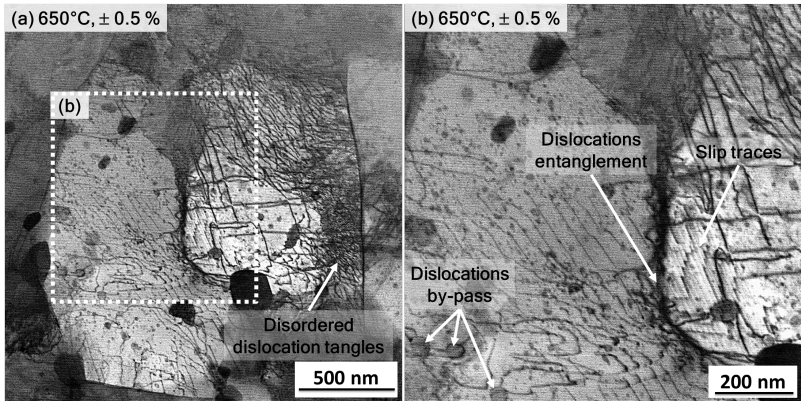
Figure 4.32: Inverted contrast HAADF-STEM micrographs showing dislocation structures after testing under $\pm$ 0.5% strain amplitude at 650 °C

At higher magnification (Fig. 4.32b), dislocations appear pinned at various locations and under the effect of stresses (resolved shear stress on a given slip system), most of them are bowed out. In Fig. 4.33a, HAADF-STEM image along with its elemental maps are shown. Here, beside two large (> 50 nm) Cr-W and Ti-O-C enriched particles; dislocations are efficiently pinned at relatively fine Y-Ti-O nanoparticles (marked with arrows). Nonetheless, due to thermal activation dislocations can by-pass particles through cross-slip or climb, depending upon the character of the dislocations and the nature of the particle-matrix interface. One such situation can be seen frozen in Fig. 4.32b, where dislocations by-passing over coarse Ti-enriched particles is apparent. Nevertheless, careful examination reveals dislocations pinning at the departure side of the nano-oxide particles (Fig. 4.33b). This confirms an attractive particle-dislocation interaction which is known

to occur at elevated temperatures in an incoherent interface [118]. At such interface, dislocations do not transfer shear strain and their strain field partially relax by diffusion in the particle-matrix interface which minimize dislocation energy. Hence, there exists a threshold stress to detach dislocation out of this pinning, which must be overcome for the dislocation to glide; and therefore, plastic deformation to occur [120, 206, 208, 219]. However, once threshold stress is reached, the dislocation will detach and glide until new pinning where the process of particle by-pass and detachment recurs. This results in a retarded dislocation's transgranular mobility. Howbeit, in between obstacles or in particle deficient regions, dislocations can still annihilate with those of opposite sign, leading to their reduced density. And therefore, both uniform nanoparticles distribution as well as lower inter-particle spacing is critical for suppressing the annihilation processes. Notwithstanding, as seen in Fig. 4.32b, lots of similar dislocations (due to their shuttling motion) can also entangle together to achieve lower energy configurations which could finally develop into cyclically stable SGBs. Here, more alike dislocations progressively participate/incorporate (knitting-in [220]) which is associated with the changes in lattice orientation (Fig. 4.32b). Furthermore, numerous slip traces can be noticed on the opposite side of this entanglement emphasizing that several dislocations have already moved out of this location. Finally, it is noteworthy that the above-mentioned dislocation entanglements are only seen seldom. Nevertheless, as mentioned earlier, apart from the remaining original SGBs, they also contribute to the total LABs fraction (Table. 4.10)) measured via EBSD.

Fig. 4.34a shows overall microstructure after cyclic straining at 650 °C under higher strain amplitude ($\pm$ 0.7%). Clearly, lath structures are almost absent. Moreover, grains again appear partially clean due to reduced dislocation density. At higher magnification, these cleaner regions are also found to be free of nanoparticles; see grain (1) in Fig. 4.34b. And therefore, it seems that due to their obstruction free path, since there are no
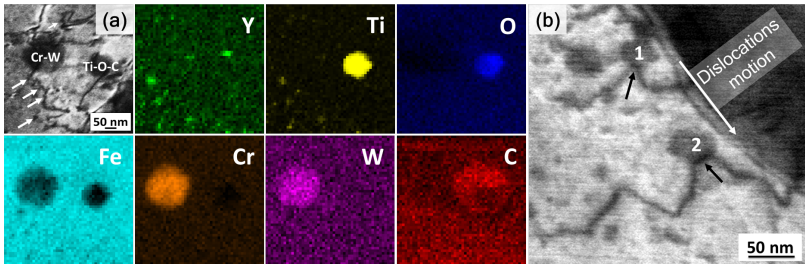
Figure 4.33: HAADF-STEM image (a) along with its elemental maps, taken from the specimen tested under $\pm 0.5\%$ strain amplitude at 650 °C, shows relatively large Cr-W and Ti-O-C enriched particles and dislocations pinning at marked Y-Ti-O nanoparticles. Inverted contrast HAADF-STEM image (b) reveals an attractive dislocation-particle interaction with dislocation pinning at departure side of the marked nano-oxide particles 1 and 2

particles to be pinned against, dislocations glide freely across whole grain. This dislocation glide is not only responsible for dislocations annihilation with those of opposite sign, leading to a reduced dislocation density, but also act as a driving force for SGB elimination. According to Sauzay et al. [221], mobile dislocations annihilate with those of opposite sign in LABs leading to the elimination of corresponding lath and sub-grain boundaries. In addition, knitting-out reactions are also known to cause SGBs dissolution [164, 220]. As seen in Fig. 4.35, dislocations next to the SGBs appear to be connected to the SGBs dislocations by local annihilation which could tear/extract boundary dislocations out of these boundaries during further glide [220]. This not only decrease SGBs dislocation density and the corresponding misorientation but later can also results in their significant dissolution (Fig. 4.36a). However, carbides are known to impede this phenomenon [164] but in their absence (for e.g. at marked SGBs in Fig. 4.35) knitting and absorption/emission reactions involving "free" dislocations and SGBs can occur. Moreover, during deformation decrease in average SGB misorientation has also been predicted by modelling, see Ref. [222]. Also in Fig. 4.34b, apart from their usual location, i.e. boundaries, carbides can be seen isolated in the grain's (1) interior. Therefore, again indicating SGB

125
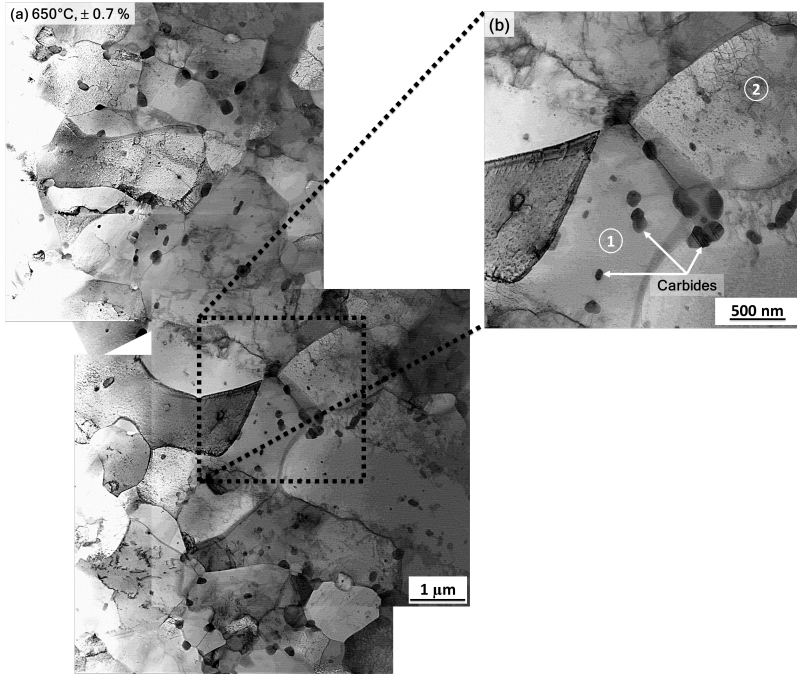
Figure 4.34: Inverted contrast HAADF-STEM micrographs, taken from the specimen tested under $\pm$ 0.7% strain amplitude at 650 °C, (a) collage shows overall microstructure where grains appear partially clean due to reduced dislocation density and (b) shows grain (1) containing isolated carbides in its interior and is free of dislocations and nanoparticles, while grain (2) manifests both nanoparticles as well as dislocations pinned at them.

elimination on which they once nucleated during tempering. Holec and Dlouhý [223] via dislocation dynamics computation proposed that when the misorientation angle is less than a critical value (0.3°), the interaction forces between the SGB dislocations and carbides are too weak to preserve SGB stability under stress loading.

On the contrary, in grains with higher nano-particles density (for e.g. grain (2) in Fig. 4.34b), a high dislocation density was observed. Furthermore, in

such grains the SGBs are only partially destroyed (Fig. 4.36b). Here, dislocations manifest relatively long straight-line segments, with sharp corners

and a serrated appearance in other locations (Fig. 4.36c). At sharp corners dislocations are pinned at the particle-matrix interfaces. This finding provides additional support that the nanoparticles act as persistent barriers to dislocation motion which suppresses microstructure evolution. However, higher stress level than under lower strain amplitudes expedites particles by-pass. Consequently, a slightly more pronounced microstructural evolution at higher strain amplitude than under lower strain amplitude.
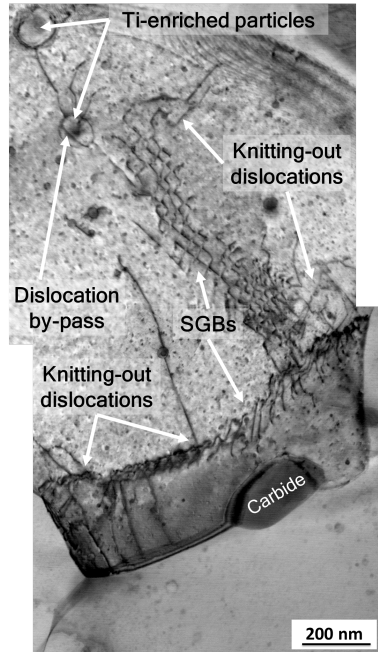
Figure 4.35: Inverted contrast HAADF-STEM micrograph collage, taken from the specimen tested under ± 0.7% strain amplitude at 650 °C, showing knitting-out reactions where dislocations are extracted out of the SGBs.

Carbides appear coarsened particularly after cycling at 650 °C. This coarsening is especially seen for those which are still in contact with boundaries. The driving force for this coarsening is probably the reduction of total carbide/matrix interfacial energy [164]. This eventuates through: (1) diffusion of alloying elements from matrix towards boundaries which additionally act as the short-circuit diffusion networks; and (2) coalescence through Ostwald ripening mechanism [165]. This coarsening altogether not only degrades one source of strength (i.e. solid solution strengthening) but

127
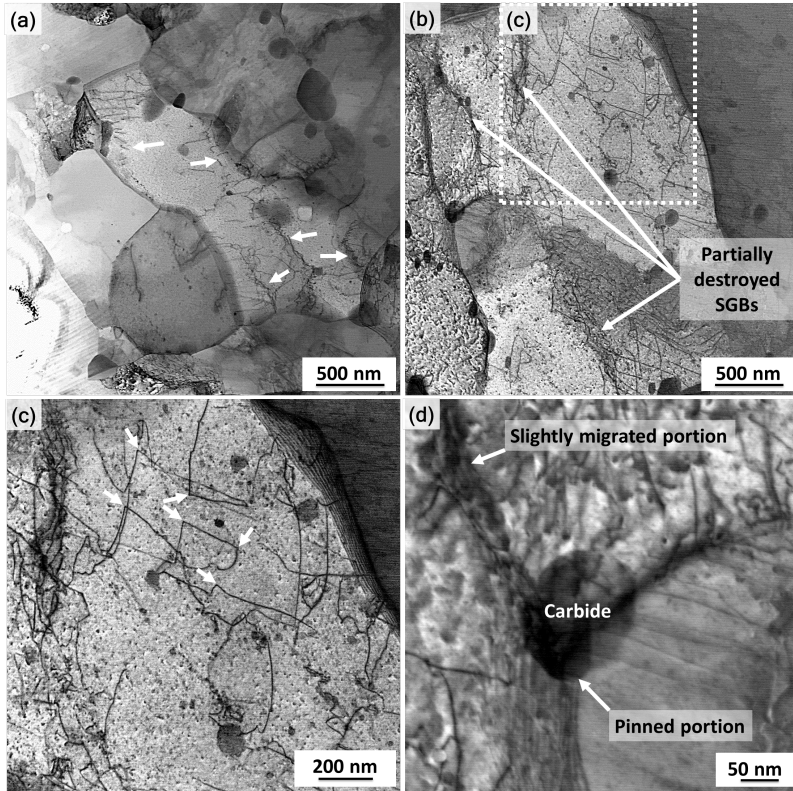
Figure 4.36: Inverted contrast HAADF-STEM micrographs, taken from the specimen tested under ± 0.7% strain amplitude at 650 °C, show (a) knitting-out reactions leading to the partial dissolution of SGBs (marked with arrows), (b) grain with partially eliminated SGBs, (c) magnified image from (b) showing dislocations at sharp corners are pinned at the particle-matrix interfaces and (d) grain boundary portion pinned by carbide and slightly migrated portion without carbide.

can also compel carbides to lose their ability of pinning boundaries [28] which might explain observed grain coarsening that leads to equiaxed grains and also possible SGBs migration. Nonetheless, this can also be attributed to the localized pinning-sources (carbides or Y-Ti-O nanoparticles) free boundary-segments migration, which otherwise could have remained

pinned, as shown in Fig. 4.36d, due to Zener drag effect. Furthermore, EDX analysis, such as shown in Fig. 4.33a, reveals the presence of carbon free Cr-W enriched phase which is commonly referred to as Laves phase (WCr_2) [9, 224]. Though seen seldom, the formation of Laves phase can be due to the presence of Si which reduces the solubility of W in the matrix [225] and their segregation on or near to the boundaries can finally weaken the effect of solid solution strengthening [226]. However, considering the short durations of LCF tests, this effect can be neglected. As according to Klueh [85] for the short-time creep tests ($\leq$ 10,000 h), the W still contributes to the solid solution strengthening, even though Laves removes W from solution. Moreover, during early stages of such tests, the precipitation hardening by Laves phase contributes to the strength, which subsequently decreases as a result of coarsening of the Laves phase particles [9]. Furthermore, as discussed in section 4.2.4, solid solution strengthening may also be irrelevant for ODS steels. Besides, Y-Ti-O nanoparticles and carbides were not sheared by dislocations which otherwise could have contributed to the cyclic softening [140]. Shearing is possible only if particles are coherent with the matrix which was not observed for the dispersoids and the carbides, respectively. Finally, the Y-Ti-O nanoparticles appeared very stable without any change in shape or size.

4.3.3 Damage characteristics

In order to understand damage mechanisms, detailed observations of the fatigue-cracked specimen surfaces, cross-sections and fracture surfaces were carried out. As shown in Fig. 4.37, for interrupted test, performed at 650 °C under $\pm$ 0.5% strain amplitude, specimen surface manifests micro-cracks even before 100 cycles which is $\sim$ 10% of its original fatigue life. This confirms that fatigue cracks nucleate at early stage of the test and LCF is mainly a crack growth phenomenon. This evolution/progress of damage could also contribute to the perceived softening [227] (discussed in detail in

section 4.3.4). The SEM micrographs taken after macroscopic failure from the specimens surfaces in the vicinity of main macro-cracks are shown in Fig. 4.38. It is evident from the figure that in comparison to lower strain amplitude ($\pm$ 0.4%) the cracks density is much higher under higher strain amplitude ($\pm$ 0.7%). This suggests an expeditious as well as pronounced damage with increase in applied strain amplitude which is a result of both higher stress level and larger induced inelastic strain.
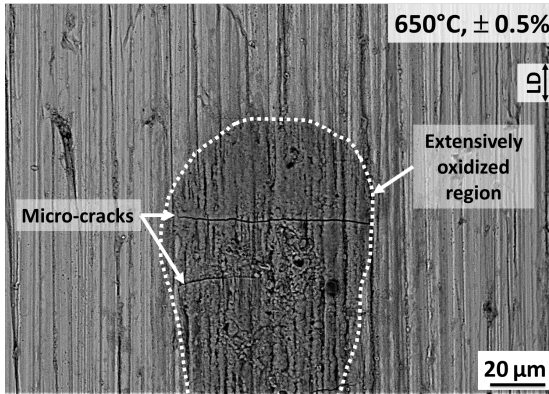
Figure 4.37: Back scattered SEM micrograph taken from the surface of the specimen cycled at 650 °C under $\pm$ 0.5% strain amplitude for only 100 times (i.e. until 10% of its original fatigue life). LD stands for loading direction.

Regarding the significance of nano-oxide particles, one may assume that pinning of dislocations by them is also affecting the onset and progress of surface damage, since the formation of 3D dislocation structures (causing strain localization) is inhibited and the associated generation of extrusions and intrusions (preliminary stage of micro-crack formation [144]) will also be constrained. However, Thiele et al. pointed out that some minimum volume ($\sim$ 1 μm in terms of grain size) is required for the creation of PSBs or 3D dislocation structures [228]. And since ODS steels are generally produced with a sub-micron sized matrix, to achieve additional superimposed grain size strengthening without adversely affecting ductility and

130

toughness [161], the crack initiation stage will also be suppressed by restricting the above-mentioned dislocation structures formation [51]. On the contrary, ODS steels with large grains and/or large volumes with similar orientations manifest both 3D dislocation structures and associated surface relief [46,51], where fatigue cracks nucleate. Indeed, in comparison to similar steel (ODS EUROFER [45]) having larger grain size (0.7 μm), 9YWT-MATISSE manifest $\sim$ 60% higher fatigue life under similar testing conditions (650 °C and $\pm$ 0.5% strain amplitude). However, independently, secondary phase particles (oxides/carbides/Laves [224]/large inclusions [45]), microstructural defects (pores/voids [46]) and fabrication induced surface imperfections can also act as preferred crack initiation sites.
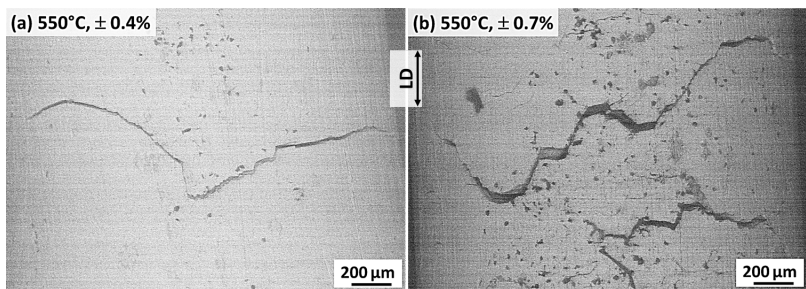
Figure 4.38: Back scattered SEM micrographs taken from the surface of the specimen tested under $\pm$ 0.4% (a) and $\pm$ 0.7% (b) strain amplitude at 550 °C. LD stands for loading direction.

Furthermore, environmental effects cannot be underestimated. As shown in Fig. 4.37, the specimen cycled for only $\sim$ 10% of its original fatigue life manifests a relatively extensive oxidation in and around the proximity of micro-cracks. Here, stress field associated with the crack nucleation site could promote oxygen diffusion which results in a localized preferential oxidation. In addition, a focused ion beam (FIB) cut (on a specimen cycled till failure) through a surface micro-crack (Fig. 4.39) exhibits oxide layer not only on the specimen's surface but also around the crack flanks. Moreover, preferred oxidation is observed along grain boundaries. This is due to the

131

fact that boundaries act as diffusion short circuits across the protective oxide layer that allows an easier path of oxygen diffusion. Here, brittle surface oxides, which form at surface-connected grain boundaries, could also initiate fatigue crack due to the "wedge effect" that results and supports stress-assisted decohesion [147]. Moreover, cycling leads to a repeated cracking of oxide scale, therefore a large number of cracks initiate in air, in comparison to that in vacuum [229, 230]. Upon cracking, surface oxide layer is no longer able to prevent oxygen from penetrating inside the material. The resulting oxidation in and around the crack advancing front (freshly exposed metal volume having oxidation prone boundaries), see Fig. 4.40, further facilitates crack propagation [231]. Therefore, an inevitable oxidation-fatigue interaction, as oxidation not only assists fatigue crack initiation owing to its brittleness but also further accelerates its propagation due to fall of the required threshold [232]. Indeed, it has been reported that the fatigue life of a conventional F/M steel (mod. 9Cr-1Mo) tested at similar temperature is shortened by a factor of 2 to 3 in air, compared to that in vacuum [22]. Here, also see Refs. [26, 229]. Besides, oxidation and its detrimental role to some extent not only depends on testing temperature but also on the time of exposure, as it is found to be more pronounced under lower strain amplitude and higher test temperature than at higher strain amplitude and lower temperature [216]. The chemical composition of oxides on similar non-ODS steel was found to be of duplex morphology with an inner layer consisting of Fe-Cr spinel type oxide and an outer layer made up of iron oxide [230].

Fig. 4.41 presents views of the fracture surfaces obtained from the specimens tested under $\pm$ 0.5% strain amplitude at 550 °C (a, b) and 650 °C (c). The fatigue fracture region reveals single crack initiation site at the outer periphery. The crack initiation site unveils large chunks of oxides present near its proximity. In addition, stable crack growth region exhibits secondary cracks (marked with arrows in Fig. 4.41a) that are oriented normal to the main crack propagation direction and tear ridges which are oriented parallel
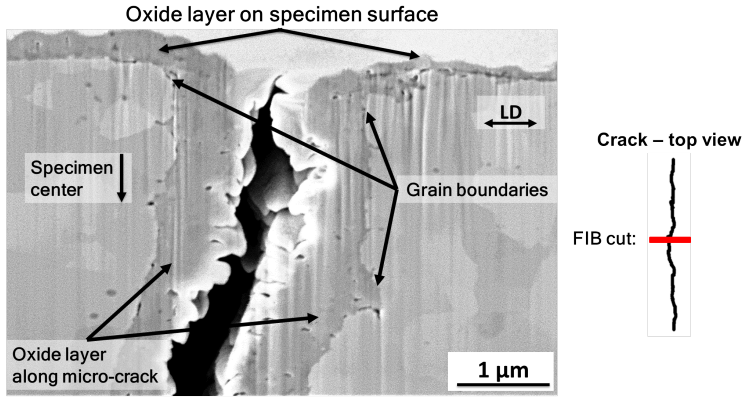
Figure 4.39: SEM micrograph taken from the specimen tested at 650 °C under ± 0.7% strain amplitude showing a FIB cut section through a surface micro-crack that exhibits protective oxide layer not only on specimen surface but also along the micro-crack. Surface-connected grain boundaries are marked where micro-crack initiated. Also shown is a schematic of the crack top view showing the position of the FIB cut. LD stands for loading direction.
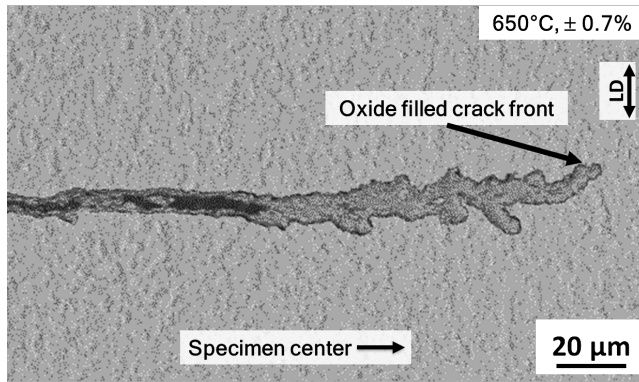
Figure 4.40: Back scattered SEM micrograph taken from the longitudinally-sectioned specimen tested at 650 °C under ± 0.7% strain amplitude showing oxide filled crack advancing front. LD stands for loading direction.

to the crack growth direction. At higher magnification (Fig. 4.41b, c), the classical fine-scale transgranular ductile fatigue features called striations are

apparent. During fatigue crack propagation, striations usually form by a repeated crack blunting and sharpening process due to the slip of dislocations in the plastic zone at the fatigue crack tip [138]. The fatigue fracture surface morphology with this terrace-like pattern indicates multiple deflections of the fatigue crack along its propagation path. Such crack deflections might be attributed to the interaction of the glide dislocations with obstacles, e.g. particles, precipitates and grain boundaries. Therefore, striations form as a result of a plastic flow to release the stress around the crack tip. However, here, the stress relaxation might not be fast enough [233]. Consequently, a significant tensile stress acts on the notch-like striation; and thereby, initiating micro-cracks. Moreover, boundaries can provide favorable sites for micro-cracks nucleation [56] which might further accelerate due to the presence of carbides. These micro-cracks can subsequently propagate by their linking up and conjoining to form evident bigger secondary cracks. The tear ridges form to join grains that are not coplanar. Here, the material fails by shearing resulting in the apparent continuity of the fatigue advancing front [234].

Fig. 4.42 presents views of the fracture surface obtained from the specimens tested under higher strain amplitude ($\pm$ 0.7%) at 650 °C. In Fig. 4.42a, several surface initiated cracks propagated and finally coalesced (leaving behind tear ridges) to form one main macro-crack which resulted in failure. In addition to the observation mentioned for the lower strain amplitude (secondary cracks perpendicular to the fracture surface; marked with black arrows in Fig. 4.42b), here fracture surface also exhibits features which are difficult to comprehend (Fig. 4.42c). Nevertheless, these fracture features resemble those observed after high temperature tensile loading (Fig. 4.14), where they were attributed to the intergranular cracking.
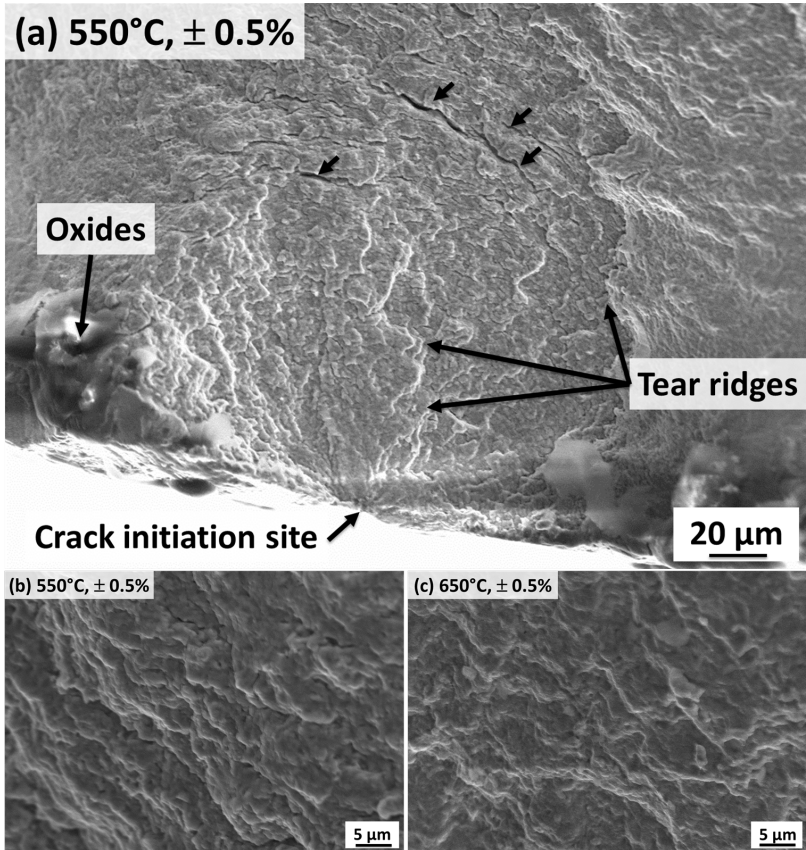
Figure 4.41: SEM micrographs taken from the fracture surface of the specimen tested under ± 0.5% strain amplitude at 550 °C (a, b) and 650 °C (b).

4.3.4 Discussion

In this section, firstly microstructural modifications are discussed in respect to the cyclic stress response. Thereafter, damage's role in softening is argued based on its progression. Finally, comparisons are made in respect
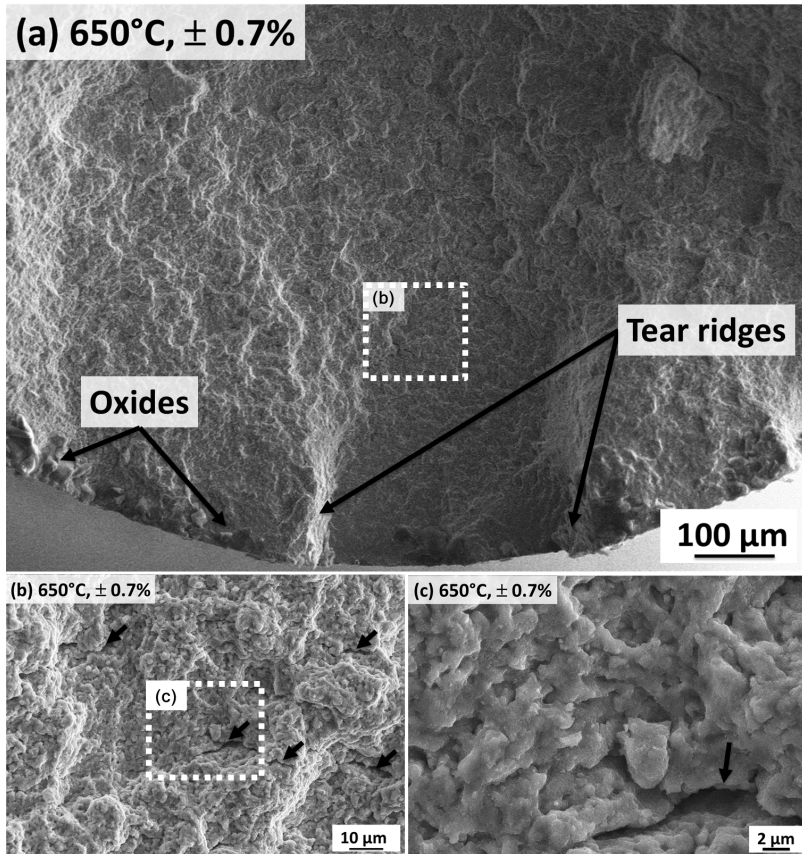
Figure 4.42: SEM micrographs taken from the fracture surface of the specimen tested under ± 0.7% strain amplitude at 650 °C.

to the similar non-ODS as well as other ODS steels tested and taken from literature.

Microstructural evolution and cyclic stress response

During cyclic deformation, microstructural modifications transpire in order to achieve stable low-energy configurations. Here, modifications rate and

amount precisely depend upon the testing conditions such as deformation rate (strain rate), its extent (amplitude) and temperature. In case of 9YWT-MATISSE, after cycling at 550 °C, microstructure appears almost unaffected. The average grain size as well as the boundaries fractions are only slightly altered. The main changes however are in respect to the dislocations rearrangement and/or annihilation which finally cause reduction in their density. At 650 °C, microstructural evolution hastens and becomes prominent mainly in nano-oxides/carbides deficient regions. Here, in addition to the reduced dislocation density, partially eliminated original sub-grain structures, grain growth, $M_{23}C_6$ carbides coarsening and Cr-W enriched Laves phase precipitation are evident. Similar observations have also been previously documented for the ODS variants of EUROFER97 and conventional P91 [30, 148]. The microstructural modifications, concerning dislocation density and sub-grain structures, intensify even further with increase in applied strain amplitude. This is due to the fact that under such conditions larger inelastic strain has to be accommodated per cycle than under lower temperature and applied strain amplitude. And therefore, a higher degree of softening with increase in applied strain amplitude (Fig. 4.22). However, a relatively less pronounced softening at 650 °C than at 550 °C (Fig. 4.21) can be an outcome of accelerated static and/or dynamic recovery at higher temperature. Static recovery occurs during the dwell time prior to the test start where specimens were held under zero stress for at least 30 min after achieving the test temperature in order to stabilize testing system. Due to thermally-activated annihilation processes, static recovery could cause reduction in dislocation density (especially in the particle deficient regions), since no other major microstructural changes were observed after annealing at 650 °C in air for even much longer duration (10 h) (c.f. Fig. 4.27 and Fig. 4.43). Therefore, it is expected that dislocation density will increase during first few loading cycles, depending upon the applied strain amplitude, until the equilibrium between the dislocation annihilation and their generation is reached, which could lead to the evident initial minor cyclic

hardening. Furthermore, in comparison to 550 °C, higher potency of dynamic recovery accelerates microstructural evolution at 650 °C. This ultimately incites earlier attainment of steady state at 650 °C with relatively minor microstructural changes in the following cycles. Hence, progressive but a minor descend of peak stresses at 650 °C than at 550 °C. Nevertheless, apart from the reduced dislocation density at 550 °C, the overall microstructure evolution is only significant at 650 °C. Therefore, it can be concluded that the reorganization and annihilation of martensitic transformation induced high dislocation density is the main cause for the loss of cyclic strength.

Damage
as a possible source of softening

As already seen in section 4.3.3, fatigue cracks nucleate at the early stage of the test (Fig. 4.37) and then continuously propagate as well as coalesce until macroscopic failure. Hence, in addition to the microstructural evolution, progress of damage (microcracks propagation) can also contribute to the observed minor softening
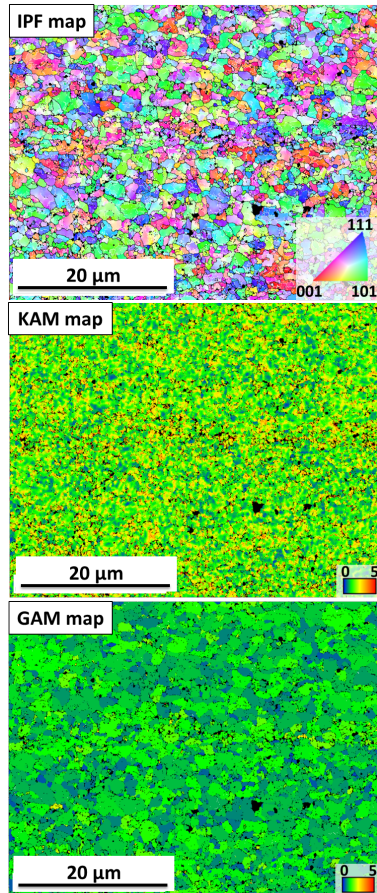
Figure 4.43: EBSD maps obtained from the sample annealed at 650 °C in air for 10h. Here, no major microstructural changes are visible when compared with those observed after cycling at 650 °C for comparable duration (see Fig. 4.27). Hence, microstructure evolution is not an influence of temperature alone but occurs with a synergistic effect of cyclic straining.

[227] in some way, since the reduction of effective cross-section area, caused by increasing surface damage, is not taken into account while calculating stresses. This effect becomes even more crucial under corrosive environmental conditions and higher strain amplitudes. For e.g., micro-crack initiation in air occurs earlier and is much more extensive than in the vacuum environment [147, 229]. Indeed, environmental effects were also confirmed by others like Kim et al. [22] where slightly higher cyclic softening is observed in air for a conventional F/M steel (mod. 9Cr-1Mo) than in vacuum. Additionally, under higher strain amplitude, not only the progress of damage is faster but is also more extensive (higher cracks density) than under lower strain amplitude (see section 4.3.3). This damage contribution becomes even more decisive, upon considering the miniaturized specimen geometry used in this work. In addition, relatively less pronounced softening at 650 °C can also be associated to fact that easier deformation (higher induced inelastic strain per cycle at 650 °C than at 550 °C) in front of crack tip restricts the progress of damage (lower crack growth rate). Therefore, the microstructural evolution as well as damage acts either in sequence or in parallel to contribute to the cyclic softening which cannot be easily separated. One of the ideas can be to carry out interrupted tests. However, due to the limited amount of material such investigations are unfortunately not possible under this work.

Comparison with other commercial and experimental non-ODS and ODS steels

Comparison of the cyclic stress response: The comparison of the cyclic stress response and hysteresis loops at $\frac{N_f}{2}$ of 9YWT-MATISSE with similar non-ODS F/M steels, for e.g. EUROFER97 and P91, is shown in Fig. 4.44. Besides higher peak stresses and thus lower inelastic strain amplitudes, the studied ODS steel manifests a significantly reduced cyclic softening at both investigated temperatures. This is due to the fact that highly stable Y-Ti-O nanoparticles reduce microstructural degradation by acting as

139

persistent barriers for dislocations motion. However, cyclic straining assisted by thermal activation as well as inhomogeneous nanoparticles distribution resulted in similar microstructural changes as those observed and often reported for conventional non-ODS F/M steels [17, 22, 26] at lower temperature (550 °C), but to a lesser extent.
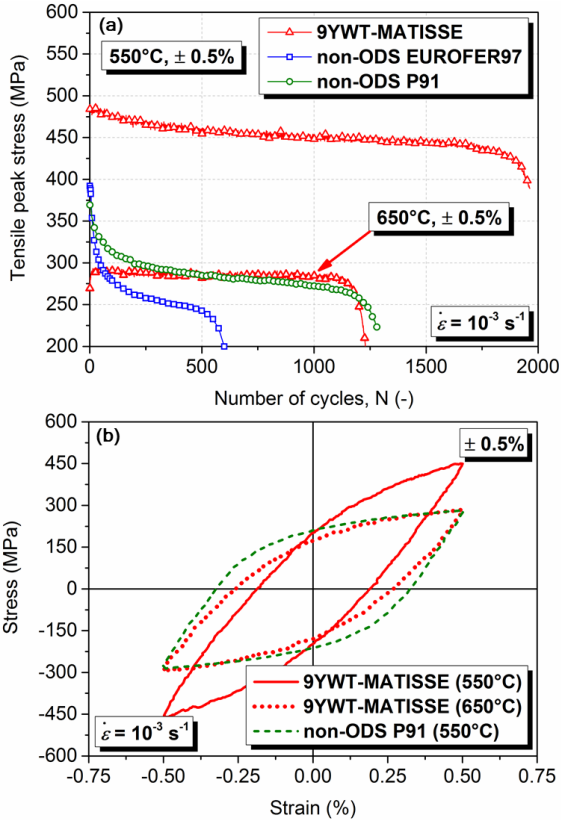
Figure 4.44: (a) Comparison of the cyclic stress response of 9YWT-MATISSE with that of conventional non-ODS F/M steels (EUROFER97 and P91) and (b) corresponding hysteresis loops at $\frac{N_f}{2}$ under $\pm\,0.5\%$ strain amplitude.

The amount of the cyclic softening can be quantitatively judged from the linear stage of cyclic stress response. Batista et al. [235] reported that the quasi linear stage of the F/M steels in a log-log scale follows an analytical expression of the type:

$$\sigma = A(N)^{-s} \tag{4.11}$$

where A is a temperature dependent constant and S is the cyclic softening coefficient. S represents the magnitude of cyclic softening and is a slope of the linear softening stage in the log-log plot. Fig. 4.45 illustrates the behavior of obtained S as function of temperature, for ODS 9YWT-MATISSE, ODS 12YWT-GETMAT [51], non-ODS F/M steels and other commercial steels taken from literature [235]. The variation of S for non-ODS F/M steels is attributed to the difference in their dislocation density which is a consequence of their different chemical compositions and the corresponding resulting martensitic start temperature [235]. It is evident form the figure that both ODS steels clearly manifest lower cyclic softening than non-ODS steels. However, in comparison to ODS 12YWT-GETMAT, 9YWT-MATISSE manifests a relatively more pronounced softening. This can be mainly attributed to their distinct initial microstructure which was obtained by phase transformation in 9YWT-MATISSE and by thermo-mechanical processing in 12YWT-GETMAT [51]. As mentioned in section 4.2.4, F/M matrix of 9YWT-MATISSE is weaker than that of ferritic 12YWT-GETMAT.

As already seen, oxide dispersion assists is mitigating cyclic softening. However, it does not itself guarantee stable cycle response. Moreover, the steel's processing route and hence, developed matrix appears to play a critical role in defining the overall LCF behavior. In this regards, two other ODS steels with different matrix (one a ferritic bimodal 12%Cr based (12YWT-GETMAT) ODS steel and other austenitic (MS XVI) ODS steel) were tes-
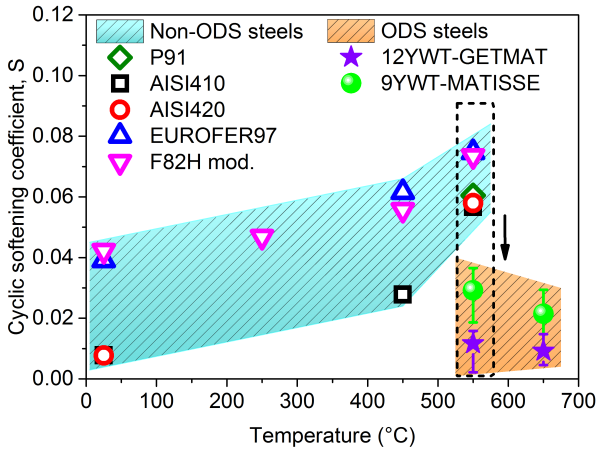
Figure 4.45: Comparison of the cyclic softening coefficients of the ODS 9YWT-MATISSE, obtained from the slope of the linear cyclic softening stage in the log-log plot, with ODS 12YWT-GETMAT [51] and other non-ODS F/M steels from [235]. The error bars represent the maximum and minimum values obtained at highest and lowest strain amplitudes, respectively.

ted[6]. The detailed microstructural characterizations for both steels in as-fabricated state were reported separately, see Refs. [51, 142]. Briefly, while the ferritic 12YWT-GETMAT exhibits a unique elongated bimodal grain size distribution, the austenitic MS XVI manifests mostly a sub-micron equiaxed grains with low dislocation density. The 12YWT-GETMAT consists of a larger fraction of heavily-deformed small grains ($< 5 \, \mu$m) in comparison to that of the large deformation-free recrystallized grains ($> 5 \, \mu$m). In terms of number fraction, MSXVI exhibits an average matrix grain size of $\sim 0.32 \, \mu$m [142]. Except from some relatively coarse Cr- and Ti-enriched particles, mostly complex Y-Ti-O nanoparticles are distributed within the matrix of both steels that have a size distributions ranging from 1 to 90 nm.

---

[6] Tests on ferritic 12YWT-GETMAT and austenitic MS XVI were performed on the same type of sample, using the same test set-up. For more details about these materials see Refs. [51, 142]

Their corresponding cyclic stress response curves along with that of the F/M ODS 9YWT-MATISSE at similar testing condition are shown in Fig. 4.46. It is apparent that bimodal 12YWT-GETMAT offers highest cyclic strength due to its strongest microstructure. Whereas, apart from the initial comparable cyclic stress to the austenitic MS XVI, 9YWT-MATISSE exhibits lowest cyclic peak stress over rest of its life.
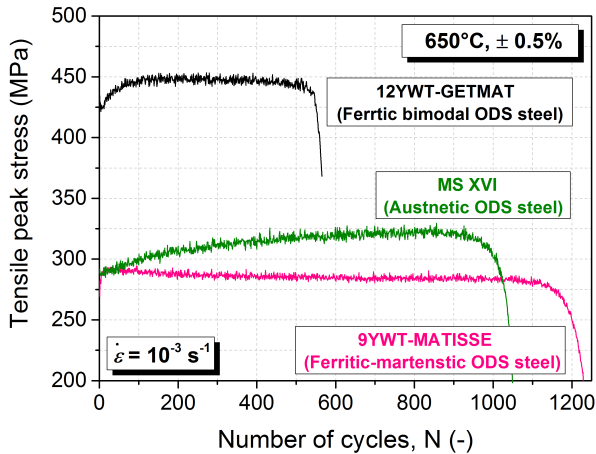
Figure 4.46: Tensile peak stress versus number of cycles curves for ferritic bimodal 12YWT-GETMAT, austenitic MS XVI and F/M 9YWT-MATISSE ODS steels at 650 °C under ± 0.5% strain amplitude [51, 142].

Furthermore, based on their distinct microstructural features different cyclic stress response is evident. As already discussed, cyclic softening in ODS 9YWT-MATISSE is mainly due to the overall reduction of the original dislocation density. The 12YWT-GETMAT, in general, as of 9YWT-MATISSE shows similar cyclic response. However, it undergoes pronounced initial hardening. This is due to the increase in dislocation density within the coarse recrystallized deformation-free grains. Whereas, the subsequent minor linear cyclic softening till failure is due to the dislocations

143

annihilation (in the original heavily-deformed small grains) and their re-arrangement into 3D dislocation structures in both smaller-deformed as well as larger-recrystallized grains [51]. Finally, austenitic MS XVI having low dislocation density undergoes continuous cyclic hardening till saturation [142]. Here, hardening, which is significantly lower than its conventional non-ODS counterparts [61, 142], is an aftermath of dislocations generation/multiplication. However, the competition between dislocations generation/multiplication and their annihilation/storage (via dislocation-dislocation annihilation and dislocation-grain boundary interaction) occurs simultaneously. This ultimately results in a stable dislocation density (which is obviously higher than in the undeformed state); and hence, leading to a stable cyclic response with constant peak stresses until approaching failure. Therefore, from here, it can be concluded that matrix plays a crucial role in defining the overall cyclic response of ODS steels.

Comparison of the lifetime: Based on their creep properties, conventional non-ODS steels are presently limited to an upper operating temperature of about 550 °C, since at higher temperature these alloys exhibit recrystallization, precipitates coarsening and their dissolution [20]. As can be seen from Fig. 4.47[7], in comparison to conventional non-ODS P91, ODS steels[8] at 550 °C offer comparable lifetime at higher strain amplitudes (> $\pm$ 0.5%) and much higher lifetime under lower strain amplitudes (< $\pm$ 0.5%). Similar results have been also reported by others, see Refs. [42, 61, 148]. These findings are consistent with the fact that stronger materials are known to offer better cyclic strain-life under lower strain amplitudes and ductile materials are acclaimed to perform better under higher strain amplitudes [150]. This is due to the fact that strong materials resist imposed strain

---

[7] Usually, such plots are plotted by selecting logarithmic scale at least for the X-axis. However, to clearly distinguish the differences of the selected steels lifetime linear scales were chosen.

[8] Tests on ODS 12YWT-GETMAT and non-ODS as well as ODS version of P91 were performed on the same type of sample, using the same test set-up. For more details about these materials see Refs. [51, 209, 236]

elastically on the basis of their strength, while ductile materials resist strain plastically on the basis of their ductility [150]. Therefore, less impressive lifetime under higher strain amplitudes can be understood as a result of the quicker exhaustion of ductility during cycling [237].
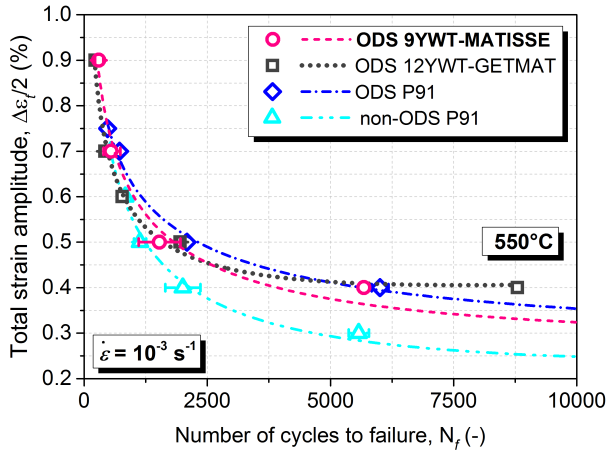
Figure 4.47: Lifetime behavior of the studied ODS 9YWT-MATISSE at 550 °C compared to that of the ODS 12YWT-GETMAT and ODS as well as non-ODS version of P91 [149].

Additionally, the similarities and differences in the lifetime can also be precisely explained on the basis of the estimated inelastic strain energies E_{in} (defined as the area within a hysteresis loop) [149]. In principle, inelastic strain energy accounts the effect of both induced inelastic strain and cyclic stress levels which are known to play a critical role in the damage process [238]. This is obviously based on a basic idea that a small amount of energy is rendered irrecoverable at every cycle owing to the plasticity. And when, as a result of repeated cycling, the total energy accumulated reaches the maximum absorbing capacity of a material, then the material will fail by "fatigue" [239]. Upon comparing E_{in} of ODS and non-ODS versions of P91, over their cyclic life, few important differences are obser-

ved (Fig. 4.48). (1) Due to significant cyclic softening, non-ODS P91 under higher strain amplitude manifest a reduction in E_{in}. Whereas, for ODS P91, initially lower E_{in} increases and becomes constant although higher than the one for its non-ODS variant for the most cyclic life (see Fig. 4.48). This in cumulative sense explains comparable lifetime of ODS steels under higher strain amplitudes. (2) Under lower strain amplitude, it is apparent from Fig. 4.48 that even though ODS P91 E_{in} increases initially with number of cycles, it is significantly lower than the one for non-ODS P91. And since lower strain amplitude regime is governed by micro-plasticity [237], ODS steels witness a comparatively lower localized deformation. Therefore, a superior lifetime for ODS steels under lower strain amplitudes. Furthermore, 9YWT-MATISSE at 650 °C (100 °C higher temperature) manifests comparable cyclic strength and lifetime to tested non-ODS steel at 550 °C (Fig. 4.44). Hence, in respect to LCF, oxide dispersion raises the limited operating temperature of conventional non-ODS F/M steels by about 100 °C.

In comparison to other novel ODS steels [42,45,149], 9YWT-MATISSE offers highest number of cycles to failure at similar testing conditions (see Fig. 4.49). Interestingly, it is apparent that all 9%Cr based F/M steels (9YWT-MATISSE, 9Cr-ODS, ODS P91 and ODS EUROFER) perform superior to ferritic ODS steels, such as 12YWT-GETMAT, at 650 °C which performed comparable at 550 °C (see Fig. 4.47). This can also be explained on the basis of their corresponding E_{in}. For example, upon comparing E_{in} of 9YWT-MATISSE and 12YWT-GETMAT, it is found that almost comparable E_{in} (area of the hysteresis loop over their cyclic life under $\pm$ 0.5% strain amplitude in Fig. 4.50a) for the two steels result in almost comparable lifetimes at 550 °C. Whereas, at 650 °C (Fig. 4.50a), 9YWT-MATISSE manifests lower E_{in} in comparison to that of 12YWT-GETMAT. Consequently, 9YWT-MATISSE presents higher lifetime than 12YWT-GETMAT. Here, the cyclic stress levels of 12YWT-GETMAT reveal a stronger effect on the
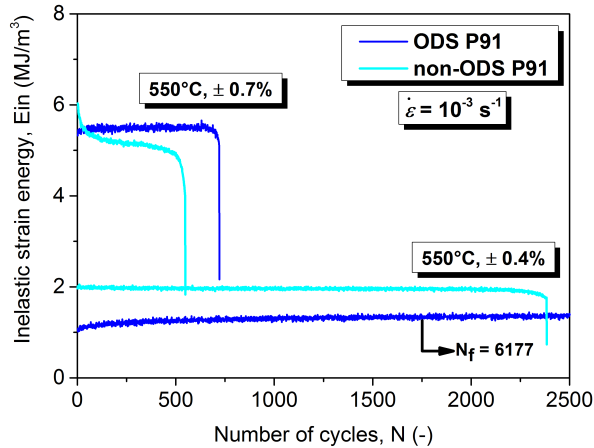
Figure 4.48: Comparison of the inelastic strain energies E_{in} (area of hysteresis loops) of the ODS and non-ODS version of P91 over their cyclic life under $\pm$ 0.7% and $\pm$ 0.4% strain amplitude at 550 °C

damage behavior than the induced inelastic strains. Since though 12YWT-GETMAT manifests lower inelastic strains than 9YWT-MATISSE (width of the hysteresis loops in Fig. 4.50b), it exhibits higher E_{in}, based on the clearly higher peak stress level. In addition, it is notable in Fig. 4.50a that almost comparable E_{in} for 9YWT-MATISSE at 550 °C and 650 °C leads to a previously shown weaker dependency of N_f on temperature (see Fig. 4.25). Furthermore, 9YWT-MATISSE higher fatigue life, in comparison to all other F/M steels, can also be attributed to its lower E_{in}, which is coming from its lower peak stresses (not shown here). Also, as explained in section 4.3.3, 9YWT-MATISSE lower average grain size, obviously resulting from the difference in the optimized chemical composition and manufacturing route, constraints damage evolution by not allowing 3D dislocation structures formation.
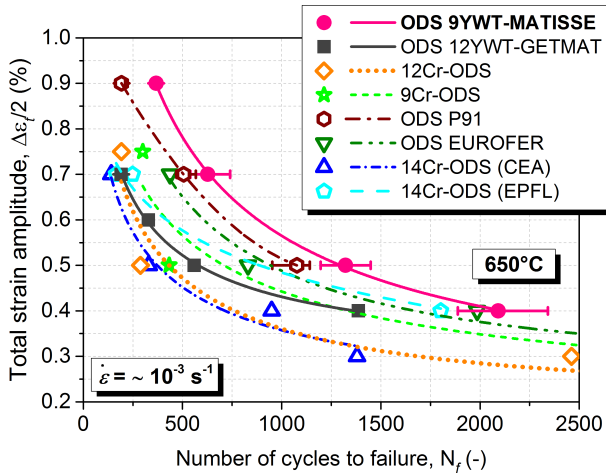
Figure 4.49: Lifetime behavior of the studied ODS 9YWT-MATISSE at 650 °C compared to that of other novel ODS steels described in the literature [42, 45, 148, 149].

4.3.5 Summary and conclusions

The fully reversed strain-controlled LCF tests conducted in air at 550 °C and 650 °C under different strain amplitudes led to following conclusions:

1. Under cyclic loading, 9YWT-MATISSE degrades as the cyclic stress response curves show complex cyclic softening with initial transitional stage representing cyclic hardening (increment in peak stresses) and/or steep softening (reduction in peak stresses) corresponding to the small fraction of cyclic life, which is followed by a continuous linear cyclic softening stage that occupies the major fraction of cyclic life until failure. Both applied strain amplitude and test temperature show a strong influence on the cyclic stress response. It is found, that the degree of linear cyclic softening decreases with decrease in imposed strain amplitude and increase in testing temperature. The effect
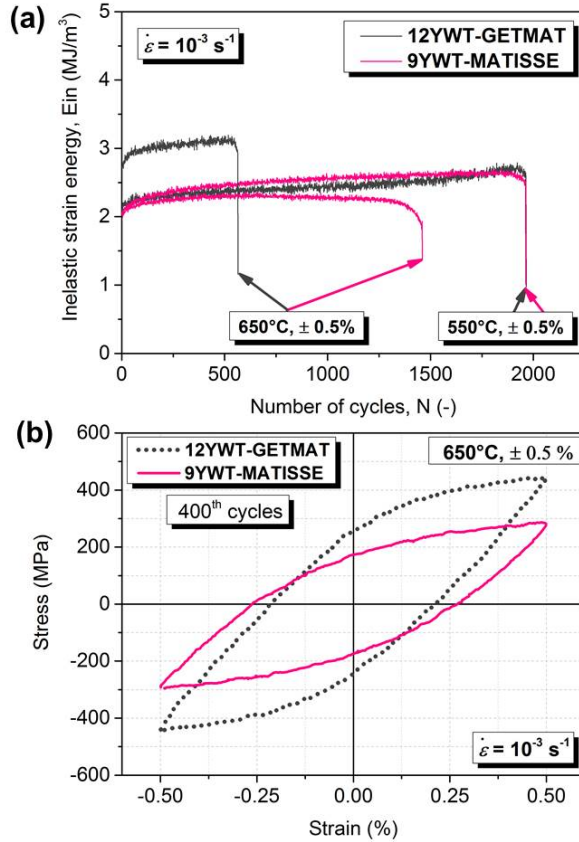
Figure 4.50: (a) Comparison of the inelastic strain energies E_{in} (area of hysteresis loops like in (b)) of ODS steels 9YWT-MATISSE and 12YWT-GETMAT at 550 °C and 650 °C under ± 0.5% strain amplitude over their cyclic life.

of temperature on inelastic strain; and hence, lifetime becomes more pronounced with decreasing applied strain amplitude.

2. In the LCF regime, the fatigue lives of the 9YWT-MATISSE can be accurately described by using models of Coffin-Manson. The estimated LCF parameters are better than those obtained for non-ODS steels

149

and in close agreement with those evaluated for other ODS steels at similar temperatures. However, the procedure of describing material's cyclic behavior by comparing CSSC with MSSC is unable to characterize the exact behavior of 9YWT-MATISSE at 650 °C.

3. EBSD complemented by TEM investigations were performed to delineate microstructural evolution after cyclic straining. At 550 °C, microstructure appears similar to that of the undeformed state. However, the main differences are in respect to the dislocations rearrangement and/or annihilation which finally result in their reduced density. At 650 °C, microstructural evolution hastens and becomes prominent mainly in nano-oxides/carbides deficient region. Here, in addition to the reduced dislocation density, partially eliminated original subgrain structures, grain growth, $M_{23}C_6$ carbides coarsening and Cr-W enriched Laves phase precipitation were also observed. The microstructural modifications, concerning dislocation density and subgrain structures, intensify even further with increase in applied strain amplitude. Nevertheless, annealing at 650 °C for comparable testing duration causes no noticeable microstructural changes. Since modest cyclic softening persists at both investigated temperatures, out of all microstructural changes the dislocations rearrangement and/or their mutual annihilation are assumed to be the main cause for the loss of cyclic strength.

4. Damage studies revealed higher cracks density under higher strain amplitude than under lower strain amplitudes suggesting an expeditious as well as pronounced damage with increase in applied strain amplitude. However, fatigue cracks nucleate at an early stage of the test which is prior to $\sim 10\%$ of original fatigue life. The crack's initiation as well as its propagation is further assisted by oxidation. On fracture surface, the stable crack growth region manifests secondary cracks, and at higher magnification, the classical fine-scale transgra-

nular ductile fatigue fracture features called striations. In addition, at 650 °C, crack path also acquires an intergranular tendency under higher strain amplitude.

5. The progress of damage (micro-cracks propagation) as well as environment effects (oxidation) are also argued to be the possible sources of evident minor cyclic softening. Damage acts either in sequence or in parallel with the microstructural evolution to contribute to the cyclic softening which cannot be easily separated.

6. Besides higher peak stresses and thus lower inelastic strain amplitudes, oxides dispersion in 9YWT-MATISSE assists in mitigating undesirable cyclic softening observed in conventional non-ODS F/M steels. This is due to fact that highly stable nano-sized oxide particles act as persistent barriers for dislocation motion which consequently reduce/slows-down typical microstructural degradation. However, cyclic straining assisted by thermal activation as well as inhomogeneous nanoparticles distribution result in similar microstructural changes as those observed in non-ODS matrix steels, but to a lesser extent. Moreover, the studied ODS steel at 650 °C manifests comparable cyclic strength and lifetime to tested non-ODS F/M steels at 550 °C. Hence, concerning LCF, oxide dispersion raises the limited operating temperature of conventional non-ODS F/M steels by about 100 °C. Finally, the obtained results depict that 9YWT-MATISSE offers highest number of cycles to failure at 650 °C, compared to other novel ODS steels described in literature.

4.4 Creep-Fatigue (CF) interaction

Creep-fatigue (CF) interaction in a TM 9YWT-MATISSE was studied at 650 °C by introducing hold-time period of up to 30 min at a peak tensile strain of 0.7%. For reader's convenience, discussions are part of results. Here, the modifications brought by introducing creep in fatigue in terms of the measured mechanical response, estimated lifetime, observed microstructural evolution and damage characteristics are presented and discussed.

4.4.1 Mechanical response

The peak tensile and compressive stresses, which are taken from the hysteresis loop at each cycle, from both PF/CC as well as CF tests for comparison are shown in Fig. 4.51. From Fig. 4.51, it is evident that all hold-time waveforms result in a similar cyclic response as under PF/CC. However, in comparison to almost symmetrical CC response, the following effects are apparent:

1. The CF peak stress versus number of cycles profiles are not symmetrical, i.e. hold-time introduction at peak tensile strain results in a drop in tensile peak stresses (i.e. additional tensile softening which is only 2 to 3% at $\frac{N_f}{2}$) with almost similar compressive peak stresses (Fig. 4.51). And therefore, compressive mean stresses are induced due to the introduction of tensile hold (TH) time. The peak stresses at $\frac{N_f}{2}$ for all tested conditions are summarized in Table. 4.11.

2. For the investigated hold-time durations, the increase in hold-time period has a negligible effect on peak stresses (i.e. saturation in softening is achieved) even though the higher amount of stress relaxation (ASR[9]) ensues (Fig. 4.51 and Fig. 4.52). On one hand, where similar behavior was observed for a non-ODS F/M F82H steel [25]. On the

---

[9] ASR is the difference in the stress values at the beginning and at the end of the hold-time.
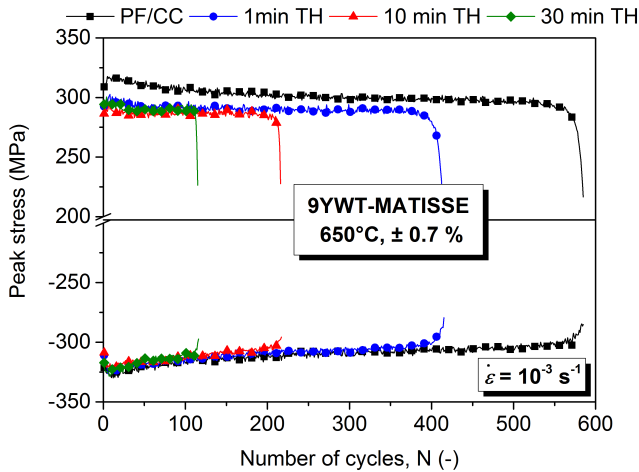
Figure 4.51: Comparison of the peak stress versus number of cycles profiles for waveforms with and without TH times at 650 °C under ± 0.7% strain amplitude.

other hand, non-ODS F/M P91 steel showed similar behavior only after introducing much longer hold-time (1-3 h) [236]. In CF testing, stress relaxation is an important feature of the hysteresis loop, which occurs during the application of hold-time at peak strain (see Fig. 3.4). Fig. 4.53 compares stress relaxation as a function of time under 10 and 30 min TH at representative $\frac{N_f}{2}$ cycles. In general, the stress decreases rapidly during the first few seconds (42% reduction in first 25 sec). Thereafter, a more gradual decrease in stress values (25% reduction during next 29.58 min) occurs which seem to saturate for longer hold-times. However, here, performing even longer hold-time tests will be beneficial in determining the underline fact. Additionally, ASR decreases with the number of cycles (Fig. 4.52). Though this reduction also accounts for the usual minor cyclic softening due to PF/CC, it suggests a reduction in viscosity [25].
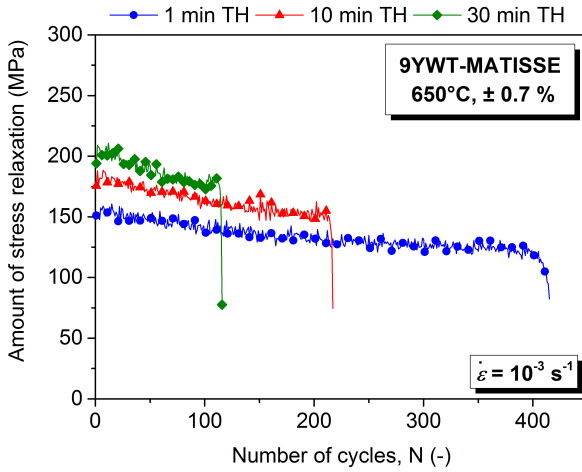
Figure 4.52: Amount of stress relaxation versus number of cycles profiles.
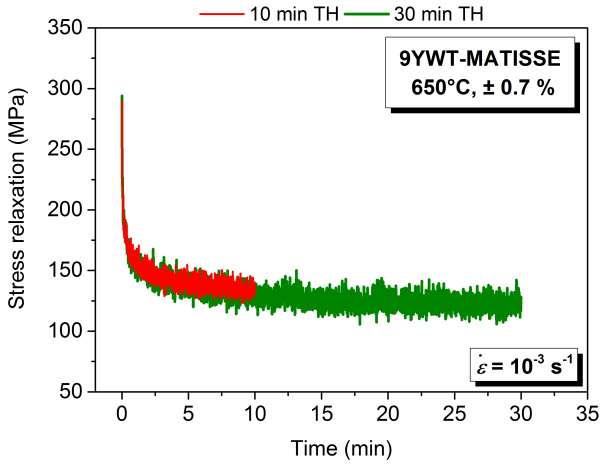
Figure 4.53: Stress relaxation curves under 10 and 30 min TH times at $\frac{N_f}{2}$.

3. Due to stress relaxation during TH, elastic strain gets partially converted into inelastic strain, $\Delta\varepsilon_{in}$ (which is measured as the width of the hysteresis loop at zero stress). Hence, hold-time introduction results in an increment of inelastic strain (this includes time-dependent strain component (creep strain) and hence, is a viscoplastic effect) which ultimately leads to a reduction in tensile peak stresses (Fig. 4.54). In comparison to PF/CC loop, 1 min TH introduction induces $\sim 8\%$ higher inelastic strain at $\dfrac{N_f}{2}$. Nevertheless, a further increase in hold-time duration leads to a comparatively minor increment in inelastic strain ($\sim 7\%$ higher inelastic strain was induced upon increasing hold-time by 29 min). This could well explain the negligible effect of hold-time duration on peak stresses. The inelastic strain amplitudes at $\dfrac{N_f}{2}$ for all tested conditions are listed in Table. 4.11.
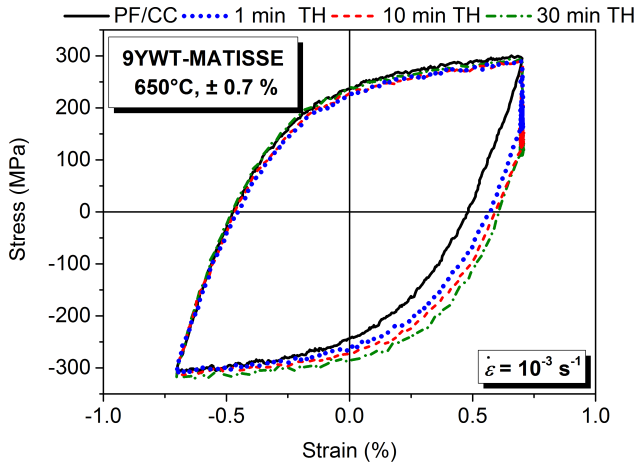
Figure 4.54: Comparison of hysteresis loops at $\dfrac{N_f}{2}$ with and without TH times at 650 °C under $\pm$ 0.7% strain amplitude.

155

4. The estimated number of cycles to failure N_f are listed in Table. 4.11. It is obvious that the introduction of hold-time at peak tensile strain results in a reduction of N_f. Moreover, the longer the hold-time the lower is the cyclic life which drops almost linearly (see Fig. A.6 in appendix A.5).

Table 4.11: Results of PF/CC and CF tests on 9YWT-MATISSE at 650 °C under $\pm$ 0.7% strain amplitude.

Condition	Peak tensile stress* (MPa)	Peak compressive stress* (MPa)	Inelastic strain* (%)	Lifetime N_f
PF/CC	300.2	307.2	0.48	627 $\pm$ 88
1 min TH	290.3	310.4	0.51	404
10 min TH	289.9	313.4	0.53	215
30 min TH	293.4	303.5	0.54	114

*Measured at $\dfrac{N_f}{2}$

4.4.2 Microstructural evolution

Microstructural investigations, via EBSD and TEM, are carried out to differentiate deformation mechanisms under PF/CC and CF waveforms.

EBSD investigations

EBSD scans taken before and after cyclic straining were analysed and the obtained results are shown in Fig. 4.55. For comparison, scans from undeformed and PF/CC tested specimens are also shown. From IPF maps (Fig. 4.55a-d), as for PF/CC, no obvious overall texture evolution is apparent after cycling under CF waveforms (i.e. grains still manifest random orientations with no preferentiality). Nonetheless, the grains appear equiax-
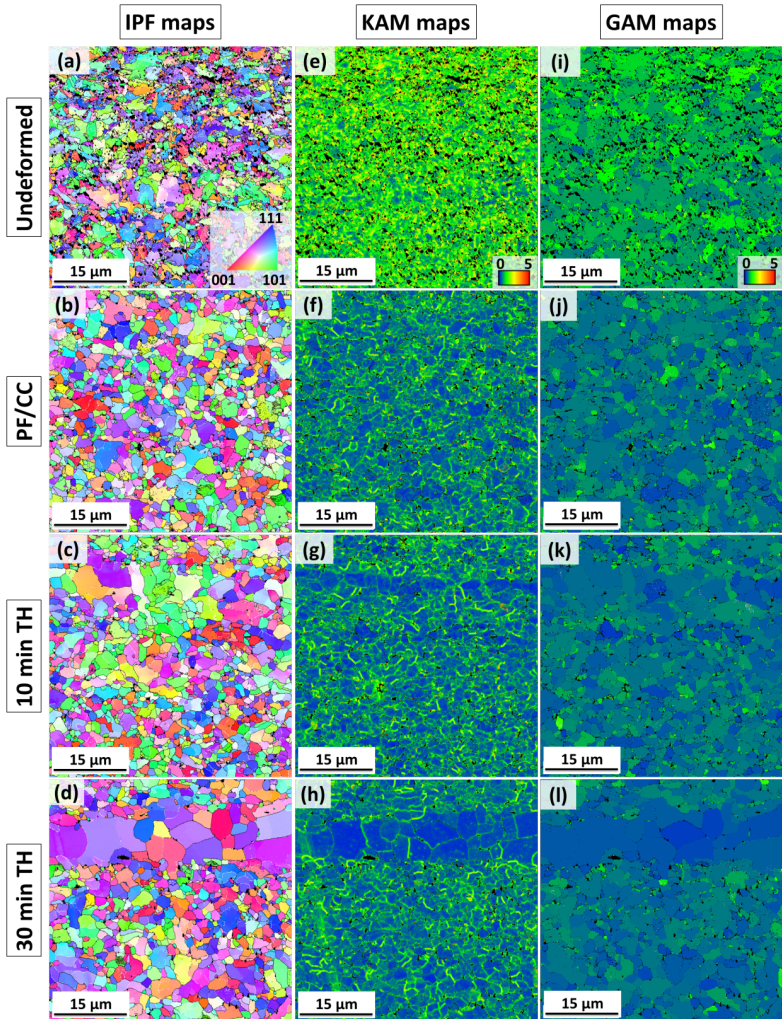
Figure 4.55: IPF (a-d), KAM (e-h) and GAM (i-l) maps obtained by analyzing EBSD scans that were taken before (undeformed) and after cyclic straining (PF/CC, 10 min TH and 30 min TH). PF/CC stands for pure fatigue/continuous cycling and TH for tensile hold waveform. Common color keys are provided for each type of maps.

ed with a prominent increment in their average size (Table. 4.12). For PF/CC tested specimen, the average grain size is 0.90 μm which is $\sim$ 55% larger than in the undeformed state. The CF tested specimens also manifest similar increment, however few regions exhibit relatively much coarser grains (see Fig. 4.55c-d). This in comparison to the PF/CC, led to a further increase in average grain size which is $\sim$ 4% and 16% higher for 10 and 30 min TH tested specimens, respectively. Since, undeformed microstructure has regions of inhomogeneous particles distribution, the localized excessive grain growth should have probably occurred in the nanoparticles deficient/free regions (see section 4.3.2). Moreover, as shown in section 4.3.2, the grain growth occurs at an expense of smaller grains, i.e. by consuming them.

Table 4.12: Average grain size (d_g) as well as LABs and HABs fractions measured before (undeformed) and after cyclic straining (PF/CC, 10 min TH and 30 min TH) via EBSD.

Condition	d_g (μm)	LABs fraction	HABs fraction
Undeformed	0.58	0.46	0.54
PF/CC	0.90	0.36	0.64
10 min TH	0.94	0.39	0.61
30 min TH	1.04	0.36	0.64

KAM and GAM are again used to visualize local misorientation changes. As mentioned earlier, undeformed state exhibits a homogeneous spread of relatively high KAM and GAM values (Fig. 4.55e and i), which implies the existence of high dislocation density and sub-grain structures, respectively. After cycling, as for PF/CC tested specimen, CF tested specimens also manifest a similar reduction in misorientation spread, with an appearance of blue color (depicting low orientation values) in both KAM and GAM maps (Fig. 4.55f-h and j-l). Hence, signifying a comparable reduction of dislocation density (see Fig. A.4b in appendix A.3) and elimination of original sub-grain structures (see section 4.3.2 for more). Similarly, as listed

in Table. 4.12, the estimated fraction of LABs decrease with a simultaneous increase in relative HABs fraction[10], which is comparable to the PF/CC tested specimen. Therefore, from EBSD studies it can be concluded that apart from an additional localized grain growth (that increases with an increase in hold-time duration), hold-time appears to have no further measurable influence in respect of dislocation density and sub-grain structure elimination.

TEM investigations

In order to differentiate microstructure evolution at even higher resolution, TEM investigations were carried out. However, under TEM, the microstructural evolution after testing under both PF/CC and TH waveforms appear similar which is hard to distinguish. And since these findings were already discussed in detail in section 4.3.2, only a brief discussion is presented here, while some of the selected TEM micrographs are documented in appendix A.6.

Similar to PF/CC, CF tested specimens under TEM revealed: (1) the rearrangement and/or annihilation of dislocations and (2) partial elimination of the original sub-grain structures (see appendix A.6). This altogether results in a reduction of overall dislocation density. In respect to the present precipitates, carbides are coarsened already after testing under PF/CC waveform (see Fig. 4.56) and no significant additional coarsening is observed even after introducing 30 min TH in PF/CC waveform. This suppressed time dependent coarsening is supposedly due to their W-enrichment (Fig. 4.4b) [16]. Furthermore, Cr-W enriched Laves phase precipitation was also already observed after PF/CC tests (see Fig. 4.33a). This is well known to exaggerate (their precipitation/coarsening) under CF loading [224] which could reduce solid solution strengthening. However, considering relatively short duration of these tests ($\sim$ 58 h for 30 min TH test), this effect can be

---

[10] In absolute sense, HABs fraction also decreased due to the coarsening of the grains.

neglected. Since, for short-time creep tests ($\leqslant 10,000$ h), W still contributes to the solid solution strengthening, even though Laves removes W from solution [85]. Moreover, during early stages of such tests, the precipitation hardening by Laves phase contributes to the strength, which subsequently decreases as a result of coarsening of the Laves phase particles [9]. Finally, the Y-Ti-O nanoparticles, as for all previous testing, appeared very stable without any change in shape or size.
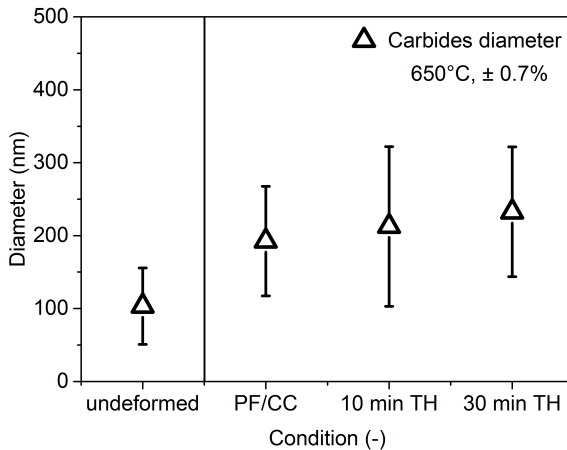
Figure 4.56: Changes in the carbides size before and after various loading conditions.

Hence, from the microstructural investigations it can be concluded that apart from additional grains coarsening, in the areas of inhomogeneous percipitates/particles distribution, no substantial microstructural differences were identified upon introducing tensile hold-time of up to 30 min.

4.4.3 Inelastic strain's relevance in reducing CF life

From Table. 4.11, it is apparent that TH introduction in PF/CC waveform leads to a reduction in cyclic life. And as already seen in section 4.3.1, ine-

lastic strain dictates the cyclic life in LCF regime ($N_f < 10^4$). This was validated by fitting PF/CC inelastic strain-life data linearly with Coffin-Manson equation (see Fig. 4.57 and section 4.3.1 for more). To further explore the influence of inelastic strain on CF life, inelastic strain-life data from CF tests were also added, see Fig. 4.57. It is apparent from the plot that, in comparison to PF/CC, TH introduction induces slighty larger inelastic strain and, results in a premature failure. This amplifies further with increase in hold-time duration. Nonetheless, all TH data points deviate from the PF/CC inelastic strain-life line. This suggests that the increment in inelastic strain is not the only liable rationale for the reduction of CF life. Howbeit, this is not surprising, since Coffin-Manson relation only accounts for phenomena, such as microstructure evolution and partly fatigue damage (generation of extrusions and intrusions i.e. preliminary stage of micro-crack formation), which are dictated by inelastic strain [224]. Whereas, additional time, temperature and stress dependent effects such as environment interactions, creep damage, and partly fatigue damage (crack propagation) are left unaccounted which could explain the deviation observed for TH inelastic strain-life data [224]. These issues will be presented and discussed in the next subsection.

4.4.4 Damage characteristics

To uncover reasons for specimens premature failure under TH waveforms, detailed investigations on their surfaces, cross-sections and fracture surfaces were carried out. The obtained results including crack initiation and its propagation mechanisms are compared with those observed for PF/CC tested specimen.

Under both PF/CC and TH waveforms, cracks initiate at the early stage of the tests and in similar fashion. For example, as reported earlier in section 4.3.3, interrupted PF/CC tested specimen manifests fatigue cracks
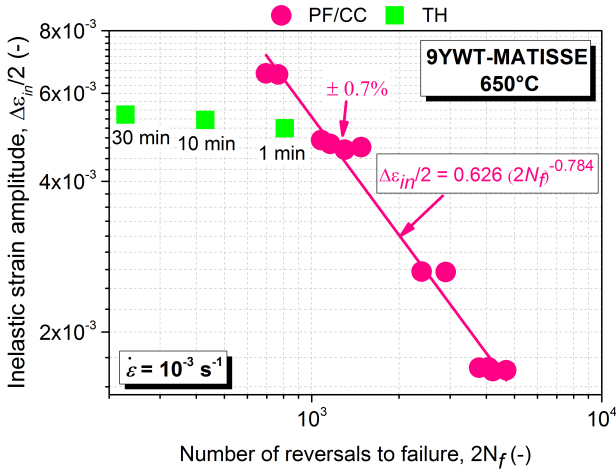
Figure 4.57: Double-logarithmic plot of the inelastic strain amplitude versus number of reversals to failure at 650 °C for PF/CC, data were fitted linearly with Coffin-Manson equation [214, 215], and for CF loading under $\pm 0.7\%$ strain amplitude.

even before $\sim 10\%$ of its original cyclic life. Moreover, micro-cracks initiate at deformation induced surface damage (probably extrusions and intrusions), for e.g. as shown for specimen tested under 1 min TH waveform in Fig. 4.58a. Nevertheless, this was expected since at least similar dislocation based deformation mechanisms are active under both PF/CC and TH waveforms. Independently, as mentioned earlier, secondary phase particles (oxides/carbides/large inclusions [45]), microstructural defects (pores/voids [46]) and fabrication induced surface imperfections can also act as the preferred crack initiation sites.

However, environmental effects cannot be underestimated, as already under PF/CC, both crack initiation as well as its propagation was assisted by oxidation (see section 4.3.3). Moreover, due to comparatively longer high-temperature exposure, the extent of oxidation obviously increased upon in-
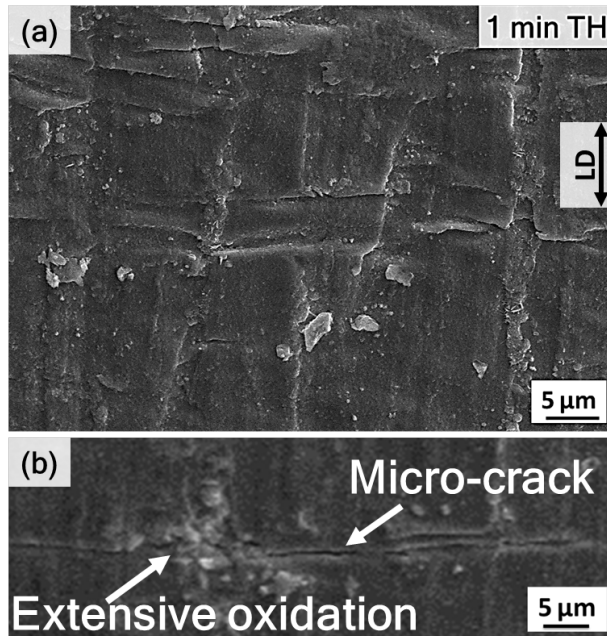
Figure 4.58: SEM micrograph taken from the surface of specimen tested under 1 min TH waveform shows (a) deformation induced surface damage covered in oxides and (b) micro-crack which nucleated from surface damage covered with oxides. LD stands for loading direction.

troducing TH which could further facilitate crack initiation owing to its brittleness and poor tensile strength (Fig. 4.58b) [232]. This is supposed to intensify even further with increase in TH duration. And as shown in Fig. 4.59, the resulting surface oxide layer is extensively damaged due to its local and repeated cracking under hold-time waveform [230, 240]. This successive micro-cracking annihilates the protective action of the oxide layer and promotes oxygen transport/ingress to the freshly exposed metallic surface [241]. The resulting oxidation, in and around the proximity of crack advancing front (e.g. Fig. 4.40), is known to reduce crack propagation thres-

hold [232]. Therefore, an accelerated oxidation kinetics under TH waveforms [230, 240, 241] further expedites damage evolution [231].
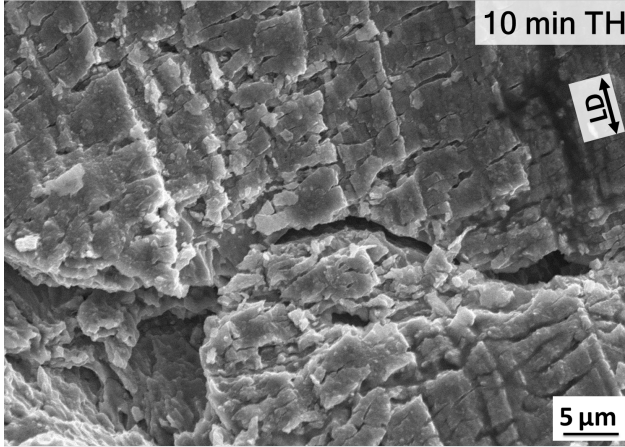
Figure 4.59: SEM micrograph taken from the surface of specimen tested under 10 min TH waveform, showing highly cracked/damaged oxide layer. LD stands for loading direction.

In addition, Laves is a brittle phase [242] and is generally accepted as being deleterious to the mechanical properties of an alloy [9]. It has been reported that Laves phase act as a preferred crack initiation and propagation site, resulting in reduced fatigue capability and accelerated fatigue crack growth rates [224, 243]. However, fracture surface investigations revealed no such Laves phase particles that underwent brittle fracture. Hence, reinforcing the fact that Laves phase particles, identified via TEM investigations (see Fig. 4.33a), have still not achieved their critical size to impose deleterious effect on the cyclic life, as recently reported for ferritic bimodal 12Cr-ODS steel [224]. Furthermore, the fracture surface investigations on 1 min TH tested specimen revealed almost similar fracture features as for PF/CC tested specimen (see Fig. 4.60 and section 4.3.3 for more). However, as reported later, this is only observed for short hold durations where creep phenomena are insignificant.
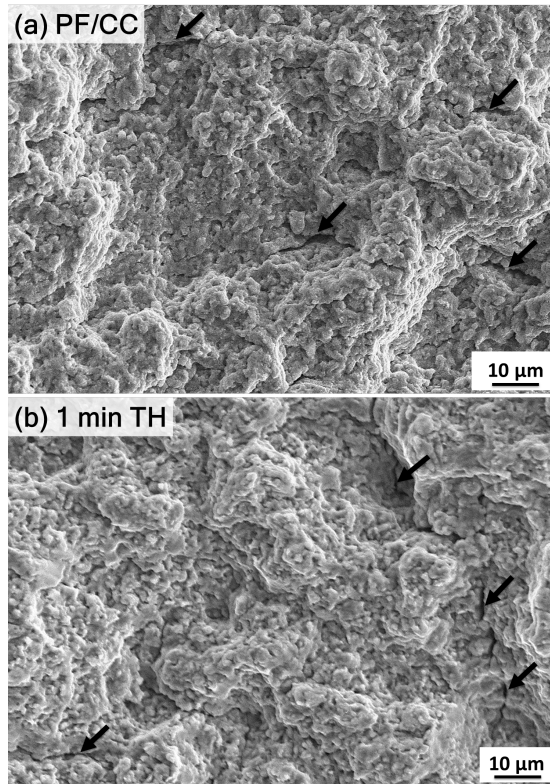
Figure 4.60: SEM micrographs taken from the stable crack-growth region of the fractured specimens that were tested under PF/CC (a) and 1 min TH (b) waveforms. Black arrows mark secondary cracking along the longitudinal direction.

Furthermore, even though multiple surface-initiated cracks propagated and coalesced under higher strain amplitude ($\pm$ 0.7%) PF/CC test, a comparatively higher surface-crack density was observed under TH waveforms. SEM micrographs taken from the longitudinally-sectioned specimen after testing under 30 min TH waveform are shown in Fig. 4.61 and Fig. 4.62. Here, along with the main surface-initiated macro-crack which resulted in failure (Fig. 4.61a), numerous surface-initiated micro-cracks are also evident that
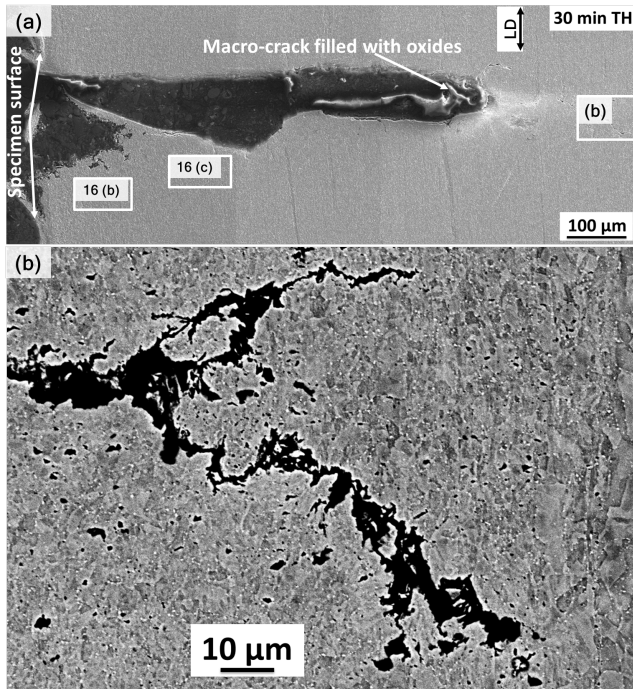
Figure 4.61: SEM micrographs taken from the longitudinally sectioned specimen, tested under 30 min TH waveform, present main surface initiated macro-crack filled with oxides (a) and its enlarged crack-tip area showing its preferential path (b). LD stands for loading direction.

are filled with oxides (Fig. 4.62a). The magnified crack's tip section suggests preferential nature of its path which was identified to be mainly along grain boundaries and appears to be aided by cavitation (Fig. 4.61b). Moreover, IPF maps (Fig. 4.63) acquired from such area also confirm that crack propagated mostly in an intergranular manner. Furthermore, high magnification micrographs from the selected area near specimen's surface unveil the presence of high density of cavities (Fig. 4.62a). These cavities were identified to have nucleated heterogeneously at triple point and/or

precipitate-boundary junction (see Fig. 4.62b and marked cavities beside bright precipitates in the inset) during creep portion (TH) of the cycle.

Nonetheless, these cavities can also form during the tensile portion of the PF/CC cycle, but are healed/sintered during the compressive portion [240]. Indeed, PF/CC tested 9YWT-MATISSE specimen revealed no such cavities. However, under unbalanced loading (i.e. tests with either lower tensile strain rate than the compressive strain rate or TH introduced in the PF/CC waveform); such cavities, as seen here, are not completely healed during compression.

Min and Raj proposed that under the influence of tensile stress, vacancies cluster together to nucleate cavities heterogeneously at the junction of grain boundaries and second phase particles [244, 245]. Nonetheless, there exist a free energy barrier and an incubation time to form vacancy
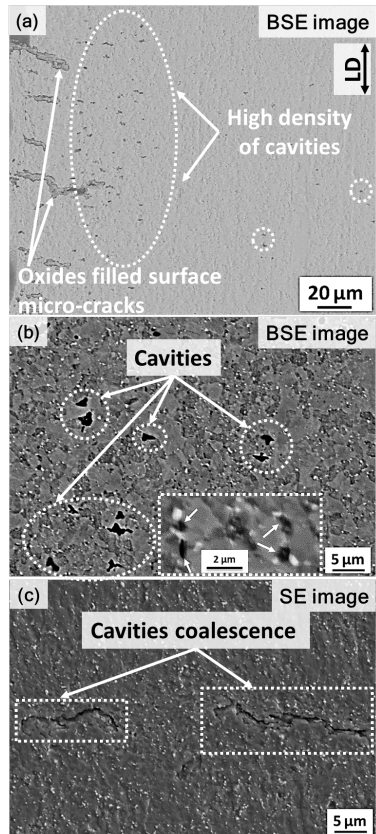
Figure 4.62: SEM micrographs taken from longitudinally sectioned specimen tested under 30 min TH waveform. (a) Presents surface initiated micro-cracks that are filled with oxides and encircled region exhibiting high density of cavities. Enlarged views from Fig. 4.61 show (b) cavities nucleation at triple point and/or precipitate-boundary interface and (c) cavities coalescence to form micro-cracks. BSE, SE and LD stand for back scattered electron, secondary electron and loading direction, respectively.

cluster of critical size which is stable. And since grain boundaries provide short-circuit diffusion networks, they reduce the incubation time for developing a vacancy cluster of critical size. Furthermore, grain boundary sliding (GBS) as well as migration (GBM) can also increase the probability of cavities nucleation at precipitates (again by decreasing the incubation time for nucleation by several orders of magnitude), if GBS/GBM produces a tensile stress (stress concentration) at the precipitate-matrix interface which is higher than the applied stress [244]. And since, in 9YWT-MATISSE, grain coarsening eventuates through GBM, the local stresses can become larger than the yield stress as a result of the stress concentration, which can lead to the cavities nucleation and their volume can increase by localized plastic flow at the precipitates or by diffusion [245].
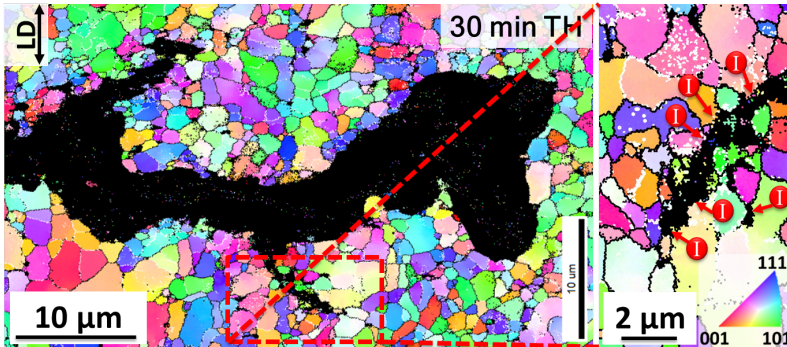
Figure 4.63: IPF maps revealing micro-crack path in the specimen tested under 30 min TH waveform. The magnified section shows marked regions where crack propagated in an intergranular (I) manner. LD stands for loading direction.

In literature, such cavities were also observed before for conventional non-ODS F/M steels, for e.g. mod. 9Cr-1Mo [246, 247], however tested at lower temperature (550 °C) and upon introducing longer hold-times (60 min and more) at lower peak tensile strain of 0.25% and 0.5%. Hence, in comparison to non-ODS F/M steels, the creep cavities in 9YWT-MATISSE developed

earlier, i.e. under short hold-time duration. Nevertheless, it is noteworthy that the 9YWT-MATISSE is tested at 100 °C higher temperature (considering both its application temperature range and observed impressive cyclic properties [149]). And therefore, if not plastic flow (due to ODS), the diffusion governed phenomena are obviously accelerated. This not only reduces the incubation time for cavity nucleation but also lower the threshold for cavities growth [244]. These cavities could not only assist intergranular crack initiation but also due to their growth/coalescence under tensile stresses provide a bridging link for accelerated crack propagation (Fig. 4.62c). Here, the cavities as well as the micro-cracks formed due to their long-range coalescence inside the material will join the surface cracks. And final fracture then occurs by a relatively rapid propagation of one of the long surface cracks (the main crack).

Hence, from damage studies it can be concluded that both environment (causing oxidation assisted damage) as well as creep (causing intergranular damage) interaction with fatigue are responsible for the reduction in cyclic life of the CF tested 9YWT-MATISSE specimens.

4.4.5 Summary and conclusions

Creep-fatigue interaction was studied at 650 °C by introducing hold-time of up to 30 min at peak tensile strain of 0.7%. The following conclusions can be drawn from the present investigation:

1. Due to stress relaxation during hold-time, elastic strain gets partially converted into inelastic strain. This additional increment in tensile inelastic strain results in a drop in tensile peak stresses with almost unaffected compressive peak stresses. Hence, symmetrical loops under PF/CC became asymmetrical upon introducing hold-time at peak tensile strain.

2. For the investigated hold-time durations, the increase in hold-time period had a negligible effect on peak stresses even though the higher amount of stress relaxation ensued. This saturation in softening is probably due to the presence of highly stable Y-Ti-O nanoparticles in the matrix which act as persistent barrier for dislocation motion.

3. In respect to lifetime, hold-time introduction results in its reduction. Moreover, the longer the hold-time the lower is the cyclic life which drops almost linearly.

4. EBSD complemented by TEM investigations were performed to delineate microstructural evolution. In general, PF/CC resulted in: (1) rearrangement and/or annihilation of dislocations, (2) partial elimination of the original sub-grain structures, (3) grain growth, (4) $M_{23}C_6$ carbides coarsening and (5) Cr-W enriched Laves phase precipitation. However, apart from additional localized grains coarsening, in the areas of inhomogeneous percipitates/particles distribution, no other substantial microstructural changes were identified upon introducing tensile hold-time.

5. Damage studies were carried out to uncover reasons for specimens premature failure under TH waveforms. These investigations led to two important conclusions. Firstly, due to their comparatively longer high-temperature exposure, the extent of oxidation increased upon introducing TH, which expedites damage evolution in terms of both crack initiation as well as its propagation. Secondly, TH induced intergranular damage in the form of creep cavities not only provide additional crack initiation sites but their growth/coalescence under tensile stresses act as a bridging link for accelerated crack propagation. Hence, the effect of hold-times is primarily due to (1) oxidation-fatigue interaction and (2) creep-fatigue interaction.

5 Summary & Conclusion

5.1 Summary

Within the framework of this work, a tempered martensitic (TM) Fe-9%Cr based ODS steel (9YWT-MATISSE) has been investigated. The main focus of this work is to understand its various active deformation and damage mechanisms under monotonic as well as cyclic loading conditions. However, prior to that, thorough microstructural characterization in its undeformed state was carried out (see section 4.1). Owning to its similar composition and heat treatment, the general microstructure of TM 9YWT-MATISSE is comparable to that of the creep resistant steels like P91 and EUROFER97. The developed microstructure typically consists of a high density of hierarchically organized internal structures with prior austenitic grains subdivided into packets of blocks of laths and sub-grains having high dislocation density. Coarse non-regular $M_{23}C_6$ carbides decorate different boundaries and are rich in Fe, Cr, and W. However, the main difference is in respect to the finer dispersoids. The carbonitrides of conventional F/M non-ODS steels are replaced by the highly stable and comparatively finer nano-oxides in 9YWT-MATISSE.

For understanding monotonic behavior, tensile tests were performed in the temperature range of room temperature (RT) to 800 °C at the nominal strain rates of 10^{-3} s^{-1} and 10^{-4} s^{-1} (see section 4.2). In order to verify the influence of heat treatment the obtained results are compared with that of the ferritic (F) state (which comparatively have larger grains and lower dis-

location density). In both states, steel displays similar decreasing trends of strength as temperature increases. However, the improvement of strength due to heat treatment is evident at RT. The strain rate at RT has no influence with respect to strength and strain hardening. Interestingly, at elevated temperatures both states present similar values of strength and elongation. The total elongation-to-failure for both states increases with increase in testing temperature until a peak is reached. Moreover, elongation is also a function of strain rate. TEM investigations on specimens taken from fractured TM state samples revealed a modification of deformation mechanism with temperature. The dislocation activity that was homogeneously distributed at RT was localized close to grain boundaries at elevated temperatures. Nevertheless, a strong particle-dislocation interaction was observed at all testing temperatures. Orowan/repulsive mechanism is supposed to govern particle-dislocation interaction at moderate temperatures. At elevated temperatures, an attractive particle-dislocation interaction phenomenon called interfacial pinning was identified. This ultimately suppressed annihilation processes and reduced microstructural degradation in comparison to that observed in similar non-ODS steels. Although reduced, the still perceived microstructural evolution that includes reduced dislocation density and partial lath/sub-grain structures elimination mostly in the particle deficient regions and $M_{23}C_6$ carbides coarsening, resulted in a loss of strength at elevated temperatures. Fracture surface investigations revealed a change in damage mechanism from intragranular fracture at moderate temperatures to intergranular fracture at elevated temperatures where it is associated with a reduced ductility. This change in damage mechanism is due to the modification of the deformation mechanism. The comparison of various estimated strengthening contributors reveals that particle strengthening, dislocation forest strengthening, and Hall-Petch strengthening are the major contributions and their mixed Pythagorean superposition rule reproduces the measured RT yield stress within experimental scatter for the whole extended set of selected alloys. Finally, it is confirmed that due to the presence

of the highly stable nano-oxide particles, TM 9YWT-MATISSE offers superior strength over similar non-ODS F/M steels e.g. EUROFER97 and P91. Furthermore, in comparison to other commercial, as well as experimental, ODS steels, TM 9YWT-MATISSE offers an excellent compromise between strength and ductility. However, the specific characteristics of dislocation structure and boundaries obtained by phase transformation in F/M 9YWT-MATISSE is less efficient than those achieved by mechanical deformation (hot rolling or forging) in ferritic ODS steels.

For application, the LCF behavior of ODS steels is of decisive importance. Therefore, fully reversed strain-controlled cyclic tests were performed in air at 550 °C and 650 °C under different strain amplitudes (see section 4.3). Under all conditions, the steel manifests transitional stages, i.e. cyclic softening and/or hardening corresponding to a small fraction of the cyclic life, which is followed by a linear cyclic softening stage that occupies the major fraction of the cyclic life until failure. Both applied strain amplitude and test temperature show a strong influence on the cyclic stress response. It is found, that the degree of linear cyclic softening decreases with decrease in imposed mechanical strain amplitude and increase in testing temperature. The effect of temperature on inelastic strain; and hence, lifetime becomes more pronounced with decreasing applied strain amplitude. EBSD complemented by TEM investigations were performed to delineate microstructural evolution after cyclic straining. Microstructural evolution at 550 °C mainly includes dislocations rearrangement and/or annihilation which finally result in their reduced density. At 650 °C, microstructural evolution hastens and becomes prominent mainly in nano-oxides/carbides deficient regions. Here, in addition to the reduced dislocation density, partially eliminated original sub-grain structures, grain growth, $M_{23}C_6$ carbides coarsening and occasional Cr-W enriched Laves phase precipitation were observed. The microstructural modifications, concerning dislocation density and sub-grain structures, intensify also with increase in applied strain amplitude. Ne-

vertheless, annealing at 650 °C for similar duration has no major influence on the microstructure. Damage studies revealed an expeditious as well as pronounced fatigue cracking with increase in applied strain amplitude. However, fatigue cracks nucleate at an early stage of the test which is prior to $\sim 10\%$ of original fatigue life. The crack's initiation as well as its propagation is further assisted by oxidation. On fracture surface, the stable crack growth region manifests secondary cracks, and at higher magnification, the classical fine-scale transgranular ductile fracture features called striations. In addition, at 650 °C, crack path also acquires an intergranular tendency under higher strain amplitude. Besides higher peak stresses and thus lower inelastic strain amplitudes, oxides dispersion in 9YWT-MATISSE assists in mitigating undesirable cyclic softening observed in conventional non-ODS F/M steels. This is due to fact that highly stable nano-sized oxide particles act as persistent barriers for dislocation motion which consequently reduce/slows-down typical microstructural degradation. However, cyclic straining assisted by thermal activation as well as inhomogeneous nanoparticles distribution result in similar microstructural changes as those observed in non-ODS matrix steels, but to a lesser extent. Moreover, the studied ODS steel at 650 °C manifests comparable cyclic strength and lifetime to tested non-ODS F/M steels at 550 °C. Hence, concerning LCF, oxide dispersion raises the limited operating temperature of conventional non-ODS F/M steels by about 100 °C. Finally, the obtained results depict that 9YWT-MATISSE offers higher number of cycles to failure at 650 °C, compared to other novel ODS steels described in literature.

Testing includes creep-fatigue (CF) investigations at 650 °C by introducing hold-time of up to 30 min at peak tensile strain of 0.7% (see section 4.4). Such a hold period simulates the loading of a component under stationary operation. Due to stress relaxation during hold-time, elastic strain gets partially converted into inelastic strain and the symmetrical loops under pure fatigue/continuous cycling (PF/CC) became asymmetrical. Moreover, this

also resulted in a reduction of cyclic life. However, for the investigated hold-time durations, the increase in tensile hold (TH) period had a negligible effect on peak stresses, but a further reduction in lifetime. EBSD and TEM were used to compare microstructural evolution under both PF/CC and TH waveforms. In general, TH waveforms results in a similar microstructural modifications as for PF/CC waveform. However, in addition to this, further localized grains coarsening, in the areas of inhomogeneous precipitates/particles distribution, was identified upon introducing TH-time. To uncover reasons for specimens premature failure under TH waveforms, detailed investigations on their surfaces, cross-sections and fracture surfaces were carried out. These investigations led to two important conclusions. Firstly, due to comparatively longer high-temperature exposure, the extent of oxidation increased upon introducing TH which expedited damage progression. Secondly, TH induced intergranular damage in the form of creep cavities does not only provide additional crack initiation sites but also their growth/coalescence under tensile stresses act as a bridging link for accelerated crack propagation. These two findings are associated with a reduction of cyclic life due to introduction of hold-time. Hence, the effect of hold-times is primarily due to (1) oxidation-fatigue interaction and (2) creep-fatigue interaction.

5.2 Conclusion

From the overall investigations it can be concluded that due to oxide particles strengthening, ODS 9YWT-MATISSE in comparison to non-ODS F/M steels offers higher tensile strength, higher cyclic strength and moderate cyclic softening. Moreover, due to its optimized chemical composition and manufacturing route, ODS 9YWT-MATISSE offers excellent compromise between strength and ductility. This in comparison to its non-ODS counterparts leads to a comparable PF/CC life under higher strain amplitudes which became even far superior under lower strain amplitudes. Additionally, when

compared with other novel ODS steels, 9YWT-MATISSE exhibits highest PF/CC life at 650 °C. Hence, in respect to PF/CC, oxide dispersion raises the limited operating temperature of conventional F/M steels by about 100 °C. However, as microstructural evolution is mainly observed in nanoparticles/carbides deficient regions, their both uniform distribution as well as lower inter-particle spacing is critical for suppressing the annihilation processes and stabilizing microstructure further.

In respect to the CF, TH-time introduction in PF/CC waveform, results in additional asymmetric tensile softening which, in contrast to the non-ODS steels, is independent of the applied hold-time duration. This is probably due to the presence of highly stable Y-Ti-O nanoparticles which act as a persistent barrier for dislocation motion. However, despite of all this, no advantage in terms of cyclic life is observed. Moreover, the longer the hold-time the lower is the cyclic life which drops almost linearly. This is due to combined creep-fatigue-oxidation interaction, since under CF condition extensive oxidation as well as creep cavities nucleation and their coalescence is observed, which ultimately accelerates damage evolution. Therefore, to avail ODS benefits to the maximum; at least creep cavities formation and their coalescence must be suppressed (for F/M ODS steels at 650 °C). One of the basic ideas can be by adding certain alloying elements which either reduce the diffusivity of vacancies in grain boundary (for e.g. microalloying Boron (especially [11]B isotope, as these steels are intended for nuclear application [9, 248, 249]) and Zirconium) that increases the incubation time for cavity nucleation [244] or heal creep cavities by precipitating on their surface (for e.g. [11]B and Nitrogen which forms BN) as it is already shown in literature for conventional austenitic steels [250].

6 Outlook

In addition to this work, further investigations of the following aspects are proposed:

1. As in this study all cyclic tests were carried out at only one strain rate (10^{-3} s^{-1}), further investigations by varying strain rate are proposed to understand its influence on cyclic behavior.

2. In order to gain deeper understanding of the deformation mechanisms, such as observed grain growth upon high-temperature cyclic straining, in situ investigations using both EBSD as well as TEM will be beneficial. These examinations can provide further insight into: (1) the driving forces for mechanisms such as grain boundaries migration, (2) if any, grain size and orientation as well as boundary-character based preferential mechanisms, (3) dislocation sources and sinks, (4) dynamic dislocation-particles interactions etc. These investigations can then be used to tailor ODS steels for their further improvements.

3. To separate out the influence of damage progression on cyclic stress response, interrupted tests need to be performed.

4. Under creep-fatigue condition, further investigations are required in order to obtain supplementary information about the influence of hold-time with respect to: (1) strain amplitude, (2) strain rate, (3) its position and (4) duration. Additionally, CF testing on ODS steels having different matrix (austenitic and ferritic) as well as varying microstructural features (e.g. grain size) will definitely be useful.

Bibliography

[1] S. J. Zinkle and J. T. Busby. Structural materials for fission & fusion energy. *Mater. Today*, 12(11):12–19, nov 2009.

[2] E. Gaganidze and J. Aktaa. Assessment of neutron irradiation effects on RAFM steels. *Fusion Eng. Des.*, 88(3):118–128, mar 2013.

[3] H. Schroeder and H. Ullmaier. Helium and hydrogen effects on the embrittlement of iron- and nickel-based alloys. *J. Nucl. Mater.*, 179-181:118–124, 1991.

[4] S. J. Zinkle. Fusion materials science: Overview of challenges and recent progress. *Phys. Plasmas*, 12(5):058101, 2005.

[5] G. R. Odette, M. J. Alinger, and B. D. Wirth. Recent Developments in Irradiation-Resistant Steels. *Annu. Rev. Mater. Res.*, 38(1):471–503, aug 2008.

[6] S. N. Rosenwasser, P. Miller, J. A. Dalessandro, J. M. Rawls, W. E. Toffolo, and W. Chen. The application of martensitic stainless steels in long lifetime fusion first wall/blankets. *J. Nucl. Mater.*, 85 & 86(1):177–182, 1979.

[7] D. R. Harries. Ferritic/martensitic steels for use in near-term and commercial fusion reactors. In *Proc. Top. Conf. Ferritic Alloy. Use Nucl. Energy Technol.*, pages 141–155. Metallurgical Society of AIME,Warrendale, PA, USA, 1984.

[8] G. J. Butterworth and O. N. Jarvis. Comparison of transmutation and activation effects in five ferritic alloys and AISI 316 stainless steel in a fusion neutron spectrum. *J. Nucl. Mater.*, 122 & 123:982–988, 1984.

[9] R. L. Klueh and D. R. Harries. *High-Chromium Ferritic and Martensitic Steels for Nuclear Applications*. ASTM International, West Conshohocken, PA 19428-2959, jan 2001.

[10] R. L. Klueh and E. E. Bloom. The development of ferritic steels for fast induced-radioactivity decay for fusion reactor applications. *Nucl. Eng. Des. Fusion*, 2(3):383–389, 1985.

[11] D. Dulieu, K. W. Tupholme, and G. J. Butterworth. Development of Low-Activation Stainless. *J. Nucl. Mater.*, 141-143:1097–1101, 1986.

[12] M. Tamura, H. Hayakawa, M. Tanimura, A. Hishinuma, and T. Kondo. Development of potential low activation ferritic and austenitic steels. *J. Nucl. Mater.*, 141-143:1067–1073, 1986.

[13] T. Noda, F. Abe, H. Araki, and M. Okada. Development of low activation Ferritic steels. *J. Nucl. Mater.*, 141-143:1102–1106, 1986.

[14] R. L. Klueh, D. S. Gelles, and T. A. Lechtenberg. Development of ferritic steels for reduced activation: The US program. *J. Nucl. Mater.*, 141-143:1081–1087, 1986.

[15] S. Shikakura, S. Nomura, S. Ukai, I. Seshimo, Y. Kano, Y. Kuwajima, T. Ito, K. Tutaki, and T. Fujita. Development of High-Strength Ferritic/Martensitic Steel for FBR Core Materials. *J. At. Energy Soc. Japan*, 33(12):1157–1170, 1991.

[16] F. Abe. Precipitate design for creep strengthening of 9% Cr tempered martensitic steel for ultra-supercritical power plants. *Sci. Technol. Adv. Mater.*, 9(1):013002, mar 2008.

[17] P. Marmy and T. Kruml. Low cycle fatigue of Eurofer 97. *J. Nucl. Mater.*, 377(1):52–58, jun 2008.

[18] R. L. Klueh, D. S. Gelles, S. Jitsukawa, A. Kimura, G. R. Odette, B. Van Der. Schaaf, and M. Victoria. Ferritic / martensitic steels - overview of recent results. *J. Nucl. Mater.*, 307-311(2002):455–465, 2008.

[19] R. Lindau, A. Möslang, M. Rieth, M. Klimiankou, E. Materna-Morris, A. Alamo, A. A. F. Tavassoli, C. Cayron, A. M. Lancha, P. Fernandez, N. Baluc, R. Schäublin, E. Diegele, G. Filacchioni, J. W. Rensman, B. V. D. Schaaf, E. Lucon, and W. Dietz. Present development status of EUROFER and ODS-EUROFER for application in blanket concepts. *Fusion Eng. Des.*, 75-79:989–996, nov 2005.

[20] R. L. Klueh, K. Ehrlich, and F. Abe. Ferritic/martensitic steels: promises and problems. *J. Nucl. Mater.*, 191-194(1992):116–124, sep 1992.

[21] M. Inoue, T. Kaito, and S. Ohtsuka. *Research and Development of Oxide Dispersion Strengthened Ferritic Steels for Sodium Cooled Fast Breeder Reactor Fuels.* Springer Netherlands, Dordrecht, 2008.

[22] S. Kim and J. R. Weertman. Investigation of microstructural changes in a ferritic steel caused by high temperature fatigue. *Metall. Trans. A*, 19(4):999–1007, apr 1988.

[23] J. F. Stubbins and D. S. Gelles. Fatigue performance and cyclic softening of F82H, a ferritic-martensitic steel. *J. Nucl. Mater.*, 233-237:331–335, 1996.

[24] M. F. Maday. Comparison of the low cycle fatigue behaviour of F82H mod. and Eurofer 97 in water coolant. *Fusion Eng. Des.*, 61-62:665–670, nov 2002.

[25] J. Aktaa and R. Schmitt. High temperature deformation and damage behavior of RAFM steels under low cycle fatigue loading: Experiments and modeling. *Fusion Eng. Des.*, 81(19):2221–2231, sep 2006.

[26] B. Fournier, F. Dalle, M. Sauzay, J. Longour, M. Salvi, C. Caës, I. Tournié, P.F. Giroux, and S.-H. Kim. Comparison of various 9-12%Cr steels under fatigue and creep-fatigue loadings at high temperature. *Mater. Sci. Eng. A*, 528(22-23):6934–6945, aug 2011.

[27] A. A. Saad, W. Sun, T. H. Hyde, and D. W. J. Tanner. Cyclic softening behaviour of a P91 steel under low cycle fatigue at high temperature. *Procedia Eng.*, 10:1103–1108, jan 2011.

[28] A. F. Armas, C. Petersen, R. Schmitt, M. Avalos, and I. Alvarez-Armas. Mechanical and microstructural behaviour of isothermally and thermally fatigued ferritic/martensitic steels. *J. Nucl. Mater.*, 307-311(1 SUPPL.):509–513, 2002.

[29] M. Walter. Private communication. Technical report, Karlsruhe Institute of Technology, 2017.

[30] I. Kuběna, J. Polák, P. Marmy, and T. Kruml. A Comparison of Microstructure Evolution due to Fatigue Loading in Eurofer 97 and ODS Eurofer Steels. *Procedia Eng.*, 74:401–404, 2014.

[31] J. J. Huet. Preparation and Properties of oxide dispersion-strengthened ferritic alloys. *Met. Powder Rep.*, 40:155–158, 1985.

[32] S. Ukai, M. Harada, H. Okada, M. Inoue, S. Nomura, S. Shikakura, K. Asabe, T. Nishida, and M. Fujiwara. Alloying design of oxide dis-

persion strengthened ferritic steel for long life FBRs core materials. *J. Nucl. Mater.*, 204:65–73, 1993.

[33] D. K. Mukhopadhyay, F. H. Froes, and D. S. Gelles. Development of oxide dispersion strengthened ferritic steels for fusion. *J. Nucl. Mater.*, 258-263:1209–1215, oct 1998.

[34] R. Lindau, A. Möslang, M. Schirra, P. Schlossmacher, and M. Klimenkov. Mechanical and microstructural properties of a hipped RAFM ODS-steel. *J. Nucl. Mater.*, 307-311:769–772, dec 2002.

[35] R. L. Klueh, J. P. Shingledecker, R. W. Swindeman, and D. T. Hoelzer. Oxide dispersion-strengthened steels: A comparison of some commercial and experimental alloys. *J. Nucl. Mater.*, 341(2-3):103–114, may 2005.

[36] J. Malaplate, F. Mompiou, J. L. Béchade, T. Van Den Berghe, and M. Ratti. Creep behavior of ODS materials: A study of dislocations/precipitates interactions. *J. Nucl. Mater.*, 417(1-3):205–208, oct 2011.

[37] B. Fournier, A. Steckmeyer, A. L. Rouffie, J. Malaplate, J. Garnier, M. Ratti, P. Wident, L. Ziolek, I. Tournie, V. Rabeau, J. M. Gentzbittel, T. Kruml, and I. Kubena. Mechanical behaviour of ferritic ODS steels-Temperature dependancy and anisotropy. *J. Nucl. Mater.*, 430(1-3):142–149, nov 2012.

[38] S. J. Zinkle and L. L. Snead. Designing Radiation Resistance in Materials for Fusion Energy. *Annu. Rev. Mater. Res.*, 44(1):241–267, jul 2014.

[39] P. Yvon and F. Carré. Structural materials challenges for advanced reactor systems. *J. Nucl. Mater.*, 385(2):217–222, mar 2009.

[40] L. Tan, L. L. Snead, and Y. Katoh. Development of new generation reduced activation ferritic-martensitic steels for advanced fusion reactors. *J. Nucl. Mater.*, 478:42–49, sep 2016.

[41] V. Banhardt, M. Nader, and E. Arzt. High-temperature low-cycle fatigue of an iron-base oxide-dispersion strengthened alloy: Grain structure effects and lifetime correlations. *Metall. Mater. Trans. A*, 26(5):1067–1077, may 1995.

[42] S. Ukai and S. Ohtsuka. Low cycle fatigue properties of ODS ferritic-martensitic steels at high temperature. *J. Nucl. Mater.*, 367-370:234–238, aug 2007.

[43] I. Kuběna, T. Kruml, P. Spätig, N. Baluc, Z. Oksiuta, M. Petrenec, K. Obrtlík, and J. Polák. Fatigue behaviour of ODS ferritic-martensitic Eurofer steel. *Procedia Eng.*, 2(1):717–724, apr 2010.

[44] I. Kuběna, T. Kruml, B. Fournier, and J. Polák. Low Cycle Fatigue Behaviour of ODS Steels for Nuclear Application. *Key Eng. Mater.*, 465:556–559, jan 2011.

[45] I. Kuběna, B. Fournier, and T. Kruml. Effect of microstructure on low cycle fatigue properties of ODS steels. *J. Nucl. Mater.*, 424(1-3):101–108, may 2012.

[46] I. Kubena and T. Kruml. Fatigue life and microstructure of ODS steels. *Eng. Fract. Mech.*, 103:39–47, may 2013.

[47] P. He, M. Klimenkov, A. Möslang, R. Lindau, and H. J. Seifert. Correlation of microstructure and low cycle fatigue properties for 13.5Cr1.1W0.3Ti ODS steel. *J. Nucl. Mater.*, 455(1-3):167–173, dec 2014.

[48] M. Bruchhausen, K. Turba, F. de Haan, P. Hähner, T. Austin, and Y. de Carlan. Characterization of a 14Cr ODS steel by means of

small punch and uniaxial testing with regard to creep and fatigue at elevated temperatures. *J. Nucl. Mater.*, 444(1-3):283–291, jan 2014.

[49] I. Kuběna, J. Polák, T. P. Plocinski, C. Hébert, V. Škorík, and T. Kruml. Microstructural stability of ODS steels in cyclic loading. *Fatigue Fract. Eng. Mater. Struct.*, 38(8):936–947, aug 2015.

[50] I. Kuběna, T. Kruml, and J. Polák. Behaviour of ODS Steels in Cyclic Loading. *Trans. Indian Inst. Met.*, pages 1–5, jan 2016.

[51] A. Chauhan, D. Litvinov, and J. Aktaa. Deformation and damage mechanisms of a bimodal 12Cr-ODS steel under high-temperature cyclic loading. *Int. J. Fatigue*, 93(1):1–17, aug 2016.

[52] J. J. Huet. Possible fast-reactor canning material strengthened and stabilized by dispersion. *Powder Metall.*, 10(20):208–215, sep 1967.

[53] F. G. Wilson, B. R. Knott, and C. D. Desforges. Preparation and properties of some ODS Fe-Cr-Al alloys. *Metall. Trans. A*, 9(2):275–282, feb 1978.

[54] J. J. Fisher. Dispersion strengthened ferritic alloy for use in liquid-metal fast breeder reactors (LMFBRS). *US Pat. 4,075,010*, 1976.

[55] A. Chauhan, D. Litvinov, and J. Aktaa. High temperature tensile properties and fracture characteristics of bimodal 12Cr-ODS steel. *J. Nucl. Mater.*, 468:1–8, jan 2016.

[56] M. K. Miller, D. T. Hoelzer, E. A. Kenik, and K. F. Russell. Stability of ferritic MA/ODS alloys at high temperatures. *Intermetallics*, 13(3-4):387–392, mar 2005.

[57] S. J. Zinkle, J. L. Boutard, D. T. Hoelzer, A. Kimura, R. Lindau, G. R. Odette, M. Rieth, L. Tan, and H. Tanigawa. Development of next generation tempered and ODS reduced activation ferritic/martensitic

steels for fusion energy applications. *Nucl. Fusion*, 57(9):092005, sep 2017.

[58] S. Ukai and M. Fujiwara. Perspective of ODS alloys application in nuclear environments. *J. Nucl. Mater.*, 307-311:749–757, dec 2002.

[59] Y. Xu, Z. Zhou, M. Li, and P. He. Fabrication and characterization of ODS austenitic steels. *J. Nucl. Mater.*, 417(1-3):283–285, oct 2011.

[60] T. Gräning, M. Rieth, J. Hoffmann, and A. Möslang. Production, microstructure and mechanical properties of two different austenitic ODS steels. *J. Nucl. Mater.*, 487:348–361, apr 2017.

[61] L Straßberger, A Chauhan, T Gräning, S Czink, and J Aktaa. High-temperature low-cycle fatigue behavior of novel austenitic ODS steels. *Int. J. Fatigue*, 93(1):194–200, dec 2016.

[62] C. Suryanarayana. Mechanical alloying and milling. *Prog. Mater. Sci.*, 46(1-2):1–184, jan 2001.

[63] M. S. El-Genk and J. M. Tournier. A review of refractory metal alloys and mechanically alloyed-oxide dispersion strengthened steels for space nuclear power systems. *J. Nucl. Mater.*, 340(1):93–112, apr 2005.

[64] F. Bergner, I. Hilger, J. Virta, J. Lagerbom, G. Gerbeth, S. Connolly, Z. Hong, P. S. Grant, and T. Weissgärber. Alternative Fabrication Routes toward Oxide-Dispersion-Strengthened Steels and Model Alloys. *Metall. Mater. Trans. A*, 47(11):5313–5324, nov 2016.

[65] M. Praud, F. Mompiou, J. Malaplate, D. Caillard, J. Garnier, A. Steckmeyer, and B. Fournier. Study of the deformation mechanisms in a Fe-14% Cr ODS alloy. *J. Nucl. Mater.*, 428(1-3):90–97, sep 2012.

[66] A. Steckmeyer, M. Praud, B. Fournier, J. Malaplate, J. Garnier, J. L. Béchade, I. Tournié, A. Tancray, A. Bougault, and P. Bonnaillie. Tensile properties and deformation mechanisms of a 14Cr ODS ferritic steel. *J. Nucl. Mater.*, 405(2):95–100, oct 2010.

[67] M. Dadé, J. Malaplate, J. Garnier, F. De Geuser, N. Lochet, and A. Deschamps. Influence of consolidation methods on the recrystallization kinetics of a Fe-14Cr based ODS steel. *J. Nucl. Mater.*, 472:143–152, apr 2016.

[68] J. Malaplate, M. Dadé, Y. de Carlan, F. Mompiou, D. Caillard, A. Chauhan, J. Aktaa, M. Hernández-Mayoral, E. Onorbe Esparraguera, and M. Serrano. Deformation mechanisms in ODS alloys: Recent highlights obtained within the MATISSE program. In *EUROMAT 2017*, Thessaloniki, Greece.

[69] A. Deschamps, F. de Geuser, J. Malaplate, and D. Sornin. When do oxide precipitates form during consolidation of oxide dispersion strengthened steels? *J. Nucl. Mater.*, 482:83–87, oct 2016.

[70] M. J. Alinger, G. R. Odette, and D. T. Hoelzer. On the role of alloy composition and processing parameters in nanocluster formation and dispersion strengthening in nanostuctured ferritic alloys. *Acta Mater.*, 57(2):392–406, jan 2009.

[71] P. Unifantowicz, Z. Oksiuta, P. Olier, Y. de Carlan, and N. Baluc. Microstructure and mechanical properties of an ODS RAF steel fabricated by hot extrusion or hot isostatic pressing. *Fusion Eng. Des.*, 86(9-11):2413–2416, oct 2011.

[72] Z. Oksiuta and N. Baluc. Optimization of the chemical composition and manufacturing route for ODS RAF steels for fusion reactor application. *Nucl. Fusion*, 49(5):055003, may 2009.

[73] T. Okuda and M. Fujiwara. Dispersion behaviour of oxide particles in mechanically alloyed ODS steel. *J. Mater. Sci. Lett.*, 14(22):1600–1603, 1995.

[74] M. A. Auger, V. de Castro, T. Leguey, M. A. Monge, A. Muñoz, and R. Pareja. Microstructure and tensile properties of oxide dispersion strengthened Fe-14Cr-0.3Y2O3 and Fe-14Cr-2W-0.3Ti-0.3Y2O3. *J. Nucl. Mater.*, 442(1-3):S142–S147, nov 2013.

[75] H. Okada, S. Ukai, and M. Inoue. Effects of Grain Morphology and Texture on High Temperature Deformation in Oxide Dispersion Strengthened Ferritic Steels. *J. Nucl. Sci. Technol.*, 33(12):936–943, dec 1996.

[76] M. Serrano, M. Hernández-Mayoral, and A. García-Junceda. Microstructural anisotropy effect on the mechanical properties of a 14Cr ODS steel. *J. Nucl. Mater.*, 428(1-3):103–109, sep 2012.

[77] R. Kasada, S. G. Lee, J. Isselin, J. H. Lee, T. Omura, A. Kimura, T. Okuda, M. Inoue, S. Ukai, S. Ohnuki, T. Fujisawa, and F. Abe. Anisotropy in tensile and ductile-brittle transition behavior of ODS ferritic steels. *J. Nucl. Mater.*, 417(1-3):180–184, oct 2011.

[78] M. Ratti. *Développement de nouvelles nuances d'aciers ferritiques-martensitiques pour le gainage d'éléments combustibles des réacteurs à neutrons rapides au sodium*. PhD thesis, Institut polytechnique de Grenoble, 2009.

[79] R. L. Klueh, P. J. Maiziasz, I. S. Kim, L. Heatherly, D. T. Hoelzer, N. Hashimoto, E. A. Kenik, and K. Miyahara. Tensile and creep properties of an oxide dispersion-strengthened ferritic steel. *J. Nucl. Mater.*, 307-311:773–777, 2002.

[80] M. A. Sokolov, D. T. Hoelzer, R. E. Stoller, and D. A. McClintock. Fracture toughness and tensile properties of nano-structured ferritic steel 12YWT. *J. Nucl. Mater.*, 367-370:213–216, aug 2007.

[81] D. A. McClintock, D. T. Hoelzer, M. A. Sokolov, and R. K. Nanstad. Mechanical properties of neutron irradiated nanostructured ferritic alloy 14YWT. *J. Nucl. Mater.*, 386-388:307–311, apr 2009.

[82] S. Ukai, T. Nishida, T. Okuda, and T. Yoshitake. R&D of oxide dispersion strengthened ferritic martensitic steels for FBR. *J. Nucl. Mater.*, 258-263:1745–1749, oct 1998.

[83] S. Ukai, T. Nishida, H. Okada, T. Okuda, M. Fujiwara, and K. Asabe. Development of Oxide Dispersion Strengthened Ferritic Steels for FBR Core Application, (I). *J. Nucl. Sci. Technol.*, 34(3):256–263, mar 1997.

[84] J. H. Schneibel, C. T. Liu, M. K. Miller, M. J. Mills, P. Sarosi, M. Heilmaier, and D. Sturm. Ultrafine-grained nanocluster-strengthened alloys with unusually high creep strength. *Scr. Mater.*, 61(8):793–796, oct 2009.

[85] R. L. Klueh. Elevated temperature ferritic and martensitic steels and their application to future nuclear reactors. *Int. Mater. Rev.*, 50(5):287–310, oct 2005.

[86] M. J. Alinger, G. R. Odette, and G. E. Lucas. Tensile and fracture toughness properties of MA957: Implications to the development of nanocomposited ferritic alloys. *J. Nucl. Mater.*, 307-311:484–489, 2002.

[87] R. L. Klueh, D. S. Gelles, M. Okada, and N. H. Packan. *Reduced Activation Materials for Fusion Reactors*. ASTM International, West Conshohocken, PA 19428-2959, jan 1990.

[88] S. Takaya, T. Furukawa, K. Aoto, G. Müller, A. Weisenburger, A. Heinzel, M. Inoue, T. Okuda, F. Abe, S. Ohnuki, T. Fujisawa, and A. Kimura. Corrosion behavior of Al-alloying high Cr-ODS steels in lead-bismuth eutectic. *J. Nucl. Mater.*, 386-388:507–510, apr 2009.

[89] S. Ukai, M. Harada, H. Okada, M. Inoue, S. Nomura, S. Shikakura, T. Nishida, M. Fujiwara, and K. Asabe. Tube manufacturing and mechanical properties of oxide dispersion strengthened ferritic steel. *J. Nucl. Mater.*, 204:74–80, 1993.

[90] T. R. Allen, J. T. Busby, R. L. Klueh, S. A. Maloy, and M. B. Toloczko. Cladding and Duct Materials for Advanced Nuclear Recycle Reactors. *JOM*, 60(1):15–23, 2008.

[91] M. K. Miller and R. G. Forbes. Atom probe tomography. *Mater. Charact.*, 60(6):461–469, jun 2009.

[92] M. K. Miller, K. F. Russell, and D. T. Hoelzer. Characterization of precipitates in MA/ODS ferritic alloys. *J. Nucl. Mater.*, 351(1-3):261–268, jun 2006.

[93] M. A. Miodownik, J. W. Martin, and E. A. Little. Grain boundary segregation in an oxide-dispersion-strengthened ferritic steel. *J. Mater. Sci. Lett.*, 12:834–835, 1993.

[94] H. Sakasegawa, L. Chaffron, F. Legendre, M. Brocq, L. Boulanger, S. Poissonnet, Y. de Carlan, J. Bechade, T. Cozzika, and J. Malaplate. Evaluation of threshold stress of the MA957 ODS ferrtic alloy. *J. Nucl. Mater.*, 386-388:511–514, apr 2009.

[95] Y. Tian, Q. Pan, G. Liu, B. Shan, and F. Yang. Effects of Ti on strengthening of ODS ferritic alloy for advanced FBR cladding application. *Acta Metall. Sin.*, 34(11):1217–1222, 1998.

[96] H. Sakasegawa, S. Ohtsuka, S. Ukai, H. Tanigawa, M. Fujiwara, H. Ogiwara, and A. Kohyama. Particle size effects in mechanically alloyed 9Cr ODS steel powder. *J. Nucl. Mater.*, 367-370(SPEC. ISS.):185–190, aug 2007.

[97] S. Yamashita *, S. Ohtsuka, N. Akasaka, S. Ukai, and S. Ohnuki. Formation of nanoscale complex oxide particles in mechanically alloyed ferritic steel. *Philos. Mag. Lett.*, 84(8):525–529, jul 2004.

[98] H. Zhu, T. Wei, R. Harrison, L. Edwards, and K. Maruyama. Development of Oxide Dispersion Strengthened Steels for High Temperature Nuclear Structural Applications. In J. Mathew, L. Ma, A. Tan, M. Weijnen, and J. Lee, editors, *Eng. Asset Manag. Infrastruct. Sustain.*, pages 1147–1160. Springer London, London, 2012.

[99] S. Ohtsuka, S. Ukai, M. Fujiwara, T. Kaito, and T. Narita. Improvement of 9Cr-ODS martensitic steel properties by controlling excess oxygen and titanium contents. *J. Nucl. Mater.*, 329-333(1-3 PART A):372–376, 2004.

[100] K. Lu, L. Lu, and S. Suresh. Strengthening Materials by Engineering Coherent Internal Boundaries at the Nanoscale. *Science (80-.).*, 324(5925):349–352, apr 2009.

[101] J. H. Schneibel, M. Heilmaier, W. Blum, G. Hasemann, and T. Shanmugasundaram. Temperature dependence of the strength of fine- and ultrafine-grained materials. *Acta Mater.*, 59(3):1300–1308, feb 2011.

[102] J. H. Kim, T. S. Byun, D. T. Hoelzer, C. H. Park, J. T. Yeom, and J. K. Hong. Temperature dependence of strengthening mechanisms in the nanostructured ferritic alloy 14YWT: Part II-Mechanistic models and predictions. *Mater. Sci. Eng. A*, 559:111–118, jan 2013.

[103] J. Shen, Y. Li, F. Li, H. Yang, Z. Zhao, S. Kano, Y. Matsukawa, Y. Satoh, and H. Abe. Microstructural characterization and strengthening

mechanisms of a 12Cr-ODS steel. *Mater. Sci. Eng. A*, 673:624–632, sep 2016.

[104] X. Zhou, Y. Liu, L. Yu, Z. Ma, Q. Guo, Y. Huang, and H. Li. Microstructure characteristic and mechanical property of transformable 9Cr-ODS steel fabricated by spark plasma sintering. *Mater. Des.*, 132:158–169, oct 2017.

[105] M. J. Alinger. On the formation and stability of nanometer scale precipitates in ferritic alloys during processing and high temperature service. *ProQuest Diss. Theses; Thesis (Ph.D.)–University Calif.*, 2004.

[106] A. Möslang, C. Adelhelm, and R. Heidinger. Innovative materials for energy technology. *Int. J. Mater. Res.*, 99(10):1045–1054, oct 2008.

[107] Strengthening mechanisms of materials. (n.d.). In Wikipedia. Retrieved 19 November 2017, from https://en.wikipedia.org/wiki/Strengthening_mechanisms_of_materials.

[108] F. J. Humphreys and M. Hatherly. *Recrystallization and related annealing phenomena*. Elsevier Ltd, 2nd edition, 2004.

[109] E. Arzt. Size effects in materials due to microstructural and dimensional constraints: a comparative review. *Acta Mater.*, 46(16):5611–5626, oct 1998.

[110] E. Orowan. Symposium on Internal Stress in Metals and Alloys. pages 451–453. The Institute of Metals, London, 1948.

[111] P. B. Hirsch. The interpretation of the slip pattern in terms of dislocation movements. *Japan Inst. Met.*, 86(13), 1957.

[112] P. B. Hirsch and F. J. Humphreys. The Deformation of Single Crystals of Copper and Copper-Zinc Alloys Containing Alumina Particles. I.

Macroscopic Properties and Workhardening Theory. *Proc. R. Soc. A Math. Phys. Eng. Sci.*, 318(1532):45–72, jul 1970.

[113] Y. Xiang, D. J. Srolovitz, L. T. Cheng, and Weinan E. Level set simulations of dislocation-particle bypass mechanisms. *Acta Mater.*, 52(7):1745–1760, apr 2004.

[114] F. J. Humphreys and P. B. Hirsch. The Deformation of Single Crystals of Copper and Copper-Zinc Alloys Containing Alumina Particles. II. Microstructure and Dislocation-Particle Interactions. *Proc. R. Soc. A Math. Phys. Eng. Sci.*, 318(1532):73–92, jul 1970.

[115] Y. Jiang, J. R. Smith, and G. Robert Odette. Prediction of structural, electronic and elastic properties of Y2Ti2O7 and Y2TiO5. *Acta Mater.*, 58(5):1536–1543, mar 2010.

[116] M. Bartsch, A. Wasilkowska, A. Czyrska-Filemonowicz, and U. Messerschmidt. Dislocation dynamics in the oxide dispersion strengthened alloy INCOLOY MA956. *Mater. Sci. Eng. A*, 272:152–162, 1999.

[117] Y. Ijiri, N. Oono, S. Ukai, S. Ohtsuka, T. Kaito, and Y. Matsukawa. Oxide particle-dislocation interaction in 9Cr-ODS steel. *Nucl. Mater. Energy*, 9:378–382, dec 2016.

[118] D. Srolovitz, R. Petkovic-Luton, and M. J. Luton. On dislocation-incoherent particle interactions at high temperature. *Scr. Metall.*, 16(c):1401–1406, 1982.

[119] D. Srolovitz, R. Petkovic-Luton, and M. J. Luton. Straight dislocation-sphericle inclusion interactions- High and low temperature solutions. *Scr. Metall.*, 18(8):1063–1068, 1984.

[120] V. C. Nardone and J. K. Tien. Pinning of dislocations on the departure side of strengthening dispersoids. *Scr. Metall.*, 17:467–470, 1983.

[121] J. Rösler and E. Arzt. A New Model-Based Creep Equation for Dispersion Strengthened Materials. *Acta Metall. Mater.*, 38(4):671–683, 1990.

[122] J. Preston, B. Wilshire, and E. A. Little. Dislocation-Particle Interactions In An Oxide-Dispersion-Strengthened Ferritic Steel. *Scr. Metall.*, 25:183–184, 1991.

[123] B. Reppach. On the dispersion strengthening mechanisms in ODS materials. *Zeitschrift für Met.*, 93(7):605–613, jul 2002.

[124] A. Ramar, P. Spätig, and R. Schäublin. Analysis of high temperature deformation mechanism in ODS EUROFER97 alloy. *J. Nucl. Mater.*, 382(2-3):210–216, dec 2008.

[125] R. Schäublin, A. Ramar, N. Baluc, V. de Castro, M. A. Monge, T. Leguey, N. Schmid, and C. Bonjour. Microstructural development under irradiation in European ODS ferritic/martensitic steels. *J. Nucl. Mater.*, 351(1-3):247–260, jun 2006.

[126] M. Serrano, A. García-Junceda, R. Hernández, and M. H. Mayoral. On anisotropy of ferritic ODS alloys. *Mater. Sci. Technol.*, 30(13b):1664–1668, nov 2014.

[127] A. Wasilkowska, M. Bartsch, U. Messerschmidt, R. Herzog, and A. Czyrska-Filemonowicz. Creep mechanisms of ferritic oxide dispersion strengthened alloys. *J. Mater. Process. Technol.*, 133(1-2):218–224, feb 2003.

[128] J. H. Kim, T. S. Byun, and D. T. Hoelzer. Tensile fracture characteristics of nanostructured ferritic alloy 14YWT. *J. Nucl. Mater.*, 407(3):143–150, dec 2010.

[129] E. J. Mittemeijer. *Fundamentals of Materials Science : The Microstructure-Property Relationship Using Metals as Model Systems*. Springer Berlin Heidelberg, 2011.

[130] R. W. Lund and W. D. Nix. High temperature creep of Ni-20Cr-2ThO2 single crystals. *Acta Metall.*, 24(5):469–481, may 1976.

[131] W. C. Oliver and W. D. Nix. High temperature deformation of oxide dispersion strengthened Al and Al-Mg solid solutions. *Acta Metall.*, 30(7):1335–1347, jul 1982.

[132] C. Biselli and D. G. Morris. The high temperature deformation of mechanically alloyed copper-based alloys. *Mater. Sci. Eng. A*, 148(2):163–173, dec 1991.

[133] C. Zakine, C. Prioul, and D. François. Creep behaviour of ODS steels. *Mater. Sci. Eng. A*, 219(1-2):102–108, nov 1996.

[134] J. Rösler, R. Joos, and E. Arzt. Microstructure and creep properties of dispersion-strengthened aluminum alloys. *Metall. Trans. A*, 23(5):1521–1393, may 1992.

[135] T. Hayashi, P. M. Sarosi, J. H. Schneibel, and M. J. Mills. Creep response and deformation processes in nanocluster-strengthened ferritic steels. *Acta Mater.*, 56(7):1407–1416, apr 2008.

[136] ASTM E2714-13. Standard Test Method for Creep-Fatigue Testing. pages 1–15. ASTM International, West Conshohocken, PA, 2013.

[137] P. Rodriguez and K. Bhanu Sankara Rao. Nucleation and growth of cracks and cavities under creep-fatigue interaction. *Prog. Mater. Sci.*, 37(5):403–480, jan 1993.

[138] F. Ellyin. *Fatigue Damage, Crack Growth and Life Prediction*. Springer Netherlands, Dordrecht, 1st edition, 1996.

[139] H. J. Christ and H. Mughrabi. Microstructure and Fatigue. In K.-T. Rie, H. W. Grünling, G. König, P. Neumann, H. Nowack, K.-H. Schwalbe, and T. Seeger, editors, *Low Cycle Fatigue Elasto-Plastic Behav. Mater.*, pages 56–69. Springer Netherlands, Dordrecht, 1992.

[140] S. Suresh. *Fatigue of Materials*. Cambridge University Press, 1998.

[141] H. Mughrabi and H. J. Christ. Cyclic Deformation and Fatigue of Selected Ferritic and Austenitic Steels: Specific Aspects. *ISIJ Int.*, 37(12):1154–1169, 1997.

[142] A. Chauhan, D. Litvinov, T. Gräning, and J. Aktaa. High-temperature low-cycle fatigue behavior and microstructural evolution of an improved austenitic ODS steel. 2018.

[143] J. Polak. *Cyclic plasticity and low cycle fatigue life of metals*. Elsevier Science Publishers B. V., Amsterdam, 1991.

[144] J. Man, K. Obrtlík, and J. Polák. Extrusions and intrusions in fatigued metals. Part 1. State of the art and history. *Philos. Mag.*, 89(16):1295–1336, jun 2009.

[145] J. Polák and J. Man. Experimental evidence and physical models of fatigue crack initiation. *Int. J. Fatigue*, 91:294–303, oct 2016.

[146] D. M. Elzey and E. Arzt. Crack initiation and propagation during high-temperature fatigue of oxide dispersion-strengthened superalloys. *Metall. Trans. A*, 22A(4):837–851, sep 1991.

[147] J. C. Earthman, G. Eggeler, and B. Ilschner. Deformation and damage processes in a 12%Cr-Mo-V steel under high temperature low cycle fatigue conditions in air and vacuum. *Mater. Sci. Eng. A*, 110:103–114, mar 1989.

[148] L. Straßberger, A. Chauhan, S. Czink, and J. Aktaa. High-temperature low-cycle fatigue behavior and microstructural evolution of an ODS steel based on conventional T91. *Int. J. Fatigue*, 100:50–57, jul 2017.

[149] A. Chauhan, M. Walter, and J. Aktaa. Towards improved ODS steels: A comparative high-temperature low-cycle fatigue study. *Fatigue Fract. Eng. Mater. Struct.*, 40(12):2128–2140, dec 2017.

[150] R. W. Landgraf. The Resistance of Metals to Cyclic Deformation. In *Achiev. High Fatigue Resist. Met. Alloy.*, pages 3–3–34. ASTM International, 100 Barr Harbor Drive, PO Box C700, West Conshohocken, PA 19428-2959, jan 1970.

[151] P. Hutař, I. Kuběna, M. Ševčík, M. Šmíd, T. Kruml, and L. Náhlík. Small fatigue crack propagation in Y2O3 strengthened steels. *J. Nucl. Mater.*, 452(1-3):370–377, sep 2014.

[152] Project MatISSE 2013-2017 (n.d.). Retrieved 14 October 2017, from http://www.fp7-matisse.eu/.

[153] C. Petersen, V. Shamardin, A. Fedoseev, G. Shimansky, V. Efimov, and J. Rensman. The ARBOR irradiation project. *J. Nucl. Mater.*, 307-311(2 SUPPL.):1655–1659, dec 2002.

[154] Transmission electron microscope (n.d.). In MyScope by Australian microscopy & microanalysis reserach facility. Retrieved 2 August 2017, from http://www.ammrf.org.au/myscope/tem/introduction/.

[155] D. B. Williams and C. Barry Carter. *Transmission Electron Microscopy*. Springer US, Boston, MA, 2nd edition, 2009.

[156] D. A. Muller. Structure and bonding at the atomic scale by STEM. *Nat. Mater.*, 8(4):263–270, apr 2009.

[157] Scanning electron microscope (n.d.). From Oregon state univeristy. Retrieved 7 November 2017, from https://openoregonstate.pressbooks.pub/microbiology/chapter/microscopes/.

[158] Scanning electron microscope (n.d.). In Wikipedia. Retrieved 19 November 2017, from https://en.wikipedia.org/wiki/Scanning_electron_microscope.

[159] Electron Backscatter Diffraction Analysis (n.d.). By Oxford Instruments. Retrieved 1 December 2017, from http://www.ebsd.com/ebsd-explained/principle-components-of-an-ebsd-system.

[160] A. J. Wilkinson and T. B. Britton. Strains, planes, and EBSD in materials science. *Mater. Today*, 15(9):366–376, sep 2012.

[161] A. Chauhan, F. Bergner, A. Etienne, J. Aktaa, Y. de Carlan, C. Heintze, D. Litvinov, M. Hernandez-Mayoral, E. Oñorbe, B. Radiguet, and A. Ulbricht. Microstructure characterization and strengthening mechanisms of oxide dispersion strengthened (ODS) Fe-9%Cr and Fe-14%Cr extruded bars. *J. Nucl. Mater.*, 495:6–19, nov 2017.

[162] A. Chauhan, J. Hoffmann, D. Litvinov, and J. Aktaa. High-temperature low-cycle fatigue behavior of a 9Cr-ODS steel: Part 1 - pure fatigue, microstructure evolution and damage characteristics. *Mater. Sci. Eng. A*, 707:207–220, nov 2017.

[163] K. Maruyama, K. Sawada, and J. Koike. Advances in Physical Metallurgy and Processing of Steels. Strengthening Mechanisms of Creep Resistant Tempered Martensitic Steel. *ISIJ Int.*, 41(6):641–653, 2001.

[164] G. Eggeler. The effect of long-term creep on particle coarsening in tempered martensite ferritic steels. *Acta Metall.*, 37(12):3225–3234, dec 1989.

[165] F. Abe, M. Taneike, and K. Sawada. Alloy design of creep resistant 9Cr steel using a dispersion of nano-sized carbonitrides. *Int. J. Press. Vessel. Pip.*, 84(1-2):3–12, jan 2007.

[166] H. Sakasegawa, L. Chaffron, F. Legendre, L. Boulanger, T. Cozzika, M. Brocq, and Y. de Carlan. Correlation between chemical composition and size of very small oxide particles in the MA957 ODS ferritic alloy. *J. Nucl. Mater.*, 384(2):115–118, feb 2009.

[167] H. Sakasegawa, F. Legendre, L. Boulanger, M. Brocq, L. Chaffron, T. Cozzika, J. Malaplate, J. Henry, and Y. de Carlan. Stability of non-stoichiometric clusters in the MA957 ODS ferrtic alloy. *J. Nucl. Mater.*, 417(1-3):229–232, oct 2011.

[168] J. Ribis and Y. de Carlan. Interfacial strained structure and orientation relationships of the nanosized oxide particles deduced from elasticity-driven morphology in oxide dispersion strengthened materials. *Acta Mater.*, 60(1):238–252, jan 2012.

[169] A. Czyrska-Filemonowicz and B. Dubiel. Mechanically alloyed, ferritic oxide dispersion strengthened alloys: structure and properties. *J. Mater. Process. Technol.*, 64(1-3):53–64, feb 1997.

[170] H. Dong, L. Yu, Y. Liu, C. Liu, H. Li, and J. Wu. Effect of hafnium addition on the microstructure and tensile properties of aluminum added high-Cr ODS steels. *J. Alloys Compd.*, 702:538–545, apr 2017.

[171] H. Xu, Z. Lu, D. Wang, and C. Liu. Microstructure Refinement and Strengthening Mechanisms of a 9Cr Oxide Dispersion Strengthened Steel by Zirconium Addition. *Nucl. Eng. Technol.*, 49(1):178–188, feb 2017.

[172] M. Klimiankou, R. Lindau, and A. Möslang. TEM characterization of structure and composition of nanosized ODS particles in reduced

activation ferritic-martensitic steels. *J. Nucl. Mater.*, 329-333:347–351, aug 2004.

[173] J. Chao, C. Capdevila-Montes, and J. L. González-Carrasco. On the delamination of FeCrAl ODS alloys. *Mater. Sci. Eng. A*, 515(1-2):190–198, 2009.

[174] *ASM Handbook, vol. 12, Fractography*. ASM International, 1987.

[175] J. Blach, L. Falat, and P. Ševc. Fracture characteristics of thermally exposed 9Cr-1Mo steel after tensile and impact testing at room temperature. *Eng. Fail. Anal.*, 16(5):1397–1403, 2009.

[176] M. Praud, J. Garnier, F. Mompiou, and J. Malaplate. Creep properties of a CEA 9 % Cr-ODS alloy for nuclear applications. *Japan Inst. Met.*, pages 2–5, 2012.

[177] F. Abe. Bainitic and martensitic creep-resistant steels. *Curr. Opin. Solid State Mater. Sci.*, 8(3-4):305–311, jun 2004.

[178] S. Ukai, R. Miyata, S. Kasai, N. Oono, S. Hayashi, T. Azuma, R. Kayano, E. Maeda, and S. Ohtsuka. Super high-temperature strength in hot rolled steels dispersing nanosized oxide particles. *Mater. Lett.*, aug 2017.

[179] M. Matijasevic and A. Almazouzi. Effect of Cr on the mechanical properties and microstructure of Fe-Cr model alloys after n-irradiation. *J. Nucl. Mater.*, 377(1):147–154, jun 2008.

[180] C. Heintze, F. Bergner, M. Hernández-Mayoral, R. Kögler, G. Müller, and A. Ulbricht. Irradiation hardening of Fe-9Cr-based alloys and ODS Eurofer: Effect of helium implantation and iron-ion irradiation at 300 Â°C including sequence effects. *J. Nucl. Mater.*, 470:258–267, mar 2016.

[181] A. Zeman, L. Debarberis, J. Kočík, V. Slugeň, and E. Keilová. Microstructural analysis of candidate steels pre-selected for new advanced reactor systems. *J. Nucl. Mater.*, 362(2-3):259–267, may 2007.

[182] M. Matijasevic, E. Lucon, and A. Almazouzi. Behavior of ferritic/martensitic steels after n-irradiation at 200 and 300Â°C. *J. Nucl. Mater.*, 377(1):101–108, jun 2008.

[183] C. Heintze, F. Bergner, A. Ulbricht, M. Hernández-Mayoral, U. Keiderling, R. Lindau, and T. Weissgärber. Microstructure of oxide dispersion strengthened Eurofer and iron-chromium alloys investigated by means of small-angle neutron scattering and transmission electron microscopy. *J. Nucl. Mater.*, 416(1-2):35–39, sep 2011.

[184] N. V. Luzginova, H. S. Nolles, P. ten Pierick, T. Bakker, R. K. Mutnuru, M. Jong, and D. T. Blagoeva. Irradiation response of ODS Eurofer97 steel. *J. Nucl. Mater.*, 428(1-3):192–196, sep 2012.

[185] F. Brain Pickering. *Physical Metallurgy and the design of steels*. Applied Science Publishers, illustrate edition, 1978.

[186] C. E. Lacy and M. Gensamer. The tensile properties of alloyed ferrites. *Trans. Am. Soc. Met.*, 32:88, 1944.

[187] F. Bergner. Elastic properties of Fe-Cr and ODS Fe-Cr alloys. In *Eur. Congr. Exhib. Adv. Mater. Process.*, Sevilla, Spain, 2013.

[188] J. E. Bailey and P. B. Hirsch. The dislocation distribution, flow stress, and stored energy in cold-worked polycrystalline silver. *Philos. Mag.*, 5(53):485–497, may 1960.

[189] R. E. Stoller and S. J. Zinkle. On the relationship between uniaxial yield strength and resolved shear stress in polycrystalline materials. *J. Nucl. Mater.*, 283-287:349–352, dec 2000.

[190] K. C. Russell and L. M. Brown. A dispersion strengthening model based on differing elastic moduli applied to the iron-copper system. *Acta Metall.*, 20(7):969–974, jul 1972.

[191] D. J. Bacon, U. F. Kocks, and R. O. Scattergood. The effect of dislocation self-interaction on the orowan stress. *Philos. Mag.*, 28(6):1241–1263, dec 1973.

[192] S. Queyreau, G. Monnet, and B. Devincre. Orowan strengthening and forest hardening superposition examined by dislocation dynamics simulations. *Acta Mater.*, 58(17):5586–5595, oct 2010.

[193] A. K. Seeger. On the theory of radiation damage and radiation hardening. In *Proc. Second United Nations Int. Conf. Peac. Uses At. Energy, Vol. 6*, pages 250– 273, Geneva, 1958.

[194] G. S. Was. Irradiation Hardening and Deformation. In *Fundam. Radiat. Mater. Sci.*, pages 581–642. Springer Berlin Heidelberg, Berlin, Heidelberg, 2007.

[195] A. J. E. Foreman and M. J. Makin. Dislocation movement through random arrays of obstacles. *Can. J. Phys.*, 45(2):511–517, feb 1967.

[196] E. Hornbogen and E. A. Starke. Overview no. 102 Theory assisted design of high strength low alloy aluminum. *Acta Metall. Mater.*, 41(1):1–16, jan 1993.

[197] N. Kamikawa, K. Sato, G. Miyamoto, M. Murayama, N. Sekido, K. Tsuzaki, and T. Furuhara. Stress-strain behavior of ferrite and bainite with nano-precipitation in low carbon steels. *Acta Mater.*, 83:383–396, jan 2015.

[198] B. Mouawad, X. Boulnat, D. Fabrègue, M. Perez, and Y. de Carlan. Tailoring the microstructure and the mechanical properties of ultra-

fine grained high strength ferritic steels by powder metallurgy. *J. Nucl. Mater.*, 465:54–62, oct 2015.

[199] M. Dadé, J. Malaplate, J. Garnier, F. De Geuser, F. Barcelo, P. Wident, and A. Deschamps. Influence of microstructural parameters on the mechanical properties of oxide dispersion strengthened Fe-14Cr steels. *Acta Mater.*, jan 2017.

[200] D. Brunner and J. Diehl. The use of stress-relaxation measurements for investigations on the flow stress of α-iron. *Phys. Status Solidi*, 104(1):145–155, nov 1987.

[201] Z. Chen. *Modelling the plastic deformation of iron*. PhD thesis, Karlsruhe Institute of Technology, 2013.

[202] Q. Li. Modeling the microstructure-mechanical property relationship for a 12Cr-2W-V-Mo-Ni power plant steel. *Mater. Sci. Eng. A*, 361(1-2):385–391, nov 2003.

[203] F. Brain Pickering. Structure-Property Relationships in Steels. In *Mater. Sci. Technol.* Wiley-VCH Verlag GmbH & Co. KGaA, Weinheim, Germany, sep 2006.

[204] D. Caillard. A TEM in situ study of alloying effects in iron. I-Solid solution softening caused by low concentrations of Ni, Si and Cr. *Acta Mater.*, 61(8):2793–2807, may 2013.

[205] J. B. Ferguson, B. F. Schultz, D. Venugopalan, H. F. Lopez, P. K. Rohatgi, K. Cho, and C. S. Kim. On the superposition of strengthening mechanisms in dispersion strengthened alloys and metal-matrix nanocomposites: Considerations of stress and energy. *Met. Mater. Int.*, 20(2):375–388, mar 2014.

[206] E. Arzt and D. S. Wilkinson. Threshold stresses for dislocation climb over hard particles: The effect of an attractive interaction. *Acta Metall.*, 34(10):1893–1898, oct 1986.

[207] J. Rösler and E. Arzt. The kinetics of dislocation climb over hard particles-I. Climb without attractive particle-dislocation interaction. *Acta Metall.*, 36(4):1043–1051, apr 1988.

[208] B. Reppich. On the attractive particle-dislocation interaction in dispersion-strengthened material. *Acta Mater.*, 46(1):61–67, dec 1998.

[209] L. Straßberger, D. Litvinov, and J. Aktaa. High temperature tensile properties of oxide dispersion strengthened T91 and their correlation with microstructural evolution. *Mater. Sci. Technol.*, 30(13):1743284714Y.000, apr 2014.

[210] S. Noh, B. K. Choi, C. H. Han, S. H. Kang, J. Jang, Y. H. Jeong, and T. K. Kim. Effects of heat treatments on microstructures and mechanical properties of dual phase ods steels for high temperature strength. *Nucl. Eng. Technol.*, 45(6):821–826, nov 2013.

[211] B. Hary, T. Guilbert, P. Wident, T. Baudin, R. Logé, and Y. de Carlan. Investigation of the relationships between mechanical properties and microstructure in a Fe-9%Cr ODS steel. *EPJ Nucl. Sci. Technol.*, 2:7, feb 2016.

[212] D. A. McClintock, M. A. Sokolov, D. T. Hoelzer, and R. K. Nanstad. Mechanical properties of irradiated ODS-EUROFER and nanocluster strengthened 14YWT. *J. Nucl. Mater.*, 392(2):353–359, jul 2009.

[213] W. Ramberg and W. R. Osgood. Description of stress-strain curves by three parameters. Technical report, National Advisory Committee For Aeronautics, Washington, DC, United States, 1943.

[214] L. F. Coffin. A study of the effects of cyclic thermal stresses on a ductile metal. *Trans. ASME*, 76:931–950, 1954.

[215] S. S. Manson. Behavior of materials under conditions of thermal stress. Technical Report 1820, National Advisory Committee for Aeronautics. Lewis Flight Propulsion Lab., Cleveland, OH, United States, 1954.

[216] A. Nagesha, M. Valsan, R. Kannan, K. Bhanu Sankara Rao, and S. L. Mannan. Influence of temperature on the low cycle fatigue behaviour of a modified 9Cr-1Mo ferritic steel. *Int. J. Fatigue*, 24(12):1285–1293, dec 2002.

[217] M. W. Kapp, T. Kremmer, C. Motz, B. Yang, and R. Pippan. Structural instabilities during cyclic loading of ultrafine-grained copper studied with micro bending experiments. *Acta Mater.*, 125:351–358, feb 2017.

[218] F. Mompiou, D. Caillard, and M. Legros. Grain boundary shear-migration coupling-I. In situ TEM straining experiments in Al polycrystals. *Acta Mater.*, 57(7):2198–2209, apr 2009.

[219] J. K. Tien, V. C. Nardone, and D. E. Matejczyk. The threshold stress and departure side pinning of dislocations by dispersoids. *Acta Metall.*, 32(9):1509–1517, 1984.

[220] W. Blum. Dislocation models of plastic deformation of metals at elevated temperatures. *Zeitschrift fuer Met. Res. Adv. Tech.*, 68(7):482–492, 1977.

[221] M. Sauzay, H. Brillet, I. Monnet, M. Mottot, F. Barcelo, B. Fournier, and A. Pineau. Cyclically induced softening due to low-angle boundary annihilation in a martensitic steel. *Mater. Sci. Eng. A*, 400-401:241–244, 2005.

[222] M. Sauzay. Modelling of the evolution of micro-grain misorientations during creep of tempered martensite ferritic steels. *Mater. Sci. Eng. A*, 510-511:74–80, jun 2009.

[223] D. Holec and A. Dlouhý. Interactions between particles and low-angle dislocation boundaries during high-temperature deformation. *Zeitschrift für Met.*, 96(6):558–565, jun 2005.

[224] A. Chauhan, L. Straßberger, U. Führer, D. Litvinov, and J. Aktaa. Creep-fatigue interaction in a bimodal 12Cr-ODS steel. *Int. J. Fatigue*, 102:92–111, sep 2017.

[225] A. Aghajani, F. Richter, C. Somsen, S.G. Fries, I. Steinbach, and G. Eggeler. On the formation and growth of Mo-rich Laves phase particles during long-term creep of a 12% chromium tempered martensite ferritic steel. *Scr. Mater.*, 61(11):1068–1071, dec 2009.

[226] M. Sauzay. Mechanical behavior of structural materials for Generation IV reactors. In *Struct. Mater. Gener. IV Nucl. React.*, pages 191–252. Elsevier, 2017.

[227] D. F. Li, R. A. Barrett, P. E. O'Donoghue, N. P. O'Dowd, and S. B. Leen. A multi-scale crystal plasticity model for cyclic plasticity and low-cycle fatigue in a precipitate-strengthened steel at elevated temperature. *J. Mech. Phys. Solids*, 101:44–62, 2017.

[228] E. Thiele, C. Holste, and R. Klemm. Influence of size effect on microstructural changes in cyclically deformed polycrystalline nickel. *Zeitschrift für Met.*, 93(7):730–736, jul 2002.

[229] G. Ebi and A. J. McEvily. Effect of processing on the high temperature low cycle fatigue properties of modified 9Cr-1Mo ferritic steel. *Fatigue Fract. Eng. Mater. Struct.*, 7(4):299–314, oct 1984.

[230] B. Fournier, M. Sauzay, C. Caes, M. Noblecourt, M. Mottot, A. Bougault, V. Rabeau, and A. Pineau. Creep-fatigue-oxidation interactions in a 9Cr-1Mo martensitic steel. Part I: Effect of tensile holding period on fatigue lifetime. *Int. J. Fatigue*, 30(4):649–662, apr 2008.

[231] J. R. Haigh, R. P. Skelton, and C. E. Richards. Oxidation-assisted crack growth during high cycle fatigue of a 1%Cr-Mo-V steel at 550Â°C. *Mater. Sci. Eng.*, 26(2):167–174, dec 1976.

[232] K. D. Challenger, A. K. Miller, and C. R. Brinkman. An Explanation for the Effects of Hold Periods on the Elevated Temperature Fatigue Behavior of 2 1/4 Cr-1 Mo Steel. *J. Eng. Mater. Technol.*, 103(1):7, jan 1981.

[233] Z. Zhang, Z. Hu, S. Schmauder, M. Mlikota, and K. Fan. Low-Cycle Fatigue Properties of P92 Ferritic-Martensitic Steel at Elevated Temperature. *J. Mater. Eng. Perform.*, 25(4):1650–1662, apr 2016.

[234] C. D. Beachem. Microscopic fracture processes. In H. Liebowitz, editor, *Fract. An Adv. Treatise*, pages 243–349. Academic Press, New York, 1968.

[235] M. N. Batista, I. Alvarez-Armas, M. F. Giordana, S. Hereñú, and A. F. Armas. Cyclic deformation and microstructural behaviour of reduced activation ferritic-martensitic steels. *Mater. Sci. Technol.*, 30(14):1826–1831, nov 2014.

[236] U. Führer and J. Aktaa. Modeling the cyclic softening and lifetime of ferritic-martensitic steels under creep-fatigue loading. *Int. J. Mech. Sci.*, dec 2017.

[237] W. Hoffelner. Structural materials containing nanofeatures for advanced energy plants. In *Struct. Alloy. Power Plants*, pages 221–249. Elsevier, 2014.

[238] D. Lefebvre and F. Ellyin. Cyclic response and inelastic strain energy in low cycle fatigue. *Int. J. Fatigue*, 6(1):9–15, jan 1984.

[239] F. Ellyin. A criterion for fatigue under multiaxial states of stress. *Mech. Res. Commun.*, 1(4):219–224, jan 1974.

[240] J. Barbehön, A. Rahmel, and M. Schütze. Behavior of the scale on a 9.5Cr steel under cyclical deformation of the base metal. *Oxid. Met.*, 30(1-2):85–94, aug 1988.

[241] J. Weiss. *Endommagement en viscoplasticite ' cyclique sous chargement multiaxial a haute tempe 'rature d'un acier inoxidable auste 'nitique*. PhD thesis, Ecole des Mines de Paris, 1992.

[242] M. F. Chisholm, S Kumar, and P Hazzledine. Dislocations in Complex Materials. *Science (80-.).*, 307(5710):701–703, feb 2005.

[243] J. J. Schirra, R. H. Caless, and R. W. Hatala. The Effect of Laves Phase on the Mechanical Properties of Wrought and Cast + HIP Inconel 718. In *Superalloys 718, 625 Var. Deriv.*, pages 375–388. TMS, 1991.

[244] R. Raj. Nucleation of cavities at second phase particles in grain boundaries. *Acta Metall.*, 26(6):995–1006, jun 1978.

[245] B. K. Min and R. Raj. Hold-time effects in high temperature fatigue. *Acta Metall.*, 26(6):1007–1022, jun 1978.

[246] K. Aoto, R. Komine, F. Ueno, H. Kawasaki, and Y. Wada. Creep-fatigue evaluation of normalized and tempered modified 9Cr-1Mo. *Nucl. Eng. Des.*, 153(1):97–110, dec 1994.

[247] T. Ogata. High Temperature Strength. Influence of Long-Term Strain Hold on Creep-Fatigue Life of Mod. 9Cr-1Mo Steel. *J. Soc. Mater. Sci. Japan*, 46(1):25–31, jan 1997.

[248] A. Chauhan, D. Litvinov, Y. de Carlan, and J. Aktaa. Study of the deformation and damage mechanisms of a 9Cr-ODS steel: Microstructure evolution and fracture characteristics. *Mater. Sci. Eng. A*, 658:123–134, mar 2016.

[249] R. L. Klueh and A.T. Nelson. Ferritic/martensitic steels for next-generation reactors. *J. Nucl. Mater.*, 371(1-3):37–52, sep 2007.

[250] J. Kyono and N. Shinya. Effect of S Segregation and BN Precipitation to Creep Cavities on Creep Rupture Properties. *Tetsu-to-Hagane*, 88(5):277–283, may 2002.

[251] M. F. Ashby. The deformation of plastically non-homogeneous materials. *Philos. Mag.*, 21(170):399–424, feb 1970.

[252] D. P. Field, P. B. Trivedi, S. I. Wright, and M. Kumar. Analysis of local orientation gradients in deformed single crystals. *Ultramicroscopy*, 103(1):33–39, apr 2005.

A Appendix

A.1 Technical drawings

1. Miniaturized tensile test specimen
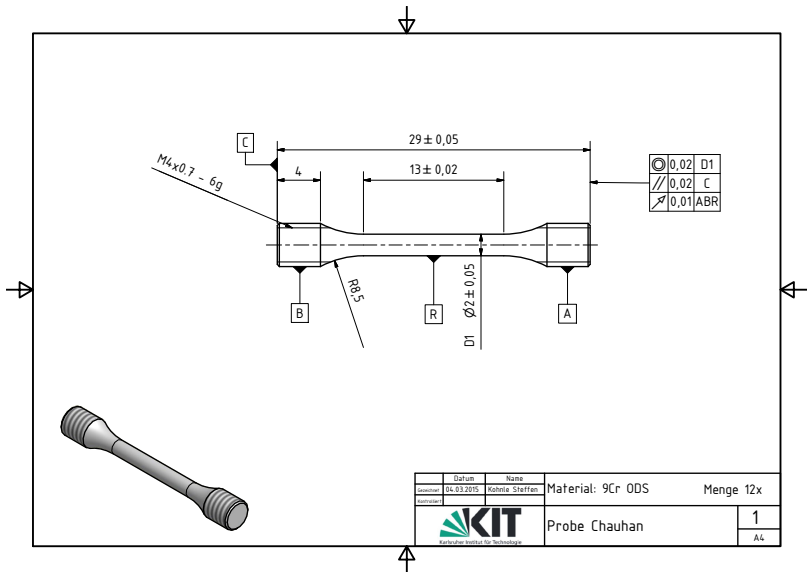
Figure A.1: Technical drawing of the tensile test specimen.

2. Miniaturized LCF test specimen
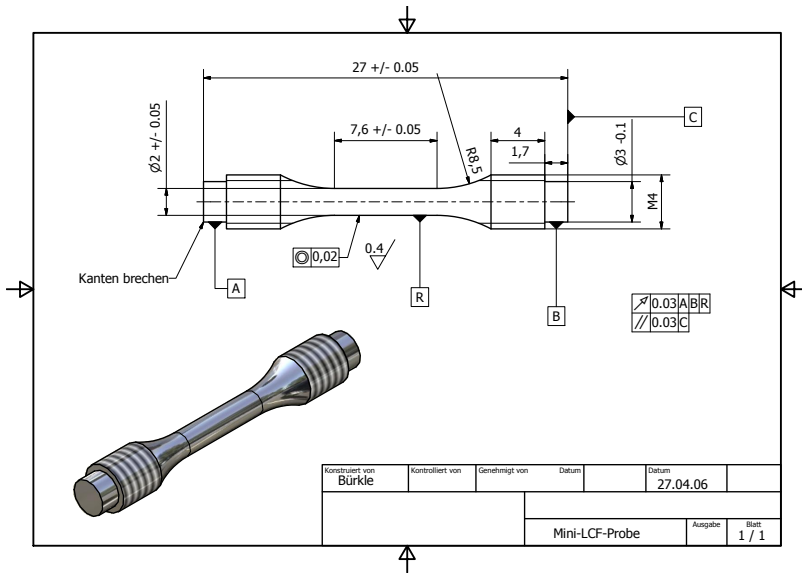
Figure A.2: Technical drawing of the LCF test specimen.

A.2 Carbides characterization

In tempered martensitic 9YWT-MATISSE, the $M_{23}C_6$ carbides are found to be Fe, Cr and W enriched (see, Fig. 4.4). Conventional TEM characterization methods reveal that these carbides have a FCC structure which is close to that of $Cr_{23}C_6$ carbides (see, Fig. A.3). Moreover, they are found to have following orientation relationship with the matrix: <112> $M_{23}C_6$ ‖ <110> α-Fe.
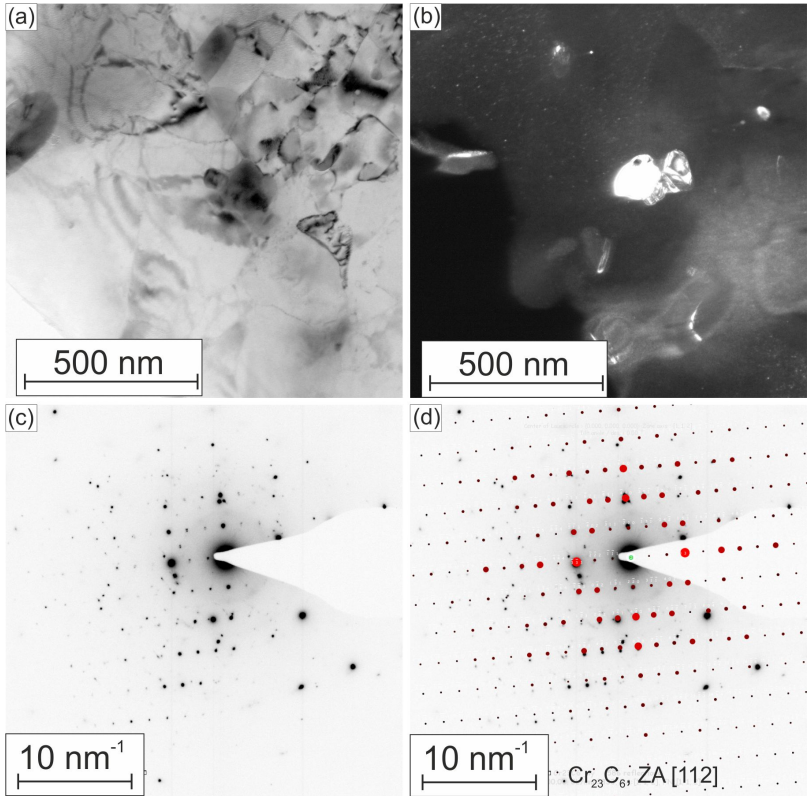
Figure A.3: BF micrograph taken from the heat treated 9YWT-MATISSE (a) along with its corresponding DF micrograph (b) made by using one of the g vectors in selected area diffraction pattern (SADP) (c) which is indexed to be near the [112] zone axis of the $Cr_{23}C_6$ carbide (d).

A.3 Dislocation density estimation via EBSD

It is clear from the Fig. A.4a that after cyclic straining (550 °C, $\pm$ 0.5%) the dislocation density[1] distribution spread reduces with a coexisting peak shift

---

[1] In actual sense, it is a density of geometrically necessary dislocations (GNDs). In descriptions of dislocations in crystals, dislocations could be separated into two different categories, GNDs which appear in strain gradient fields due to geometrical constraints of the crystal lattice, and statistically-stored dislocations (SSDs) which evolve from random trapping processes du-

towards lower values indicating a reduction in dislocation density. This exaggerates even further with increase in both temperature and applied strain amplitude (650 °C, ± 0.5% and 650 °C, ± 0.7%). However, as shown in Fig. A.4b, no further significant dislocation density reduction seems to have occurred upon introducing 10 min and 30 min hold-time at peak tensile strain of 0.7%.

A.4 EBSD investigations on interrupted PF/CC specimen

To understand microstructural evolution during cyclic straining, a specimen was cycled for only 100 times under ± 0.5% strain amplitude at 650°C. EBSD investigation results for this sectioned specimen along with those for undeformed state and specimen cycled till failure (1196 cycles) are presented below for comparison. Here, IPF, KAM and GAM maps provides a visual estimation of grain size, dislocation density and sub-grain structures, respectively, as mentioned in section. 4.3.2. It is evident that already after 100 cycles grains became coarse, while the dislocation density and sub-grain structures underwent relativity minor changes. Upon cycling further, these microstructural modifications amplify significantly, which can be easily distinguished for the specimen cycled till failure, see section. 4.3.2 for more. These results support microstructural evolution with number of cycles and its role in observed cyclic softening.

---

ring plastic deformation, see [251]. Indeed, upon plastic deformation GNDs accommodate orientation gradients (lattice rotations) within single crystallites in the material [252]. This dislocation structure is necessary to maintain lattice continuity. The lattice rotations can be measured and characterized using local orientation measurements and analyses to determine GNDs via EBSD, see [252]. However, even though the total dislocation density is not estimated through this procedure (as SSDs are left unaccounted), but an idea of the dislocations remaining after unloading, and responsible for the local misorientations is obtained.
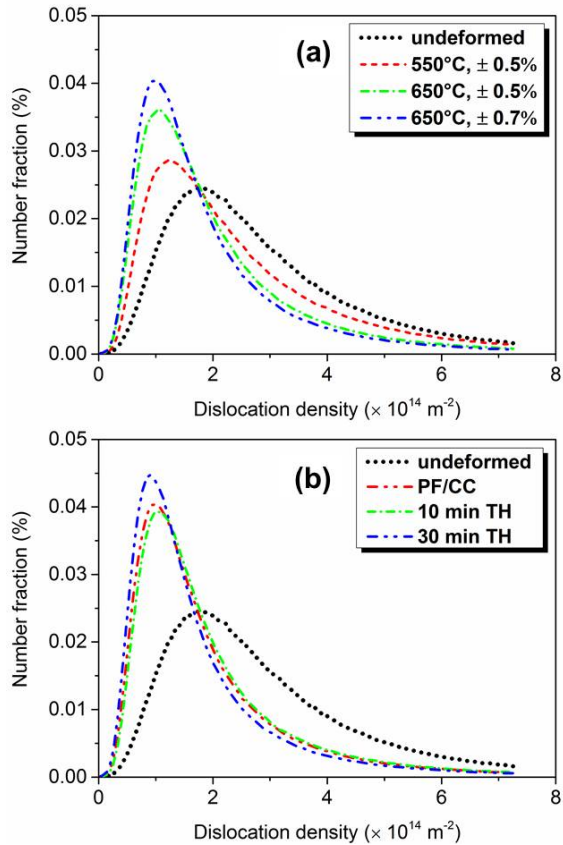
Figure A.4: Dislocation density distributions before (undeformed) and after PF/CC conditions (a) and CF conditions (10 min and 30 min TH) (b). Here, the maximum misorientation was restricted to 5 °

.
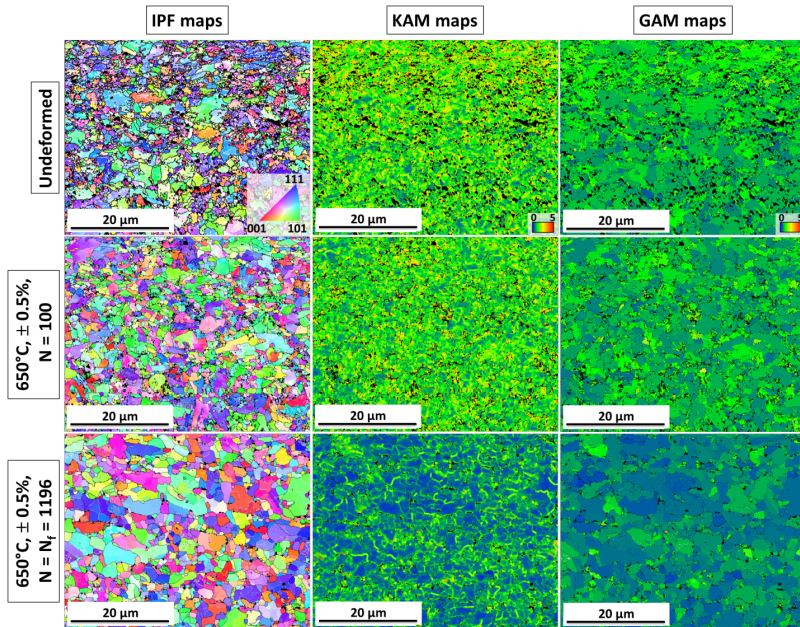
Figure A.5: IPF, KAM and GAM maps present the evolution of microstructure with number of cycles (N) for 9YWT-MATISSE. N_f depicts the number of cycles to failure.

A.5 Influence of the tensile hold-time duration on the number of cycles to failure

From Fig. A.6, it is obvious that the introduction of hold-time at peak tensile strain results in a reduction of N_f. Moreover, the longer the hold-time the lower is the cyclic life which drops almost linearly.

A.6 TEM investigations on CF tested specimens

Fig. A.7 presents the comparison of microstructures before and after cyclic straining. It is evident that after cycling grains are clearly visible and appear equiaxed as well as moderately clean due to (1) the rearrangement
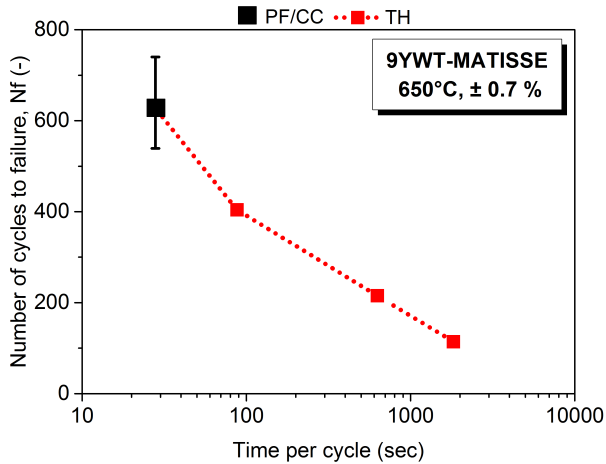
Figure A.6: Influence of the tensile hold-time duration on the number of cycles to failure of strain-controlled LCF tests at 650 °C under ± 0.7% strain amplitude.

and/or annihilation of dislocations and (2) partial elimination of the original sub-grain structures. This altogether results in a reduction of overall dislocation density. In almost all grains individual dislocations appear pinned at the nanoparticle-matrix interfaces and under the effect of stresses, most of them are bowed out (Fig. A.8a). Moreover, pinning is realized on both arrival as well as departure side of the nano-oxide particles (marked in Fig. A.8a) suggesting an attractive particle-dislocation interaction, since even after overcoming particles by cross-slip or climb (depending upon the character of the dislocations and the nature of the particle-matrix interface) dislocations are being pinned on the departure side of the nano-oxide particles. Hence, there exists a threshold stress to detach dislocation out of this pinning, which must be overcome for the dislocation to glide; and therefore, plastic deformation to occur [120, 208, 219]. However, once threshold stress is reached, the dislocation will detach and glide until new pinning (see Fig. A.8b, where remnant slip traces, formed as a result of dislocations

217

glide, in between nanoparticles are apparent) where the process of particle by-pass and detachment recurs. This results in a retarded dislocation's intragranular mobility.

However, in between obstacles or in particles deficient region, dislocations can still annihilate with those of opposite signs, leading to their reduced density. Indeed, the previously mentioned cleaner regions are mostly those that are free of nanoparticles (also refer section 4.3.2). And therefore, it seems that due to their obstruction free path, since there are no particles to be pinned against, dislocations glide freely. Hence, both uniform nanoparticles distribution as well as lower inter-particle spacing is critical for suppressing the annihilation processes. Furthermore, this dislocation glide can also acts as a driving force for sub-grain boundary (SGB) elimination, for more, see section 4.3.2.
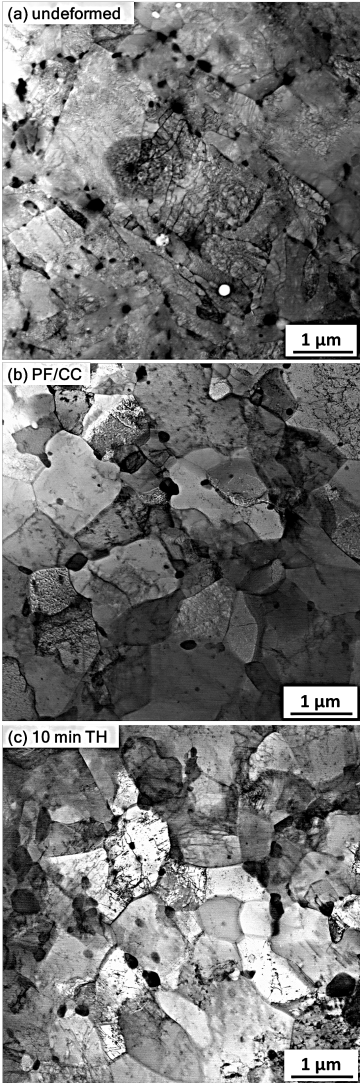
Figure A.7: Inverted contrast HAADF-STEM micrographs from undeformed state (a), after testing under PF/CC (b) and 10 min TH (c) waveforms at 650 °C under ± 0.7% strain amplitude.
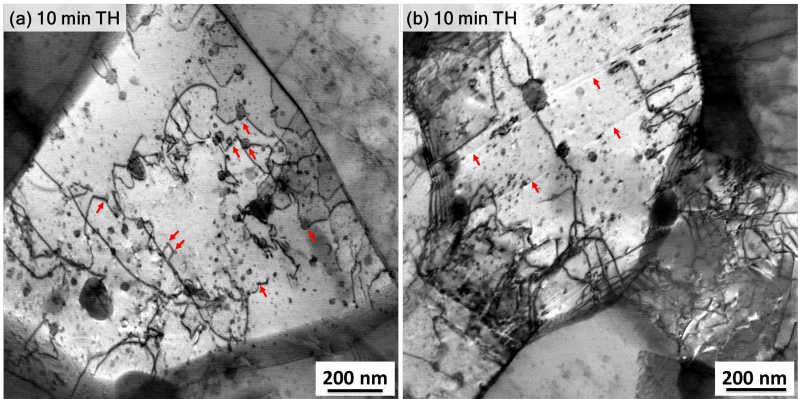
Figure A.8: Inverted contrast HAADF-STEM micrographs taken after testing under 10 min TH waveform at 650 °C under ± 0.7% strain amplitude. Dislocation-particle interactions in (a) and remnant slip traces in (b) are marked with red arrows.

List of Figures

List of Tables

Acknowledgment

First of all, I would like to give special thanks to my supervisor Prof. Dr.-Ing. Jarir Aktaa for providing me an exciting opportunity to carry out my Doctoral thesis in his department. I would also like to thank him for his exceptional commitment, support, continuous supervision and the numerous scientific discussions which have considerably contributed to the completion of this work. I would also like to thank Prof. Dr. rer. nat. Anton Möslang for the review of this thesis and for being my co-referent during Ph.D defense.

My special thanks goes to Dr. Yann De Carlan from CEA, France for providing 9YWT-MATISSE steel for investigations. I would like to thank Dr.-Ing. Tim Gräning and his team at IAM-AWP for being generous in providing me austenitic ODS (MS XVI) steel for investigations. My special thanks also goes to Dr. Annette Heinzel for providing 12YWT-GETMAT steel, which was developed and produced within the framework of project GETMAT. I would also like to thank Dr. Frank Bergner from HZDR, Dresden for numerous discussions concerning strengthening mechanisms.

I wish to express my special thanks to Dr.-Ing. Mario Walter for providing assistance in the mechanical testing and his helpful suggestions and fruitful discussions. Special thanks goes to Dr. rer. nat. Dimitri Litvinov for assisting me in handly TEM and also investigations, Dr.-Ing. Jan Hoffmann for assisting me in acquiring EBSD scans and Dr. rer. nat. Benjamin Kaiser

for his help in preparing FIB sections. In addition, I would like to thank Mr. Ewald Ernst, Mr. Steffen Kohnle and Mr. Ralf Dahm for assisting me in mechanical testing and samples preparation. Furthermore, I would like to thank all members of the institute for their support and technical assistance as well as the great environment provided during the work.

Big thanks to my colleagues Dr.-Ing. Luis Straßberger, Dipl.-Ing. Ulrich Führer and Dipl.-Ing. Marco Conte for their various insightful discussions and valuable help in reviewing my publications. I would also like to thank them for sharing with me many light moments which I will cherish my whole life.

I would like to thank my family members for their endless support, motivation and love.

Karlsruhe, in December 2017   *Ankur Chauhan*

Curriculum vitae

Personal Details

Name	Ankur Chauhan
Gender	Male
Date of birth	19. November 1988
Birth place	Ranipur, Haridwar
Nationality	Indian

Schooling Education

Till 2006	Delhi Public School, Haridwar, India

Technical Education

2007 – 2011	Uttarakhand Technical University, Dehradun, India
	Degree: Bachelor of Technology (B.Tech) in Mechanical Engineering (**Gold medal**)
2012 – 2014	Indian Institute of Technology, Roorkee, India
	Degree: Master of Technology (M.Tech) in Metallurgy and Materials Engineering (**First position**)

Professional Activities

2009 – 2010   Industrial Training at Bharat Heavy Electricals
Ltd., Ranipur, India

2013 – 2014   DAAD scholar at Max Planck Institute for Intel-
ligent Systems, erstwhile Max Planck Institute
for Metals Research, Stuttgart, Germany

2014 – 2018   Scientific Employee at Karlsruhe Institute of
Technology (KIT), Germany

List of Publications

1. A. Chauhan, D. Litvinov, T. Gräning, J. Aktaa, *High-temperature low-cycle fatigue behavior of an improved novel austenitic ODS steels*, To be submitted (2018).

2. A. Chauhan, J. Aktaa, *High-temperature low-cycle fatigue behavior of a 9Cr-ODS steel: Part 2 - Hold-time influence, microstructural evolution and damage characteristics*, To be submitted (2018).

3. A. Chauhan, J. Hoffman, D. Litvinov, J. Aktaa, *High-temperature low-cycle fatigue behavior of a 9Cr-ODS steel: Part 1 - Pure fatigue, microstructure evolution and damage characteristics*, Materials Science and Engineering: A, 707 (2017) 207-220.

4. A. Chauhan, F. Bergner et al., *Microstructure characterization and strengthening mechanisms of oxide dispersion strengthened (ODS) Fe-9%Cr and Fe-14%Cr extruded bars*, Journal of Nuclear Materials, 495 (2017) 6-19.

5. A. Chauhan, L. Straßberger, U. Führer, D. Litvinov, J. Aktaa, *Creep-fatigue interaction in a bimodal 12Cr-ODS steel*, International Journal of Fatigue, 102 (2017) 92-111.

6. A. Chauhan, M. Walter, J. Aktaa, *Towards improved ODS steels: A comparative high-temperature low-cycle fatigue study*, Fatigue &

Fracture of Engineering Materials & Structures, 40 (12) (2017) 2128-2140.

7. L. Straßberger, A. Chauhan, S. Czink, J. Aktaa, *High-temperature low-cycle fatigue behavior and microstructural evolution of an ODS steel based on conventional T91*, International Journal of Fatigue, 100 (2017) 50-57.

8. D. Litivnov, A. Chauhan, J. Aktaa, *Microstructural evolution of 9Cr-ODS steel during high temperature deformation*, European Microscopy Congress 2016: Proceedings, (2016) 850-851.

9. L. Straßberger, A. Chauhan, T. Gräning, S. Czink, J. Aktaa, *High-temperature low-cycle fatigue behavior of novel austenitic ODS steels*, International Journal of Fatigue, 93 (2016) 194-200.

10. A. Chauhan, D. Litivnov, J. Aktaa, *Deformation and damage mechanisms of a bimodal 12Cr-ODS steel under high-temperature cyclic loading*, International Journal of Fatigue, 93 (2016) 1-17.

11. A. Chauhan, D. Litivnov, Y. De Carlan, J. Aktaa, *Study of the deformation and damage mechanisms of a 9Cr-ODS steel: Microstructure evolution and fracture characteristics*, Materials Science and Engineering: A, 468 (2016) 1-8.

12. A. Chauhan, D. Litivnov, J. Aktaa, *High temperature tensile properties and fracture characteristics of bimodal 12Cr-ODS steel*, Journal of Nuclear Materials, 468 (2016) 1-8.

13. S. R. Meka, A. Chauhan, T. Steiner, E. Bischoff, P. K. Ghosh, E. J. Mittemeijer, *Generating duplex microstructures by nitriding; nitriding of iron based Fe-Mn alloy*, Materials Science and Technology, 32 (9) (2016) 883-889.

Contributions in Conferences and Scientific Meetings (* presenter)

1. J. Malaplate*, M. Dadé, Y. de Carlan, F. Mompiou, D. Caillard, A. Chauhan, J. Aktaa, M. Hernández-Mayoral, E. Oñorbe Esparraguera, M. Serrano, *Deformation mechanisms in ODS alloys: Recent highlights obtained within the MATISSE program*, EUROMAT 2017, 17-22nd September 2017, Thessaloniki, Greece.

2. A. Chauhan*, J. Aktaa, *High-temperature low-cycle fatigue behavior of a tempered martensitic 9Cr-ODS steel*, Eighth International Conference on Low Cycle Fatigue (LCF8), 27-29th June 2017, Dresden, Germany. **Best young author award**

3. A. Chauhan*, D. Litivnov, J. Aktaa, *High-temperature fatigue and creep-fatigue interaction in a tempered martensitic 9Cr-ODS steel*, 4th ODISSEUS Workshop, 26-28th June 2017, Helmholtz-Zentrum Dresden-Rossendorf, Dresden, Germany.

4. D. Litvinov*, A. Chauhan, J. Aktaa, *Microstructural evolution of 9Cr-ODS steel during high temperature deformation*, 16th European microscopy congress, 28th August-2nd September 2016, Lyon, France.

5. A. Chauhan*, J. Aktaa, *High-temperature low-cycle fatigue behavior of ODS steels: Comparison in respect to the microstructure*, XVIII International Colloquium on Mechanical Fatigue of Metals, 5-7th September 2016, Gijón, Spain.

6. A. Chauhan*, J. Aktaa, *Deformation behavior of ODS steels under tensile and cyclic loading*, MATISSE WP4 2nd Technical Meeting, 6-7th June 2016, Helsinki (Espoo), Finland.

7. A. Chauhan*, D. Litivnov, J. Aktaa, *High-temperature low cycle fatigue behaviour of a bimodal 12Cr-ODS steel*, 3rd ODISSEUS Workshop, 19-20th April, 2016, Helmholtz-Zentrum Dresden-Rossendorf, Dresden, Germany.

8. L. Straßberger, A. Chauhan, J. Aktaa, *LCF behavior of F/M and austenitic ODS steels at elevated temperatures*, 3rd ODISSEUS Workshop, 19-20th April 2016, Helmholtz-Zentrum Dresden-Rossendorf, Dresden, Germany.

9. A. Chauhan*, J. Aktaa, *Creep-Fatigue interaction in ODS steels*, 7th International conference on creep, fatigue and creep-fatigue interaction, 19-22nd January 2016, IGCAR, Kalapakkam, India.

10. A. Chauhan*, J. Aktaa, *Deformation behavior of ODS steels under cyclic loading*, MATISSE WP4 1st Technical Meeting, February 2015, CIEMAT, Madrid, Spain.

11. A. Chauhan*, J. Aktaa, *Tensile and cyclic properties of ODS steels*, 2nd ODISSEUS Workshop, Department of Materials, March 2015, University of Oxford, Oxford, United Kingdom.

12. S.R. Meka*, A. Chauhan, T. Steiner, E.J. Mittemeijer, *Development of austenite-martensite and ferrite-austenite duplex microstructure upon nitriding Fe-Mn alloys*, European Conference on Heat Treatment 2015 and the 22nd IFHTSE Congress, May 2015, Venice, Italy.